DEVELOPMENT OF TECHNIQUES FOR IN-SITU MEASUREMENT OF HEAT AND MASS TRANSFER IN AMMONIA-WATER ABSORPTION SYSTEMS

A Dissertation
Presented to
The Academic Faculty

By

Sangsoo Lee

In Partial Fulfillment
Of the Requirements for the Degree
Doctor of Philosophy in Mechanical Engineering

Georgia Institute of Technology

August 2007

DEVELOPMENT OF TECHNIQUES FOR IN-SITU MEASUREMENT OF HEAT AND MASS TRANSFER IN AMMONIA-WATER ABSORPTION SYSTEMS

Approved by:

Dr. Srinivas Garimella, Advisor
G. W. Woodruff School of Mechanical Engineering
Georgia Institute of Technology

Dr. Amyn Teja
School of Chemical and Biomolecular Engineering
Georgia Institute of Technology

Dr. S. Mostafa Ghiaasiaan
G. W. Woodruff School of Mechanical Engineering
Georgia Institute of Technology

Dr. Tom Fuller
School of Chemical and Biomolecular Engineering
Georgia Institute of Technology

Dr. Sheldon M. Jeter
G. W. Woodruff School of Mechanical Engineering
Georgia Institute of Technology

Date Approved: 28th of June 2007

To my parents – Their endless love and dedication all through their life

To my uncle and aunt –- Their support, trust and belief in my ability

To my sister and brother-in-law – Their efforts of taking care of my parents during my absence

To my other family – My fountain of joys and happiness

To my friends – Their valuable advice

To my God – Directing me to the way I need to go

I appreciate all of you and I could not be in this position without all your support and dedication.

ACKNOWLEDGEMENTS

I would like to thank my advisor Dr. Srinivas Garimella for supporting me for five years and his continuous efforts to bring the best out of me. The improvements I have earned through his guidance will help me for the rest of my career.

I would like to thank Lalit Bohra and Matt Determan for their cooperation and assistance in fabricating the test facility, which helped me get over several huddles. Discussion and collaboration with Mr. Bohra also provided invaluable guidance to me.

I would like to thank Brain Fronk and Todd Bandhauer for revising and making corrections to my thesis. I also would like to thank all STSL members: Jesse Killion, Akhil Agarwal, Biswajit Mitra, Vishwanath Subramanium, Ulf Andresen, and others. Together, they formed a good support structure and they always listened my questions. Without these, I would have never made it through.

Finally, I would like to thank my Ph.D. Reading Committee for their guidance and encouragement.

TABLE OF CONTENTS

LIST OF TABLES

LIST OF FIGURES

NOMENCLATURE

A	Area (m^2)
a	Inverse of the Characteristic Length of Packing (m^2/m^3)
$A_{effective}$	Effective Area (m^2)
A_{free}	Free Area (m^2)
$A_{frontal}$	Frontal Area (m^2)
Ar	Archimedes Number
C	Molar Concentration
C_T	Total Molar Concentration ($kMol/m^3$)
Cp	Specific Heat Capacity (kJ/kg-K)
C_V	Flow Coefficient
D	Binary Diffusion Coefficient (m^2/s)
$d\dot{m}$	Differential Mass Flow Rate (kg/s)
g	Acceleration due to Gravity (m^2/s)
Ga	Galileo Number
GAX	Generator-Absorber-Exchange
Gr	Grashof Number
h	Enthalpy (kJ/kg-K)
H_2O	Water
I.D.	Inner Diameter (mm, m)
Ja	Jacob Number
k	Conductivity (W/m-K)
L	Length (mm, m)
Le	Lewis Number
LiBr	Lithium Bromide
LMTD	Log Mean Temperature Difference (^oC)
$\dot{m}$	Mass Flow Rate (kg/s)
M	Molecular Weight (kg/kMol)
N	Number
$\dot{n}$	Molar Flux ($kMol/m^2$-s)

NH_3	Ammonia
Nu	Nusselt Number
O.D.	Outer Diameter (mm, m)
P	Absolute Pressure (kPa)
ppm	Parts per Million
Pr	Prandtl Number
q	Quality
Q	Heat duty (kW)
R	Thermal Resistance (K/W or m^2-K/W), Gas Constant (J/kmol-K)
Ra	Rayleigh Number
Re	Reynolds Number
Ref	Refrigerant
Reflux	Reflux
Sc	Schmidt Number
Sh	Sherwood Number
t	Thickness (mm)
T	Temperature (^oC)
Tube	Tube
U	Overall heat Transfer Coefficient (W/m^2-K)
V	Velocity (m/s)
x	Mass Concentration
$\tilde{x}$	Molar Concentration
y	Mass Concentration in Vapor Phase
$\tilde{y}$	Molar Concentration in Vapor Phase
z	Concentration of Condensing Flux or Condensate
$\tilde{z}$	Molar Concentration of Condensing Flux

Greek Symbols

α	Heat Transfer Coefficient (W/m^2-K)
β	Mass Transfer Coefficient (m/s)
Δ	Difference, Differential

δ	Film Thickness (m), Boundary Layer Thickness (m)
ε	Maximum Energy of Attraction between a pair of Molecules
Γ	Concentrated Solution Mass Flux (kg/m-s)
μ	Dynamic Viscosity (kg/m-s)
ν	Kinematic Viscosity (m^2/s)
ρ	Density (kg/m^3)
σ	Surface Tension (N/m), Collision Diameter
τ	Shear Stress (N/m^2)
Φ	Potential Energy of Interaction
Ω	Collision Integral or Angle in Cylindrical Coordinate

Subscripts

10	Interface condition for species 1
1	Species 1
1b	Bulk condition for species 1
A	Ammonia
Abs	Absorber
Ave	Average
amb	Ambient
air	Air
area	Heat Transfer Area (m^2)
$area_M$	Mass Transfer Area (m^2)
aw	Ammonia-Water
bulk	Bulk values
C	Coolant
Con	Condenser
Condensing	Condensing Flux
conv	Convection
cross , cr	Cross-sectional
Des	Desorber
DT	Drip tray

Eva	Evaporator
fg	Latent (Phase Change)
Film	Solution Film
ID	Inner Diameter (mm, m)
in	Inlet
ins	Insulation
int	Interface
L,l	Liquid
Latent	Latent Heat
m	Mass
max	Maximum
min	Minimum
o.t.	Outer Tube
out	Outlet
pool	Solution Pool
r	Tube Row
rad	Radiation
Rec	Rectifier
Ref	Refrigerant
Reflux	Reflux
sensible	Sensible heat
Sep	Separator
sol	Solution
shell	Absorber Shell
surf	Surface
t	Total or Tube
V, v	Vapor
W	Wall
w	Water or Mass Concentration

SUMMARY

An experimental investigation of heat and mass transfer in a horizontal tube falling-film ammonia-water absorber was conducted. A tube bank consisting of four columns of six 9.5 mm (3/8") nominal OD, 0.292 m (11.5") long tubes was installed in an absorber shell that allowed heat and mass transfer measurements and optical access. A test facility consisting of all the components of a functional absorption chiller was fabricated specifically for this investigation. Thus, a steam-heated desorber was used to generate ammonia-water vapor over a wide range of conditions. The ammonia-water vapor was rectified and condensed, followed by recuperative heat exchange before being expanded to the evaporator pressure. The cooling load was supplied to the evaporator by a combination of resistance heating and closed loop fluid heating. The evaporated refrigerant was preheated recuperatively by the fluid exiting the condenser and then flowed to the absorber to be absorbed in the test section. A solution heat exchanger between the absorber and desorber (and in some tests, a solution pre-conditioner upstream of the absorber) completed the ammonia-water loop.

Several variations of the basic system set up were fabricated to enable testing over the wide range of conditions (nominally, desorber solution outlet concentrations of 5 - 40% for three nominal absorber pressures of 150, 345 and 500 kPa, over solution flow rates of 0.019 – 0.034 kg/s.) Heat transfer rates were measured independently for both

sides of each component and energy balances were established based on mass, species and enthalpy balances for each component before test results were deemed acceptable. Care was also taken throughout the study to not only establish the desired conditions, but also to maintain the solution-side thermal resistance as the governing resistance so that absorption heat and mass transfer phenomena could be measured accurately. Measurements at the absorber were used to determine heat transfer rates, overall thermal conductances, solution and vapor-side heat and mass transfer coefficients for each test condition. The trends in heat and mass transfer coefficients were discussed, highlighting the effect of solution flow rate, solution concentration and absorber pressure. For the range of experiments conducted, the solution heat transfer coefficient varied from 923 to 2857 W/m^2-K while the vapor mass transfer coefficient varied from 0.0026 to 0.25 m/s and the liquid mass transfer coefficient varied from 5.51×10^{-6} to 3.31×10^{-5} m/s depending on the test condition. The solution heat transfer coefficient increased with increasing solution flow rate; however, the vapor and liquid mass transfer coefficients seem to remain unaffected with the variations in solution flow rate and were found to be primarily determined by the vapor and solution properties.

Pertinent dimensionless parameters were also computed from the measured solution heat and vapor mass transfer coefficients. The experimental heat and mass transfer coefficients were compared with the relevant studies from the literature. Based on the observed trends in the experimental data and from comparisons with the other studies, correlations were developed to predict heat and mass transfer coefficients in the vapor and liquid phases for the range of conditions tested. These correlations can be used to design horizontal tube falling-film absorbers for ammonia-water absorption systems.

CHAPTER 1. INTRODUCTION

1.1 Background

Although ammonia-based absorption systems have been developed from the mid 18th century (Burgett *et al.*, 1999), electric vapor-compression systems are more widely used at present. But national and international interest in the global climate change problem has focused attention on these absorption heat pumps, which are alternatives to CFC-based ozone-depleting vapor compression space-conditioning systems because of the use of environmental friendly natural refrigerants. In addition, absorption systems could be cost effective when the natural gas or steam is cheaper than electric rates, or when waste heat or hot water is available, and the peak electric utility load must be decreased.

Absorption systems generally have higher initial costs and larger overall system size than a comparable vapor-compression system. However, these high initial costs can be compensated for by the lower operating cost of absorption systems compared to vapor-compression systems. Many studies have been conducted to reduce the operating cost by increasing system performance. Heat-driven absorption systems, particularly those employing advanced cycles, could offer higher efficiencies than the corresponding vapor compression systems in the heating mode, and have the potential to be part of an overall Integrated Energy System that provides building cooling, heating, and power. A variety of absorption systems have been developed to improve performance. Advanced

cycles such as the Generator-Absorber-Heat Exchange (GAX) (Engler *et al.*, 1996; Garimella *et al.*, 1996), double-effect (Gommed and Grossman, 1990; Garimella *et al.*, 1992; McGahey *et al.*, 1994), triple-effect (DeVault and Marsala, 1990; Grossman *et al.*, 1994; Ivester and Shelton, 1994; Garimella *et al.*, 1997), and even quadruple- and multiple-effect absorption chillers (Ziegler and Alefeld, 1994; Grossman *et al.*, 1995) have been proposed to increase system performance. However, these advanced cycles increase the complexity of the system by using numerous heat exchangers and control systems, which could adversely affect the practical feasibility and economic viability of these systems.

The larger physical size of an absorption system compared to that of a vapor compression system is the main hurdle for the adoption of the absorption systems. The additional absorber and desorber components are generally larger than the compressor of a comparable vapor-compression system. Therefore, the reduction of overall system size by developing compact heat and mass exchangers is essential for the absorption system to be used for residential purposes. Absorption systems usually use one of two different working fluid pairs: ammonia/water or water/LiBr. In absorption systems with ammonia/water, ammonia is the refrigerant and requires rectification, while absorption systems with LiBr/water are susceptible to crystallization and also operate at sub-atmospheric pressures. The operating pressure and pressure difference of a system are especially important when compact systems are required, because a large operating pressure difference in a system allows compact heat and mass exchangers without significant adverse effects on system performance due to pressure drops in components and fluid lines. An ammonia/water absorption system operates at a higher operating

pressure difference (>1000 kPa) between the low pressure-side and the high pressure-side than a water/LiBr absorption system (- 100 kPa). Therefore, the ammonia/water working fluid pair is preferable for the design of compact absorption systems.

The absorber, in which refrigerant vapor is absorbed into the dilute solution with the release of a substantial amount of heat of absorption, governs the viability of the entire cycle and has been referred to as the "bottleneck" in the absorption heat pump. The ammonia-water fluid pair (unlike the $LiBr/H_2O$ fluid pair) has a volatile absorbent, thus presenting both heat and mass transfer resistances across the respective temperature and concentration gradients in both the liquid and vapor phases. The highly non-ideal ammonia-water fluid pair releases considerable amount of heat of absorption at the vapor-liquid interface that must be transferred across a liquid film and ultimately into the absorber coolant. Some of this heat released at the interface is also transferred to the vapor, depending on the local temperature differences. Furthermore, since there are different regions in the overall absorption process, particularly over the extremely wide concentration and temperature ranges of cycles such as the GAX cycle, the local concentration difference between the bulk and interface liquid and vapor phases could be so large that species are desorbed into the vapor phase, rather than being absorbed into the solution at some locations within the component.

1.2 Issues of Ammonia-Water Absorption

Absorption is a complex, coupled heat and mass transfer phenomenon governed by liquid and vapor phase saturation conditions, operating pressures and component geometry. Models for ammonia-water absorbers that account for heat and mass transfer resistances have been developed in literature. The results and predictions from these

models show a basic understanding of transport phenomena in the absorption process. However, these studies show contradicting conclusions about the roles of heat and mass transfer resistances in the vapor and liquid phases. Comprehensive critical reviews of absorption heat and mass transfer models (Killion and Garimella, 2001) and experiments (Killion and Garimella, 2003b) showed conflicting conclusions about absorption processes such as the relative importance of heat and mass transfer resistances in the two phases by different investigators, which means that there is still a lack of understanding of the inherently coupled heat and mass transfer process that leads to inaccurate and often grossly expensive and oversized heat and mass exchangers. The various driving potentials and local gradients inherent in the vapor and liquid phases can be quite different at conditions close to saturation and those that involve subcooling of the incoming liquid solution. Many studies in the literature have circumvented this issue by conducting studies on individual absorber components, in which a single-pressure test facility is used to supply dilute solution and vapor at near-saturation conditions that can be readily obtained because of the relative independence from conditions at the heat source (evaporator) and heat sink (condenser). In such cases, the inlet subcooling absorption portion is fairly minimal and does not significantly affect the overall process. In addition, the definition of the driving temperature difference is fairly straightforward in such cases, with most investigators choosing the saturation temperature of the liquid phase to establish quantities such as the log-mean-temperature difference between the solution and the coolant. However, inlet subcooling of the dilute solution entering an absorber is often inevitable in an actual absorption system, representing challenges to the isolation of the contribution of subcooling to the absorption process.

1.3 Scope of the Research

1.3.1 Objectives of the Current Research

The above discussion highlights the need to investigate absorber performance in a complete operational absorption system to yield insights about the influence of system operating conditions on the performance of the absorber. A full scale absorption system operating over a wide range of operating conditions is investigated to understand the influences of system operating conditions over a large range of flow rates, concentrations and pressures on the absorber heat and mass transfer characteristics. The test facility was designed and constructed with numerous control and plumbing options to enable measurements of heat and mass transfer coefficients in the absorber. Test results representative of realistic operating conditions and the basic understanding of heat and mass transfer processes obtained from this study can assist in the design of higher performance absorbers.

1.4 Organization of Thesis

Chapter 2 reviews selected literature on absorption. The experimental test facility and procedures used to acquire data for the present study are described in Chapter 3. In Chapter 4, methods for the analysis of data obtained from the present study are presented and explained. In Chapter 5, the results obtained from the data analysis are reported with interpretation. In Chapter 6, techniques to develop heat and mass transfer correlations are discussed in terms of non-dimensional numbers corresponding to the heat and mass transfer characteristics. In Chapter 7, a summary of results and conclusions from the present study is presented and recommendations for further research are provided.

CHAPTER 2. LITERATURE REVIEW

The literature related to the present study is reviewed in this chapter. The studies are subdivided into component level investigations and studies related to heat and mass transfer phenomena.

2.1 Component Level

Takuma *et al.* (1993) analytically and experimentally investigated heat transfer during condensation of ammonia/water vapor mixtures on a shell-and-tube heat exchanger. Prior to experiments on a full scale shell-and-tube condenser, simple tests were conducted to understand heat transfer mechanisms for the condensation of binary mixtures. A shell and two tubes with outside diameter of 10 mm and length of 30 mm were used for these simple tests. The ammonia concentration was measured using the Coherent Anti-Stokes Raman Spectroscopy (CARS) technique. A theoretical analysis based on the analogy between heat and mass transfer was developed and verified using the experimental results. This analysis was applied to predict heat duties of the full-size shell-and-tube condenser. The full size shell-and-tube condenser consisted of finned tubes with an outside diameter of 15.9 mm including fins and an inside diameter of 11.2 mm and length of 1 m. There were 38 tube rows with 17 tubes per row. The condenser was tested with an inlet vapor flow rate between 0.199 kg/s and 0.399 kg/s with a concentration of 54% at temperature between 139.2^{o}C and 146.8^{o}C. The coolant flow

rate ranged between 0.0661 kg/s and 0.01180 kg/s at temperatures between 24.3°C and 37.2°C. System pressure ranged between 181 kPa and 226 kPa. It was concluded from the ammonia concentrations in the vapor layer obtained by CARS technique that the accumulation of ammonia at the interface presented an important mass transfer resistance to condensation.

Panchal *et al.* (1997) developed a model of condensation of ammonia-water mixtures flowing on the outside of vertical tubes using the Colburn and Drew (1937) approach, and compared the results of their model with tests on similar geometries conducted at Oak Ridge National Laboratory. Their work focused not on absorption into an incoming liquid solution stream, but rather on condensation of a vapor stream of varying ammonia-water concentrations. The tested condenser was a vertical single tube with a nominal diameter of 25.4 mm, and length of 1.22 m. The vapor flow rate ranged between 1.1×10^{-3} kg/s and 2.5×10^{-3} kg/s with an ammonia concentration of about 90% at temperatures between 104°C and 113.7°C. The tested pressure was between 910 kPa and 960 kPa, and the condenser heat load between 1 kW and 3.75 kW. They found that the mass transfer coefficient increased as the vapor flow rate and the heat flux increased. The rate of condensation was calculated with three limiting conditions: an equilibrium condition, a perfect liquid mixing condition (the interfacial concentration equals that of the bulk liquid), and a no-mixing condition (the liquid phase mass transfer coefficient is negligible). The rates of condensation obtained from measured heat fluxes were compared with the results predicted by analytical methods. They noted that the assumption of perfect liquid mixing predicted the data better than the other limiting conditions at an intermediate vapor mass flow rate of around 8.5×10^{-3} kg/s, while it over-

predicted heat fluxes at low vapor mass flow rates of around 1.25×10^{-3} kg/s. They concluded that diffusion in the vapor phase presented a significant resistance to the binary-fluid condensation process.

Potnis *et al* (1997) developed a computer program that simulated the GAX process with liquid-film absorption over a coiled fluted tube with counter-current vapor flow, and convective desorption inside the fluted tube. The component consisted of a 39 m long fluted helical coil surrounded by cylindrical jackets. Desorption occurred inside the tube, while absorption occurred on the outside of the tube. A solution for desorption flowed on the inside of tube with a flow rate of 9.9×10^{-3} kg/s at 39.9°C, concentration of 52.2%, and pressure of 1534 kPa. The solution for absorption flowed on the outside of tube with a flow rate of 1.1×10^{-2} kg/s at 74.8°C and a concentration of 30.9%. The vapor flow rate was 3.4×10^{-3} kg/s at 74.8°C with a concentration of 95.8% and pressure of 560 kPa. The tube-side solution temperature increased due to the heat of absorption on the outside of the tube. The Colburn and Drew (1937) approach was used to model absorption as the condensation of binary mixtures. It was found that the mass transfer resistance was primarily in the vapor phase, although the liquid-phase mass transfer resistance was not negligible. The heat transfer coefficients of flow-boiling (desorption) were higher than those of the absorption-side by an order of magnitude. This difference between the heat transfer coefficients showed that the component was controlled by the absorption-side resistance. It was also found that the mass transfer boundary layer of the gas phase was thicker than the heat transfer boundary layer of the gas phase. Therefore, a promoter to increase turbulence was suggested for the mass transfer boundary layer on the gas side.

Kang *et al.* (1997) developed a generalized design model with a combined heat and mass transfer analysis for components for the NH_3-H_2O GAX cycle. In their model, the mass transfer resistance within the liquid film was neglected on the basis of an assumption of thin film flow. A solution-heated desorber with a vertical fluted tube on the inside and a smooth tube on the outside was modeled. The ammonia concentration in the absorbing/desorbing vapor film was obtained by using combined heat and mass transfer analysis. The analysis of ammonia composition in the absorbing/desorbing vapor, z, was used to generate a composition map by considering both diffusion and mass transfer equations for each component of ammonia/water. It was found that the direction of mass transfer of ammonia and water were the same for the rectifier, evaporator, and condenser, while these directions were opposite to each other for the absorber and desorber. The generalized design tool was capable of modeling several components within an absorption system.

2.2 Falling-Film Absorption

Falling-film type absorbers with horizontal or vertical geometry are used in absorption systems. This type of absorber has high heat and mass transfer coefficients with a simple geometry. In this section, studies related to heat and mass transfer during the absorption process, and experimental or theoretical studies of falling-film absorbers are reviewed.

2.2.1 Heat and Mass Transfer Processes

As early as 1924, a fundamental basis for absorption and escape of gas from a liquid-gas system was provided by Lewis and Whitman (1924), who noted that these

processes occurred at non-equilibrium conditions tending toward equilibrium. They noted that the absorption rate of a solute from gas to liquid was limited by the process of diffusion, and other reaction processes had no appreciable effect upon the absorption rate because they took place relatively faster than the rate of diffusion. Keeping other variables constant, the rate of absorption was controlled by the diffusion rate of solute through gas and liquid surface films at the gas-liquid interface. The dominant resistance to the rate of absorption was determined by the gas solubility. They noted that the mass transfer resistance on the gas-side was more dominant than that of the liquid-side mass transfer resistance for a high solubility gas, while the mass transfer resistance of the liquid-side is more dominant for a low solubility gas, and the gas-side and liquid-side mass transfer resistances were comparable for an intermediate solubility gas. Absorption processes were classified into two categories: gas bubbles through the liquid phase and gas passed over the liquid surface. They noted that gas bubbles flowing through the liquid phase were particularly suitable for the absorption of the less soluble gases, because a thinner liquid film layer around the gas bubbles can be obtained due to the low solubility of gas. Gas flow over a liquid surface was considered more suitable for the absorption of highly soluble gases. They also stated that the rate of absorption can be increased considerably by liquid mixing.

Higbie (1935) conducted an analysis of the resistance in the liquid film to absorption for relatively low solubility gases. He noted that the assumption "since the surface films are very thin, the actual amount of solute in the them at any one time is usually negligible compared to the amount diffusing through them" made by Lewis and Whitman (1924) was not valid if the period of contact between the gas and liquid was not

much longer than the penetration period which is the time for the dissolved gas to penetrate the liquid film. In other words, when the exposure time of liquid to gas is not long enough to attain steady-flow conditions by absorbing gas, the liquid-film mass transfer resistances are dependent on what occurs during the penetration period. By conducting experiments at exposure times between 0.01 to 0.1 second on the absorption of CO_2 gas into liquid water, he found that the rate of absorption increases to a maximum as exposure time is decreased; however he also found that there was a mass transfer resistance at the liquid-gas interface itself for shorter exposure times between 0.032 and 0.07 second.

Erickson *et al*. (1998) modified the Colburn-Drew equations for binary mixtures including phase change into a simplified form, which combined diffusion and bulk flow mass transfer contributions into one coefficient. They noted that this modified form of the Colburn-Drew equations could be used in a two-film resistance model of the vapor and liquid-side.

2.2.2 Experimental Work

Dorokhov and Bochagov (1983) conducted tests on the flow of water/LiBr (57% LiBr by weight) over a column of six horizontal tubes, where the heat duties were measured only for the last two tubes. The tests were conducted at absorber pressures of ~10 kPa, with the solution mass flux varying between 0.05 and 0.25 kg/m-s. Heat transfer coefficients were calculated from measured temperatures of the liquid incident on the tubes, heat fluxes, and water vapor pressures. A Nusselt number correlation was developed as a function of the solution Peclet number ($Pe_l = \mathrm{Re}_l \cdot \mathrm{Pr}_l$), film thickness and a characteristic length (half of the tube periphery in the case of a cylindrical tube). This

correlation was valid for $1 < 2 \cdot Pe_l \cdot \delta_l / (\pi \cdot d) < 20$. However, mass transfer was not considered in their study.

Nomura et al. (1994) conducted falling film tests on a bank of 13 horizontal tubes with Water/LiBr. Tubes of 16 mm outer diameter, 200 mm length, and a tube pitch of 21 mm were used in the study. Glass windows of 220 mm × 380 mm were installed to observe solution flow behavior and wetting conditions on the surface of each heat-transfer tube. The absorbent flow rate was 2.78×10^{-6} m^3/s - 1.22×10^{-5} m^3/s (10 - 44 l/h) at 55°C, while the refrigerant vapor flow rate was 2.78×10^{-5} m^3/s - 7.78×10^{-5} m^3/s (100 - 280 l/h) with an evaporating temperature between 7.5°C and 12.1°C. The cooling water flow rate was 5.56×10^{-5} m^3/s (200 l/h) at 32°C. The inlet concentration of the absorbent was 62% by weight. The concentration was measured by an ultrasonic concentration meter and the temperatures were measured at each tube and between tubes. Solution wetting was investigated by tracing photographs taken during the tests and laser holographic interferometry. From these investigations, it was found that the wetting ratio decreased from 0.822 at the upper tubes to 0.233 at the bottom. With measured solution temperature profiles, it was noted that absorption occurred on the tube surface as well as between tubes. Also, the amount of absorbed refrigerant vapor was not uniform and decreased gradually from the upper to lower tubes. The solution temperature was seen to rise between tubes due to adiabatic absorption of vapor. The authors suggested that the actual surface area wetted by the solution should be used for determining heat and mass transfer coefficients in horizontal falling-film absorbers.

Hu and Jacobi (1996a; 1996b) presented a flow regime map for flow over horizontal tubes and investigated the effect of the fluid properties. The experiments were

conducted using water, ethylene glycol, water/glycol, oil and alcohol as liquid streams and air as the gas stream. Five different tubes of 9.5 mm, 12.7 mm, 15.9 mm, 19.0 mm and 22.2 mm diameter were used in the tests with tube spacings between 5 mm and 50 mm. The mass flow rate per unit length was up to 0.22 kg/m-s. Air was provided to the test section with a flow rate up to 15 m/s. They defined droplet, jet, and sheet-modes of flow based on the modified Galileo number ($Ga_l = \left(\rho_l \cdot \sigma_l^3\right) \Big/ \left(\mu_l^4 \cdot g\right)$). At low flow rates, droplet sites were not active simultaneously and droplets fell alternately from neighboring sites. As the flow rate increased, many sites became active. In the Jet mode, depending on the flow rate and the liquid, in-line (impinging and departure sites are the same), staggered and mixed type of jets were observed. Based on their criteria, they concluded that inertia-driven flows (high solution Reynolds number) will be in sheet mode, while gravity or surface tension driven flow (high modified Ga, where the modified Ga includes the influence of both surface tension and gravitational forces) will be in droplet mode. They used three tubes of 15.9 mm, 19.0 mm and 22.2 mm diameter with tube spacings between 5 mm and 50 mm to develop Nusselt number correlations for each regime. The mass flow rate per unit length was up to 0.72 kg/m-s with an inlet temperature between 20^{o}C and 40^{o}C and heat flux of up to 1.15×10^5 W/m^2. They developed Nu correlations for each flow regime using Re_l, Pr_l, Archimedes number ($Ar_l = \left(\sigma_l^3 \Big/ \left(\nu^4 \cdot \rho^2 \cdot g \cdot (\rho_l - \rho_v)\right)\right)^{1/2}$), tube spacing, and the tube diameter as the parameters for the flow of a water/glycol mixture on a horizontal tube. It was found that in the droplet mode, the effect of tube spacing was weak and the dependences of Reynolds and Prandtl numbers on the Nusselt number were more prominent than those of other modes.

However, these correlations did not account for gas absorption and were only for single-phase heat transfer in films falling around horizontal tubes.

Nosoko *et al*. (2002) investigated the absorption of oxygen in films of water on a completely wetted horizontal tube. Tubes of 16 mm outer diameter and 284 mm length were tested in 2, 4, 6, and 8 tube arrays with tube spacings of 2 mm, 5 mm, 10 mm, and 15 mm. The solution distributor had capillary tubes with an inner diameter of 1.5 mm and length of 8 mm and intervals of 15 mm or 30 mm. Criteria for various flow regimes (uniform sheet, jet, and droplet) were developed based on tube spacing and solution Reynolds number. Sheet-wise flow was observed at a 2 mm tube spacing, while droplet flow was the main mode for 5 mm and larger spacing. For droplet-flow, rapidly spreading waves on the film (generated from a droplet falling on the tube with absorbing vapor) were observed. These spreading waves became more intense as tube spacing increased. The solution Reynolds number was determined using the flow rate at the last row of the tube bank rather than the first row, since in many cases, droplets jumping off from the tubes at reasonably high solution Reynolds number resulted in a decrease in flow rate from the first row to the last row. The Reynolds number ranged between 10 and 150. Mass transfer coefficients were calculated for the absorption of oxygen in water at ambient pressure and temperature. The 15 mm distance capillary tubes caused more number of dripping sites than the 30 mm distance capillary tubes, and the number of dripping sites decreased toward the bottom of the tube bank. The number of tubes did not show an appreciable effect on the Sherwood number. It was observed that Sherwood number increased with an increase of Reynolds number, and also with an increase in tube spacing up to 5 mm, while the Sherwood number leveled off at a tube spacing of 10 mm

or higher. These observations were attributed to changes in the flow mechanism from film-wise to droplet-wise. They also quantified the compactness of the absorber using a coefficient of tube surface area per unit volume of absorber. It was suggested that a horizontal tube absorber, where tubes are arranged in a staggered pattern, would result in a more compact geometry than vertical surface absorbers.

Haselden and Malaty (1959) reported experiments on the absorption of anhydrous ammonia at atmospheric pressure into water and into weak ammonia solution. A vertical tube of 12.7 mm outside diameter was used. The exposed length of the tube was varied from 0.152 m to 1.219 m. Before testing, successive surface treatments of degreasing, building a layer of rust, and "Blueing" (which heats a tube to redness and quenches it in water) were conducted to obtain better wetting at lower solution flow rates. The absorbent flow rates ranged between 2.5×10^{-4} kg/s and 3.0×10^{-3} kg/s, and the cooling water flow rate was 3.667×10^{-5} m^3/s at 20^oC. It was observed that absorption enhanced tube-wetting at lower solution flow rates because the change in surface tension due to absorption increased the intensity of the ripples. They noted that the absorption conditions were mainly controlled by the cooling water temperature and the absorbent concentration. They compared their experimental results with Higbie's Penetration Theory (Higbie, 1935). They found that mass transfer coefficients from their experiment (7.87×10^{-5} m/s - 1.3×10^{-4} m/s) were 2-5 times larger than those predicted by the Penetration Theory (3.05×10^{-5} m/s - 3.81×10^{-5} m/s), and these differences were attributed to the mixing produced by the ripples in the liquid layer.

Wilke (1962) developed Nusselt number correlations for the flow of a water-glycol mixture over a vertical tube (42 mm O.D. and 2.4 m long) for different ranges of

the solution Reynolds number ($Re_l < 400$; $400 < Re_l < 800$; $Re_l > 800$). Tests were conducted with five different water-glycol mixture concentrations of 0, 16%, 55.5%, 77.1%, and 95% by weight. However, this study was on single-phase flow of solution, and not absorption of vapor into a liquid.

Kang *et al.* (1999) developed correlations for heat and mass transfer using data obtained on a plate heat exchanger with offset strip fins for surface enhancement. The ammonia/water solution flow rate ranged from 4.0×10^{-3} kg/s to 1.02×10^{-2} kg/s at concentrations of 5%, 10%, and 15% and at 17°C - 37.2°C. The vapor flow rate ranged from 0.62×10^{-3} kg/s to 0.90×10^{-3} kg/s with concentrations of 64.7% - 79.7% at 54.5°C - 66.5°C. They studied the effects of inlet sub-cooling, concentration difference between inlet solution and vapor, and solution and vapor flow rates on the heat and mass transfer performance of a counter current ammonia-water falling film absorber. The difference in temperature at vapor inlet and solution inlet ranged from 22.5°C to 40.0°C, and the inlet concentration difference (difference in concentrations at vapor inlet and solution inlet) was between 60% and 70%. The heat transfer coefficients were between 500 and 2100 W/m^2-K, while the mass transfer coefficients were between 1.0×10^{-5} m/s and 5.5×10^{-4} m/s. It was found that inlet sub-cooling could influence the absorber performance significantly. They noted that a lower inlet solution temperature and a higher vapor temperature improved heat and mass transfer performance; however, inlet sub-cooling had a more pronounced effect on the heat transfer and the Nusselt number decreased as the inlet liquid concentration decreased, while the Sherwood number increased. It was observed that there was some rectification of the vapor at the top, and desorption of water at the bottom end of the absorber. The rectification at the top of absorber occurred as the

bulk vapor concentration was lower than the equilibrium value at the liquid-vapor interface. Film Reynolds number affected the Nusselt number more than the Sherwood number, while vapor Reynolds number affected the Sherwood number more. Empirical correlations were developed for absorber Nusselt number and liquid Sherwood number in terms of liquid and vapor Reynolds numbers, the ratio of the amount of sub-cooling to inlet temperature, and the ratio of concentration difference to inlet solution concentration. Complete wetting in the absorber was assumed.

Jeong *et al.* (1998) investigated a helical coiled-tube ammonia/water absorber in which dilute solution flowed over the outside of the tubes with the ammonia vapor flowing upward in the shell and coolant flowing within the tube. Experiments were conducted with and without absorption. The solution flow rate with absorption ranged between 4.9×10^{-3} kg/s and 1.97×10^{-2} kg/s with a concentration of 1.2% - 2.2% at 66°C - 69°C. The vapor flow rate ranged from 0.9×10^{-4} kg/s to 0.42×10^{-3} kg/s with a concentration of 63% - 77% at 66°C - 69°C. The coolant flow rate was 2.7×10^{-2} kg/s at 41°C - 46°C. The absorber working pressure was between 20 kPa and 40 kPa. Correlations for the Nusselt number were developed based on the solution Reynolds number. It was found that film heat transfer coefficients were lower with absorption than those without absorption, possibly due to insufficient wetting caused by vapor shear. Kwon and Jeong (2004) studied the effect of vapor flow direction on heat and mass transfer in a helical coil falling-film type absorber and developed Nu_l correlations for a helical coil absorber used in ammonia/water absorption for both counter-current and parallel flow arrangements using the solution Reynolds number and the liquid-vapor interfacial shear stress ratio. They used a 12.7 mm diameter tube coiled over an 82.7 mm

diameter for this study. The absorber was 600 mm long with a shell diameter of 114 mm. The solution mass flux varied from 4.43×10^{-3} kg/m-s to 90.9×10^{-3} kg/m-s at dilute solution concentrations of 3.13%, 14% and 30.0%. The tests were conducted at absorber pressures of 17 - 193 kPa and the solution temperatures were close to the saturation temperature corresponding to the absorber pressure and solution concentration. They found that despite the solution film being in the laminar regime, the total heat transfer rate increases with an increase of the solution flow rate and Nu_l is primarily affected by the solution Reynolds number. This was attributed to intensified mixing and wetting. The large specific volume results in higher vapor velocities, which in turn causes unfavorable distribution of the falling-film. The effect of vapor flow direction decreases as the ammonia solution concentration is increased and the effect of liquid-vapor interfacial shear stress can be neglected in the parallel flow arrangement.

2.2.3 Relevant Studies

Andberg and Vliet (1987) presented a model of vapor absorption into a water/LiBr solution film flowing over a cooled horizontal tube. Velocity, temperature, and concentration profiles, and absorption and heat transfer rates were investigated by solving momentum, energy, and species equations with boundary layer assumptions and finite difference methods. A tube of 19 mm outer diameter was used with a solution flow rate per unit length of 0.02 kg/s-m and impinging velocity of 0.6 m/s at temperatures between 32^{o}C and 46^{o}C. A cooling water heat transfer coefficient of 4000 W/m^{2}K at 30^{o}C was assumed. The solution film was introduced as a plane jet impinging on the top of the tube and limited to developing laminar non-wavy film flow. Three solution regions were considered in the mathematical model: turning jet region, turned jet region,

and fully viscous region. The turning jet region was considered at the location where the plane jet impinged on the top of the tube similar to the impingement of an inviscid jet on a flat plate. The turned jet region was located between the turning jet region and the fully viscous region, so that the jet is completely turned around the tube, but the boundary layer is not developed in the entire flow. The fully viscous region was at the location where the boundary layer flow rate equaled the total film flow rate, and viscous effects fully permeated into the film. It was found that the velocity distribution in the film was not significantly different from the classical solution by Nusselt except in a small region of solution impingement. The film entry temperature showed strong influences on the absorption rate. The absorption with a lower inlet temperature was 1.8 times higher than that with a higher inlet temperature. For an inlet mass flow rate of 2.0×10^{-2} kg/m-s, the outlet mass flow rates were 2.02×10^{-2} kg/m-s, with the low inlet temperature of 32^{o}C and 2.0106×10^{-2} kg/m-s with the high inlet temperature of 46^{o}C, respectively.

Kirby and Perez-Blanco (1994) developed a simultaneous heat and mass transfer model for a horizontal tube falling-film absorber with water/LiBr. They defined three distinct solution flow regimes in a horizontal tube absorber: falling-film regime, droplet-formation regime, and droplet free fall regime. In their model, three governing equations were used with three different mass transfer correlations for each flow regime due to the differences in the flow characteristics of each regime. Six tubes per row with an outer diameter of 19 mm and total length of 0.28 m were used in their simulation. The solution flow rate ranged between 0.006 kg/s - 0.04 kg/s (Re number of 13 - 98) with inlet concentrations of 60% and 62% at saturation temperature. The upper limit of the film Re number represented the onset of solution bridging, while the lower limit of the film Re

number represented the minimum solution flow rate to obtain complete wetting of the coolant tubes. The coolant flow rates ranged from 0.025 kg/s to 0.125 kg/s at 20°C - 33°C. The working pressure of the absorber was between 0.767 kPa - 0.933 kPa (5.75 - 7.0 mmHg). They found from the simulated results that most of the absorption occurred during the droplet-formation flow regime, and the "bridging" of solution between tubes decreased the overall mass transfer. Although the film thickness was obtained from the solution Reynolds number and a thick film could absorb more water than a thin film, the concentration change of the thin film was much higher than that of a thick film. They also found that a major part of the mass transfer occurred in the droplet-formation flow regime, while the heat transfer to the coolant occurred in the falling-film flow regime. Sub-cooling of solution film increased to a maximum as the film Re number increased in the mid-range of the film Re number (13 - 38); however, solution sub-cooling decreased with a further increase in the film Re number because the solution was not cooled efficiently due to an increase in the film thickness.

Jeong and Garimella (2002) investigated a LiBr-water falling film absorber using a three flow regime model (falling film, droplet formation, droplet fall) and addressed the effect of incomplete wetting on the heat and mass transfer processes by introducing a surface wetting ratio. Their predictions were compared with the experimental results of Nomura *et al.* (1994). The tube bank consisted of 13 tubes with an outer diameter of 16 mm, length of 200 mm, and a tube pitch of 21 mm. The absorbent flow rate ranged between 0.6×10^{-2} kg/s and 0.106 kg/s with an evaporating temperature between 6°C and 12°C. The cooling water flow rate was 0.0556 kg/s at 32°C. It was found that with the wetting ratio was significant in determining the performance of an absorber with low

solution flow rate, and absorption occurred mainly in the falling-film and droplet-formation regimes. It was also found that the vapor was absorbed more near at the top tube than at the bottom, and more in the falling-film regime than the other regimes. The portion of absorbed vapor in the droplet-formation regime increased as the flow rate increased.

Killion and Garimella (2003a) utilized high-speed digital video to investigate the details of flow on a horizontal tube bank and presented the characteristics of droplet formation and its effects on the heat and mass transfer processes in an absorption system. A single column of six horizontal brass tubes with diameter of 12.7 mm, length of 300 mm, and tube spacing of 38.1 mm was used to visualize falling-films of water over the tubes. A tube with a diameter of 6.4 mm and six holes of 0.9 mm surrounded by a tube with a diameter of 13 mm was used as the solution distributor. From their observations, the mechanisms of flow over horizontal tubes and various interactions between these mechanisms were identified: the development of droplet formation sites from the bottom of a smooth film, progression of shape transitions through the development of the droplets, stretching of the liquid bridge between the tubes and droplets, breakup of the liquid bridge, generation of satellite droplets, and waves on the tube surface generated by droplet impact. It was noted that a significant portion of the liquid ended up as a droplet at the underside of the tube within 30 ms from impact. They suggested two areas of future research: the contribution of a forming droplet to the total absorption including the circulation patterns during droplet formation, and the analysis of the absorption process by tracking the fluid flow from the formation of the droplet through the impact process.

Killion and Garimella (2004) conducted a three-dimensional simulation of LiBr-water solution flow around an array of 15.9 mm diameter tubes with a 15.9 mm tube spacing using the volume of fluid method. A simple 2-D model based on an axi-symmetric column of spheres was also conducted to compare with the 3-D model results. It was found that a fully three dimensional model was required to capture the detailed droplet mode and falling film behavior such as droplet sizes, interaction between droplets, and saddle waves in the falling-film type absorber which were discussed in their earlier paper (Killion and Garimella, 2003a).

Goel and Goswami (2005b) presented a new design of a falling film absorber with ammonia/water to reduce the absorber size, and numerically investigated the performance of the proposed design. It was noted that the key features of an efficient design included high heat and mass transfer coefficients and a large contacting surface area. Tubes with an outer diameter of 3.2 mm and length of 100 mm were used with a vertical pitch of 8 mm and traverse pitch of 16 mm. There were 15 tube rows per pass and 4 tubes per row. Since the interfacial surface area (between the liquid and vapor phases) of conventional falling-film type horizontal absorber was limited to the surface area of the coolant tubes, the proposed design used a mesh between horizontal tubes to form a liquid film between horizontal tubes. This mesh increased the interfacial surface area and improved solution wetting. The absorber with the mesh had a liquid-vapor interface area of 0.266 m^2 area and a coolant surface area of 0.185 m^2. The simulated absorbent flow rate was 0.01 kg/s at a temperature of 50^oC with a concentration of 25%. The vapor flow rate was 0.15×10^{-2} kg/s at 27^oC with a concentration of 99.7%. The cooling water flow rate was 0.05 kg/s at 29.5^oC. The system pressure was 300 kPa. The resulting heat duty was 2.68 kW with an

outlet solution concentration of 34.7%. The proposed absorber was compared with a horizontal falling-film absorber with a liquid-vapor interface and coolant surface area of 0.245 m^2. It was found that a 25% size reduction could be achieved with the proposed absorber design compared to a conventional horizontal falling-film absorber.

Ruhemann (1947) developed a method for modeling a vertical helical tube absorber with anhydrous ammonia vapor. A simplified absorption model was used for a vertical helical absorber. This model considered a vertical wall with cooling water flowing up on one side and a liquid film falling down the other side. Boundary layers were considered at the coolant-wall interface, the wall-liquid interface, the liquid-vapor interface for the liquid, and the liquid-vapor interface for the vapor. Several assumptions were made in the modeling including: the gas occupied the whole absorber at the same composition, the heat of absorption was generated at the liquid-vapor interface, the liquid layer was thin, and heat transfer resistances were considered in only the liquid film near the wall and the water film on the other side of the wall. It was also assumed that ammonia vapor was free of air and the liquid was heavily stirred. For the purpose of illustration to understand the effect of heat and mass transfer coefficients on absorption, two arbitrary cases were compared with both having heat duties of 8.72 kW, an inlet concentration of 9.5% at 30^oC and cooling water temperature of 20^oC. Case A had a high heat transfer coefficient (581.5 W/m^2-^oC) with a low mass transfer rate (6.33×10^{-3} kg/s-m^2 at atmospheric pressure), while Case B had a low heat transfer coefficient (232.6 W/m^2-^oC) with a high mass transfer rate (1.39×10^{-2} kg/s-m^2 at atmospheric pressure). Although absorber lengths required for these two cases with the same heat duty were different, temperature profiles for these two cases were compared up to the same length

of absorber. It was found that in Case A, the temperature profile of the liquid fell through the whole length of the absorber; however, in Case B, it rose steeply from the initial given temperature, reached a maximum and then decreased rapidly. Based on these observations, he noted that appreciable errors would result if the performance of the absorber was predicted based on the heat transfer coefficient without taking the mass transfer coefficient into account.

Perez-Blanco (1988) presented a simple 1-D model for the absorption process in a falling-film absorber in which water transport was accounted for both into and out of the solution film. To avoid unrealistic excessively high mass transfer rates at the interface, he used a two-film model to decouple the interface concentrations of ammonia in the liquid and vapor. He assumed a linear temperature profile inside the film, and the interface temperature was related with the bulk-film and vapor temperatures through the vapor-side and liquid-side heat transfer coefficients. A film mass transfer coefficient obtained from a simple penetration theory was used to compare with the data. A tube of 12.7 mm diameter coiled with six turns of diameter 82.6 mm was simulated as an absorber. The solution flow rate was 6.3×10^{-3} kg/s with inlet and outlet concentrations of 3.3% and 17.94% respectively. The absorbed mass flow rate was 1.12×10^{-3} kg/s. It was found that the solution flow rate and liquid-phase mass transfer coefficient influenced the absorber performance significantly and the importance of the coolant heat transfer coefficient increased as the solution approached saturation conditions. It was also found that there was excessive water evaporation and migration in the vapor phase, which degraded the absorber performance.

Palmer and Christensen (1996) developed a model for predicting the performance of three different fluid distribution inserts in a vertical fluted-tube absorber for the GAX cycle. The simulated absorber consisted of coaxial tubes. The outer annulus consisted of a smooth tube on the outside and a fluted tube on the inside, and the inner annulus was formed between the fluted tube and an insert. Cooling water flowed through the outer annulus from bottom to top, while solution flowed through the inner annulus from top to bottom. The vapor was introduced at the bottom to form counter-current flow with the solution. It was assumed that the liquid film was well mixed, so that there was no concentration gradient across the film, and a 33% wetting fraction of the actual surface area was used in the model. It was found the wetting ratio increased as the concentration of the concentrated solution was increased.

Chen and Christensen (2000) developed a mathematical model for heat and mass transfer in an ammonia-water vertical falling-film type absorber to understand the effect of inlet solution sub-cooling. It was noted that frequent breaks of the thermal and concentration boundary layers in the film due to mixing were desirable to maintain thin thermal and species boundary layers. Absorption was considered to occur in two different processes: inlet solution sub-cooling with an adiabatic wall, and absorption in the saturated solution by a cooled wall. With assumptions of linear concentration and temperature profiles, the solutions of these two processes were superposed. It was found that heat and mass transfer coefficients were affected by the sub-cooling of the inlet solution and the film thickness, and heat and mass transfer coefficients decreased as the degree of solution sub-cooling increased.

Gommed *et al.* (2001) numerically studied heat and mass transfer during absorption of ammonia-water vapor into a laminar falling-film inside a vertical tube where the vapor flows parallel to the solution. They solved momentum, heat and mass transfer equations in both axial and radial directions. The numerical method was based on the finite volume method to calculate heat and mass fluxes, which yielded heat and mass transfer coefficients. In the modeling, a tube with an outer diameter of 15 mm and vertical length of 1 m was considered. The flow rate of solution was 0.06 kg/s at an inlet temperature of 55^{o}C with a concentration of 35% and a system pressure of 600 kPa. The vapor was superheated by 2^{o}C at the absorber inlet and the vapor flow rate was 0.015 kg/s at a temperature of 10.9^{o}C with concentration of 99.9%. It was found that the heat transfer coefficient increased as the liquid flow rate decreased because the thinner film yielded an increase in the absorption rate along the tube, although the absorption rate at the entrance region was reduced. It was also found that the inlet conditions of the liquid and vapor affected the absorption rate significantly, and the diffusion coefficient and thermal conductivity of the liquid had a pronounced effect on the absorbed vapor mass. The absorption process was controlled by the liquid solution side and the diffusion coefficient in the gas phase had a small effect on the absorption process.

Goel and Goswami (2005a) analytically investigated heat and mass transfer in an ammonia/water absorber based on lamella plates with an assumption of complete wetting. Four lamella plates per row with a width of 150 mm and spacing of 10 mm between adjacent cooling plates were considered. The simulated absorbent flow rate was 0.02 kg/s at a temperature of 50^{o}C with a concentration of 25%. The vapor flow rate was 0.4×10^{-2} kg/s at 27^{o}C with a concentration of 99.7%. The cooling water flow rate was

0.504 kg/s at 29.5°C. The system pressure was 200 kPa. The resulting heat duty was 8.34 kW with an outlet solution concentration of 37.5% and a coolant temperature of 33.5°C. By accounting for the heat and mass transfer resistances in both the vapor and liquid phases and using a finite difference numerical scheme, they concluded that the liquid-side heat transfer resistance was negligible, the coolant-side heat transfer resistance dominated the overall absorption process at the solution inlet, and the liquid phase mass transfer resistance controlled the overall absorption process. Sub-cooling the solution was found to improve the performance slightly, but the coolant inlet temperature was found to have a significant effect on the absorption rate. Water desorption was observed near the vapor inlet. It was also concluded that the film-side mass transfer resistance was dominant overall and the coolant inlet temperature had a significant effect on absorption rate.

Fernandez-Seara *et al.* (2005) presented an analysis of the heat and mass transfer processes taking place in a co-current vertical shell-and-tube type absorber. The 0.9 m long simulated absorber consisted of 40 tubes with an outer diameter of 25 mm and 12 baffles for the distribution of coolant. The absorbent flow rate was 0.0278 kg/s at a temperature of 45°C and a concentration of 22.5%. The vapor flow rate was 4.17×10^{-3} kg/s at 10°C with a concentration of 99.9%. The cooling water flow rate was 0.417 kg/s at 25°C. The ammonia vapor was distributed by small nozzles and the weak solution was introduced at the bottom of the absorber in co-current flow. A differential mathematical model accounted for churn, slug and bubbly flow patterns separately, and simultaneous heat and mass transfer processes in both the liquid and vapor phases. The churn flow regime had an entrance effect just after the inlet nozzle. The slug flow pattern was

characterized as bullet shape bubbles separated by slugs of liquid during the rising of the vapor, and bubbly flow was characterized by isolated spherical bubbles rising co-current with the liquid at the end of absorption. The absorption process was rapid in the churn and in the slug regions, and slow in bubbly flow. Water desorption was predicted at the beginning of the absorption process. It was found that the interface temperature was the same as the bulk solution temperature, which implied the heat transfer resistance was mainly located in the vapor phase. However the heat and mass transfer coefficients in the vapor phase had no significant effect on the absorption process.

Lee *et al.* (2005) developed a combined empirical and numerical method to investigate the heat and mass transfer characteristics of falling film absorption in a shell-and-tube ammonia/water absorber. The absorber consisted of a shell with a diameter of 300 mm and a length of 0.15 m and 91 tubes with a diameter of 10 mm, length of 0.1 m, and tube pitch of 15 mm. It was noted that the falling-film thickness of a horizontal tube in the shell-and-tube absorber was three times thicker than that of the ideal film on a vertical flat plate with the same heat transfer area. It was also noted that the absorption rate decreased as the inlet temperatures of the solution and coolant increased. The lower coolant temperature significantly increased the heat transfer performance and the rate of absorption of ammonia.

2.3 Bubble Absorption

In bubble-type absorbers, vapor and dilute solution flow through a tube in forced convection, rejecting the heat of absorption to a coolant.

Merrill *et al.* (1994) studied compact bubble type absorbers experimentally at generator-absorber heat exchange conditions using passive enhancement techniques.

They investigated bubble behavior for effective bubble injection and increasing the interfacial area per unit volume of vapor and liquid mixing at the vapor-liquid interface by breaking the vapor up into small bubbles and injecting them into the liquid using a finite difference method and calculated local heat and mass transfer coefficients. The first generation absorber was a U-shaped concentric tube heat exchanger with a height of 0.5 m and width of 127 mm. A tube with a diameter of 12.7 mm was used for the solution-side and a tube with a diameter of 23.8 mm was used for the coolant-side. The solution flow rate ranged from 2.83×10^{-3} kg/s to 5.59×10^{-3} kg/s at 120^{o}C with a concentration of 10% and a system pressure of 503 kPa. The vapor flow rate ranged between 1.55×10^{-4} kg/s and 1.85×10^{-4} kg/s at 41.1^{o}C with a concentration between 91% and 93%. The coolant flow rate ranged from 3.1×10^{-3} kg/s to 5.52×10^{-3} kg/s at a temperature of approximately 76^{o}C. The coolant heat transfer coefficient was 1500 W/m^{2}-K. Since the resulting GAX loads of the first generation absorber ranged between 0.43 kW and 0.5 kW and these GAX loads were less than the proposed baseline GAX load of 2.6 kW, they used numerous passive enhancement techniques in their second generation vertical-tube bubble type absorber. The tested solution conditions for the second generation absorber were similar to those of the first generation. Heat transfer was enhanced by repeated roughness and internal spacers. Mass transfer was enhanced by the use of static mixers, variations of flow cross-section areas, and numerous vapor injector designs. The resulting GAX load of the second generation absorber ranged between 1.44 kW and 1.56 kW. This increase in GAX load was because of an increased heat transfer coefficient on the coolant-side due to the enhancement techniques. In their continued work (Merrill *et al.*, 1995), performance results of three different compact

bubble absorbers with similar configurations to those in their earlier work (Merrill *et al.*, 1994) were presented. Two absorbers (Absorber I, Absorber II) employed internal repeated roughness and external flow spacers, while the other absorber (Absorber III) employed fluted tubing and external spacers to increase turbulence within the fluted tubing. The change in design from absorber I to absorber II focused on increasing the residence time of the vapor bubble and simplification of the injection process by increasing the length of the heat exchanger from 2.54 m to 3.05 m and increasing heat exchanger surface area from 0.087 m^2 to 0.11 m^2. It was found that passive heat transfer enhancement techniques could increase the GAX load, and decrease the absorber size. However, it was suggested that the knowledge of variations in the internal heat transfer coefficient with vapor flow rate are required for further absorber development.

Herbine and Perez-Blanco (1995) modeled a vertical-tube bubble ammonia-water absorber with co-current solution and vapor flow in an inner tube, and countercurrent coolant flow in the annulus. Several simplifying assumptions were made including: the absorption process was at steady state, the process occurred at a constant pressure, all bubbles had the same diameter and velocity at a given location along the absorber length, bubble breakup and coalescence were negligible, resistance to mass transfer in the bubble was negligible, and no direct heat transfer took place between the vapor and the coolant. They found that as the ammonia concentration within the bubble decreased to that at equilibrium, water transfer was in a direction opposite to that of ammonia transfer; however, when the ammonia concentration dropped below that at equilibrium, water and ammonia transfer were in the same direction.

Dence *et al.* (1996) designed and simulated an annulus-shaped co-flow bubble absorber with a helical bubble injector for a GAX cycle application using helical cooling water channels. For designing the GAX absorber with a heat duty of 4.7 kW, a maximum bubble diameter of 4 mm and vapor and liquid mass flow rates were predicted by using empirical heat transfer coefficients. The solution and vapor flows were introduced at the bottom of the absorber, and cooling water was introduced at two different locations at the side and bottom of the absorber. Vapor was injected into the absorber using a helical tube with a diameter of 6.35 mm. There were a total of 8.5 helix turns with a height of 44.45 mm for each turn and 3.18 mm diameter holes at every 12.7 mm along the injector length. The solution flow rate was 9.49×10^{-3} kg/s with a concentration of 21% at 94.4^{o}C. The vapor flow rate was 1.91×10^{-3} kg/s with a concentration of 86.6% at 93.3^{o}C. The cooling water flow rate was 1.31×10^{-2} kg/s at 88.3^{o}C, yielding heat transfer coefficients of 13000 W/m^{2}-K for the outer channel and 18000 W/m^{2}-K for the inner channel.

Kang *et al.* (1998) evaluated heat and mass transfer resistances within liquid and bubble phases for a countercurrent bubble absorber made of plate heat exchangers with offset strip fins (OSF). It was concluded that the mass transfer resistance was dominant in the liquid region, and the heat transfer resistance was dominant in the vapor. The size of the bubble absorber was affected more by the interfacial mass transfer area and vapor hold up than by the heat transfer area.

Kang *et al.* (2002) developed an empirical correlation of the mass transfer coefficient and carried out parametric analyses on ammonia-water bubble absorption. In this study, orifice diameter, liquid concentration, and vapor velocity were considered as

key parameters for the mass transfer coefficient. A test section with dimensions of 80 mm × 53.4 mm × 300 mm was used with sight glasses for visualization with a high speed camera (shutter speed of 1/500 s). A tube with a diameter of 10 mm was used as a vapor distributor with three holes of 3.0 mm, 3.8 mm and 5.5 mm diameter. The ammonia velocity ranged between 1.25 m/s and 8.5 m/s with liquid concentrations of 0%, 10% and 20%, and liquid temperature of 22.5^{o}C. The bubble behavior and volumetric diameter of bubbles during absorption were observed. Based on this visualization, bubble absorption was divided into two processes: bubble growth and bubble disappearance. The bubble growth process occurred before the bubble detachment from the orifice, and the bubble disappearance process occurred after bubble detachment. A correlation of mass transfer coefficient in the bubble growth process was developed with liquid Schmidt number, vapor Reynolds number, and concentration difference between vapor and liquid. A correlation for mass transfer coefficient in the bubble disappearance process was developed with liquid Schmidt number, vapor Galileo number, and concentration difference between vapor and liquid as parameters. The mass transfer coefficient increased as the liquid concentration decreased and vapor Reynolds number increased for the bubble growth process, while the mass transfer coefficient increased as the Galileo number increased for the bubble disappearance process.

Lee *et al.* (2002) compared heat and mass transfer in two plate-type falling-film absorbers and a bubble type absorber with ammonia/water. Absorbers with dimensions of 11.2 mm × 26.4 mm × 3.0 mm and plates with three different surface treatments: smooth, hair-lined treated by laser, and sand-papered finish were considered and the plate with sand-paper finished was chosen because of good wettability through the plate. The

solution flow rate was 0.005 kg/s with solution concentration between 0% and 30% at 20^{o}C. The ammonia vapor flow rate ranged from 1.667×10^{-5} m^3/s to 1.5×10^{-4} m^3/s. For both absorbers, the heat transfer performance increased while mass transfer performance was not affected as the flow rate of solution increased. For the bubble absorber, heat transfer performance of the absorber increased as vapor flow rate increased due to the influence of the vapor flow rate on the thermal boundary layer, while the heat transfer performance of the falling-film absorber decreased as this flow rate of vapor increased due to the decrease in heat transfer area caused by channeling of the film at high vapor flow rates. Although the mass transfer performance of the plate-type bubble absorber was better than that of the plate-type falling film absorber, the amount of heat transferred with the falling-film absorber was higher than that with the bubble absorber at a high solution flow rate and a low vapor flow rate. They noted that a plate–type bubble absorber showed better performance overall than a plate-type falling-film absorber at low solution and high vapor flow rates.

2.4 Miniaturization of Absorbers

Since the use of additional heat exchangers and high initial cost are the disadvantages of an absorption system compared to a vapor compression system, attempts have been made to overcome these disadvantages by developing compact ammonia-water absorbers with higher heat and mass transfer performance. These attempts have included counter-current fluted-tube absorbers (Kang and Christensen, 1994; Kang *et al.*, 1994; Kang and Christensen, 1995) and a miniaturization technology for ammonia-water absorbers (Garimella, 1999; 2000).

Kang and Christensen (1995) investigated combined heat and mass transfer during ammonia/water absorption and developed a model for a fluted tube absorber based on porous medium considerations. The fluted tube absorber was considered to mitigate flooding phenomena at the liquid-vapor interface. The effect of thermal conductivities and porosities of porous media on the absorption rate, and geometric parameters of a fluted tube on heat exchanger size were investigated. A spirally coiled fluted tube was placed inside a cylindrical annular shell. The absorber adopted a confined cross-flow configuration with solution flowing perpendicular to the axis of the tube. A weak liquid solution with a flow rate of 0.071 kg/s at 352 K entered from the top of the absorber, and ammonia vapor at a flow rate of 0.034 kg/s at 283 K entered from the bottom. The coolant was 35% K_2CO_3 aqueous solution with a flow rate of 3.1 kg/s at a temperature between 315.4K and 318K. The system pressure was 600 kPa. A tube with an inner bore diameter of 19.1 mm and coiling diameter of 0.31 m was used. The absorption process was separated into three regions: a vapor region without a porous medium, a vapor region within a porous medium, and a liquid region within a porous medium. It was found that the absorption rate increased with an increase in the thermal conductivity and a decrease in the porosity of the porous medium. The size of the heat exchanger with a fluted tube could be reduced by 28% comparing to a heat exchanger with a smooth tube due to an increase in the heat transfer coefficient by 35% on the coolant side and 100% on the vapor side.

Garrabrant and Christensen (1997) developed a heat and mass transfer model validated by data on a compact absorber consisting of a corrugated and perforated fin surface placed between rectangular coolant channels for an ammonia/water absorption

system. A heat exchanger with dimensions of 0.432 m × 0.127 m and 6 or 7 perforations placed per row alternatively was used. Two channels with perforated and offset fins were machined into a 38.1 mm block of carbon steel, and a wall with a thickness of 11.3 mm was used to separate these two channels. The vapor flowed upward through perforations in the corrugated fins, while absorbent solution flowed through the corrugated fins. Solution pools were created at the corners formed by the perforated fin and the wall, until the solution level reached the bottom of perforations and then flowed downward through these perforations. The coolant flowed through the offset fin channel from the bottom to top of the absorber. The absorber with the perforated fin provided heat duties between 1.55 kW and 5.1 kW with a concentrated solution flow rate between 4.16×10^{-3} kg/s and 11.8×10^{-3} kg/s. The model was calibrated with a wetted fin area fraction, a film to fin heat transfer coefficient, and an adjustment factor to the mass transfer coefficient. It was found that the absorber performance was influenced significantly by solution concentration, solution and vapor Reynolds numbers and the shear force of the vapor.

Garimella (1999; 2000) developed a miniaturization technology for ammonia-water absorbers that used short lengths of very small diameter tubes placed in a square array, with several such arrays being stacked vertically and placed in a transverse orientation perpendicular to the tubes in adjacent levels. Liquid solution flowed in the falling-film mode counter-current to the coolant through the tube rows. Vapor flowed upward through the lattice formed by the tube banks, counter-current to the falling solution. The effective vapor-solution contact minimized heat and mass transfer resistances, the solution and vapor streams were self-distributing, and wetting problems were minimized. Coolant-side heat transfer coefficients were extremely high without any

passive or active surface treatment or enhancement, due to the small tube diameter. For the development of the model, a tube with a diameter of 1.59 mm and a length of 0.127 m was placed with a transverse pitch of 3.18 mm and a vertical pitch of 6.35 mm. Seventy five tube rows with 40 tubes per row and 15 rows per pass were used. The resulting absorber had a total surface area of 1.9 m^2 and a height of 0.476 m. To predict the absorber performance, an inlet solution flow rate of 0.0189 kg/s with a concentration of 20.6% at temperature of 98.5^oC was used. Vapor flowed at 0.0095 kg/s with a concentration of 0.995 at a temperature of 38^oC. The ethylene glycol/water solution of 50% concentration was used as the coolant with a flow rate of 0.5 kg/s at a temperature of 42^oC. The operating pressure was assumed to be 510 kPa. A preliminary model using the Price and Bell (1973) approach demonstrated that a 19.3 kW absorber, which corresponds to a 3-ton cooling system, could be built in a very small 0.127 m × 0.127 m × 0.476 m envelope. The average heat transfer coefficient of the solution-side was 2790 W/m^2-K and the coolant side heat transfer coefficient was 1604 W/m^2-K. It was noted that this modular design concept could be adapted for a wide range of absorption loads, and the concept could be extended to other components such as desorbers, evaporators, and condensers without major modifications. Meacham and Garimella (2002a) conducted absorption experiments on a prototype micro-channel falling-film absorber using the concept proposed by Garimella (1999; 2000). The absorber geometry consisted of short lengths (140 mm) of micro-channel tubes (1.575 mm O.D.) arranged in a square array. These tubes were arranged in 5 passes, where each pass consisted of 16 tube rows and each of the tube rows had 27 tubes. The resulting absorber had a total of 2160 tubes with a surface area of 1.5 m^2. The solution mass flux varied in the range 0.0014 - 0.0053

kg/m-s and the vapor flow rate generation fraction varied in the range 5 - 50%. The average absorber heat duties transferred were 4.86 kW - 16.23 kW with overall heat transfer coefficients between 133 W/m^2-K and 403 W/m^2-K and solution heat transfer coefficients of 145 - 510 W/m^2-K. Meacham and Garimella (2003) developed a heat and mass transfer model for the absorber using a technique first proposed by Colburn and Drew (1937) and adapted by Price and Bell (1973) for analyzing absorption as condensation of a binary vapor with a miscible condensate. This model was experimentally validated with the data of Meacham and Garimella (2002a) to predict the detailed temperature, concentration and mass flow rate profiles through the absorber. The effective surface area fraction ranged between 0.22 and 0.31. This ratio was used to account for the solution distribution and inadequate wetting of the tube surface. The predictions showed excellent agreement with the measured data both for the overall absorber and also for the individual passes. Meacham and Garimella (2004) subsequently fabricated an absorber with optical access which consisted of 1.575 mm outer diameter and 0.137 m long tubes with 10 passes, 2 rows per pass and 33 tubes per row. The overall size of this absorber was 0.162 × 0.157 × 0.150 m with a surface area of 0.456 m^2. The solution flow rate ranged from 1.51×10^{-2} kg/s to 2.66×10^{-2} kg/s with an inlet solution concentration between 28% and 35%. The absorber inlet pressure and temperature were varied from 355 kPa at 52°C to 680 kPa at 81°C. The absorber outlet conditions were 353 kPa at 34°C for a low temperature case, and 674 kPa at 52°C for a high temperature case with an outlet solution concentration between 44% and 52%. The vapor concentration varied between 93% and 98%. The coolant flow rate ranged from 9.5×10^{-5} m^3/s to 1.58×10^{-4} m^3/s. The heat and mass transfer process was monitored at 10

ms intervals using high-speed flow visualization to document different modes of absorption including falling film, droplet formation, detachment, fall, and redistribution. Absorption loads between 4.51 kW and 15 kW were transferred with overall heat transfer coefficients between 545 W/m^2-K and 940 W/m^2-K, and solution-side heat transfer coefficients between 638 W/m^2-K and 1648 W/m^2-K. Guided by the flow patterns, and after incorporating a revised flow distribution device, increased heat transfer and absorption rates were achieved compared to the earlier data of Meacham and Garimella (2002a) due to improvements in solution distribution and wetting of the tubes. In related research (Meacham and Garimella, 2002b), a shell-and-tube heat exchanger with small diameter tubes was also demonstrated as an absorber for residential heat pumps. An extremely compact absorber (76.2 mm outside diameter, 0.508 m long, 2.54 mm inside diameter, 1.026 m^2 overall heat transfer area) with a high surface/volume ratio, and vapor and solution flowing co-currently through 253 tubes was experimentally investigated. Experiments over a wide range of solution and coolant flow rates and vapor fractions were used to deduce overall and tube-side absorption heat transfer coefficients. The concentrated solution flow rate ranged between 0.018 kg/s and .0.30 kg/s with inlet qualities of 15%, 20%, 25%, and 30%. The coolant flow rates were 5.05×10^{-4} m^3/s, 3.79×10^{-4} m^3/s, and 3.79×10^{-4} m^3/s. It was noted that the effect of coolant flow rate was relatively small due to the high thermal resistance ratio between the solution-side and the coolant-side (10 to 33). Tube-side heat transfer coefficients between 376 W/m^2-K and 896 W/m^2-K were obtained. The shell-and-tube heat exchanger with small diameter tubes could transfer an absorption duty of a 10.55 kW. It was noted that improvement in

the distribution of the vapor-liquid mixture would further reduce potential mal-distribution at the entrance, resulting in even larger transfer rates.

Jeong and Garimella (2005) evaluated the applications of small diameter tubes for falling-film Water/LiBr absorbers using their three-flow-regime (falling-film, droplet formation, and droplet fall) model (Jeong and Garimella, 2002). It was noted that the increase in the number of small diameter tubes for a given surface area increases heat and mass transfer in the absorber because the total residence time of solution and the mixing frequency were increased. The total residence time of solution increased because the surface area occupied by the droplet formation region was increased by increasing droplet sites at the bottom of each tube, while the time required to form a droplet was not strongly dependent on tube diameter. The increase of mixing frequency also helps solution concentration redistribution and generation of fresh solution surface by mixing the solution as it impinged on the tubes below. Tube banks with different tube diameters (15.9 mm, 6.35 mm and 3.18 mm) were analyzed with a vertical pitch of 5.12 mm and horizontal pitch of 5.12 mm. Fourteen different arrangements were configured while keeping the total surface area of the absorber constant while changing the number of passes. An absorber with small diameter tubes (6.35 mm or 3.175 mm) delivered higher capacity than that with conventional diameter tubes (15.88 mm) of the same heat transfer area. This increase in capacity was attributed to the fact that vapor absorption in the droplet mode increased significantly with smaller diameter tubes.

2.5 Summary of Literature

From the above reviews of the literature, it can be seen that an understanding of heat and mass transfer resistances is important for the design of components used in

absorption systems (Ruhemann, 1947). Parameters such as vapor flow rate and liquid mixing are important in reducing heat and mass resistances (Potnis *et al.*, 1997). Although the absorption cycle consists of many components, heat and mass transfer in the absorber is more important than that in other components in determining overall cycle performance. Some early studies on the absorption process (Lewis and Whitman, 1924; Higbie, 1935) identified the importance of gas solubility and the contact period between vapor and liquid, and the concept of liquid and vapor side mass transfer resistances was used to understanding the absorption process. However, there are conflicting conclusions in the literature; the liquid-phase mass transfer resistance is considered dominant in some studies (Perez-Blanco, 1988; Gommed *et al.*, 2001; Fernandez-Seara *et al.*, 2005; Goel and Goswami, 2005b), while others concluded that the vapor-phase mass transfer resistance was dominant (Panchal *et al.*, 1997; Potnis *et al.*, 1997).

In studies on falling-film type absorbers, heat transfer correlations were developed for falling films with (Dorokhov and Bochagov, 1983) or without (Wilke, 1962) absorption. However, these studies were conducted with fluid pairs other than ammonia-water; e.g., LiBr/Water (Dorokhov and Bochagov, 1983), and Water/Glycol mixture (Wilke, 1962).

Recent experimental and theoretical studies (Hu and Jacobi, 1996b; Nosoko *et al.*, 2002) have addressed flow modes (sheet, jet, and droplet) in such absorbers. These studies were also conducted with fluid pairs other than ammonia-water, i.e., Water/Glycol mixture (Hu and Jacobi, 1996a, b), and Water/Oxygen (Nosoko *et al.*, 2002).

Some studies (Perez-Blanco, 1988; Kang *et al.*, 1999; Inoue *et al.*, 2004) have also developed models for heat and mass transfer resistances in the liquid and vapor phases. However, these studies were conducted at idealized and often unrealistic operating conditions compared to those in actual operating systems. Many of these studies were conducted at absorber operating pressures in the range 20 – 40 kPa (Jeong *et al.*, 1998) and at atmospheric pressures (Haselden and Malaty, 1959), whereas the absorber pressure in actual NH_3/H_2O absorption systems for even the refrigeration mode is greater than 150 kPa. Yet other studies were conducted with extremely low vapor concentrations such as 64.7 - 79.7% (Kang *et al.*, 1999) compared to the almost pure ammonia concentration in actual NH_3/H_2O absorption systems. Other studies used very low solution inlet concentrations such as 1.2 – 2.2% (Jeong *et al.*, 1998) at very low pressures (20 to 40 kPa), whereas such low concentrations are rarely seen in absorption systems except at GAX conditions that must also exhibit simultaneously high pressures.

Many of these test conditions do not represent a range wide enough to cover the operating conditions of the heating and cooling modes in higher efficiency cycles. The operating pressures for these studies were limited to a narrow range of pressures 17 – 193 kPa (Kwon and Jeong, 2004) or were conducted in test facilities where absorption and desorption occurred at the same absorber operating pressure and did not include the rectification, condensation, expansion, and evaporation steps (Perez-Blanco, 1988; Garimella, 1999; Garimella, 2000; Gommed *et al.*, 2001; Meacham, 2002; Meacham and Garimella, 2002a, 2004; Goel and Goswami, 2005b, a). As stated above, absorber pressures in actual NH_3/H_2O absorption systems are typically between 150 – 500 kPa for refrigerating, cooling, and heating mode operation.

Some studies on the bubble absorption (Merrill *et al.*, 1994; 1995; Lee *et al.*, 2002) have stated that heat and mass transfer in a bubble absorber can be better than that in a falling-film type absorber. However, heat and mass transfer processes in bubble absorption are also not well understood.

Recently, miniaturization technologies (Garimella, 1999; Meacham and Garimella, 2002a) have been introduced to develop compact absorbers with higher heat and mass transfer performance by using small diameter tubes. Although the results from these technologies showed better performance than those with conventional absorbers, the reasons for this improvement and a detailed understanding of the absorption process over a wide range for operating modes of an absorption system is still not available.

2.6 Research Needs

It can be seen from the studies discussed above that models for ammonia-water absorbers to account for heat and mass transfer resistances have been developed, and the results and predictions from these models show an understanding of some aspects of transport phenomena in absorption with binary fluids. However, conclusions from these studies about the role of the heat and mass transfer resistances in the vapor and liquid phase are not widely applicable. Also, the findings of these studies often contradict each other regarding the role of heat and mass transfer resistances in absorption, although it is commonly mentioned that the temperature and flow rate of the absorber coolant play an important role in absorption heat and mass transfer. Some investigators (Perez-Blanco, 1988; Gommed *et al.*, 2001; Fernandez-Seara *et al.*, 2005; Goel and Goswami, 2005b) report that the dominant mass transfer resistances is on the liquid-side, while other investigators (Panchal *et al.*, 1997; Potnis *et al.*, 1997) report that the mass transfer

resistances in the vapor phase dominates. Some of these different findings are due to the fact that heat and mass transfer in binary fluid ammonia/water absorption are different from condensation of single-component vapors. Also, many of the experimental studies thus far have been conducted over a narrow range of absorber operating conditions. The tested absorber conditions in many studies were considered as independent of the other operating conditions of the system, although the conditions of the absorber do depend on conditions of the other components during system operation. Therefore, the results from these studies could be valid in their range of test conditions, but not valid for a wide range of operating conditions that apply in a real system over its design range of operation. In addition, theoretical studies have been conducted with assumptions that are not clearly supported through experiments.

Based on the above discussion, there are still several areas of binary-fluid heat and mass transfer that are not well understood. The role of heat and mass transfer resistances in the vapor and liquid phases must be investigated over the wide range of commonly encountered operating conditions. To obtain such a wide range of realistic operating conditions at the absorber, a full-size test facility consisting of a condenser, an evaporator, a rectifier, a desorber, an absorber, and recuperative heat exchangers is required.

2.7 Objectives of the Present Study

The overall objectives of the present study are to understand heat and mass transfer phenomena in an ammonia-water absorber of a representative geometry and develop heat and mass transfer models with experimental validation over a wide range of

test conditions. Specific objectives to accomplish this overall objective are outlined below.

- Conduct ammonia-water absorption experiments on a representative horizontal tube-bank geometry
- Obtain heat and mass transfer coefficients in the absorber while operating in an overall operating absorption system over a range of commonly encountered operating conditions
- Interpret the relative influences of the heat and mass transfer resistances in the vapor and liquid phases that govern the absorption process
- Analyze the resulting heat and mass transfer coefficients, and develop correlations for ammonia-water absorption over the range of conditions investigated.

Table 2.1 Summary at the Relevant Studies at the Component Level

	Working Fluid	Mass Transfer /Phase Change	Geometry (mm)	Conditions			Specific Details	Major Findings
				Solution Side	Coolant Side	Pressure		
Condenser								
Takuma *et al.* (1993)	NH_3/H_2O	Yes	Shell–and–Tube Outside Tube OD: 15.9 Inside Tube OD: 11.2 Tube Length: 1 m Tubes per Row: 17 Rows per pass: 33	Inlet Vapor Flow Rate: 0.12 – 0.4 kg/s Vapor Concentration: 54% Vapor Temperature: 139.2 – 146.8°C	Flow Rate: 0.01180 – 0.0661 kg/s Temperature: 24.3°C – 37.2°C	181 – 226 kPa	Tests with a shell and two condenser tubes with outside diameter of 10 mm and length of 30 mm	Accumulation of ammonia at the interface presents an important mass transfer resistance to condensation
Panchal *et al.* (1997)	NH_3/H_2O	Yes	Vertical Single Tube Tube OD.: 25.4 Tube Length: 1.22 m Coil OD: 82.7 Coil Windings: 30	Vapor Flow Rate: 1.1×10^{-3} and 2.5×10^{-3} kg/s Vapor Temperature: 104 – 113.7°C Heat Load: 1 – 3.75 kW	Heat Transfer Coefficient: 23 kW/m^2–K Temperature: 22.9 or 25.2°C	910 – 960 kPa	Experiments and Analyses Perfect liquid mixing condition/ no–mixing conditions	The assumption of perfect liquid mixing predicted the data better than the other limiting conditions. Diffusion in the vapor–phase showed a significant resistance to the binary–fluid condensation process.
GAX Component								
Potnis *et* (1997)	NH_3/H_2O	Yes	Fluted Helical Coil Tube Length: 39 m	Desorption Solution Flow Rate: 9.9×10^{-3} kg/s at 39.9°C, Concentration: 52.2%, Absorption Solution Flow Rate: 1.1×10^{-2} kg/s at 74.8°C, Concentration: 30.9% Vapor Flow Flow Rate: 3.4×10^{-3} kg/s at 74.8°C Concentration 95.8%		Inside tube: 1534 kPa Outside tube: 560 kPa	Colburn and Drew (1937) approach	The mass transfer resistance was primarily in the vapor phase, although the liquid–phase mass transfer resistance was not negligible. The mass transfer boundary layer of the gas–phase was thicker than the heat transfer boundary layer of the gas–phase.

Table 2.1 Continued

	Working Fluid	Mass Transfer /Phase Change	Geometry (mm)	Conditions			Specific Details	Major Findings
				Solution Side	Coolant Side	Pressure		
GAX Component								
Kang *et al*. (1997)	NH_3 /H_2O	Yes	Solution–Heated Desorber Vertical Fluted Tube and Smooth Tube Smooth Tube Diameter: 36.7 Inner Bore Diameter: 22.7 Outer Envelope Diameter of Fluted Tube: 36.7 Number of Flutes: 29 Number of Starts: 5.	N/A	N/A	N/A	Provide component design procedures	The analysis of ammonia composition in the absorbing/desorbing vapor, z, was used to generate a composition map by considering both diffusion and mass transfer equations for each component of ammonia/water. The generalized design tool was capable of modeling several components within an absorption system.

Table 2.2 Summary of Relevant Experimental Studies on Falling–Film Absorption

	Working Fluid	Mass Transfer /Phase Change	Geometry (mm)	Test Conditions			Specific Details	Major Findings
				Solution Side	Coolant Side	Pressure		
Horizontal Tube Geometry Experiments								
Dorokhov and Bochagov (1983)	H_2O/ LiBr	Yes	Six Horizontal Tubes Tube OD: 19 Tube Length: 240 Tube Spacing: 28.12	Concentration: 57% Solution Flow Rate: 0.05 – 0.25 kg/m–s		Pressure: – 10 kPa	Heat duties calculated at the last two tubes.	Heat transfer coefficients were calculated from measured temperatures of the liquid incident on the tubes, heat fluxes, and water vapor pressures.
Nomura *et al.* (1994)	H_2O/ LiBr	Yes	13 Horizontal Tubes Tube OD: 16 Tube Length: 200 Tube Spacing: 21	Absorbent Flow Rate: 2.78×10^{-6} – 1.22×10^{-5} m^3/s at 55°C Inlet Concentration: 62% Refrigerant Flow Rate: 2.78×10^{-5} – 7.78×10^{-5} m^3/s	Flow Rate: 5.56×10^{-5} m^3/s (200 l/h) at 32°C		Concentration measured by an ultrasonic concentration meter. Temperatures measured by thermocouples at each tube and between tubes.	Solution wetting investigated by tracing photographs taken during the tests and laser holographic interferometry. The wetting ratio decreased from 0.822 at the upper tubes to 0.233 at the bottom. Absorption occurred on the tube surface as well as between tubes.
Hu and Jacobi (1996a; 1996b)	Water, ethylene glycol, water/glycol, oil, and alcohol	No	Horizontal Tube Tube OD: 15.88, 19.05, 22.22 Tube Spacing: 5 – 50 Groove Depth : 0.51, 0.76 Groove Width : 2.54, 0.81	Flow Rate: – 0.72 kg/m–s T_{in}: 20 – 40°C Heat Flux: up to 1.15×10^5 W/m^2				Defined droplet, jet, and sheet modes of flow based on the modified Galileo number. In the droplet mode, the effect of tube spacing was weak and the dependences of the Nusselt number on Reynolds and Prandtl numbers were more prominent than those in other modes.
Nosoko *et al.* (2002)	Water/ Oxygen	Yes	Horizontal Tube Tube OD: 16 Tube Length: 284 Tube Spacing: 2, 5, 10, 15 Tube Number: 2, 4, 6, 8	$10 < Re < 150$ Inlet Temperature: 18 – 23°C		Atmospheric Pressure	Only Mass Transfer considered. The solution Reynolds number was determined using the flow rate at the last row of the tube bank.	Criteria for various flow regimes (uniform sheet, jet, and droplet) were developed based on tube spacing and solution Reynolds number. Sherwood number increased with an increase in Reynolds number, and also with an increase in tube spacing up to 5 mm, while the Sherwood number leveled off at a tube spacing of 10 mm or higher. Quantified the compactness of the absorber using a coefficient of tube surface area per unit volume of absorber.

Table 2.2 Continued

	Working Fluid	Mass Transfer /Phase Change	Geometry (mm)	Test Conditions			Specific Details	Major Findings
				Solution Side	Coolant Side	Pressure		
Vertical Tube and Offset Strip Fin Geometry Experiments								
Haselden and Malaty (1959)	NH_3 /H_2O	Yes	Vertical Tube Exposed Length: 0151 – 1.219 m Tube OD: 12.7	Concentration: Water, 18.8% Solution Flow Rate: 2.5×10^{-4} – 3.0×10^{-3} kg/s	Flow Rate: 3.667×10^{-5} m^3/s at 20°C	Atmospheric Pressure	Surface Treatment to improve wetting: Degreasing, Layer of rust , and Blueing	Absorption enhanced tube–wetting at lower solution flow rates because the change in surface tension due to absorption increased the intensity of the ripples. Absorption conditions were mainly controlled by the cooling water temperature and the absorbent concentration. Higher mass transfer coefficients obtained than those from Penetration Theory due to improved mixing by ripples.
Wilke (1962)	H_2O/ Glycol mixture of	No	Vertical Tube Tube Length: 2.5 m Tube OD: 42	Concentration: 0, 16%, 55.5%, 77.1%, 95%			Re < 400 400 < Re < 800 Re > 800	Three heat transfer correlations for the film solution were developed for different film Reynolds number ranges.
Kang *et al.* (1999)	NH_3 /H_2O	Yes	Offset Strip Fin Fin Length: 4.88 Fin Height: 3.18 Fin Pitch: 1.95 Regular Fin Fin Length: 4.88 Fin Height: 3.18 Fin Pitch: 1.95	Solution Flow Rate: 4.0×10^{-3} – 1.02×10^{-2} kg/s Inlet Temperature: 17 – 37.2°C with 5%, 10%, and 15% Vapor Flow Rate 0.62×10^{-3} – 0.90×10^{-3} kg/s Inlet Temperature: 54.5 – 66.5°C with 64.7 – 79.7%	Flow Rate: 9.88×10^{-2} – 12.1×10^{-2} kg/s		Heat transfer coefficients: 500 – 2100 W/m^2–K Mass transfer coefficients: 1.0×10^{-5} – 55×10^{-5} m/s. Inlet sub–cooling: 22.5 – 40.0°C. Inlet concentration difference: 60.0 – 70%.	Inlet sub–cooling could influence the absorber performance significantly. A lower inlet solution temperature and a higher vapor temperature improved heat and mass transfer performance Some rectification of the vapor at the top, and desorption of water at the bottom end of the absorber. Empirical correlations developed for absorber Nusselt number and liquid Sherwood number.
Helical Coil–Tube Geometry Experiments								
Jeong *et al.* (1998)	NH_3 /H_2O	Yes	Helical Coil Tube Tube OD.: 12.7 Coil OD: 82.7 Tube Length: 600 Coil Windings: 30	Solution Flow Rate: 4.9×10^{-2} – 1.97×10^{-2} kg/s Inlet Temperature: 66 – 69°C with 1.2 – 2.2%	Flow Rate: 2.7×10^{-2} kg/s, Inlet Temperature: 41 – 46°C	20 – 40 kPa	Tests conducted with and without absorption	Film heat transfer coefficients were lower with absorption than those without absorption, possibly due to insufficient wetting caused by vapor shear.

Table 2.2 Continued

	Working Fluid	Mass Transfer /Phase Change	Geometry (mm)	Test Conditions			Specific Details	Major Findings
				Solution Side	Coolant Side	Pressure		
				Outlet Temperature: 37 – 47°C with 1.8 – 3.7% Vapor Flow Rate 0.9×10^{-4} – 0.42×10^{-3} kg/s Inlet Temperature: 66 – 69°C with 63 – 77%	Outlet Temperature: 45 – 54°C			
Helical Coil–Tube Geometry Experiments								
Kwon and Jeong (2004)	NH_3/ H_2O	Yes	Helical Coil Tube Tube OD.: 12.7 Tube Length: 600 Coil OD: 82.7 Coil Windings: 30	Solution Flow Rate 4.43×10^{-3} – 90.0×10^{-3} kg/s–m x_{dilute}: 3.13%, 14%, 30% T_{in}: 45 °C, 55 °C, 60 °C		17 – 193 kPa		The total heat transfer rate increases with an increase in the solution flow rate The effect of vapor flow direction decreases as the ammonia solution concentration is increased.

Table 2.3 Summary of Relevant Studies on Falling–Film Absorption

	Working Fluid	Mass Transfer /Phase Change	Geometry (mm)	Conditions			Specific Details	Major Findings
				Solution Side	Coolant Side	Pressure		
Horizontal Tube Geometry								
Andberg and Vliet (1987)	H_2O/ LiBr	Yes	Horizontal Tube Tube OD: 19	Solution Flow Rate: 0.02 kg/s–m Impinging Jet Velocity: 0.6 m/s Solution Temperature: 32°C and 46°C	Heat Transfer Coefficient: 4000 W/m^{2}K Temperature: at 30°C	935 Pa at 6°C		The film entry temperature had a influence on the absorption rate.
Kirby and Perez–Blanco (1994)	H_2O/ LiBr	Yes	Six Horizontal Tubes Tube OD: 19 Tube Length: 0.28 m	Solution Flow Rate: 0.006 – 0.04 kg/s Saturation Temperature at Concentration: 60%, 62%	Flow Rate: 0.025 to 0.125 kg/s 20 – 33°C	0.767 – 0.933 kPa		Defined three distinct solution flow regimes in a horizontal tube absorber: falling–film, droplet–formation, and droplet free fall. A major part of the mass transfer occurred in the droplet–formation flow regime, while the heat transfer to the coolant occurred in the falling–film flow regime.
Jeong and Garimella (2002)	H_2O/ LiBr	Yes	13 Horizontal Tubes Tube OD: 16 Tube Length: 0.2 m Tube Pitch: 21	Solution Flow Rate: 0.6×10^{-2} and 0.106 kg/s, Evaporating Temperature: 6 – 12°C	Flow Rate: 0.0556 kg/s 32°C		Compared with the experimental results of Nomura *et al.* (1994)	The wetting ratio was significant in determining the performance of an absorber and absorption occurred mainly in the falling–film and droplet–formation regimes. The portion of absorbed vapor in the droplet–formation regime increased as the flow rate increased.
Killion and Garimella (2003a)	Water	No	Six Horizontal Tubes Tube OD: 12.7 Tube Length: 300 m Tube Spacing: 38.1				Distributor Tube ID: 6.4 Tube OD: 13 Number of Holes: 6 Hole OD: 0.9 Tube Length: 300 m	The details of flow on a horizontal tube bank and the characteristics of droplet formation and its effects on the heat and mass transfer processes in an absorption system were investigated. A significant portion of the liquid ended up as a droplet at the underside of the tube.

Table 2.3 Continued

	Working Fluid	Mass Transfer /Phase Change	Geometry (mm)	Conditions			Specific Details	Major Findings
				Solution Side	Coolant Side	Pressure		
Horizontal Tube Geometry								
Goel and Goswami (2005b)	NH_3 /H_2O	Yes	Horizontal Tube Micro–channel Tube OD: 3.2 Tube Length: 0.1 m Tube Tansverse Pitch: 16 Tube Vertical Pitch: 8 Tubes per Row: 4 Number of Passes: 15 Absorber Area: 0.185 m^2	Solution Flow Rate 0.01 kg/s–m, 25% at 50°C Vapor Flow Rate Transfer Coefficient 0.15×10^{-2} kg/s, 99.7% at 27°C	Flow Rate: 0.05 kg/s at 29.5°C	300 kPa		The proposed design used a mesh between horizontal tubes to form a liquid film between horizontal tubes. A 25% size reduction could be achieved with the proposed absorber design compared to a conventional horizontal falling–film absorber.
Vertical Tube and Offset Strip Fin Geometry Experiments								
Perez–Blanco (1988)	NH_3 /H_2O	Yes	Six turns Coiled Tube Coil OD: 82.6 Tube OD: 12.7	**Case I** Solution Side: 0.02 kg/s–m, 5% at 115°C Mass Transfer Coefficient 2.62×10^{-2} kg–mol/m^2–s Vapor Side: 90 % Heat and Mass Transfer Coefficient 70 W/m^2K, 0.1 kg–mol/m^2–s **Case II** Solution Side: 0.04 kg/s–m, 45% at 44°C Transfer Coefficient Vapor Side: 99.9 % Heat and Mass Transfer Coefficient	**Case I** Temperature: 110°C Heat Transfer Coefficient: 3000 W/m^2K **Case II:** Temperature: 38°C Heat Transfer Coefficient: 3000 W/m^2K	481 kPa	1–D model for absorption Compared with experimental data Geometry: 12.7 mm diameter tube with six turns coiled in 82.6 mm diameter Solution Flow Rate: 6.3×10^{-3} kg/s Concentration In and Out: 3.3% and 17.94% Heat Load: 2.14 kW Mass Absorbed: 1.12×10^{-3} kg/s	A two–film model to decouple the interface concentrations of ammonia in the liquid and vapor. The solution flow rate and liquid–phase mass transfer coefficient influenced the absorber performance significantly. The importance of the coolant heat transfer coefficient increased as the solution approached saturation conditions.

Table 2.3 Continued

	Working Fluid	Mass Transfer /Phase Change	Geometry (mm)	Conditions			Specific Details	Major Findings
				Solution Side	Coolant Side	Pressure		
				100 W/m^2K 1.47×10^{-2} kg–mol/m^2–s				
Vertical Tube and Offset Strip Fin Geometry Experiments								
Palmer and Christensen (1996)	NH_3 /H_2O	Yes	Vertical Fluted Tube Absorber	Concentrated Concentration: 28% Dilute Concentration: 16% Interface Temperature: 105 – 130°C Vapor temperature: 98 – 130°C	Temperature 85 – 90°C		33% of actual surface area wetted	The wetting ratio increased as the concentration of the concentrated solution was increased.
Gommed *et al*. (2001)	NH_3 /H_2O	Yes	Vertical Tube Tube OD: 15 Tube Length: 1 m	Solution Flow Rate: 0.06 kg/s Solution Temperature: 55°C Concentration: 35% Vapor Flow Rate: 0.015 kg/s Vapor Temperature: 10.9°C Concentration: 99% Superheated 2°C		450 kPa	Finite volume method	The inlet conditions of the liquid and vapor affected the absorption rate significantly, and the diffusion coefficient and thermal conductivity of the liquid had a pronounced effect on the absorbed vapor mass. The absorption process was controlled by the liquid solution side and the diffusion coefficient in the gas phase had a small effect on the absorption process.
Vertical Tube and Offset Strip Fin Geometry Experiments								
Goel and Goswami (2005a)	NH_3 /H_2O	Yes	Four lamella plates Width: 150 mm Spacing: 10 mm	Solution Flow Rate: 0.02 kg/s at 50°C Concentration: 25% Vapor Flow Rate: 0.4×10^{-2} kg/s at 27°C Concentration: 99.7%	Flow Rate: 0.504 kg/s Temperature: 29.5°C	200 kPa		The liquid–side heat transfer resistance was negligible, the coolant–side heat transfer resistance dominated the overall absorption process at the solution inlet, and the liquid phase mass transfer resistance controlled the overall absorption process. The film–side mass transfer resistance was dominant overall and the coolant inlet

Table 2.3 Continued

	Working Fluid	Mass Transfer /Phase Change	Geometry (mm)	Conditions			Specific Details	Major Findings
				Solution Side	Coolant Side	Pressure		
								temperature had a significant effect on absorption rate.
Shell–and–Tube Geometry								
Fernandez–Seara *et al*. (2005)	NH_3 /H_2O	Yes	Shell–and–Tube Length: 0.9 m Tube OD: 25 Number of Tubes: 40 Nozzle Diameter: 9	Solution Flow Rate: 0.0278 kg/s Solution Temperature: 45ºC Concentration: 22.5% Vapor Flow Rate: 4.17×10^{-3} kg/s Vapor Temperature: 10ºC Concentration: 99.9%	Flow Rate: 0.417 kg/s Temperature: 25ºC			The absorption process was rapid in the churn and in the slug regions, and slow in bubbly flow. Water desorption was predicted at the beginning of the absorption process. The interface temperature was the same as the bulk solution temperature, which implied the heat transfer resistance was mainly located in the vapor phase. The heat and mass transfer coefficients in the vapor phase had no significant effect on the absorption process.
Lee *et al* .(2005)	NH_3 /H_2O	Yes	Shell–and–Tube Diameter: 300 Length: 0.15 m Tube Diameter: 10 Tube Length: 0.1 m Number of Tubes: 91 Tube Pitch: 15 Nozzle Diameter: 1 Nozzle Distance: 130				Ammonia absorption refrigeration system was built. Empirical and numerical combined method was used.	The falling–film thickness of a horizontal tube in the shell–and–tube absorber was three times thicker than that of the ideal film on a vertical flat plate with the same heat transfer area . The absorption rate decreased as the inlet temperatures of the solution and coolant increased.

Table 2.4 Summary of Relevant Studies on Bubble Absorption

	Working Fluid	Mass Transfer /Phase Change	Geometry (mm)	Conditions			Specific Details	Major Findings
				Solution Side	Coolant Side	Pressure		
Merrill *et al.* (1994; 1995)	NH_3 /H_2O	Yes	U–shaped concentric tubes Height: 0.5 m Width: 127 Inner Tube OD: 12.7 Outer Tube OD: 23.8	Solution Flow Rate: 2.83×10^{-3} – 5.59×10^{-3} kg/s at 120°C with 10% Vapor Flow Rate: 1.55×10^{-4} – 1.85×10^{-4} kg/s at 41.1°C with 91 – 93%	Flow Rate: 3.1×10^{-3} – 5.52×10^{-3} kg/s at 76°C Heat Transfer Coefficient: 1500 W/m^2–K	503 kPa	Passive Enhancement Techniques: Repeated Roughness, Internal spacers	Heat transfer was enhanced by repeated roughness and internal spacers. Mass transfer was enhanced by the use of static mixers, variations of flow cross–section areas, and numerous vapor injector designs. The knowledge of variations in the internal heat transfer coefficient with vapor flow rate are required for further absorber development.
Dence *et al.* (1996)	NH_3 /H_2O	Yes	Annulus–Shaped Co–flow Helix Turn: 8.5 Helix Height per Turn: 44.45 Holes Diameter: 3.18 Hole Pitch: 12.7	Solution Flow Rate: 9.49×10^{-3} kg/s at 94.4°C with 21% Vapor Flow Rate: 1.91×10^{-3} kg/s at 93.3°C with 86.6%	Flow Rate: 1.31×10^{-2} kg/s at 88.3°C Heat Transfer Coefficients: 13000 W/m^2–K for Outer Channel and 18000 W/m^2–K for Inner channel.		Designing the GAX Absorber with a Heat Duty: 4.7 kW Maximum Bubble Diameter: 4 mm	Designed and simulated an annulus-shaped co-flow bubble absorber with a helical bubble injector for a GAX cycle application using helical cooling water channels.
Kang *et al.*(2002)	NH_3 /H_2O	Yes	Dimension: 80 × 53.4 × 300 Vapor Distributor Tube OD: 10 Number of Holes: 3 Hole Diameter: 3.0 3.8, 5.5 mm.	Ammonia Velocity: 1.25 – 8.5 m/s Liquid Concentrations: 0%, 10%, 20% Liquid Temperature: 22.5°C			Visualization with a High Speed Camera (Shutter Speed of 1/500 s)	The mass transfer coefficient increased as the liquid concentration decreased and vapor Reynolds number increased for the bubble growth process, while the mass transfer coefficient increased as the Galileo number increased for the bubble disappearance process.
Lee *et al.* (2002)	NH_3 /H_2O	Yes	Plate–Type Dimensions: 11.2 × 26.4 × 3.0	Solution Flow Rate: 0.005 kg/s with 0% – 30% at 20°C. Ammonia Vapor Flow Rate: 1.667×10^{-5} – 1.5×10^{-4} m^3/s			Three Different Surface–Treated Plates: Smooth, Hair–Lined, and Sand–Papered	The heat transfer performance of absorbers was increased as the flow rate of solution increased, while the mass transfer performance was not influenced. For the bubble absorber, heat transfer performance of the absorber increased as vapor flow rate increased due to the influence of the vapor flow rate on the thermal boundary layer, while the heat transfer performance of the falling–film absorber decreased as this flow rate of vapor increased due to the decrease of the heat transfer area by an increase of vapor flow interfering a solution flow.

Table 2.5 Summary of Relevant Studies on Miniaturization of Absorber

	Working Fluid	Mass Transfer /Phase Change	Geometry (mm)	Conditions			Specific Details	Major Findings
				Solution Side	Coolant Side	Pressure		
Kang and Christensen (1995)	NH_3 /H_2O	Yes	Fluted Tube based on Porous Medium 4 Flute Starts, Inner Bore Diameter: 19.1 Coiling Diameter 0.31	Flow Rate: 0.071 kg/s at 352 K Vapor Flow Rate: 0.034 kg/s at 283 K	35% K_2CO_3 Aqueous Solution Flow rate: 3.1 kg/s Temperature: 315.4 – 318 K	600 kPa	Effect of thermal conductivities and porosities of the porous medium on the absorption rate, and geometric parameters of a fluted tube on the heat exchanger size were investigated	The absorption rate increased with an increase in the thermal conductivity and a decrease in the porosity of the porous medium.
Garrabrant and Christensen (1997)	NH_3 /H_2O		Corrugated and Perforated Fin Surface 0.432 m × 0.127 m Perforations Alternating per Row: 6 or 7	Flow Rate: 4.16×10^{-3} – 11.8×10^{-3} kg/s.			Two channels for the perforated fin and offset fins. Model was validated with empirical data.	Absorber performance influenced significantly by solution concentration, solution and vapor Reynolds numbers and the shear force of the vapor with falling film flow.
Garimella (1999; 2000)	NH_3 /H_2O	Yes	Horizontal Tube Micro channel Tube OD:1.59 Tube Length: 127 Tube Pitch : 3.18 Tube Row Vertical Pitch: 6.35 Tubes per Row: 40 Rows per Pass: 15 Number of Passes: 5 Absorber Area: 1.9 m^2	Flow Rate: 0.0189 kg/s with 20.6% at 98.54°C Vapor Flow Rate: 0.0095 kg/s with 99.5% at 38°C	50% ethylene glycol/water Flow rate: 0.5 kg/s at 42°C	510 kPa		Developed miniaturization technology for ammonia–water absorbers that used short lengths of very small diameter tubes.

Table 2.5 Continued

	Working Fluid	Mass Transfer /Phase Change	Geometry (mm)	Test Conditions			Specific Details	Major Findings
				Solution Side	Coolant Side	Pressure		
Meacham and Garimella (2002a)	NH_3 /H_2O	Yes	Horizontal Tube Micro channel Tube OD:1.575 Tube Length: 140 Tube Pitch : 4.76 Tube Row Vertical Pitch: 4.76 Tubes per Row: 27 Rows per Pass: 16 Number of Passes: 5 Height: 0.508 m Absorber Area: 1.50 m^2	Solution Flow Rate: 0.010 – 0.040 kg/s Concentration: Concentrated : 38% Dilute: 22.9% Vapor Fraction: 10 – 50% Concentration: 87%	Temperature: 30°C	0.17 – 1.93 bar		Compact absorber delivered large heat duties and heat transfer coefficients using microchannel tubes.
Meacham and Garimella (2004)	NH_3 /H_2O	Yes	Horizontal Tube Micro–channel Tube OD: 1.575 Tube Length: 0.137 m Tube Pitch: 7.94 Tube Row Vertical Pitch: 7.94 Tubes per Row: 33 Rows per pass: 2 Number of Passes: 10 Height: 0.15 m Absorber Area: 0.45m^2	Solution Flow Rate: 1.51×10^{-2}–2.66×10^{-2} kg/s Vapor Generation Fraction: 15%, 20%, 25%, 30% Concentration: 87% 0.93 – 0.98 % Inlet Temperature (Pressure) 52°C (355 kPa) 81°C (680 kPa)		355 kPa 680 kPa	Flow visualization on different modes of absorption including falling film, droplet formation, detachment, fall, and redistribution	Revised flow distribution device, increased heat transfer and absorption rates over previous study achieved.

CHAPTER 3. EXPERIMENTAL APPROACH

The following sections describe the test facility and the details of the absorber as well as other components of the system. The test facility underwent several stages of modifications to enable testing over the wide range of conditions under consideration. Testing was conducted at three absorber pressures of 150, 345 and 500 kPa (21.8, 50.0 and 72.5 psi), and four different concentrations of 5, 15, 25 and 40% for three different flow rates for each combination of concentration and pressure to result in a total of 36 data points. The rationale for the selection of these conditions and the system designed to achieve these conditions are described below.

3.1 Test Matrix Design

The test conditions were chosen with the intention of replicating the operating conditions in an absorption chiller/heat pump. As mentioned in the previous chapter, system operation depends on ambient conditions such as ambient temperature, coolant temperatures, and heat source temperature. These system-level conditions in turn influence and establish the absorber conditions. In this study, three pressures and four concentration conditions were chosen. This set of conditions represents the range encountered in a variety of ammonia-water cycles, including higher efficiency cycles such as the GAX cycle that relies on a wide concentration range to enable a significant amount of internal recuperation. The three pressures in the absorber account for three

Table 3.1 Test Matrix

Pressure		150 kPa			345 kPa			500 kPa		
Flow Rate		Low	Mid	High	Low	Mid	High	Low	Mid	High
Concentration	5%	GAX Cycle Condition								
	15%	Cold Ambient Heat Pump Mode			Moderate Ambient Heat Pump Mode			Warm Ambient Heat Pump Mode		
	25%									
	40%									

different modes of system operation: cold ambient heat pump mode with an evaporating temperature between -25°C and -20°C, moderate ambient heat pump mode with an evaporating temperature between -5°C and 0°C, and warm ambient heat pump mode with an evaporating temperature between 3°C and 8°C. The four different concentrations span the range seen in an absorption cycle as the system adjusts to operate at these various heat source and sink temperatures. In addition, the solution flow rate was varied to investigate the effect of the solution film mass flux on the heat and mass transfer coefficients. The resulting test matrix is shown in Table 3.1.

3.2 Design Specifications

Prior to development of the test facility, a preliminary estimate of the various component sizes was obtained and the expected flow rates and heat duties in each component around the loop were predicted. The initial design of the test facility was based on the following parameters:

- Evaporator cooling duties of up to 5 kW
- Condenser temperatures in the range 30-40°C
- Absorber pressures of 150 kPa (21.5 psi), 345 kPa (50.0 psi) and 500 kPa (72.5 psi)

- Nominal dilute solution concentrations at the desorber outlet of 5%, 15%, 25%, and 40%.

A system simulation program was developed to estimate system performance and the various heat exchangers and pump sizes. The program used these initial design parameters, basic principles of absorption cycle analysis such as mass, species and enthalpy balances, and assumptions regarding effectivenesses of heat exchangers. Estimates from these preliminary analyses provided guidelines for selecting and designing different components and flow rates. A test facility with dimensions of 2.74 × 1.37 × 1.98 m (9 × 4.5 × 6.5 ft) was designed and fabricated to accommodate the system size and complexity of the experiments. The test facility consists of numerous heat exchangers functioning as components in an ammonia absorption system, pumps, and extensive instrumentation. The system can be subdivided into two broad categories: solution loop and auxiliary loops. The main loop consists of the absorber, solution heat exchanger, desorber, separator, rectifier, condenser, pre-cooler and the evaporator. The rectifier is directly coupled to its cooling source, while the absorber, desorber, condenser and evaporator are coupled through intermediate loops. Steam is the ultimate heat source for the desorber. A chilled water-glycol supply from the Carrier AquaSnap 50 RT chiller is used as the ultimate heat sink for heat removal from the absorber and the condenser. Use of intermediate loops provides improved control over test conditions and heat duties. Each component was located in the facility with a consideration of its function and ease of operation and maintenance. The desorber, separator, rectifier and condenser were mounted as high as possible on the basic frame, while the evaporator and absorber were

mounted as low as possible to enhance the opportunities for providing a static pressure head between high and low pressure sides of the loop as necessary.

3.3 Test Facility Overview

The system operates at two different nominal pressure levels: high pressure at the condenser, rectifier and desorber, and low pressure at the absorber and evaporator. The different solution concentrations at different absorber pressures are obtained by controlling heat duties and temperatures of the desorber, condenser, rectifier and absorber cooling loops. It should be noted that several different versions of the test facility were designed, constructed and installed during the course of this study to address different regions of the operating condition ranges. A general description of the system layout is provided before the details of each component and of the several system layout modifications to accommodate the wide range of operating conditions are described. A schematic of the final version of the test facility is shown in Figure 3.1 while a photograph is shown in Figure 3.2. In Figure 3.1, dotted lines show vapor flow while solid lines show solution flow.

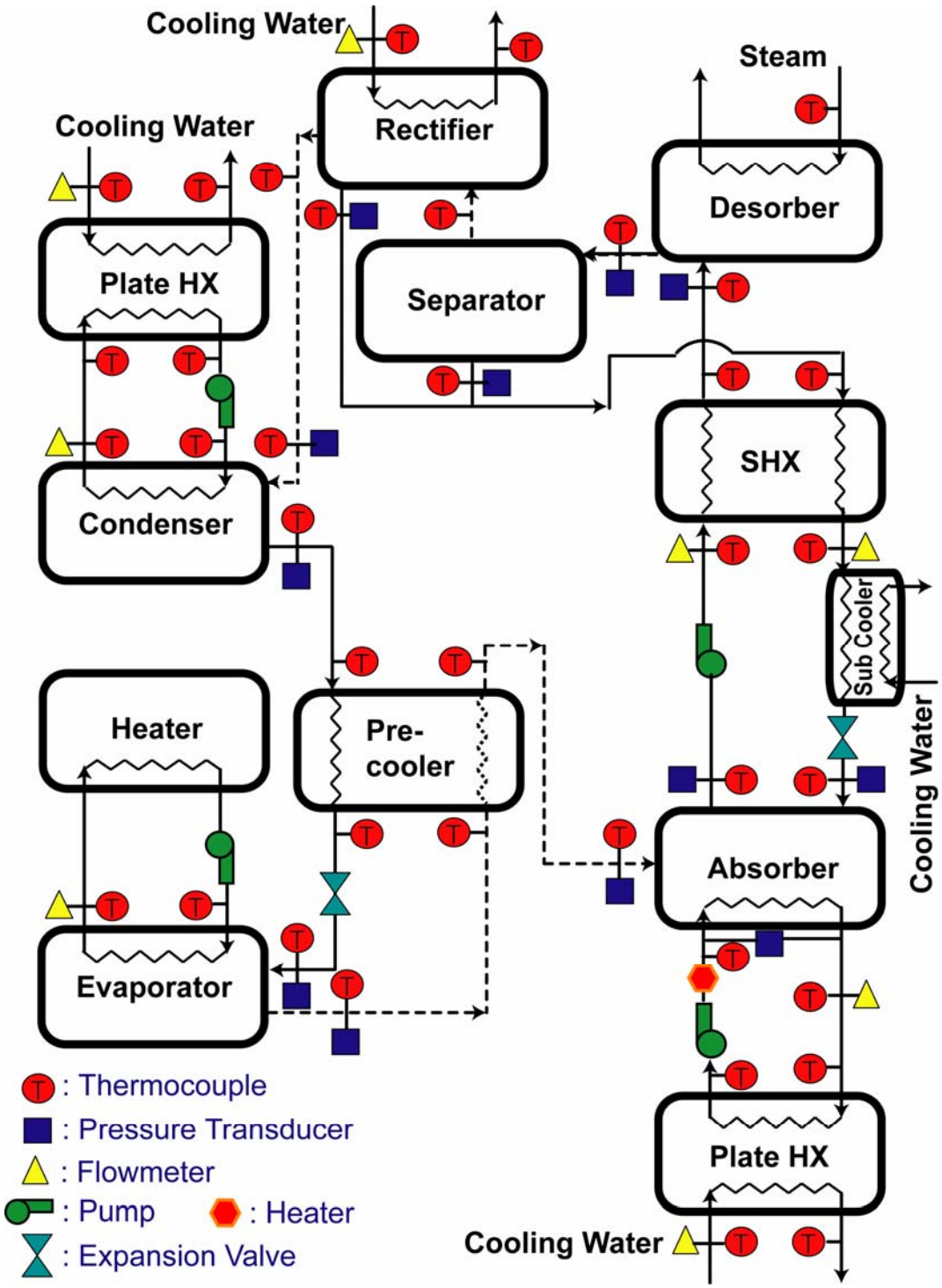

Figure 3.1 Test Facility Schematic

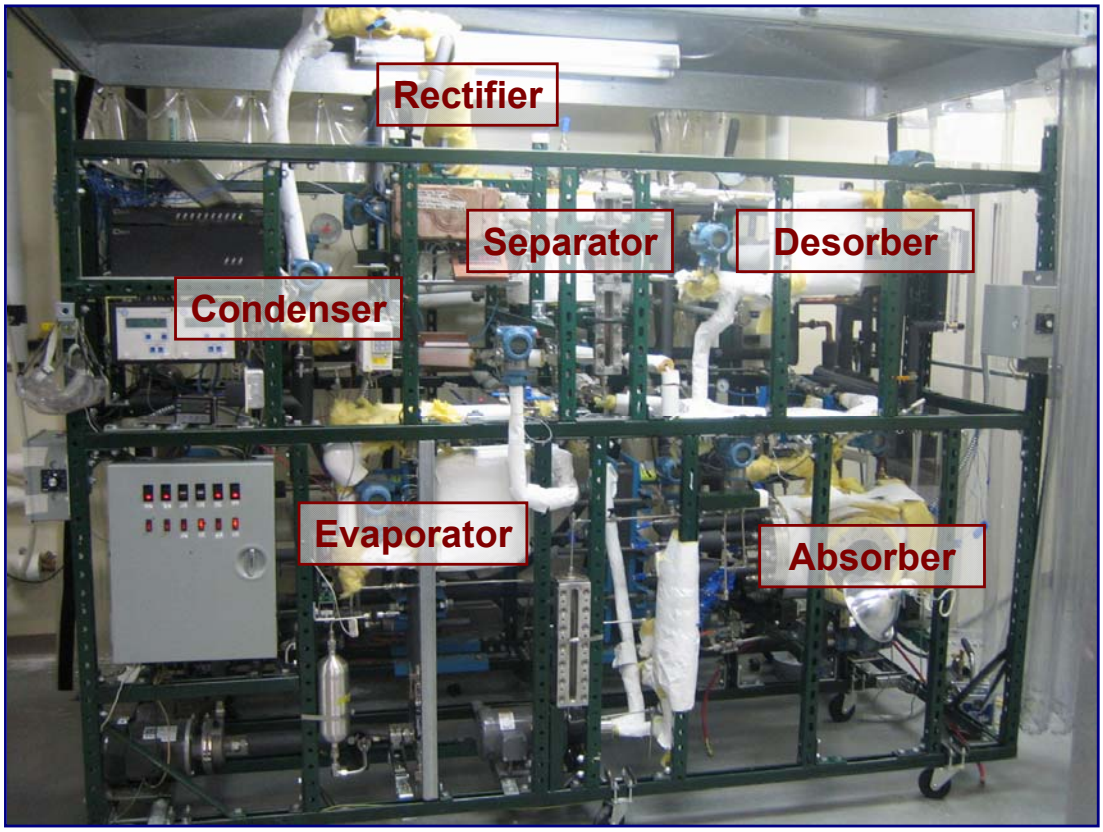

Figure 3.2 Photograph of Test Facility

Concentrated solution is pumped from the low pressure at the absorber to the desorber at high pressure. Before entering the desorber, the solution flows through a solution heat exchanger, which recuperatively heats the concentrated solution toward the desorber inlet conditions. At the desorber, the necessary heat input is supplied to generate ammonia vapor and dilute solution from the concentrated solution. The ammonia vapor is separated from the dilute solution in a vapor-liquid separator, after which the vapor flows to the rectifier, while dilute solution flows through the solution heat exchanger. Downstream of the solution heat exchanger, the pressure of the dilute solution is reduced by an expansion device before it flows into the absorber to complete the solution circuit. The ammonia vapor is purified at the rectifier and sent to the condenser, while the reflux at the rectifier produced during rectification is mixed with the dilute solution exiting the separator. The ammonia vapor is condensed in the condenser and flows to the pre-cooler. Here, the ammonia enthalpy is reduced by recuperatively heating the ammonia vapor stream from the evaporator outlet. At this reduced enthalpy, the ammonia solution is expanded to the evaporator pressure using an expansion device and flows through the evaporator, where it receives the cooling load. Ammonia exiting the evaporator flows through a pre-cooler, where it serves as the coolant for the condenser outlet stream. After exiting the pre-cooler, the ammonia vapor is introduced to the absorber, where it is absorbed in the dilute solution while rejecting heat to a coolant stream, thus completing the refrigerant circuit. The details of these components and the various primary and secondary loops are described below.

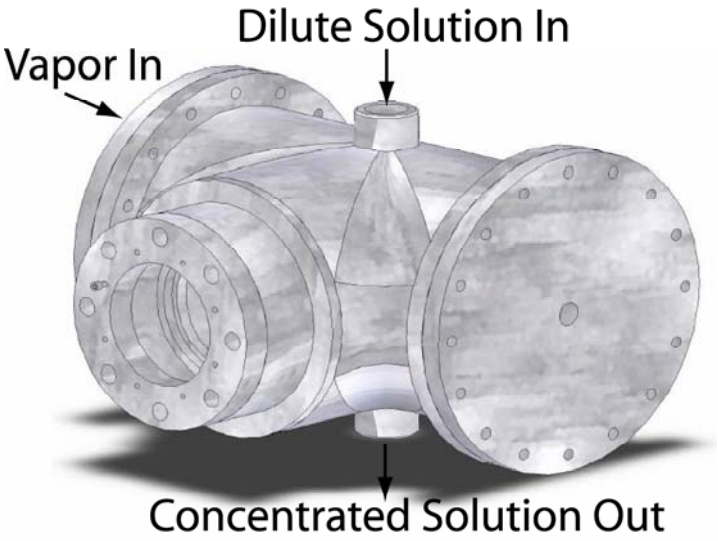

Figure 3.3 Drawing of the Absorber Outer Shell

3.4 Details of Individual Components

3.4.1 Absorber and Absorber Coolant Loop

The absorber is the main component for this study, in which ammonia vapor flowing from the evaporator is absorbed by the dilute solution from the desorber, rejecting its heat to a coolant loop. Figure 3.3 shows a drawing of the outer shell, while Figure 3.4 shows a drawing of the tube array. In this falling-film absorber, the solution flows by gravity from the top to the bottom of the tube array. The heat of absorption is transferred to the absorber coolant flowing through the tubes. The absorber tube array is housed in a 0.5 m long × 0.31 m diameter (19.5" long × 12" diameter) outer shell with a large 0.27 m (10") port, and three additional 64 mm (2.5") sight ports for illumination and viewing at other angles. The tube array inside the shell consists of four columns of 9.5 mm (3/8") nominal OD, 0.7 mm (0.28") wall thickness, 0.29 m (11.5") long tubes, each column containing 6 tubes for a total of 24 tubes in the bundle. The two absorber coolant headers at either side of the tube array are 0.13 m (5.12") long, 0.12 m (4.72")

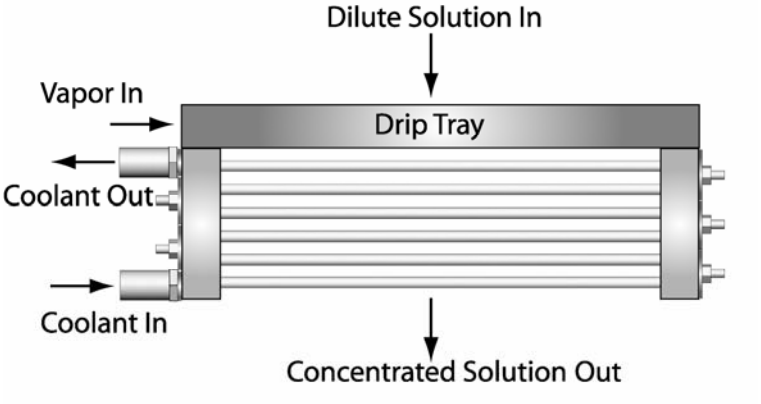

Figure 3.4 Drawing of the Absorber Tube Array

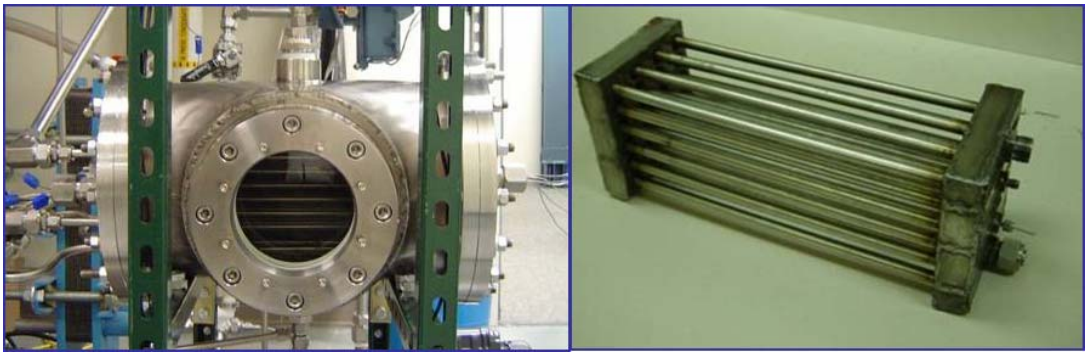

Figure 3.5 Absorber Photograph (Installed Assembly, Tube Bundle)

wide, and 25 mm (1") in depth. The drip tray that distributes the dilute solution from above the tube array is 0.343 m (13.5") long × 0.12 m (4.72") wide × 38 mm (1.5") in height. The absorber as installed in the loop is shown in Figure 3.5.

The large port of the outer shell is located at the front and equipped with a sight glass that facilitates visualization. This front port is equipped with a B-weld sight glass manufactured by Pressure Products Company, Inc. It consists of a stainless steel body, cap, cap screws, compression ring, lens, lens packing, compression adjustment screws and two cushion gaskets. The body dimensions are 0.32 m (12.5") OD and 89 mm (3.5") height (or thickness). The view port diameter is 0.15 m (6"). The 0.15 m OD (6 3/16"),

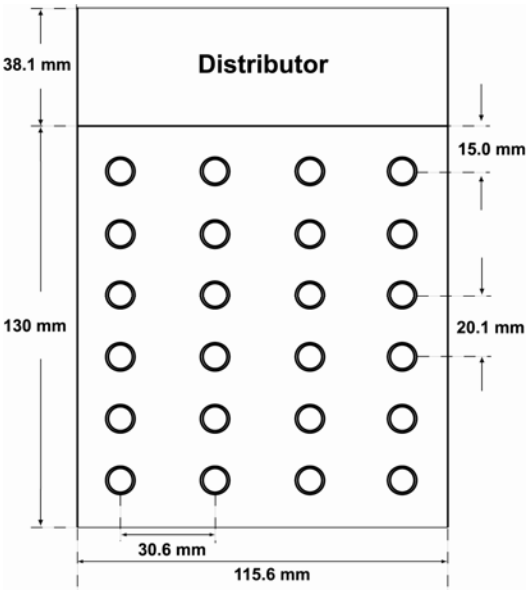

Figure 3.6 Tube Array Dimensions

51 mm (2") thick tempered borosilicate lens can withstand a maximum pressure of 2068 kPa (300 psi). Two of the smaller ports are located at the top and bottom and one is located at the back, aligned with the large front port, and therefore used to illuminate the inside of the shell. A Bull's Eye NPT 38 mm (1½") sight glass from Pressure Products Company, Inc. rated for 4137 kPa (600 psi), 232.2^{o}C (450^{o}F) service is installed at the back port. Teflon gaskets, compression rings, and O-rings are used for the sight glasses for compatibility with ammonia. The two other ports at the top and bottom are used as a solution inlet and outlet, respectively.

The tube array (Figure 3.6) is connected to one of the flanges and inserted from one end of the shell. Ammonia vapor is introduced into the chamber through the same flange. The tubes are arranged in a serpentine configuration with a horizontal pitch of 30 mm (1.2"), a vertical pitch of 20 mm (0.79"), and a surface area of 0.210 m^2 (2.26 ft^2). The tube array was initially designed for one header and U-bends at the other header to

achieve the serpentine flow arrangement; however, fabricating the U-bends with such a small bend radius using stainless steel was not feasible, which necessitated the two headers. The two headers have six coolant passes from the bottom to the top of the assembly with a total of seven ports for temperature measurements at each level. Thermocouples are placed at each level of the absorber to allow determination of row-wise heat duties, which, in turn, assist in the estimation of the variation of heat and mass transfer coefficients within the absorber. The drip tray is placed above the tube bundles, supported by the headers and designed to distribute dilute solution on the tubes. The tray has 4 rows of 75 holes (on a 30 mm × 3.8 mm or 1.2" × 0.15" pitch) for the insertion of 1.5 mm (0.06") capillary tubes (a total of 300), which distribute the dilute solution on the first row of the tube bundle. The distributor is located 15.0 mm above the centerline of the first row of tubes. The headers and the drip tray are welded from 1.5 mm (0.06") thick 316 stainless steel plate. The geometry of the absorber is summarized in Table 3.2. As mentioned in the literature review section, flow regimes can influence heat and mass transfer during the absorption process. Vapor absorption also occurs during formation and fall of the solution droplet. The vertical pitch of the tube array is designed to have enough space to form droplets at the bottom of each tube and fall on next tubes with satellite droplets. The pitch of the tube array was verified with isothermal water tests before the absorber was installed in the test facility. The numbers of columns and rows were determined based on heat transfer areas required for the descried nominal duties, and to provide enough space for visualization from the top tube to the bottom tube during absorption tests.

Table 3.2 Absorber Geometry

Shell	
Diameter	0.31 m
Length	0.5 m
Number of ports	1 Large (0.27 m), 3 Small (64 mm)
Tube Arrays	
Envelope dimension	0.32 m(L)×0.12 m(W)×0.13 m(H)
Tube outer diameter	9.5 mm
Tube thickness	0.7 mm
Tube length	0.29 m
Number of column	6
Number of row	4
Number of pass	6
Tube vertical pitch	20 mm
Tube horizontal pitch	30 mm
Absorber surface area	0.210 m^2
Header	
Number of header	2
Header length	0.13 m
Header width	0.12 m
Header depth	25 mm
Drip Tray	
Drip tray length	0.343 m
Drip tray width	0.12 m
Drip tray height	38 mm
Hole diameter	1.5 mm
Number of hole	300
Number of row	4
Holes per row	75
Hole row pitch	30 mm
Hole pitch	3.8 mm

Absolute pressures and temperatures at the solution inlet, outlet and vapor inlet are measured using absolute pressure transducers (Rosemount Model 2088). Measurements of pressures and temperatures at three different locations enable independent estimates of thermodynamic states at these locations.

A closed coolant loop with distilled water as the coolant is used to remove the heat of absorption from the absorber, which is eventually transferred to the lab chilled water-glycol coolant (cooled by a 50 RT Carrier AquaSnap Chiller) in a plate heat exchanger (Superchanger Model UX-016-UJ-21 by Tranter with a total heat transfer area of 1.65 m^2 or 17.8 ft^2). Most of the plumbing for the closed coolant lines is fabricated using 25.4 mm (1") nominal O.D. tubes to minimize frictional pressure drop except at the inlet and outlet of the absorber (12.7 mm (0.5") nominal O.D. tubes). To measure the coolant pressure drop in the absorber, a differential pressure transducer by Rosemount is used. The coolant is circulated using a centrifugal pump (Little Giant Model TE-7-MD-HC) with a ¾ hp motor. An expansion tank is used upstream of the pump inlet to compensate for thermal expansion of water and to provide additional positive head for the pump. The coolant flow rate is measured using a magnetic flow meter (Rosemount Model 8711). Temperatures of the absorber coolant and the chilled water are measured at the inlets and outlets of the plate heat exchanger. Chilled water-glycol flow rate is measured using a rotameter. An energy balance at the plate heat exchanger provides an additional means of verifying the accuracy of the results over and above the energy balance between the ammonia and primary coolant in the absorber.

Figure 3.7 Photograph of the Desorber and Evaporator

3.4.2 Desorber and Desorber Heating Loop

The desorber (Figure 3.7) for generating the refrigerant from the concentrated solution is a 5.9 m (19.3 ft) long coiled tube-in-tube heat exchanger from Exergy, Inc. (Model 00528), with a 12.7 mm (0.5") O.D. inner and 25.4 mm (1" O.D.) outer tube, each 1.7 mm (0.065") thick for a total heat transfer area of 0.26 m^2 (2.5 ft^2). The maximum rated tube-side and annulus-side operating pressures are 31,026 and 13,790 kPa (4500 psi and 2000 psi), respectively at 93.3^oC (200^oF). Concentrated solution enters the desorber and exits as a two-phase mixture of dilute solution and ammonia vapor at the top of the desorber due to the heat supplied from the steam (supplied by a boiler at up to 1379 kPa (200 psi) saturation pressure). Concentrated solution flows inside the inner tube, while steam flows through the annulus. The desorber essentially determines the concentration of the dilute solution, although reflux from the rectifier changes the concentration of dilute solution entering the absorber to some extent. The concentration of the dilute solution is determined at the co-flow desorber outlet from pressure and

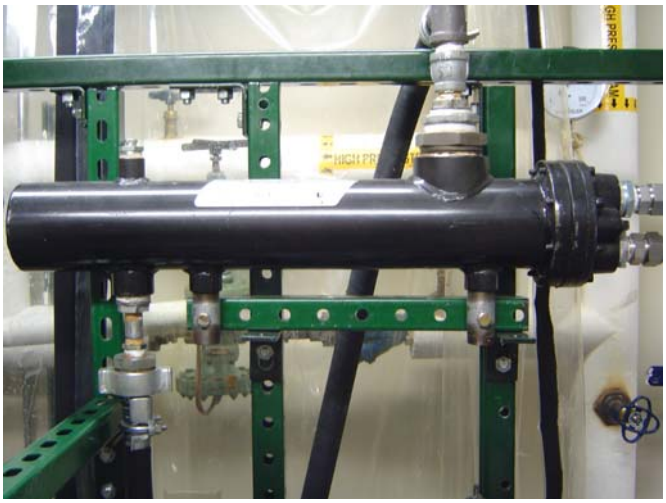

Figure 3.8 Steam Heat Exchanger

temperature measurements and the two-phase exit condition. The two-phase mixture flows to the separator where the two streams are separated. Solution temperatures are measured by 3-wire RTDs and pressures are measured by Rosemount (Model 2088) pressure transducers at the inlet and outlet of the desorber. The desorber pressure is determined by the temperature at the condenser, which is in turn set by the coolant temperature.

In the initial design, the concentrated solution was heated by a heat transfer fluid (Syltherm HF fluid, Dow Chemical) in a closed heating loop. Syltherm HF can be used over a wide temperature range of -73^{o}C (-100^{o}F) to 260^{o}C (500^{o}F). This fluid flowed on the annulus side of the tube-in-tube heat exchanger in a counter-current manner with the ammonia-rich solution in the tube side of the desorber. The heat transfer fluid was heated in a shell-and-tube heat exchanger (American Industrial Heat Transfer, Inc., Model URCS by) using steam on the shell side (Figure 3.8). The heat transfer fluid was circulated in the closed loop by a centrifugal pump (Model AC4 by Finish Thompson) that has a maximum pressure limit of 689 kPa (100 psi) and a temperature limit of 149^{o}C

(300^{o}F). The heat transfer fluid was circulated in a 25.4 mm (1") nominal OD SS-316L tube between the two heat exchangers to minimize the flow velocity and frictional pressure drop. The mass flow rate of the heat transfer fluid was measured using a Coriolis mass flow meter (model RFT9739-Field Mounted, Micromotion). Fluid temperatures were measured at the inlets and outlets of the two heat exchangers. With the flow rate and temperatures known, the heat duties of the two heat exchangers in the loop could be calculated. The heat transfer fluid duty in the tube-in-tube desorber provided a means to check the accuracy of the results by comparison with the solution side duty. In addition, a balance between the heat transfer fluid duties in the two exchangers (desorber and steam-to-Syltherm heat exchanger) further validated these results.

The circulation pump for the heat transfer fluid in the desorber loop had a maximum temperature limit of 149^{o}C. This restricted the operating temperature limit for the pump for testing at the 5% and 15% concentrations, as higher desorber duties and temperatures are required for these concentrations. To partially mitigate this problem, a tube-in-tube heat exchanger was fabricated using 0.61 m (2 ft) long 25.4 mm (1") and 12.7 mm (½") O.D. tubes and installed between the desorber heating fluid outlet and the pump inlet. This heat exchanger reduced the heating fluid temperature at the pump inlet by 10-15^{o}C, allowing the testing of a few additional operating conditions. However, it was still not possible to obtain desorber temperatures higher than 150^{o}C. Therefore, it was decided to remove the auxiliary heating loop altogether, and the steam line was directly connected to the tube-in-tube desorber, which removed the high temperature operation restrictions.

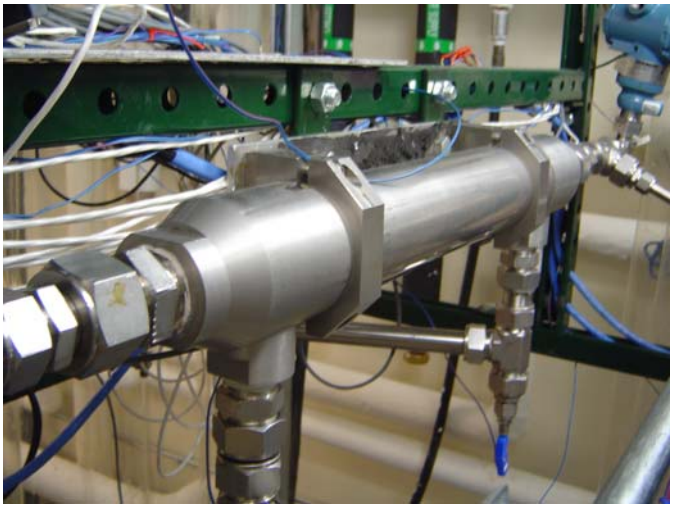

Figure 3.9 Photograph of the Condenser

3.4.3 Condenser and Condenser Coolant Loop

A shell-and-tube exchanger (Model 00677-3, Exergy, Inc.) is used as the condenser (Figure 3.9). The ammonia vapor from the rectifier flows on the tube side, while the coolant flows on the shell side of this heat exchanger. The 76.2 mm (3") O.D. shell contains 253, 0.5 m (20") long tubes of 3.2 mm (0.125") nominal O.D. and 0.3 mm (0.0125") wall thickness for a total heat transfer area of 1.24 m^2 (13.4 ft^2). The maximum rated tube-side operating pressure is 5171 kPa (750 psi) at 427^{o}C (800^{o}F), while the shell-side rating is 3447 kPa (500 psi) at the maximum temperature of 427^{o}C (800^{o}F). Refrigerant temperatures at the inlet and outlet of the condenser are measured using 3-wire RTDs and the absolute pressure is measured using absolute pressure transducers (Model 3051, Rosemount). The refrigerant mass flow rate is measured using a Coriolis mass flow meter (Model C25, Micro-motion), which can measure mass flow rates from 0 to 0.023 kg/s (3 lb_m/min) and can be configured to different ranges. Measurements of temperatures and pressures at the inlet and outlet along with the concentration at the outlet of the rectifier provide a means to estimate the refrigerant-side heat duty.

Figure 3.10 Plate Heat Exchangers

A closed coolant loop is used to remove the heat of condensation that is eventually transferred to the lab chilled water-glycol solution in a plate heat exchanger (Superchanger UX-016-UJ-21, by Tranter) with a total heat transfer area of 1.65 m^2 (17.8 ft^2). Figure 3.10 shows a photograph of this plate heat exchanger. In the initial design, the condenser coolant loop was combined with the evaporator heating loop so that the heat load for the evaporator could be supplied by the condenser. This configuration minimized the required electric heater duty to supply the load for the evaporator. However, after some of the tests were conducted, the condenser coolant loop was separated from the evaporator heating loop to achieve precise and more independent control of coolant flow rates and temperatures. Most of plumbing for this loop also consists of 25.4 mm (1") nominal OD tubes to maintain low pressure drops. The coolant is circulated using a centrifugal pump (TE-7-MD-HC, Little Giant, with a 3/4 hp motor). An expansion tank is used upstream of the pump inlet to supply the requisite positive head for the pump and also to compensate for the thermal expansion of the coolant. The pressure in the coolant loop is monitored by a dial pressure gauge, which helps in the

detection of any severe fluctuations or overshoot of the coolant pressure and the prevention of potential pump failures. The coolant flow rate is measured by a Coriolis mass flow meter (Model RFT9739-Field Mounted, Micromotion). Temperature measurements at the inlets and outlets of the condenser enable the calculation of heat duties on the respective sides. Coolant temperatures are measured using T-type thermocouples. Heat balances between the refrigerant side and the coolant side of the condenser establish the accuracy of the results.

3.4.4 Evaporator and Evaporator Heating Loop

A tube-in-tube heat exchanger similar to the desorber (Model 00528 by Exergy Inc., Figure 3.7) is used as the evaporator. The refrigerant flows in the inner tube while the heating fluid flows through the annulus. As mentioned above, the evaporator heating loop was initially combined with the condenser loop, but was subsequently separated into an individual, electrically heated loop to ensure precise control of the fluid flow rate and temperature. A 5 kW electric firerod immersion heater by Watlow (Model L12NX4B) was installed into the loop upstream of the evaporator. The coolant is circulated by a centrifugal pump (Model AC4 by Finish Thompson, with a 3/4 hp motor, similar to the heat transfer fluid pump) through the mostly 25.4 mm (1") nominal OD plumbing in this loop. An expansion tank is also used in this loop as described for the other fluid loops above. The pressure in the coolant loop is monitored using a dial pressure gauge. The flow rate of the coolant in the evaporator loop is measured by a positive displacement flow meter by AW company (Model JVM-60KL) coupled to a flow transmitter (Model FEM-03 by AW Company.) Temperature measurements using T-type thermocouples at the inlets and outlets of the evaporator enabled calculation of evaporator heat duties.

Figure 3.11 Photograph of the Separator

Heat duty calculations on the refrigerant side and the coolant side in the evaporator provided a means to validate the accuracy of the results.

3.4.5 Separator

The two-phase mixture exiting the desorber is separated into individual vapor and liquid streams in the separator. The dilute solution flows to the absorber through the solution heat exchanger, while the ammonia vapor is routed to the rectifier. Figure 3.11 shows a photograph of the separator, which consists of an assembly of meshes and tubing inside a 0.3 m long, 0.15 m O. D. stainless steel flanged cylindrical shell. Blind flanges are bolted to the flanged cylinder with a Teflon gasket interface to form the enclosure. These blind flanges have ports for the various inlet and outlet streams. The two-phase mixture enters the separator at the center of the top flange through a 12.7 mm (0.5") diameter tube that is extended halfway down the length of the separator where it is capped and 32 holes of 1.6 mm diameter are drilled along its length to decrease the

Figure 3.12 Photograph of the Rectifier

velocity of the two-phase mixture. A 0.15 m long, 50 mm diameter stainless steel pipe nipple with 56 holes of 3.2 mm diameter along its length results in additional expansion and separation. Inside this separator, the vapor rises towards the top due to buoyancy and the dilute solution drains to the bottom due to gravity. An assembly of varying density meshes arranged concentrically around the central tube at the top and the bottom further prevents any liquid from flowing through the top of the separator. A sight glass is installed in parallel with the separator to provide an indication of the liquid level in the separator. Temperatures were measured at the dilute solution and ammonia vapor outlets, and pressure was measured at the dilute solution outlet.

3.4.6 Rectifier and Rectifier Coolant Loop

The rectifier reduces the water content in the vapor generated in the desorber so that the refrigerant does not undergo an undesirable temperature rise as it evaporates in the evaporator. An externally cooled rectifier provided by Rocky Research is used in this

test facility. The rectifier (Figure 3.12) consists of a 0.48 m (19") long, 0.11 m (4.5") diameter shell that encloses a helical coil of about 12.7 mm (0.5") diameter, with appropriate fill material in the space between the coil and the shell. Vapor enters at the bottom of the rectifier and the purified vapor exits at the top. The external coolant (chilled water-glycol solution) enters at the top of the rectifier and exits at the bottom. The rectifier is placed at an approximately 30^{o} tilt from vertical since the vapor is condensed by the coolant line and condensate drops fall on the cylindrical wall of the rectifier and collect at the bottom end. The reflux exit is located at the lowest point of the intersection of the cylindrical wall and end cap, thus preventing any vapor from exiting due to the liquid pool collected at this location. Temperatures are measured at the ammonia vapor inlet and at the outlets of the purified ammonia vapor and reflux, and the pressure is measured at the reflux outlet. External coolant (laboratory chilled water-glycol solution) temperatures are measured using T-type thermocouples at the inlet and outlet, with the flow rate being measured by a rotameter. The high concentration refrigerant vapor exiting the rectifier flows to the condenser and the liquid reflux is mixed with dilute solution exiting the separator.

3.4.7 Solution Heat Exchanger

The solution heat exchanger preheats the concentrated solution flowing to the desorber by cooling the dilute solution exiting the separator. This heat exchanger reduces the desorber heat duty requirement by preheating the concentrated solution, and the

Figure 3.13 Solution Heat Exchanger

Figure 3.14 Photograph of the Pre–Cooler

absorber heat duty by reducing the dilute solution temperature entering the absorber. A shell-and-tube exchanger (Model 00256-3 by Exergy Inc) is used as the solution heat exchanger, as shown in Figure 3.13. The 38.1 mm (1.5") O.D. shell contains 55, 0.38 m (15") long tubes of 3.2 mm (0.125") nominal OD and 0.3 mm (0.0125") wall thickness, for a total heat transfer area of 0.20 m^2 (2.2 ft^2). The maximum rated tube and shell side pressures are 8274 and 5516 kPa (1200 and 800 psi), respectively, at a maximum temperature of 427^{o}C (800^{o}F). Temperatures are measured at the inlet and outlet for both fluids and used to establish a heat balance across this component.

3.4.8 Pre-Cooler

In the pre-cooler, vapor exiting the evaporator is used to cool refrigerant liquid exiting the condenser before it enters the evaporator. The pre-cooler also recuperatively heats the vapor entering the absorber. The pre-cooler reduces the enthalpy of the condensate at the evaporator inlet, which increases the cooling capacity of the evaporator. Since the pre-cooler preheats the refrigerant vapor entering the absorber, the absorber duty is increased. The pre-cooler also causes an additional pressure drop that leads to a high evaporator pressure or lower heat rejection temperature for the absorber, or low mass flow rate of the refrigerant. However, another important function the pre-cooler serves is that it handles the evaporation in the high quality, high temperature glide region, thereby maintaining a relatively constant temperature in the evaporator, which is

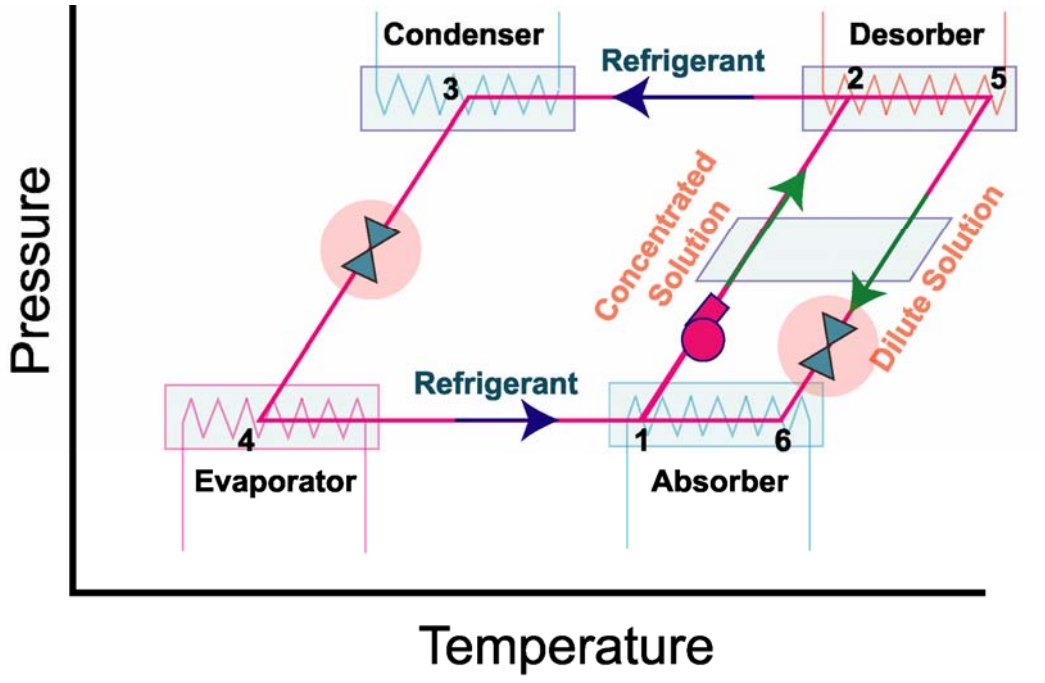

Figure 3.15 Absorption Schematic Diagram

desirable for ensuring that adequate driving temperature differences between the cooled fluid and the refrigerant are maintained. A shell-and-tube exchanger (Model 00256-2 by Exergy Inc.) is used as the pre-cooler, as shown in Figure 3.14. The 38.1 mm (1.5") O.D. shell contains 55, 0.25 m (10") long tubes of 3.2 mm (0.125") nominal O.D. and a 0.3 mm (0.0125") wall thickness for a heat transfer area of 0.13 m^2 (1.43 ft^2). The maximum rated tube-side and shell-side pressures are 8274 and 5516 kPa (1200 and 800 psi), respectively, at a maximum temperature of 427^oC (800^oF). Temperatures are measured at the inlet and outlet of the refrigerant liquid and vapor streams of this heat exchanger and energy balances established.

3.4.9 Expansion Valve

Two expansion devices were required to handle the pressures between the high-side (at the desorber, rectifier, and condenser) and the low-side pressures (at the evaporator, and the absorber) as shown in the schematic diagram marked with circles

(Figure 3.15). A constant superheat thermostatic expansion valve (Model #TEA 20-2 by Danfoss) located between the pre-cooler and the evaporator was initially used as an isenthalpic expander for the refrigerant ammonia. This valve could be used for evaporator temperatures of -20 to 30^{o}C with up to 7 kW cooling duties, which was the anticipated range of evaporator temperatures for the pressures of interest in this study. However, this expansion valve did not work at intermediate cooling capacities, and was suspected to be oversized for the tests under consideration. Thus, to account for the variable cooling capacity at the evaporator, a manual metering needle valve (SS-4MG-MH, max C_V of 0.03, Swagelok) was installed in parallel with the existing thermostatic expansion valve. By installing two additional shut-off valves, it was possible to use any of these two expansion valves one at a time.

3.4.10 Pressure Reduction Valve

The system was initially designed to have a pressure reduction valve for achieving the required pressure reduction from the high side pressure to the low side pressure. Two pressure reduction valves were used, one for the dilute solution between the solution heat exchanger and the absorber, and the other for the reflux flow from the rectifier. Suitable pressure reduction valves for ammonia-water solution (Model A2BO V-series by Parker) were installed. The pressure range of the valve is between 66.7 kPa (500 mm Hg) and 800 kPa (8 bar) with 180 kPa (1.8 bar) change per turn, and a maximum operating pressure of 2070 kPa (20.7 bar). These valves are outlet-set pressure regulators that also contain stainless steel strainers to protect the valve from foreign material present in the system. The absorber pressure was expected to be maintained at the desired test condition by appropriate settings of this valve. Use of the tube-in-tube co-flow heat

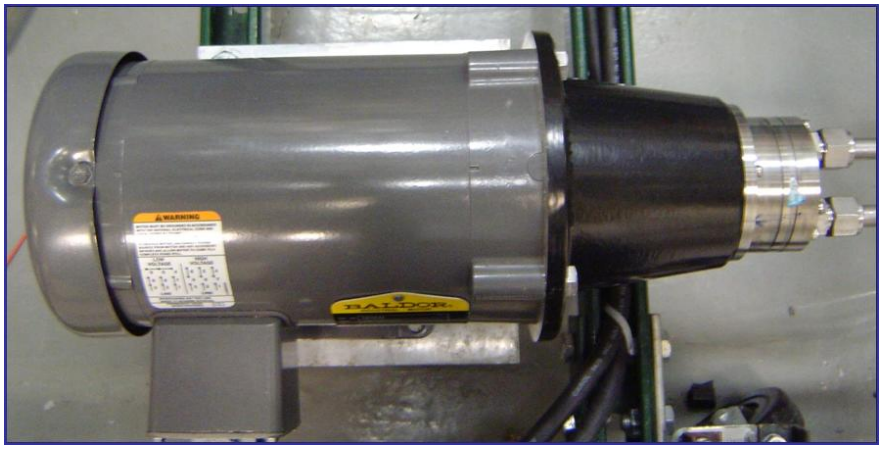

Figure 3.16 Solution Pump

exchanger for the desorber prevents the reflux from entering the desorber. Therefore, using the above-mentioned pressure regulator, it was decided that the reflux could be introduced in the concentrated solution stream from the absorber before it enters the solution pump. However, these pressure reduction valves proved to be ineffective in controlling the pressure precisely, and were replaced with manually controlled needle valves (SS-4L-MH-NE by Swagelok with a maximum C_V of 0.15 between the solution heat exchanger and the absorber; SS-26VS8 by Swagelok with a maximum C_V of 0.21 in the reflux line) to achieve precise control of solution flow rates and the low-side pressure.

3.4.11 Solution Pump

The solution pump (Figure 3.16) for delivering the concentrated solution from the absorber to the desorber is a variable-speed Tuthill magnetic gear pump with 1.44×10^{-4} m^3/s (2.3 gpm) maximum flow rate at zero pressure difference. This pump operates between 1034 kPa (150 psi) pressure difference for continuous duty and 1724 kPa (250 psi) for intermittent duty at a maximum system pressure of 3447 kPa (500 psi). The

operating temperature is between -46^{o}C and 176^{o}C, and the maximum operational viscosity is 2 kg/m-s (2000 cP).

A summary of the specifications of components used in the test facility is provided in Table 3.3.

Table 3.3 Component Specifications

Location/ Component	Manufacturer (Part Number)	Dimensions (m)/ Specification	Operation Range	Limitation
Pump				
Solution Pump	Tuthill Pump (TXS2.6EEET3WND3001)	Type: Magnetic Gear Pump (Continuous Duty) 0 to 1034 kPa (Intermittent Duty) 0 to 1724 kPa 230V	Flow Rate: 1.44×10^{-4} m^3/s at 0 kPa 1.2×10^{-4} m^3/s at 1030 kPa Differential Pressure: 1724 kPa	Pressure: 3447 kPa Temperature: –46 to 176°C Viscosity: 2 kg/m–s (2000 cP)
Absorber/ Condenser Coolant Pump	Little Giant Pump (Model TE–7–MD–HC)	Centrifugal Pump ¾ hp 115/230V	Flow Rate: 3.344×10^{-3} m^3/s at 0.3 m of Head Fluid Temp.: Up to 93.3°C	Specific Gravity: up to 1.1 Ambient Temp.: 25°C
Evaporator	Finish Thompson Pump (Model AC4STS1V35060015C015)	Centrifugal Pump ¾ hp 115/230V	Max. Flow Rate: 2.341×10^{-3} m^3/s at 3450 rpm (1.861×10^{-3} m^3/s at 2900 rpm) Max Head: 16.6 m at 3450 rpm (10.4 m at 2900 rpm)	Pressure: 6895 kPa Temperature: 148.9°C
Heat Exchanger				
Condenser	Exergy, Inc. (Model 00677–3)	Stainless steel Type: Shell–and–tube Length: 0.5 m Shell O.D.: 76.2 mm Number of Tube: 253 Tube O.D.: 3.2 mm Tube Wall Thickness: 0.3 mm Heat Transfer Area: 1.24 m^2		Pressure: Tube–side: 5171 kPa Shell–side: 3447 kPa Temperature: 427°C

Table 3.3 Continued

Location/ Component	Manufacturer (Part Number)	Dimensions (m)/ Specification	Operation Range	Limitation
Desorber/ Evaporator	Exergy, Inc. (Model 00528)	Type: Tube–in–Tube Material: Stainless Steel Length:5.9 m Inner Tube: O.D.: 12.7 mm Outer Tube O.D.: 25.4 mm Wall Thickness: 1.7 mm Heat Transfer Area: 0.26 m^2		Pressure (kPa): Tube–side: 31,026 Annulus–side: 13,790 at temperature (^oC) 93.3 Temperature (^oC) 427^oC
Rectifier	Provided by Rocky Research	Type: Shell–Coiled Tube Material: Steel Shell Length: 0.48 m Shell O.D.: 0.11 m Coil O.D.: 12.7 mm		
Separator	In–House	Material: Stainless Steel Shell Length: 0.3 m Shell O.D.: 0.15 m Tube O.D.: 12.7 mm Tube Length: 0.15 m Number of Holes: 32 (1.6 mm) Pipe Nipples O.D.: 50 mm Pipe Nipples Length: 0.15 m Number of Holes: 56 (3.2 mm)		
Solution Sub–cooler	In–House	Type: Shell–Coiled Tube Material: Stainless steel Length: 0.61 m Inner Tube: O.D.: 12.7 mm Outer Tube O.D.: 25.4 mm Wall Thickness: 1.7 mm Heat Transfer Area: 0.024 m^2		
Solution–Solution Heat Exchanger	Exergy Inc (Model 00256–3)	Type: Shell–and–tube Material: Stainless steel		Pressure (kPa): Tube–side: 8274

Table 3.3 Continued

Location/ Component	Manufacturer (Part Number)	Dimensions (m)/ Specification	Operation Range	Limitation
		Length: 0.38 m Shell O.D.: 38.1 mm Number of Tube: 55 Tube O.D.: 3.2 mm Tube Wall Thickness: 0.3 mm Heat Transfer Area: 0.20 m^2		Shell–side: 5516 Temperature: 427^oC
Pre–cooler Heat Exchanger	Exergy Inc (Model 00256–2)	Type: Shell–and–tube Material: Stainless Steel Length: 0.25 m Shell O.D.: 38.1 mm Number of Tube: 55 Tube O.D.: 3.2 mm Tube Wall Thickness: 0.3 mm Heat Transfer Area: 0.13 m^2		Pressure (kPa): Tube–side: 8274 Shell–side: 5516 Temperature: 427^oC
Absorber/ Condenser Coolant	Superchanger (Model UX–016–UJ–21)	Type: Plate Heat Transfer Area: 1.65 m^2 Height: 0.774 m, Length: 0.3 m, Depth: 63–67.3 mm, Weight: 95.7 kg		Maximum Pressure: 1034 kPa (150 psi), Maximum Temp.: 93.3^oC
Heater				
Evaporator/ Absorber Coolant Side	Watlow (Model L12NX4B)	Type: Electric Firerod Immersion Length: 324mm, Diameter: 15.88 mm 240V	5000 Watts, Watt Density: 46.5 W/cm^2	Temperature: 100^oC at atmospheric Pressure
Heater Controller	Payne Engineering (18TB–2–25)	Height: 162.4 mm, Width: 101.6 mm, Depth: 88.9 mm, 240V	Max Fuse Amps: 25 Amps, Max kVA = 5.9	Temperature -10 to 50^oC
Expansion Devices				
Solution Side	Swagelok	Type: Flow Metering Valve	9.46×10^{-5} m^3/s	Pressure: 6895 kPa

Table 3.3 Continued

Location/ Component	Manufacturer (Part Number)	Dimensions (m)/ Specification	Operation Range	Limitation
	(SS–4L–MH–NE)	Body Material: Stainless Steel O–rings Material: Neoprene Feature: Micrometer Handle, Fittings: 1/4" Neoprene O–rings, No shut off service	at 690 kPa difference for water Max: 0.15 C_V	Temperature: –23 to 121°C (Neoprene O–rings)
Refrigerant Side	Swagelok (SS–4MG–MH–NE)	Type: Flow Metering Valve Body Material: Stainless Steel O–rings Material: Neoprene Feature: Venire Handle Fittings: 1/4"	Max: 0.03 C_V	Pressure: 3447 kPa Temperature: –23 to 148°C
Fittings and Plumbing				
Sight Glass	Pressure Product (Bulls Eye)	Case Material: 316/316L Stainless Steel Lens Material: Tempered Soda Lime Lens Outer Diameter: 26.06 mm Lens Thickness: 17.2 mm O–rings, Cushion, and Gaskets Material: Teflon PTFE	Bulls Eye(See–Thru), Sight Flow Indicator Connections 1/2"NPT–3–3/4"	Pressure: 4137 kPa Temperature: 232.2°C
Plumbing	Swagelok (SS–T16–S–083,1") (SS–T8–S–035,0.5")	Outer Diameter: 25.4 mm Thickness:2.1 mm Outer Diameter: 17.2 mm 0.035in Thickness:2.1 mm		21,374 kPa (25.4 mm) 17,926 kPa (17.2 mm)
Data Acquisition System				
Data Acquisition System	IO Tech (Tempscan/1000A Expansion Chassis	Channel Configuration: Minimum: 32 input channels Maximum: 992 input channels	Number of Slots: Tempscan/1000A: 2 EXP/11A: 10	

Table 3.3 Continued

Location/ Component	Manufacturer (Part Number)	Dimensions (m)/ Specification	Operation Range	Limitation
	EXP/11A)			
I/O Card Pressure	IO Tech (TempV/32B)	Type: Voltage Scanning Module Input: Current 4–20 mA Output : Voltage 1–5 V with 250 ohm resistors	Input Channels Number: 32 Output Values: 10 V, 5 V, 1 V, or 100 mV	
I/O Card Thermocouples	IO Tech (TempTC/32B)	Type: Voltage Scanning Module Thermocouple types J, K, T, E, R, S, B, and N Output : ^{o}C, ^{o}F, K, R, or volts	Input Channels Number: 32	
I/O Card RTD	IO Tech (TempRTD/16B)	Type: Voltage Scanning Module Output : ^{o}C, ^{o}F, K, R, or volts RTDs Type: 3– or 4–wire	Input Channels Number: 16	
Hazardos Chemical Gas Dectector				
Ammonia Sensor	LUMIDOR SAFETY PRODUCTS (SAM–NH308N) (SAM–SB–NH3 Ammonia sensor assembly) (EGS257 Ammonia sensor)	Dimension: 15.24 cm × 15.24 cm × 10.16 cm Weight: 1.13 kg Relay Output: 3 Dry Contacts (Alarm, Warn, Fail) Rated 30W max. 250 VAC Accuracy: Ammonia (NH_3): 0–99 ppm PPM	Alarm : 25 ppm Audible Over 100 dB at 0.3 m from a sensor Visual: HIGH Alarm: Continuously lit red LED LOW Alarm: Continuously Lit Yellow LED MALFUNCTION: Continuously lit green LCD	Temperature: –15°C to 45°C Humidity: 0–90% RH (non–condensing)

3.5 Instrumentation

3.5.1 Temperature and Pressure Measurements

Temperatures are measured by 3-wire RTDs and T-type thermocouples. T-type thermocouples (Omega Engineering) can be used over the temperature range -270 to 400^{o}C with an accuracy of ±0.5^{o}C while 3-wire RTDs (Pr-13, Omega Engineering) can be used to measure temperatures in the range -60 to 400^{o}C with an accuracy of ±0.8^{o}C.

Absolute pressures are measured using Rosemount model 2088 and 3051 pressure transducers. These absolute pressure transducers are capable of measuring pressures in the range 0 kPa to 27,579 kPa (4,000 psia), with an accuracy of ±0.075% of the calibrated span. However, for improving accuracy, the span was set to 0 kPa to 2048.5 kPa (300 psi). Differential pressures were measured using a Rosemount model 3051 transducer that is capable of measuring pressures up to 13,790 kPa, with an accuracy of ±0.075% of span for spans larger than 2758 kPa. For smaller spans, the accuracy of the transducer is ±[0.025 + 10/span] % of span. These pressure transducers produce 4-20 mA output signals that are converted to 1-5 V signals for use in the data acquisition system. The pressure transducers are rated for the temperature range of -40 to 121^{o}C.

3.5.2 Flow Meters

To measure mass flow rates of the dilute and concentrated solutions, Micromotion Coriolis flow meters (model CMF025 ELITE) are installed in the test facility. The flow rates are displayed on Micromotion RFT 9739 rack-mounted displays. These meters can be configured for the desired ranges of the parameters using the HART communicator. The flow meters can read 0 - 0.605 kg/s or 0 - 6.309×10^{-4} m^{3}/s (0 – 10 gpm) with an

accuracy of ±0.10% of the flow range. The operating temperature range is -240 to 204°C, with a maximum operating pressure of 10000 kPa (100 bar). The meters provide one primary and one secondary analog output and one frequency output. The flow meters generate 4 - 20 mA output signals that are converted to 1 - 5 volt signals for use by the data acquisition system.

The heat transfer fluid flow rate, and subsequently, the coolant flow rate in the condenser loop, was measured using a Coriolis flow meter from Micromotion (model CMF100 Elite). This flow meter can measure flow rates of 0 - 7.56 kg/s (1000 lb_m/min) with an accuracy of ±0.10% and density in the range 0 - 5000 kg/m^3 with an accuracy of ±0.5 kg/m^3. It can be used over a wide range of temperatures -240 to 204°C up to a maximum system pressure of 100 bar (10000 kPa or 1450 psi). The meter reading is transmitted by a field mount transmitter (RFT9739 by Micromotion).

The flow rate of the absorber coolant is measured by a magnetic flow meter from Rosemount (model 8711) coupled to a model 8712C flow transmitter, with an accuracy of ±0.5%, and can be used over the range -29 to 149°C up to system pressures of 5102 kPa (740 psi). The flow rate of the coolant in the evaporator loop is measured using a positive displacement flow meter from AW company (model JVM-60KL) coupled to a flow transmitter (FEM-03 by AW Company). It can be used to measure flow rates in the range 0 – 1.262×10^{-3} m^3/s (0 - 20 gpm) with ±0.5% accuracy up to 34474 kPa (5000 psi) system pressure. Chilled water-glycol flow rates are measured using rotameters for the different cooling loops. The flow rate in the plate heat exchanger of the absorber coolant loop is measured using a VFC-143 series rotameter from Dwyer over the range 1.2618×10^{-4} - 12.618×10^{-4} m^3/s (2 - 20 gpm) with an accuracy of ±2% of full scale. The

flow rate in the plate heat exchanger of the condenser coolant loop is measured using a 7530-7C-08 rotameter from King Instrument over the range 0.6309×10^{-4} - 6.309×10^{-4} m^3/s (1 – 10 gpm) with an accuracy of ±0.5% of full scale. There are two rotameters in the rectifier loop. One of the two is used depending upon the flow rate for the data point under consideration. One rotameter (model VFB-85-EC) has a range of 0.126×10^{-4}-1.262×10^{-4} m^3/s (0.2 – 2.0 gpm), while the other (model VFB-86-EC) has a range of 0.379×10^{-4} –3.155×10^{-4} m^3/s (0.6 – 5.0 gpm). Both of these have an accuracy of ±3% of full scale.

A summary of the specifications of each instrument used in this study is provided in Table 3.4.

Table 3.4 Instrumentation Specifications Summary

Parameter/ Instrument	Model	Manufacturer	#	Range	Accuracy	Operating Limits
Flow Meters and Transmitters Specifications						
Dil/Conc Solution	CMF025 Elite	MicroMotion Inc.	2	0 – 0.6048 kg/s 0 – 6.309×10^{-4} m^3/s	±0.1% (Flow) ±0.5 kg/m^3 (Density)	T: –240 to 204°C P: 10000 kPa
Dil/Conc (Trans)	RFT9739–Rack Mounting	MicroMotion Inc.	2	0–5000 kg/m^3 –240 to 450°C		T: 0 to 50°C (Ambient)
Refrigerant	C25	MicroMotion Inc.	1	0 – 0.02268 kg/s	±0.1%	
Abs Coolant	8711	Rosemount	1	0 – 1.262×10^{-3} m^3/s	±0.5%	T: –29 to 149°C P: 5.1MPa
Abs Coolant (Trans)	8712C	Rosemount	1			T: –29 to 60°C (Ambient)
Evap Coolant	JVM–60KL	AW Company	1	1.262×10^{-4} – 1.262×10^{-3} m^3/s	±0.5% @ $\nu = 3 \times 10^{-5}$ m^2/s	P: 34474 kPa
Evap Coolant (Trans)	FEM–03	AW Company	1			
Cond Coolant	CMF100 Elite	MicroMotion Inc.	1	0–7.56 kg/s (Density)	±0.1% (Flow) ±0.5 kg/m^3	T: –240 to 204°C P: 10000 kPa
Cond Coolant (Trans)	RFT9739–Field Mounting	MicroMotion Inc.	1	0–5000 kg/m^3 –240 to 450°C		T: 0 to 50°C (Ambient)
Pressure Transducers and Dial Gauges Specifications						
Absolute	2088	Rosemount	5	0–5516 kPa	±0.25% of Calibrated Span	T: –40 to121˚C
Absolute	3051	Rosemount	2	0–27579 kPa	±0.075% of Calibrated Span	T: –40 to121˚C
Absolute	3051	Rosemount	4	0–68948 kPa	±0.075% of Calibrated Span	T: –40 to121˚C
Differential	3051C	Rosemount	1	0–13790 kPa	±0.075% of Calibrated Span	T: –40 to 121˚C P: 31MPa
Dial Gauge	1005P (ABS–Black)	Ashcroft	2	0–689.5 kPa	±3% of Span	T: –40 to 65°C
Dial Gauge	1005P (ABS–Black)	Ashcroft	1	0–2068 kPa	±3% of Span	T: –40 to 65°C
Thermocouples and RTDs Specifications						
Thermocouple	T–type	Omega Engineering	44	–270 to 240°C	±0.5°C	
RTD	Pr–13	Omega Engineering	12	–60 to 240°C	±0.5–0.8°C	
Rotameters Specifications (m^3/s)						
Absorber	VFC–143 series	Dwyer Instrumentation	1	1.262×10^{-4}– 1.262×10^{-3}	±2% of Full Scale	T: 49°C P:690kPa
Condenser	7530 7C–08	King Instrument Company	1	6.309×10^{-5}– 6.309×10^{-4}	±2% of Full Scale	T: 54°C P:862kPa
Rectifier	VFB –85–EC	Dwyer Instrumentation	1	1.262×10^{-4}– 1.262×10^{-3}	±3% of Full Scale	T: 65°C P:690kPa
Rectifier	VFB –86–EC	Dwyer Instrumentation	1	3.155×10^{-5}– 3.155×10^{-4}	±3% of Full Scale	T: 65°C P:690kPa
Sub–cooler	7530 7C–06	King Instrument Company	1	2.524×10^{-5}– 3.155×10^{-4}	±2% of Full Scale	T: 54°C P:862kPa

3.5.3 Data Acquisition

A PC-based data acquisition system (supplied by IO Tech) is used to display and record data during the tests. The Tempscan/1000A with an expansion unit EXP/11A interfaced with the computer through the program TempView 4.1 allows real-time display and recording of temperatures, pressures, and flow rates. Together with an expansion chassis, the Temp Scan/1100 enables the capacity to add up to 10 modules that could monitor up to 992 input channels. Data acquisition rates and durations can be programmed at desired scan rates using the TempView interface. Pressure transducers are connected to the Tempscan using a voltage scanning module (TempV/32B) that converts 4-20 mA current input to 1-5 V with 250 ohm resistors, while thermocouples and RTDs are directly connected to Tempscan through thermocouple scanning modules (TempTC/32B) and RTD scanning modules (TempRTD/16B). The thermocouple scanning module (TempTC/32B) can read 32 differential input channels, which can be configured for thermocouple types J, K, T, E, R, S, B, and N for a 100 mV input.

Measurements can be designated in units of ^{o}C, ^{o}F, K, R, or volts. The RTD scanning module (TempRTD/16B) can read 16 channels of 3- or 4-wire RTDs in units of ^{o}C, ^{o}F, K, or R. The voltage scanning module (TempV/32B) can read 32 input channels with programmable ranges of 10 V, 5 V, 1 V, or 100 mV. A Windows-based TempView program provides a graphical user interface for easy configuration of hardware, acquisition, and display parameters. Real time data can be monitored by the TempView program in graphical or spread-sheet mode.

For the current tests, a total of 4 scanning modules, two (TempTC/32B) for T-type thermocouples, one (TempRTD/16B) for RTDs, and one (TempV/32B) for pressure

transducers as well as for flow meters that have 4-20 mA output, are used. For these experiments, 44 thermocouples, 12 RTDs, 11 absolute and 1 differential pressure transducers, and 6 flow meters are connected to Tempscan using these 4 scanning modules. For each data point therefore, 56 temperatures, 12 pressures, 6 flow rates and 2 densities are recorded over a span of 5 minutes at 3 second intervals yielding 100 readings.

3.6 Tailoring the Test Facility for Wide Operating Range

During this study, after the test facility became functional and a regular program of testing was initiated, the facility underwent major modifications in different stages to enable testing at vastly different test conditions. These modifications included changes to the coolant loops for each component including new heat exchangers and plumbing orientations, changes to ammonia (e.g. reflux flow rate) and coupling fluid measurement techniques, changes to control devices such as refrigerant expansion valves, changes to the heat source supply method, and numerous other minor modifications that provided the ability to progressively conduct tests and measurements over an extremely large range of high and low temperature, pressure and concentration, and flow rate conditions. It should be noted that these changes were most often not because of inadequate design or operation, but simply because no single test facility configuration can accomplish testing at all the conditions required in this study. The most significant of these changes and different test facility configurations are described briefly in the following sections.

3.6.1 Two-Pressure Operation

During the initial phase of experiments, steady operation while maintaining high and low side pressures and the desired desorber outlet conditions could not be obtained. It was determined that the thermostatic expansion valve did not provide the required external pressure equalization. An external pressure equalizer was installed and connected to the thermostatic expansion valve from a location downstream of the evaporator. However, this thermostatic expansion valve did not provide intermediate cooling capacities and fine control of pressures and refrigerant flow rates for the tests under consideration. Thus, to account for the variable cooling capacity and the fine control required on the pressures and the refrigerant flow rates at the evaporator, a manual metering needle valve (SS-4MG-MH, max C_V of 0.03, Swagelok, Figure 3.17) was installed in parallel with the existing thermostatic expansion valve. Two shut-off valves upstream of the expansion valves allowed the use of any of these two expansion valves one at a time. One additional shut off valve was installed between the evaporator and absorber to provide isolation between different segments of the loop for flexibility for maintenance and operation. A 6.4 mm (1/4") liquid line was also installed

Figure 3.17 Manual Needle Valve

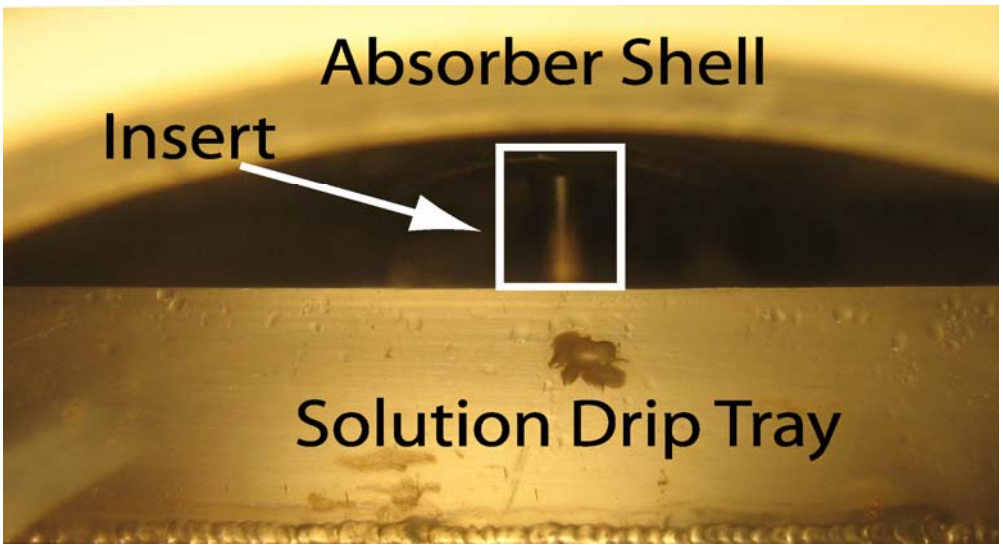

Figure 3.18 Absorber Inlet Modification

between the evaporator inlet and the pump inlet, which, if necessary, allowed removal of water-rich liquid accumulated in the evaporator to be mixed with the solution from the absorber outlet.

3.6.2 Absorber Solution Inlet

At very small solution flow rates, the dilute solution was observed to flow along the inner wall of the absorber shell. This was attributed to the previous absorber inlet design, in which the inlet line ended abruptly at the shell, allowing a portion of the solution flow along the shell wall rather than over the tube bank, particularly at the low flow rate cases. With a portion of the absorption occurring on the shell without any adequate heat removal, the absorber temperature and pressure were unduly high. To avoid this, the 12.7 mm (½") inlet tubing to the absorber (Figure 3.18) was extended into the absorber shell half way through the depth of the drip tray to make the solution fall on the tubes and not along the wall.

3.6.3 Solution Pumping

It was also found that often, the solution pump inlet was starved of solution, primarily due to unstable running conditions. In such instances, the pressure in the expansion tank upstream of the solution pump rose to levels higher than that in the absorber, thus preventing solution flow. To avoid pressure spikes in the expansion tank, a pressure equalization line was installed to connect the top of the sight glass and expansion tank to the absorber. Thus, when solution at the pump inlet was lost, the expansion tank could be filled soon.

3.6.4 High-Side Pressure Regulation

Maintaining pressure levels with the two outlet-set pressure regulators (in the reflux line and in the dilute solution return line to the absorber) proved to be challenging. The regulators operating between relatively similar pressures were interfering with each other, making stable operation difficult. Whenever the pressure at the absorber, which is downstream of the regulator in the solution line, was increased, the regulator interrupted the flow. A manually controlled needle valve with a variable C_V (flow coefficient) was therefore used to replace the pressure reduction valve and provide much better control over the flow rates and pressures. The pressure reduction valve in the reflux line, which was causing unstable operation, was also removed and the reflux was directly introduced at the separator outlet. To enable this modification, the rectifier was further elevated to increase the static head available for drainage of the reflux.

3.6.5 Refrigeration Flow Rate Measurement

It was deemed that because the refrigerant flow rate was a particularly critical quantity for the measurement of absorption rates, a direct measurement of this flow rate should be conducted rather than inferring it from the differences of two flow rates or indirectly from other quantities such as the evaporator or condenser coupling-side heat duty. Since measuring refrigerant flow rate in vapor form is quite challenging, based on the anticipation that the refrigerant exiting the condenser is subcooled, a Coriolis mass flow meter was installed downstream of the condenser to measure the liquid-phase refrigerant mass flow rate. To ensure sub-cooling at the condenser outlet, a sight glass (Figure 3.19) was mounted at the outlet of the condenser. Subcooling ensured that the refrigerant mass flow meter measured the refrigerant flow rate accurately. Similarly, another sight glass was installed at the reflux outlet.

3.6.6 Extreme Pressure and Concentration Conditions

The above modifications, along with many other minor plumbing modifications, allowed experiments to be conducted at a majority of the desired test conditions.

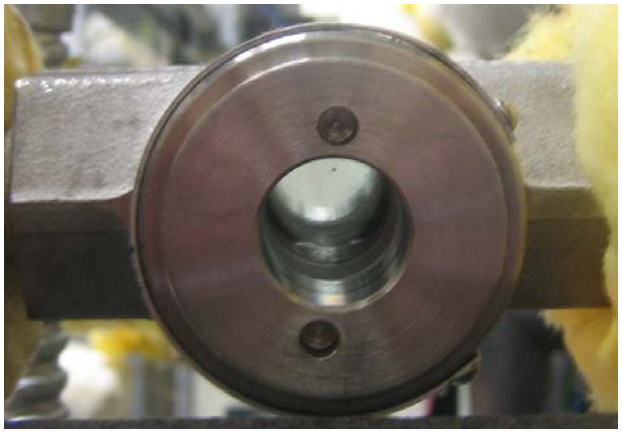

Figure 3.19 Sight Glass on Refrigerant Side

It was, however, found that the 150 kPa (21.8 psi) absorber pressure cases for 25%, and 345 (50.0 psi) and 150 kPa (21.8 psi) absorber pressure cases for 40% dilute solution concentration at the desorber could not be obtained using the above test configuration. For example, despite using the absorber coolant and the chilled water-glycol supply at their full capacities, it was not possible to obtain the lower pressures at the higher dilute solution concentrations. Therefore, it was decided that pre-cooling this absorber inlet solution over and above what was achievable in the solution heat exchanger would decrease the heat load that must be handled by the absorber in some of these higher dilute solution concentration cases. Such a provision would offer independent control of the dilute solution temperature at the absorber inlet, and also lower the sensible cooling component of the absorber heat load, making the latent heat load dominant. High fractions of sensible heat loads in the absorber could unduly overestimate the absorption heat transfer coefficient. Based on these considerations, a 0.61 m (2 ft) long water-cooled, tube-in-tube dilute solution subcooler (Figure 3.20) was designed, fabricated and installed between the solution heat exchanger and the absorber.

Figure 3.20 Dilute Solution Sub-Cooler

This stainless steel heat exchanger consists of a 12.7 mm (0.5") nominal O.D. inner tube and a 25.4 mm (1") nominal O.D. outer tube. Dilute solution flows through the inner tube, while chilled water-glycol solution flows through the annulus in a counterflow orientation.

3.6.7 Absorber Coolant Temperature Difference

It was also found that for some of the data at the 345 and 500 kPa (50 and 72.5 psi) absorber pressure cases, there were large temperature differences from the inlet to the outlet of the absorber coolant due to the relatively small absorber coolant flow rates required to maintain these specific conditions in the first place. Since coolant flow rate measurement errors would be relatively large at such low required coolant flow rates, and also since large coolant ΔTs could affect absorption characteristics, it was decided to find an alternate means to reduce absorber coolant ΔTs, while maintaining reasonably large coolant flow rates. The heat sink for the closed coolant loop of the absorber is the large plate heat exchanger, which is coupled to the common glycol-water solution coolant from the chiller. This heat sink cools the closed-loop coolant to temperatures very close to the

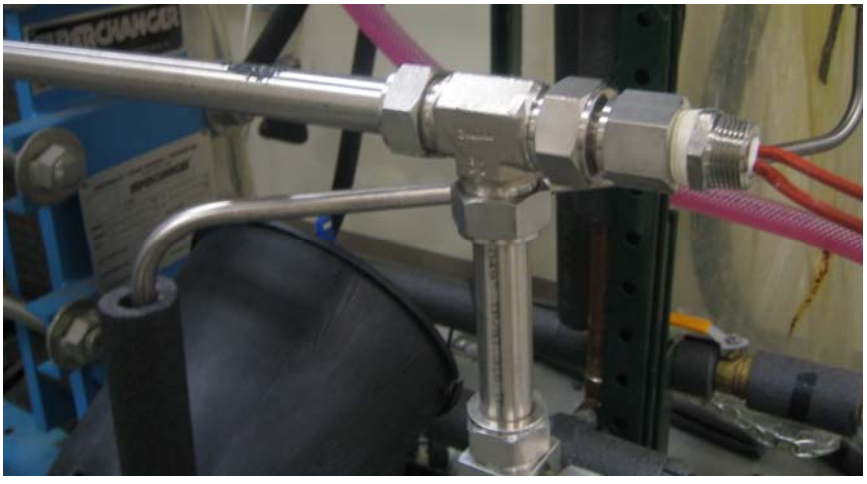

Figure 3.21 Electric Heater at Absorber Coolant Side

chiller temperature, restricting the amount of control available over the absorber coolant inlet temperature. In view of these considerations, it was decided to use a high flow rate closed loop coolant for these test cases, but raise the temperature at the absorber inlet by introducing a 5 kW resistance heater (Figure 3.21) between the plate heat exchanger and the absorber inlet. This heater therefore enabled the use of reasonably large (and measurable) absorber coolant flow rates while reducing the coolant temperature rise within the absorber, and added considerable flexibility to the control of the absorber conditions.

With the measures described above, it was possible to obtain the very wide range of test conditions that presented conflicting requirements to the coupling loops and control arrangements.

3.7 Experimental Procedures

This section describes the test procedures and precautions used to ensure safety. Leak checking and charging procedures are also described. Safety issues are especially important since the system contains ammonia and operates at pressures higher than ambient.

3.7.1 Safety Precautions

Safety issues are of high priority when working with chemicals that are harmful to humans. Ammonia has toxic and corrosive characteristics and causes freeze burns from its cold temperatures, and may affect the immune system in the case of large acute exposures. Ammonia vapor is toxic, corrosive, depletes oxygen, and acts as a poison when ingested. Whenever eyes are exposed to ammonia, immediate first aid is necessary.

To avoid any possible mishaps, many safety and precautionary measures are taken throughout this study. Some of these important test practices are described here. A full face mask fitted with an ammonia/methylamine cartridge and gloves are worn whenever there is a possibility of direct contact with ammonia, especially during charging and discharging of the loop with ammonia. The system is located under the fume hood enclosed with a plastic curtain on all sides. An exhaust fan in the fume hood is turned on to trap and discharge any ammonia that might be present during charging and operation, or during plumbing modifications, to the outside atmosphere. An ammonia monitor that is always functional is installed on the wall next to the test facility. This monitor (SAM by Lumidor Safety Products) has a working range of 0-99 ppm and an accuracy of ±2 ppm, and is calibrated to provide a loud alarm at 25 ppm of ammonia in its vicinity. Operators also wear protective safety glasses while operating the system.

3.7.2 Leak Testing and Charging

Before charging the system, it must be ensured that there are no leaks in the system. Extensive leak tests are performed before charging the system. The system is first charged with air at up to 793 kPa (115 psi), and fittings, gaskets, welded parts and sight glasses are checked for leaks using soap detection. In several instances, in addition to soap detection, the system is charged with air and R-134a up to 1379 kPa (200 psi) and a refrigerant leak detector (CPS model L-709) is used to detect leaks. The system is then kept pressurized overnight. If there is no appreciable pressure drop, the evacuation process is started using a vacuum pump (model DV-85N by DV industries) and maintained until the pressure in the system decreases to 20 Pa or lower. A vacuum gauge (model 14571 by Thermal Engineering) is used to monitor the vacuum level, and pressure

transducers are also used to run a pressure trace. This evacuation process removes non-condensable gases, and also provides enough pressure difference to enable charging with water and ammonia. Distilled water is charged before charging ammonia so that when ammonia is charged, it is absorbed into water and the pressure can be maintained in a controlled manner. The total required charge for the system is estimated using expected void fractions and concentrations in the various components and plumbing of the loop at nominal test conditions. Because test conditions vary over a wide range of concentrations, the amount of charge is determined based on the conditions to be tested in a given period. The mass fraction of ammonia in the loop is generally kept within 15% of the desired test concentration to keep the desorber heat duties within a reasonable range. More ammonia is added whenever higher concentration cases are to be tested.

3.7.3 Testing

A set of well established test procedures was developed and used to ensure that data were obtained with acceptable accuracies. The tests were initiated after appropriate amounts of ammonia and distilled water were charged into the system. The data acquisition system and Tempview software are started first so that the progress of the changing states in the system can be monitored continuously. Before starting a test, the system is checked for leaks, and valves that need to be in the open mode are opened. It is also ensured that there is enough liquid level at the pump inlet. The laboratory chiller is turned on and is set to the appropriate temperature. Since the desired dilute solution concentration depends on the pressure and temperature at the desorber outlet, and the desorber pressure depends on the condenser temperature, the laboratory chiller temperature to obtain the desired condensing temperature is first estimated. This

laboratory chiller provides chilled water-glycol solution to serve as the heat sink for the rectifier, condenser and absorber. Once the laboratory chiller is turned on, condenser, absorber, and evaporator coolant pumps are started. After all coolant pumps are turned on and it is determined that they are running at steady state, the variable speed solution pump is started at a low frequency to yield a low solution flow rate. Since there is no pressure differential across the pump at the beginning, the status of the pump is carefully monitored based on the solution level using the sight level indicator that is connected to the expansion tank upstream of the solution pump. After the solution pump is started, steam supply to the desorber is turned on. Addition of steam starts heating up the solution from the pump and raising the high side pressure. The heat duty is increased in gradual steps. Expansion valves for the dilute solution and refrigerant are kept wide open during the above procedure to reduce any flow restriction before some steady circulation is achieved. The solution level in the separator is also checked to ensure that there is no significant accumulation, which avoids the possibility of inadvertently starving the pump of solution supply. The solution pump speed is then gradually increased while the steam supply is also increased according to the solution flow rate. As steam supply is increased, the desorber outlet temperature and pressure increase; however, the solution flow rate decreases since the differential pressure is now higher. It takes some time before vapor actually starts flowing out of the rectifier and condenses in the condenser. As the amount of vapor generated at the desorber and flowing to the condenser is increased, the temperature at the evaporator starts decreasing. The heater in the evaporator heating loop is turned on when the evaporator heating fluid temperature starts decreasing. The steam supply to the desorber and the solution flow rate are adjusted to

obtain the desired concentrations at the desorber outlet, and solution flow and rectifier coolant flow are adjusted to obtain get the desired refrigerant concentration. When the system is running in a quasi-steady state, the evaporator expansion valve is gradually closed to achieve better pressure separation and therefore obtain a liquid phase at the condenser outlet. Sometimes, this increases the high side pressure and decreases the low side pressure, resulting in increased differential pressure and decreased solution flow rate. The decreased solution flow rate is compensated by increasing the pump speed accompanied by an adjustment of the steam supply. If the high side pressure becomes too high, the laboratory chiller flow rate for the condenser loop is first increased, and in addition, if necessary, the rectifier flow rate is increased. The differential pressure is monitored to keep it within 1034 kPa (150 psi), which is the maximum operational differential pressure for the pump. Throughout this process, the dilute solution flow rate is controlled using the solution expansion valve in the dilute solution line, and the difference between the concentrated and dilute solution flow rates is kept close to the refrigerant flow rate measured at the condenser outlet. The absorber pressure is continuously varying during this startup process, and is controlled by varying the absorber coolant flow rates and temperatures. Once the desired concentration at the desorber outlet, the concentrated solution flow rate, and the absorber pressure are obtained, the system is observed for some time without changing any of the parameters. If the values remain fairly steady, a preliminary data point is recorded and energy balances and concentrations are checked at various positions. If any of the heat balances at the different components are unacceptable, the coolant side flow rate or temperature or both are varied to improve the agreement between the ammonia-water and coolant-side

duties. If the dilute concentration at the desorber outlet is different from the desired concentration, the steam duty is varied accordingly. These processes are repeated until the dilute solution concentration, solution flow rate, and the desired absorber pressure are achieved, combined with acceptable energy balances at the absorber, evaporator and condenser. After acceptable heat balances are obtained for each component, the system is observed until the various measured quantities do not change for a significant amount of time, and the data are recorded and checked again. A full data set consisting of 100 readings over a span of 5 min is then recorded.

In this study, concentration, solution flow rate and absorber pressure vary over wide ranges. Three absorber pressures of 150, 345 and 500 kPa (21.8, 50.0 and 72.5 psi), and four different concentrations of 5, 15, 25 and 40% for three different flow rates for each combination of concentration and pressure result in 36 data points. To obtain data over these wide ranges, the ultimate driving forces are the laboratory chiller that works as the heat sink, and the steam that provides the required heat duty at the desorber. The laboratory chiller and the steam are adjusted accordingly for each data point. The laboratory chiller has a cooling capacity of 50 tons (175.8 kW or 600,000 Btu/h) and can provide coolant at temperatures as low as -9.5^{o}C. Water-glycol solution (approximately 50% by volume) is the coolant, and serves as the heat sink for the rectifier, condenser, and absorber. The laboratory steam lines can supply steam at up to 1379 kPa (200 psi). Two pressure regulators in the range 0 to 689 kPa (100 psi) and 0 to 2068 kPa (300 psi) are used to control the steam pressure. The steam line is directly connected to the desorber and determines desorber outlet temperature and the dilute solution concentration.

3.8 Test Conditions

Nominally, three solution flow rates, 0.019, 0.026, and 0.034 kg/s (2.5, 3.5, and 4.5 lb_m/min) designated as low, medium and high flow rate are tested at each of the nominal absorber pressures of 150, 345 and 500 kPa (21.8, 50.0 and 72.5 psi) representing a wide range of heat source/sink combinations. Nominal concentrations at the desorber outlet of 5, 15, 25, and 40% are tested for the above combinations of absorber pressures and concentrated solution flow rates. Tests were conducted at conditions as close to the nominal values as possible with the test facility described in previous sections.

Table 3.5 shows the matrix of data points obtained in this study. Table 3.6 outlines the primary challenges in obtaining nominal conditions, along with techniques used to maintain conditions close to nominal values. The cells without shading represent test conditions obtained without the heater in the absorber coolant loop and also without the subcooler upstream of the dilute solution inlet to the absorber. The cells with shading represent tests conditions obtained with the help of either the absorber coolant heater or the subcooler. The overall test matrix can be subdivided into twelve blocks based on absorber inlet pressures and dilute solution concentrations at the desorber. Tests for four of these blocks (no shading) are conducted without the absorber coolant heater and the subcooler. The absorber coolant heater is used for test conditions in three of these blocks, while the subcooler is used for test conditions in seven of these blocks. Note that the darker cells represent conditions that were progressively difficult to obtain for the reasons shown.

Table 3.5 Test Conditions for the Present Study

		150kPa			345 kPa			500 kPa		
		Flow Rate (kg/s)			Flow Rate (kg/s)			Flow Rate (kg/s)		
		0.0189	0.0265	0.0340	0.0189	0.0265	0.0340	0.0189	0.0265	0.0340
5%	Flow Rate (kg/s)	0.0186	0.0265	0.0342	0.0189	0.0263	0.0301	0.0223	0.0262	0.0337
	Concentration (%)	9.8	9.3	10.9	9.1	10.1	10.3	9.88	10.4	11.5
	Pressure (kPa)	174.7	177.7	179.5	341.6	358.3	358.5	469.9	480.8	496.6
15%	Flow Rate (kg/s)	0.0193	0.0264	0.0341	0.0189	0.0264	0.0339	0.0191	0.0265	0.0343
	Concentration (%)	13.5	15.2	15.6	15.5	14.5	15.4	14.78	14.65	15.64
	Pressure (kPa)	172.9	167.5	175.9	354.2	340.7	336.0	476.1	513.1	480.8
25%	Flow Rate (kg/s)	0.019	0.0263	0.0338	0.0188	0.0265	0.0337	0.0186	0.0264	0.0341
	Concentration (%)	24.0	24.1	25.9	23.9	23.9	25.2	26.8	24.9	25.6
	Pressure (kPa)	183.6	175.8	180.5	349.3	351.8	350.9	512.4	511.9	515.7
40%	Flow Rate (kg/s)	0.0195	0.0263	0.0329	0.0186	0.0266	0.0343	0.019	0.0264	0.0341
	Concentration (%)	38.34	40.16	39.39	36.2	39.8	40.8	34.2	37.4	38.7
	Pressure (kPa)	247.3	260.1	277.4	358.9	352	343.7	509	501.4	510.4

Table 3.6 Primary Challenges and Techniques Used

<table>
<tr><th colspan="2" rowspan="3"></th><th colspan="3">150kPa</th><th colspan="3">345 kPa</th><th colspan="3">500 kPa</th></tr>
<tr><th colspan="3">Flow Rate (kg/s)</th><th colspan="3">Flow Rate (kg/s)</th><th colspan="3">Flow Rate (kg/s)</th></tr>
<tr><th>0.0189</th><th>0.0265</th><th>0.0340</th><th>0.0189</th><th>0.0265</th><th>0.0340</th><th>0.0189</th><th>0.0265</th><th>0.0340</th></tr>
<tr><td rowspan="3">5%</td><td>Flow Rate (kg/s)</td><td>0.0186</td><td>0.0265</td><td>0.0342</td><td colspan="3" rowspan="3">Very small coolant flow rate, large coolant ΔT. Electric heater is used at absorber coolant loop</td><td colspan="3" rowspan="3">Low shut down pressure, difficult to maintain high pressure while running. Very small coolant flow rate, large coolant ΔT. Electric heater is used at absorber coolant loop</td></tr>
<tr><td>Concentration (%)</td><td>9.8</td><td>9.3</td><td>10.9</td></tr>
<tr><td>Pressure (kPa)</td><td>174.7</td><td>177.7</td><td>179.5</td></tr>
<tr><td rowspan="3">15%</td><td>Flow Rate (kg/s)</td><td colspan="3" rowspan="3">Sub − cooler is used to obtain low absorber pressure.</td><td>0.0189</td><td colspan="2" rowspan="3">Sub − cooler is used to obtain low absorber pressure.</td><td colspan="3" rowspan="3">Low shut down pressure, difficult to maintain high pressure while running. Very small coolant flow rate, large coolant ΔT. Electric heater is used at absorber coolant loop</td></tr>
<tr><td>Concentration (%)</td><td>15.5</td></tr>
<tr><td>Pressure (kPa)</td><td>354.2</td></tr>
<tr><td rowspan="3">25%</td><td>Flow Rate (kg/s)</td><td colspan="3" rowspan="3">Sub − cooler is used to obtain low absorber pressure.</td><td>0.0188</td><td>0.0265</td><td>0.0337</td><td>0.0186</td><td>0.0264</td><td>0.0341</td></tr>
<tr><td>Concentration (%)</td><td>23.9</td><td>23.9</td><td>25.2</td><td>26.8</td><td>24.9</td><td>25.6</td></tr>
<tr><td>Pressure (kPa)</td><td>349.3</td><td>351.8</td><td>350.9</td><td>512.4</td><td>511.9</td><td>515.7</td></tr>
<tr><td rowspan="3">40%</td><td>Flow Rate (kg/s)</td><td colspan="3" rowspan="3">High shut down pressure, difficult to get and maintain low pressure. Large coolant flow rate, very small coolant ΔT. Sub − cooler is used to obtain low absorber pressure.</td><td colspan="3" rowspan="3">Sub − cooler is used to obtain low absorber pressure.</td><td>0.019</td><td>0.0264</td><td>0.0341</td></tr>
<tr><td>Concentration (%)</td><td>34.2</td><td>37.4</td><td>38.7</td></tr>
<tr><td>Pressure (kPa)</td><td>509</td><td>501.4</td><td>510.4</td></tr>
</table>

Tests conducted without the use of the heater or the subcooler were typically at absorber pressures only slightly higher than the ammonia-water solution saturation pressures at the charged concentrations in the loop and room temperature. For example, to obtain the 5% and 15% dilute solution concentration conditions at the desorber outlet, the loop is charged with ammonia-water solution yielding approximately a maximum of 25% ammonia mass fraction that yields a saturation pressure of 57.2 kPa (8.3 psi) at 25^{o}C room temperature. Likewise, to obtain the 25% dilute solution concentration, the loop is charged with about 35% ammonia mass fraction, which yields a solution saturation pressure of 122.1 kPa (17.7 psi) at 25^{o}C room temperature. To obtain 40% dilute solution concentration, the loop is charged with about 50% ammonia mass fraction, which yields a solution saturation pressure of 303 kPa (44 psi) at 25^{o}C room temperature. These are the saturation pressures when the system is in the shut-down state. When the system is operating, the absorber temperature increases because of the high temperature of the solution coming from the desorber, and due to the heat of absorption in the absorber. Therefore, when system is running, the absorber pressures are slightly higher than the system shut down state pressures.

Tests could be conducted with relative ease for the conditions where the nominal absorber pressure is relatively close to the system shut down state pressure, e.g., 150 kPa (21.8 psi) cases at 5% dilute solution concentration, which were obtained without the heater or subcooler. Similarly, the 345 and 500 kPa (50.0 and 72.5 psi) cases at 25%, and the 500 kPa (72.5 psi) cases at 40% could be obtained without the heater or the subcooler. If the nominal absorber pressures are either too low or too high compared to the system shut down state pressure for the respective charged concentrations, it was necessary to

modify the test facility to overcome the large pressure difference, as the absorber coolant also poses limitations. When the nominal absorber pressures are much higher than the system shut down state pressure at charged concentrations, it is necessary to use the heater in the absorber coolant loop for increasing the solution temperature, which in turn increases the absorber pressure to the required value. It should be noted that if the heater is not used, the absorber pressure can be increased by using an extremely small absorber coolant flow rate, which would raise the heat rejection temperature and therefore the absorber pressure. However, the resulting temperature rise in the coolant would be unrealistically high, and would confound the absorber solution heat transfer coefficient measurement. By raising the coolant inlet temperature through the use of the heater, a higher coolant flow rate can be maintained (leading to lower uncertainties in the solution-side heat transfer coefficient) and also the coolant temperature difference can be maintained within reasonable limits. When the nominal absorber pressure is much less than the system shut down state pressure at the charged concentration, it is necessary to use the subcooler to decrease the temperature of the solution flowing to the absorber to values below what is possible with the solution heat exchanger. The subcooler therefore helps in decreasing the sensible cooling load on the absorber and the absorber pressure. Test conditions with the light gray shaded blocks in Table 3.6 are obtained with the use of either the absorber coolant heater or the subcooler.

At the absolute extremes of the test matrix, despite using the heater in the absorber coolant loop and the subcooler upstream of the absorber, it is very difficult to obtain test conditions where the absorber pressure is substantially different from the system shut down state pressure at the charged concentration. For example, for the 500

kPa (72.5 psi) test conditions, the absorber coolant heater is used for the 5% and 15% concentration cases. However, it is still quite difficult to increase the absorber pressure up to 500 kPa (72.5 psi) while maintaining reasonable coolant flow rates. Even if the 500 kPa (72.5 psi) pressure is obtained, the absorber coolant flow rates required are extremely small, and in some cases, result in very small coolant heat transfer coefficients that in turn result in unreasonable and inaccurate solution-side heat transfer coefficients. Similarly, even if the subcooler is used at its fullest capacity, at the 40% concentration cases, the lowest absorber pressure achievable while still retaining acceptable uncertainties in heat transfer coefficient determination was 241 kPa (35 psi) – lower pressures could in fact be obtained; however, this would be at the expense of heat transfer coefficient accuracies.

CHAPTER 4. DATA ANALYSIS

As explained in the previous chapter, pressure, temperature and flow rate values at various points of interest were recorded using the Data Acquisition System. For each data point, 100 readings are recorded over a duration of 5 minutes, and the average value is used to represent the conditions for that data point. This chapter describes the analysis procedures for the data obtained from the present study. Ammonia/water properties and mass, species and energy balance equations for the major components (absorber, desorber, evaporator, condenser and rectifier), and the corresponding uncertainties are explained. The assumptions required to obtain mass transfer coefficients are also described. The thermodynamic properties of ammonia-water solution in the liquid and vapor phases were obtained from *Engineering Equation Solver* (EES) V7.697-3D software (Klein, 2006). A test conditions at the representative data is shown in Appendix A, and a sample calculation for the case with a pressure of 345 kPa, concentration of 25%, and concentrated solution flow rate of 0.02646 kg/s is shown in Appendix B.

4.1 Ammonia/Water Mixture Properties

4.1.1 Ammonia/Water Properties

The equilibrium and thermodynamic solution properties of ammonia/water mixture are calculated from the internal library in EES by Klein (2006), which uses correlations developed by Ibrahim and Klein (1993). The correlations used for the

solution mixture properties have less than 5% average deviations (Ibrahim and Klein, 1993) from the measured data, and these correlations are valid for pressures between 0.2 and 110 bar, and temperatures between 230 and 600 K. Although the properties of ammonia/water in liquid and vapor phases can be obtained from EES, vapor phase transport properties are not readily available. Therefore, these mixture transport properties are estimated as described below.

Transport properties of ammonia-water vapor mixture are calculated using the Chapman-Enskog kinetic theory (Mills, 1995) for pure substances and mixture rules of Wilke (1950). The viscosities of ammonia and water are obtained using a Lennard-Jones potential model, which represents the potential energy of interaction between a pair of molecules during collision. Although the Lennard-Jones potential model is valid only for non-polar molecules, in the absence of other reliable approaches, it is deemed to be adequate for ammonia and water molecules, which have appreciable dipole moments.

$$\mu_v = 2.67 \times 10^{-6} \cdot \frac{\sqrt{M_v \cdot T_{v,bulk}}}{\sigma_v^{\,2} \cdot \Omega_{\mu,v}} \tag{4.1}$$

where, σ_v is the collision diameter at zero potential energy in angstroms,

$T_{v,bulk}$ is the bulk temperature in K of each component in the vapor phase,

M_v is molecular mass of each component,

$\Omega_{\mu,v}$ is the collision integral as a function of temperature and maximum energy attraction,

ε_v is the maximum energy of attraction between a pair of molecules tabulated for chemical species.

To calculate the thermal conductivities of ammonia and water, the relationship between thermal conductivity and the viscosity for monatomic gases is used and the modified Eucken correction is applied to account for the rotational and vibrational modes caused by nonlinearity of polyatomic ammonia and water vapor.

$$k_{v,translational} = \frac{5}{2} C_{v,v} \cdot \mu_v \tag{4.2}$$

$$k_v = k_{v,translational} + 1.32 \cdot \left(C_{p,v} - \frac{5}{2} \frac{R}{M_v} \right) \cdot \mu_v \tag{4.3}$$

where, $C_{v,v} = \frac{3}{2} \frac{R}{M_v}$, $C_{p,v} = \left(5 + N_r\right) \cdot \left(\frac{1}{2} \frac{R}{M_v} \right)$, and N_r is the rotational degree of freedom of each molecule. Both ammonia and water molecules have three rotational degrees of freedom.

Once the viscosities and thermal conductivities of pure ammonia and water are obtained, ammonia-water mixture viscosity and thermal conductivity are estimated using mixture rules (Wilke, 1950).

$$\mu_{12,v} = \sum_{i=1}^{2} \frac{x_{i,v} \cdot \mu_{i,v}}{\sum_{j=1}^{n} x_{j,v} \cdot \Phi_{ij,v}} \tag{4.4}$$

$$k_{12,v} = \sum_{i=1}^{2} \frac{x_{i,v} \cdot k_{i,v}}{\sum_{j=1}^{2} x_{j,v} \cdot \Phi_{ij,v}} \tag{4.5}$$

$$\Phi_{12,v} = \frac{\left[1 + \left(\mu_{1,v} / \mu_{2,v} \right)^{1/2} \cdot \left(M_{2,v} / M_{1,v} \right)^{1/4} \right]^2}{\sqrt{8} \cdot \left[1 + \left(M_{1,v} / M_{2,v} \right) \right]^{1/2}} \tag{4.6}$$

The binary vapor-phase diffusion coefficient is obtained from the following formula.

$$D_{12,v} = 1.86\times10^{-7} \cdot \frac{\sqrt{T_{v,bulk}{}^{3} \cdot \left(\frac{1}{M_{1,v}} + \frac{1}{M_{2,v}} \right)}}{\sigma_{12,v}{}^{2} \cdot \Omega_{D,v} \cdot P_{v,bulk}} \tag{4.7}$$

where, $P_{v,bulk}$ is the bulk vapor pressure in atmospheres,

$\Omega_{D,v}$ is the collision integral for diffusion and is different from $\Omega_{\mu,v}$

$$\sigma_{12,v} = \tfrac{1}{2} \cdot \left(\sigma_{w,v} + \sigma_{a,v} \right)$$

$$\varepsilon_{12,v} = \sqrt{\varepsilon_{w,v} \cdot \varepsilon_{a,v}}$$

In all these equations, 1 and 2 refer to ammonia and water vapor, respectively. The specific heat of the ammonia-water mixture is obtained from the enthalpy change for a temperature change of 1°C at the temperature of the vapor of interest at the given pressure and concentration. The comparison between these properties obtained from the Chapman-Enskog kinetic theory (Mills, 1995) and values obtained from the literature is shown in Appendix D.

The liquid phase surface tension, σ_l, viscosity, μ_l, and conductivity, k_l are evaluated by fitting equations to existing ammonia-water property plots found in Herold *et al.* (1996), and the International Institute of Refrigeration (1994). The liquid phase binary diffusion coefficient, $D_{12,l}$ is obtained from Frank *et al.* (1996).

4.2 Calculation Methodology

The working fluid, which is a binary mixture of ammonia and water, requires three independent parameters to define its state at any location in the system. As stated above, 11 absolute pressures, 1 differential pressure, and 56 temperatures are measured at

various locations and used as two of the required independent parameters for directly establishing the state. For these state points, the additional required parameter is typically either concentration or quality. In this study, the quality at any given state was chosen as a third independent parameter (wherever appropriate), and other properties such as enthalpy and specific volume are typically obtained using these three known independent parameters. (In some instances, the enthalpy obtained from energy balances is used as an input to compute quality or concentration, depending on the specific state point under consideration.). Also, qualities of 0 or 1 as appropriate are used to obtain concentrations at three locations in the test loop from measured temperatures and pressures: desorber outlet, rectifier vapor outlet, and rectifier reflux outlet. The qualities were used as the third independent parameter instead of direct concentration measurements because the uncertainties in concentration measurements were expected to be considerable when samples of the vapor and solution states were obtained at different locations around the test loop during system operation. These uncertainties could significantly affect the enthalpies that are important for the heat transfer analysis. At such state points, measured temperatures and pressures, and the expected quality (e.g., saturated liquid or saturated vapor) are used to obtain the solution concentration. Three different flow rates are also measured: dilute solution, concentrated solution, and refrigerant flow rate. The steps to analyze the processes around the test loop are described below.

The ammonia-water solution exits as a two-phase mixture from the desorber, with the liquid and vapor phases in equilibrium with each other. Therefore, the liquid and vapor phase concentrations are computed (Figure 4.1) based on the measured temperature

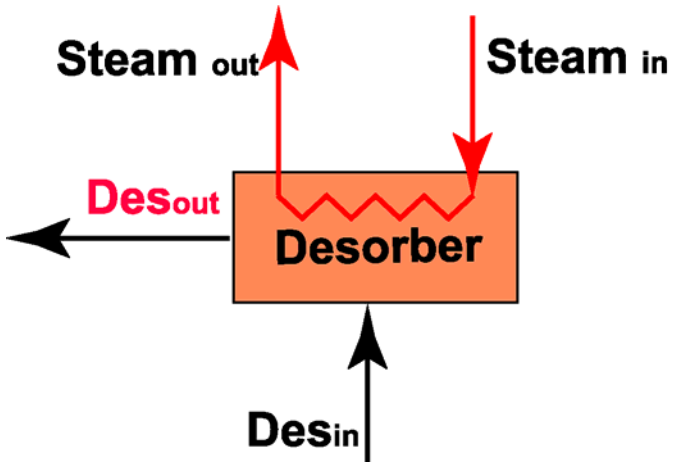

Figure 4.1 Schematic of the Desorber

and pressure at the desorber outlet as follows, where q represents the quality of the particular stream:

$$x_{Dilute,Des} = f\left(T_{Des,out},\ P_{Des,out},\ q=0\right) \tag{4.8}$$

$$x_{Dilute,Des} = f\left(122.4°C,\ 1110\ \text{kPa},\ 0\right) = 0.2386 \tag{4.9}$$

$$x_{V,Des} = f\left(122.4°C,\ 1110\ \text{kPa},\ 1\right) = 0.8427 \tag{4.10}$$

$$x_{V,Des} = f\left(T_{Des,out},\ P_{Des,out},\ q=1\right) \tag{4.11}$$

The ammonia concentration flowing through the refrigerant circuit of the loop is obtained using an assumption of a saturated vapor condition at the measured rectifier outlet temperature and pressure (Figure 4.2). (The condenser inlet pressure is used as the rectifier outlet pressure, since there is no local pressure measurement at the rectifier vapor outlet.) The resulting refrigerant concentration applies for the condenser, evaporator, pre-cooler and absorber inlet. Thus,

$$x_V = f\left(T_{\mathrm{Re}c,V,out},\ P_{Con,in},\ q=1\right) \tag{4.12}$$

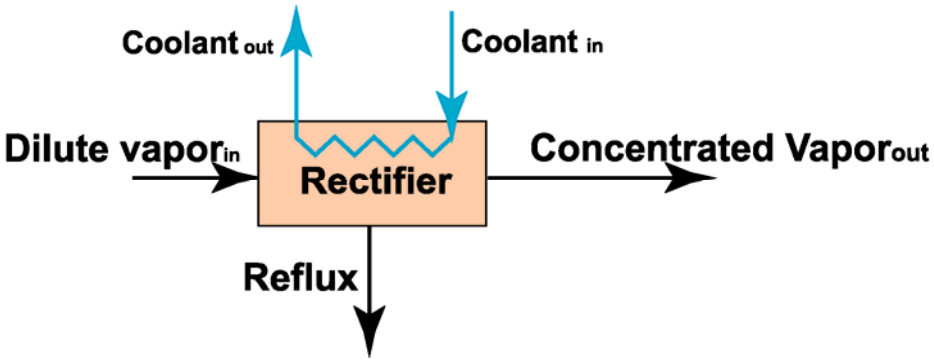

Figure 4.2 Schematic of the Rectifier

$$x_V = f\left(80.99°C,\ 1127\ \text{kPa},\ 1\right) = 0.9781 \tag{4.13}$$

The reflux concentration is estimated by assuming a saturated liquid state leaving the rectifier at the measured temperature and pressure at the reflux outlet location, as follows:

$$x_{\text{Reflux}} = f\left(T_{\text{Reflux}}, P_{\text{Reflux}}, q = 0\right) \tag{4.14}$$

$$x_{\text{Reflux}} = f\left(51.4°C,\ 1121\,\text{kPa},\ 0\right) = 0.6182 \tag{4.15}$$

The vapor concentration at the rectifier inlet is the same as the concentration of the vapor leaving the separator (and therefore, also the desorber, because the separator simply accomplishes physical separation of the two phases exiting the desorber). The reflux flow rate and the rectifier inlet flow rate are calculated using mass and species balances at the rectifier using the refrigerant flow rate, and the concentrations at the rectifier inlet, rectifier vapor outlet and the reflux outlet as follows:

$$x_{V,Des} = x_{Sep,V,out} = x_{\text{Rec},in} = 0.8427 \tag{4.16}$$

$$\dot{m}_{\text{Reflux}} = \dot{m}_{\text{Rec,in}} - \dot{m}_{\text{Ref},Measured} \tag{4.17}$$

$$\dot{m}_{\text{Reflux}} = \dot{m}_{\text{Rec},in} - 0.002826\ \text{kg/s} \tag{4.18}$$

$$\dot{m}_{\text{Rec},in} \cdot x_{V,Des} = \dot{m}_{\text{Reflux}} \cdot x_{\text{Reflux}} + \dot{m}_{\text{Ref},measured} \cdot x_V \tag{4.19}$$

$$\dot{m}_{\text{Rec},in} \cdot 0.8427 = \dot{m}_{\text{Reflux}} \cdot 0.6182 + 0.002826\,\text{kg/s} \cdot 0.9781 \tag{4.20}$$

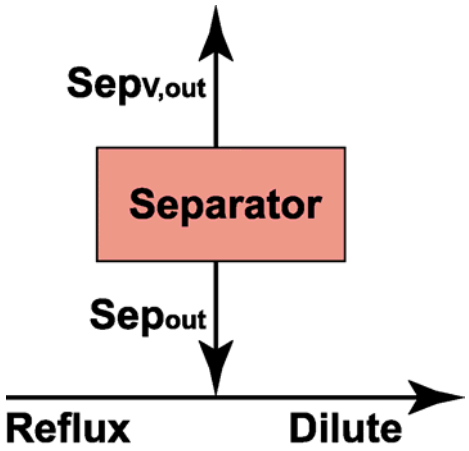

Figure 4.3 Separator Liquid–Phase Balance

$$\dot{m}_{\mathrm{Rec},in} = 0.004532 \ \mathrm{kg/s} \tag{4.21}$$

$$\dot{m}_{\mathrm{Reflux}} = 0.001706 \ \mathrm{kg/s} \tag{4.22}$$

Mass and species balances at the separator outlet (Figure 4.3) are used to find the dilute solution concentration entering the absorber, and a species balance at the absorber is used to find the concentrated solution concentration, as follows:

$$\dot{m}_{Sep,out} = \dot{m}_{Dilute} - \dot{m}_{\mathrm{Reflux}} \tag{4.23}$$

$$\begin{aligned} \dot{m}_{Sep,out} &= 0.02276\,\mathrm{kg/s} - 0.001706\,\mathrm{kg/s} \\ &= 0.02105\,\mathrm{kg/s} \end{aligned} \tag{4.24}$$

$$x_{Dilute} \cdot \dot{m}_{Dilute} = \dot{m}_{\mathrm{Reflux}} \cdot x_{\mathrm{Reflux}} + \dot{m}_{Sep,out} \cdot x_{Dilute,Des} \tag{4.25}$$

$$x_{Dilute} \cdot 0.02276\,\mathrm{kg/s} = 0.001706\,\mathrm{kg/s} \cdot 0.6182 + 0.02105 \cdot 0.2386 = 0.2671 \tag{4.26}$$

$$x_{Concentrated} \cdot \dot{m}_{Concentrated} = \dot{m}_{\mathrm{Ref},Measured} \cdot x_V + \dot{m}_{Dilute} \cdot x_{Dilute} \tag{4.27}$$

$$\begin{aligned} &x_{Concentrated} \times 0.02651\,\mathrm{kg/s} \\ &\quad = 0.002826\,\mathrm{kg/s} \times 0.9781 + 0.02276\ \mathrm{kg/s} \times 0.2671 = 0.3336 \end{aligned} \tag{4.28}$$

It should be noted that the dilute solution concentration entering the absorber is different from the concentration at the desorber outlet, because the reflux mixes with the solution leaving the separator before it enters the absorber.

4.2.1 Concentration Range

Using the above methodology, concentrations of the various streams of interest are computed. Figures 4.4-4.6 show concentration ranges (change in concentration from the desorber outlet to the absorber solution inlet and then to the absorber solution outlet) for each data point obtained in the study. Thus, each data point is represented by three symbols, representing the solution concentration at the desorber outlet, the absorber inlet and the absorber outlet, with the symbols being plotted as a function of the concentrated solution flow rate. It should be noted that the absorber inlet concentration is different from the desorber outlet concentration because the reflux is mixed with the dilute solution stream before it flows to the absorber. The difference in these two

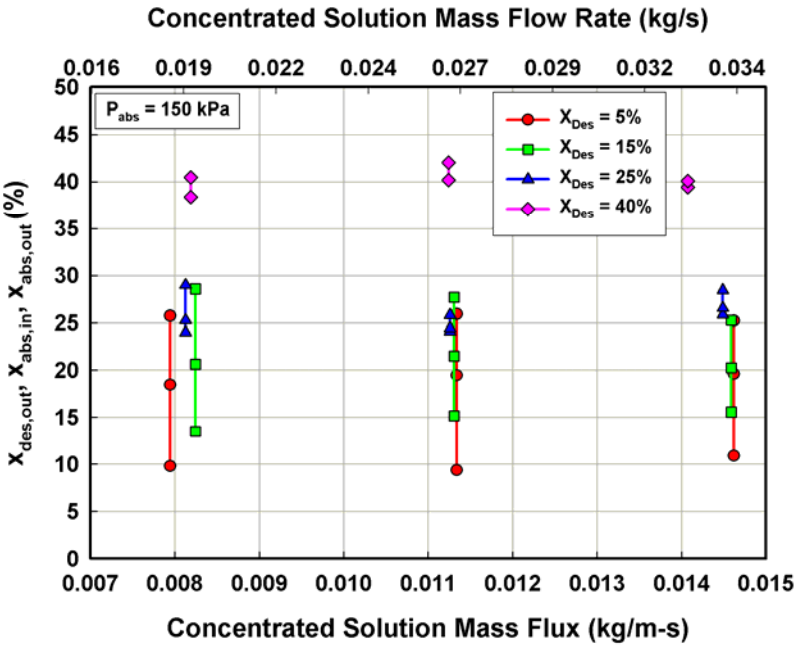

Figure 4.4 Concentration Ranges at Nominal 150 kPa (21.8 psi)

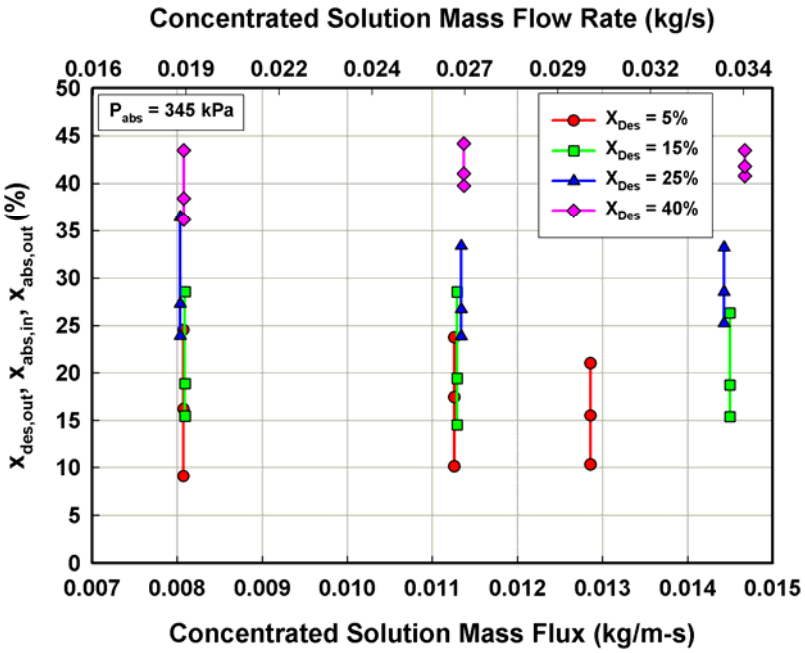

Figure 4.5 Concentration Ranges at Nominal 345 kPa (50.0 psi)

concentrations, therefore, depends on the reflux concentration and flow rate, which in turn change as the test conditions are varied. For the nominal 150 kPa (21.8 psi) case (Figure 4.4), for a given dilute solution concentration, the concentration range decreases slightly with increasing solution flow rate. As the dilute solution concentration increases, the concentration range decreases at any given flow rate. Concentration ranges are small for the 40% and 25% concentration cases, while the ranges are large for the 5% and 15% concentration cases. The smaller concentration ranges at the higher dilute solution concentration cases are primarily due to the lower refrigerant flow rates in these cases.

Figure 4.5 shows the variation of the concentration ranges for various dilute solution concentrations at the desorber outlet at a nominal absorber pressure of 345 kPa (50.0 psi). The concentration range shows similar trends as those for the 150 kPa (21.8 psi) cases. However, concentration ranges are larger at this pressure than for the 150 kPa (21.8 psi) nominal cases for 40% and 25% concentration, while the concentration ranges

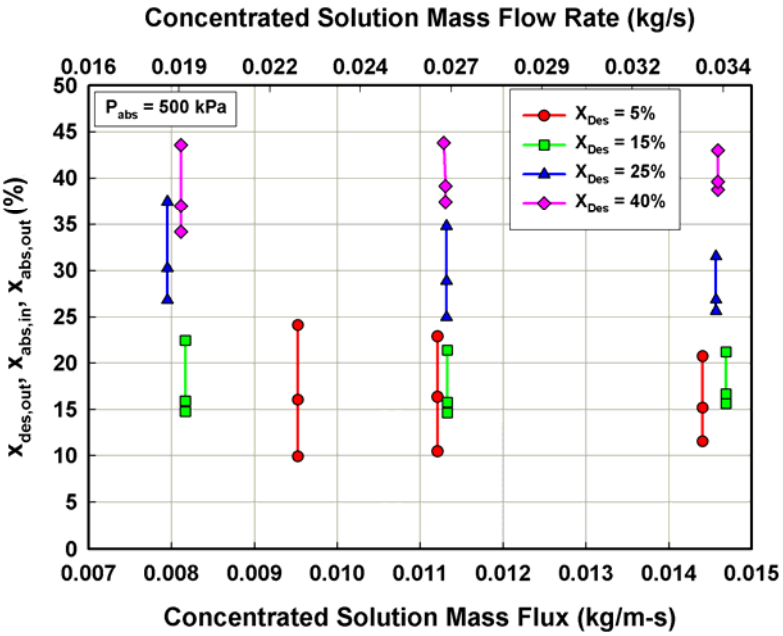

Figure 4.6 Concentration Ranges for Nominal 500 kPa (72.5 psi)

for the 5% and 15% concentration cases are similar to those of the 150 kPa (21.8 psi) nominal cases.

Figure 4.6 shows the variation of concentration ranges for various dilute solution concentrations at the desorber outlet at a nominal absorber pressure of 500 kPa (72.5 psi). As with the 150 kPa (21.8 psi) and 345 kPa (50 psi) cases, the concentration ranges decrease slightly as the solution flow rate increases. The concentration ranges for the various flow rates for 40% concentration are much larger than those at 150 and 345 kPa (21.8 and 50.0 psi), while for 5% and 15%, the concentration ranges are smaller than those at 150 and 345 kPa (21.8 and 50.0 psi). The various concentration ranges observed at these conditions can also be taken as an indicator of difficulties in establishing the particular test condition. In general, the more challenging test conditions result in smaller concentration ranges.

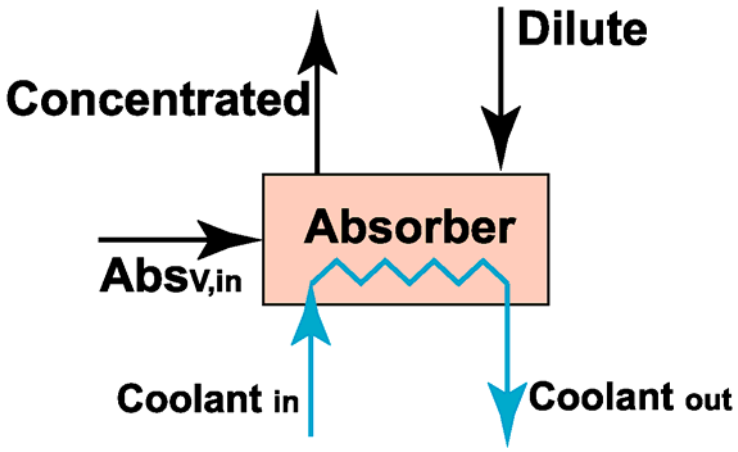

Figure 4.7 Schematic of the Absorber

4.3 Heat Transfer Calculations

With the concentrations calculated as described above and measured temperatures and pressures at the various locations, the other properties at each location are obtained. The following sections describe the calculation of the heat duties and energy balances at each component, and the calculation of the measured absorber heat transfer coefficient.

4.3.1 Absorber Calculations

There are three different working fluid streams entering and exiting the absorber: entering dilute solution, exiting concentrated solution and the entering refrigerant vapor (Figure 4.7). Pressures and temperatures are measured at these three locations. All three concentrations are calculated as explained in the previous section. Therefore, these states are fully established and the enthalpies at these three locations can be obtained as follows:

$$h_{Abs,in} = f\left(T_{Abs,in}, P_{Abs,in}, x_{Dilute}\right) \tag{4.29}$$

$$h_{Abs,in} = f\left(70.42°C, 351.8\ \text{kPa}, 0.2671\right) = 128.9\ \text{kJ/kg} \tag{4.30}$$

$$h_{Abs,out} = f\left(T_{Abs,out}, P_{Abs,out}, x_{Concentrated}\right) \tag{4.31}$$

$$h_{Abs,out} = f\left(30.99°C, 350.6\ \text{kPa}, 0.3336\right) = -69.93\ \text{kJ/kg} \tag{4.32}$$

$$h_{Abs,V,in} = f\left(T_{Abs,V,in}, P_{Abs,V,in}, x_{V}\right) \tag{4.33}$$

$$h_{Abs,V,in} = f\left(-0.25°C, 362.8\ \text{kPa}, 0.9781\right) = 1086\ \text{kJ/kg} \tag{4.34}$$

With the three enthalpies known, the solution side absorber heat duty is calculated as follows:

$$Q_{Abs} = \dot{m}_{Dilute} \cdot h_{Abs,in} + \dot{m}_{\text{Re}f,Measured} \cdot h_{Abs,V,in} - \dot{m}_{Concentrated} \cdot h_{Abs,out} \tag{4.35}$$

$$\begin{aligned} Q_{Abs} &= 0.02276\,\text{kg/s} \times 128.9\,\text{kJ/kg} + 0.002826\,kg/s \times 1086\,\text{kJ/kg} \\ &\quad -(-0.02651\,\text{kg/s} \times 69.93)\,\text{kJ/kg} \\ &= 7.854\ \text{kW} \end{aligned} \tag{4.36}$$

The coolant-side heat duty is calculated using the absorber coolant flow rate and temperatures at the inlet and outlet:

$$Cp_{\text{Abs,C}} = f\left(T_{Abs,C,Ave}\right) \tag{4.37}$$

$$Cp_{\text{Abs,C}} = f\left(15.61°C\right) = 4.183\ \text{kJ/kg} \cdot °C \tag{4.38}$$

$$Q_{\text{Abs,C}} = \dot{m}_{Abs,c} \cdot Cp_{Abs,C} \cdot (T_{Abs,C,out} - T_{Abs,C,in}) \tag{4.39}$$

$$Q_{\text{Abs,C}} = 0.3028\,\text{kg/s} \times 4.183\,\text{kJ/kg} \cdot °C \times \left(18.75°C - 12.47°C\right) = 7.954\ \text{kW} \tag{4.40}$$

The coolant specific heat is calculated at the average absorber coolant temperature. After the absorber heat duty is obtained, the overall heat transfer coefficient is obtained using the log mean temperature difference.

4.3.1.1 Selection of LMTD

As mentioned above, the solution and the coolant temperatures at the inlet and outlet of the absorber are known from measurements. To estimate an overall heat transfer coefficient in the absorber, a representative temperature difference is required between the solution and coolant streams. Initially, a log mean temperature difference (LMTD) was defined, along the lines of much of the literature, based on the solution saturation temperatures (corresponding to measured solution pressure, concentration and saturated liquid quality) and the measured coolant temperatures. The LMTD based on saturation temperatures represents the idealized driving temperature difference for heat transfer in the absorption process. This LMTD definition is preferable when the solution temperature in the absorber is close to its saturation state. However, it is observed in the current study that the bulk solution is typically sub-cooled throughout the absorber. Because the LMTD based on saturation temperatures is considerably higher than an LMTD based on actual temperatures, it may not correctly represent the heat transfer performance of the absorber. Thus, in the present study, the LMTD is defined based on the measured solution and coolant temperatures to calculate the overall heat transfer coefficient in the absorber.

$$LMTD_{\mathrm{Abs}} = \frac{\left(T_{Abs,in} - T_{Abs,C,out}\right) - \left(T_{Abs,out} - T_{Abs,C,in}\right)}{\ln\left(\frac{T_{Abs,in} - T_{Abs,C,out}}{T_{Abs,out} - T_{Abs,C,in}}\right)} \tag{4.41}$$

For this representative data point,

$$LMTD_{\mathrm{Abs}} = \frac{\left(70.42°C - 18.75°C\right) - \left(30.99°C - 12.47°C\right)}{\ln\left(\frac{70.42°C - 18.75°C}{30.99°C - 12.47°C}\right)} = 30.87°C\,(\text{or K}) \tag{4.42}$$

4.3.1.2 Overall Heat Transfer Coefficient

The average of the solution- and coolant-side absorber heat duties is used as the representative absorber heat duty for the calculation of the overall heat transfer coefficient. The log mean temperature is calculated as discussed above.

$$U_{\text{Abs}} = \frac{Heat\ Duty_{Abs,ave}}{Abs_{Area} \cdot LMTD_{Abs}} \tag{4.43}$$

$$U_{\text{Abs}} = \frac{\left(7.854\ \text{kW} + 7.954\ \text{kW}\right)/2}{0.2098\ \text{m}^2 \times 30.87°C} = 1221\ \text{W/m}^2 \cdot °C \tag{4.44}$$

4.3.1.3 Coolant Side Heat Transfer Coefficient

On the coolant side, the coolant flow rate, the inlet and outlet temperatures, and the pressure drop are measured. Also, coolant side geometrical details such as the tube length and the tube flow area are known. For the calculation of the coolant-side heat transfer coefficient, the coolant velocity and Reynolds number are first calculated:

$$V_{Abs,C} = \dot{V} / \left(Tube_{Cross,Area} \cdot N_{Column}\right) \tag{4.45}$$

$$V_{Abs,C} = \left(3.04 \times 10^{-4}\ \text{m}^3/\text{s}\right) / \left(5.156 \times 10^{-5}\ \text{m}^2 \times 4\right) = 1.472\ \text{m/s} \tag{4.46}$$

$$\text{Re}_{Abs,C} = \frac{\rho_{Abs,C} \cdot V_{Abs,C} \cdot Tube_{ID}}{\mu_{Abs,C}} \tag{4.47}$$

$$\text{Re}_{Abs,C} = \frac{997.1\ \text{kg/m}^3 \times 1.472\ \text{m/s} \times 8.103 \times 10^{-3}\ \text{m}}{8.9808 \times 10^{-4}\ \text{kg/m} \times \text{s}} = 13353 \tag{4.48}$$

Here, the absorber coolant density, viscosity, conductivity (0.595 W/m-K), and Prandtl number (6.265) are calculated at the average absorber coolant temperature (15.6°C). The tube-side friction factor and Nusselt number are calculated using Churchill's (1977a;

1977b) equations to yield f = 0.02867 and Nu = 104.3. The coolant-side heat transfer coefficient is obtained from the Nusselt number as follows:

$$\alpha_{Abs,C} = \frac{k_{Abs,C} \cdot Nu_{Abs,C}}{Tube_{ID}} \tag{4.49}$$

$$\alpha_{Abs,C} = \frac{0.595\ \mathrm{W/m\text{-}K} \times 104.3}{8.103 \times 10^{-3}\ m} = 7653\ \mathrm{W/m^2\text{-}K} \tag{4.50}$$

4.3.1.4 Solution Heat transfer Coefficient

A thermal resistance network consisting of the coolant-side, tube-wall, and solution-side resistance is used to calculate the solution-side heat transfer coefficient. The coolant-side heat transfer coefficient is calculated as discussed above. The tube-wall thermal resistance is calculated as follows:

$$R_{\mathrm{W}} = \frac{Tube_{OD}}{2 \cdot k_W} \ln\left(\frac{Tube_{OD}}{Tube_{ID}}\right) \tag{4.51}$$

$$R_{\mathrm{W}} = \frac{9.525 \times 10^{-3}\ \mathrm{m}}{2 \times 14.64\ \mathrm{W/m\text{-}K}} \ln\left(\frac{9.525 \times 10^{-3}\ \mathrm{m}}{8.103 \times 10^{-3}\ \mathrm{m}}\right) = 5.267 \times 10^{-5}\ \mathrm{m^2\text{-}K/W} \tag{4.52}$$

With the coolant-side heat transfer coefficient and tube-wall resistance known, the solution-side heat transfer coefficient is calculated as follows:

$$\frac{1}{\alpha_{Abs,Film}} = \frac{1}{U_{Abs}} - \left(R_W + \frac{Tube_{OD}}{\alpha_{Abs,C} \cdot Tube_{ID}}\right) \tag{4.53}$$

$$\frac{1}{\alpha_{Abs,Film}} = \frac{1}{1221\ \mathrm{W/m^2 \cdot °}C} - \left(5.267 \times 10^{-5}\ \mathrm{m^2 \cdot °}C/\mathrm{W} + \frac{9.525 \times 10^{-3}\ \mathrm{m}}{7653\ \mathrm{W/m^2 \cdot °}C \times 8.103 \times 10^{-3}\ \mathrm{m}}\right) \tag{4.54}$$

$$\alpha_{Abs,Film} = 1632\ \mathrm{W/m^2 \cdot °}C$$

4.3.2 Desorber Calculations

The desorber inlet state is specified by the concentrated solution concentration, and the measured temperature and pressure:

$$h_{\text{Des,in}} = f\left(T_{\text{Des,in}}, P_{\text{Des,in}}, x_{\text{Concentrated}}\right) \tag{4.55}$$

$$h_{\text{Des,in}} = f\left(87.41°C, 1191\ \text{kPa}, 0.3336\right) = 177.9\ \text{kJ/kg} \tag{4.56}$$

The desorber outlet enthalpy is assumed to be the same as the separator inlet enthalpy due to the small insulated line separating them (Figure 4.8), and it is further assumed that the separator is adiabatic. The various enthalpies at the separator are calculated as follows:

$$h_{\text{Sep,out}} = f\left(T_{\text{Sep,out}}, P_{\text{Sep,out}}, x_{\text{Dilute,Des}}\right) \tag{4.57}$$

$$h_{\text{Sep,out}} = f\left(119°C, 1115\ \text{kPa}, 0.2386\right) = 357.3\ \text{kJ/kg} \tag{4.58}$$

$$h_{Sep,V,out} = f\left(T_{Sep,V,out}, P_{Sep,V,out}, x_{Des,V}\right) \tag{4.59}$$

$$h_{Sep,V,out} = f\left(122.4°C, 1115\ \text{kPa}, 0.8427\right) = 1707\ \text{kJ/kg} \tag{4.60}$$

Since the separator vapor and solution outlet states were fully established, mass and

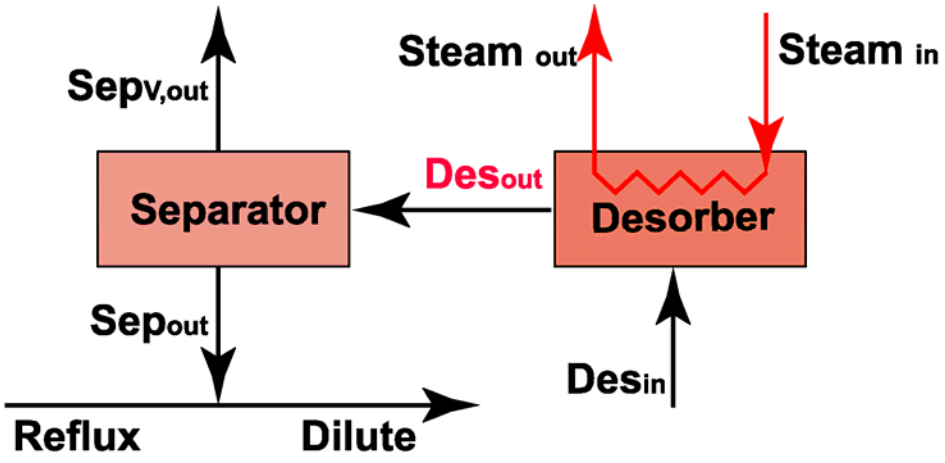

Figure 4.8 Desorber and Separator Balance

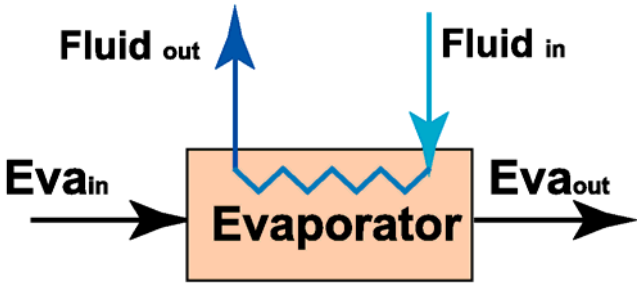

Figure 4.9 Evaporator Energy Balance

energy balances at the separator are used to calculate the separator inlet enthalpy, which is in turn used to compute the desorber heat duty:

$$h_{Sep,in} = h_{Des,out} \tag{4.61}$$

$$h_{Des,out}\,\dot{m}_{Concentrated} = \left(\dot{m}_{\mathrm{Ref},Measured} + \dot{m}_{\mathrm{Reflux}}\right)\cdot h_{Sep,V,out} + \left(\dot{m}_{Dilute} - \dot{m}_{\mathrm{Reflux}}\right)\cdot h_{Sep,out} \tag{4.62}$$

$$\begin{aligned} h_{Des,out}\times 0.02651\ \mathrm{kg/s} &= \left(0.002826\ \mathrm{kg/s} + 0.001706\ \mathrm{kg/s}\right)\times 1707\ \mathrm{kJ/kg} \\ &\quad + \left(0.02276\ \mathrm{kg/s} - 0.001706\ \mathrm{kg/s}\right)\times 357.3\ \mathrm{kJ/kg} \\ h_{Des,out} &= 575.6\ \mathrm{kJ/kg} \end{aligned} \tag{4.63}$$

$$Q_{\mathrm{Des}} = \dot{m}_{Concentrated}\cdot\left(h_{Des,out} - h_{Des,in}\right) \tag{4.64}$$

$$Q_{\mathrm{Des}} = 0.02651\ \mathrm{kg/s}\times\left(575.6\ \mathrm{kJ/kg} - 177.9\ \mathrm{kJ/kg}\right) = 10.54\,\mathrm{kW} \tag{4.65}$$

4.3.3 Evaporator Calculations

The measured refrigerant flow rate, temperature and pressure, and the previously obtained concentration specify both the inlet and outlet states (Figure 4.9). Enthalpies at the inlet and outlet are obtained from these measured and deduced quantities as follows:

$$h_{\mathrm{Eva,in}} = f\left(T_{Eva,in}, P_{Eva,in}, x\right) \tag{4.66}$$

$$h_{\mathrm{Eva,in}} = f\left(-3.781°C, 378.9\ \mathrm{kPa}, 0.9781\right) = -33.28\ \mathrm{kJ/kg} \tag{4.67}$$

$$h_{\text{Eva,out}} = f\left(T_{Eva,out}, P_{Eva,out}, x\right) \tag{4.68}$$

$$h_{\text{Eva,out}} = f\left(\text{-}1.906°C, 351\ \text{kPa}, 0.9781\right) = 1051\ \text{kJ/kg} \tag{4.69}$$

Based on these enthalpies, the evaporator duty is calculated as follows:

$$Q_{\text{Eva}} = \dot{m}_{\text{Ref},Measured} \cdot \left(h_{Eva,out} - h_{Eva,in}\right) \tag{4.70}$$

$$Q_{\text{Eva}} = 0.002826\ \text{kg/s} \times \left(1051\ \text{kJ/kg} - (-33.28)\ \text{kJ/kg}\right) = 3.065\ \text{kW} \tag{4.71}$$

The evaporator heating fluid heat duty is obtained from the flow rate and inlet and outlet temperatures of the water-glycol solution (50% by volume). The evaporator heating fluid specific heat is calculated based on the water-glycol properties at the average fluid temperature:

$$Cp_{\text{Eva,C}} = f\left(T_{Eva,C,Ave}\right) \tag{4.72}$$

$$Cp_{\text{Eva,C}} = f\left(15.07°C\right) = 3.299\ \text{kJ/kg} \cdot °C \tag{4.73}$$

$$Q_{\text{Eva,C}} = \dot{m}_{Eva,C} \cdot Cp_{Eva,C} \cdot \left(T_{Eva,C,in} - T_{Eva,C,out}\right) \tag{4.74}$$

$$Q_{\text{Eva,C}} = 0.2056\,\text{kg/s} \times 3.299\,\text{kJ/kg} \cdot °C \times \left(17.14°C - 13.01°C\right) = 2.801\,\text{kW} \tag{4.75}$$

4.3.4 Condenser Calculations

The refrigerant flow rate and measured temperatures and pressures, along with the previously obtained refrigerant concentration are used to obtain the condenser heat duty. The enthalpies at the inlet and outlet of the condenser are obtained readily as both the inlet and outlet states of the condenser are fully specified:

$$h_{\text{Con,in}} = f\left(T_{Con,in}, P_{Con,in}, x\right) \tag{4.76}$$

$$h_{\text{Con,in}} = f\left(57.51°C, 1127\ \text{kPa}, 0.9781\right) = 1321\ \text{kJ/kg} \tag{4.77}$$

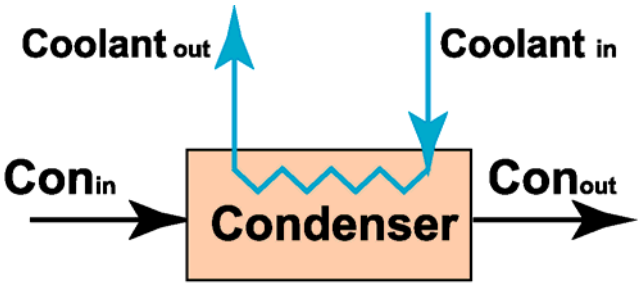

Figure 4.10 Condenser Energy Balance

$$h_{\text{Con,out}} = f\left(T_{Con,out}, P_{Con,out}, x\right) \tag{4.78}$$

$$h_{\text{Con,out}} = f\left(20.93°C, 1133\ \text{kPa}, 0.9781\right) = 82.3\ \text{kJ/kg} \tag{4.79}$$

Now the condenser duty is given by:

$$Q_{\text{Con}} = \dot{m}_{\text{Ref},Measured} \cdot \left(h_{Con,in} - h_{Con,out}\right) \tag{4.80}$$

$$Q_{\text{Con}} = 0.002826\ \text{kg/s} \times \left(1321\ \text{kJ/kg} - 82.3\ \text{kJ/kg}\right) = 3.501\ \text{kW} \tag{4.81}$$

The condenser coolant heat duty (Figure 4.10) is calculated in a manner similar to that used for the evaporator. The condenser coolant is also water-glycol solution (50% by volume), and its specific heat is calculated based at the average coolant temperature. Thus,

$$Cp_{\text{Con,C}} = f\left(T_{Con,C,Ave}\right) \tag{4.82}$$

$$Cp_{\text{Con,C}} = f\left(18.59°C\right) = 3.323\,\text{kJ/kg}\cdot°C \tag{4.83}$$

$$Q_{\text{Con,C}} = \dot{m}_{\text{Con},C} \cdot Cp_{\text{Con},C} \cdot \left(T_{\text{Con},C,out} - T_{\text{Con},C,in}\right) \tag{4.84}$$

$$Q_{\text{Con,C}} = 0.3313\,\text{kg/s} \times 3.323\,\text{kJ/kg}\cdot°C \times \left(20.38°C - 16.79°C\right) = 3.952\ \text{kW} \tag{4.85}$$

4.3.5 Rectifier Calculation

The mass flow rates of the entering and leaving vapor and the reflux, as well as enthalpies of these streams are necessary for the calculation of the rectifier heat duty. The refrigerant vapor outlet state is fully defined based on the measured temperature and pressure and the saturated vapor state. The mass flow rates of the reflux and the vapor entering the rectifier are calculated using mass and species balances as explained in a previous section. The enthalpies at the rectifier vapor inlet and outlet, and for the reflux are obtained as follows:

$$h_{\text{Rec,in}} = f\left(T_{\text{Rec},in}, P_{\text{Rec},in}, x_{\text{Rec},in}\right) \tag{4.86}$$

$$h_{\text{Rec,in}} = f\left(119.6°C, 1115\,\text{kPa}, 0.8427\right) = 1648\,\text{kJ/kg} \tag{4.87}$$

$$h_{\text{Rec},V,out} = f\left(T_{\text{Rec},V,out}, P_{\text{Rec},V,out}, x_{\text{Rec},V,out}\right) \tag{4.88}$$

$$h_{\text{Rec},V,out} = f\left(80.99°C, 1127\,\text{kPa}, 0.9781\right) = 1458\,\text{kJ/kg} \tag{4.89}$$

$$h_{\text{Reflux}} = f\left(T_{\text{Reflux}}, P_{\text{Reflux}}, x_{\text{Reflux}}\right) \tag{4.90}$$

$$h_{\text{Reflux}} = f\left(51.4°C, 1121\,\text{kPa}, 0.6182\right) = 12.13\,\text{kJ/kg} \tag{4.91}$$

Now, the rectifier heat duty is calculated as follows:

$$Q_{\text{Rec}} = \left(\dot{m}_{\text{Ref},Measured} + \dot{m}_{\text{Reflux}}\right) \cdot h_{\text{Rec},in} - \left(\dot{m}_{\text{Reflux}} \cdot h_{\text{Reflux}} + \dot{m}_{\text{Ref},Measured} \cdot h_{\text{Rec},V,out}\right) \tag{4.92}$$

$$\begin{aligned} Q_{\text{Rec}} = &\left(0.002826\,\text{kg/s} + 0.001706\,\text{kg/s}\right) \cdot 1648\,\text{kJ/kg} \\ &- \left(0.001706\,\text{kg/s} \cdot 12.13\,\text{kJ/kg} + 0.002826\,\text{kg/s} \cdot 1458\,\text{kJ/kg}\right) = 3.326\,\text{kW} \end{aligned} \tag{4.93}$$

The rectifier coolant heat duty is calculated using the rectifier coolant (50% water-glycol mixture) flow rate and inlet and outlet temperatures. The coolant specific heat is calculated at the average coolant temperature, yielding the coolant-side duty as follows:

$$Cp_{\text{Rec,C}} = f\left(T_{\text{Rec},C,Ave}\right) \tag{4.94}$$

$$Cp_{\text{Rec,C}} = f\left(25.67°C\right) = 3.494\,\text{kJ/kg}\cdot°\text{C} \tag{4.95}$$

$$Q_{\text{Rec,C}} = \dot{m}_{\text{Rec},C}\cdot Cp_{\text{Rec},C}\cdot\left(T_{\text{Rec},C,out} - T_{\text{Rec},C,in}\right) \tag{4.96}$$

$$Q_{\text{Rec,C}} = 0.0277\,\text{kg/s}\times 3.494\,\text{kJ/kg}\cdot°C\times\left(41.78°C - 9.57°C\right) = 3.125\,\text{kW} \tag{4.97}$$

4.4 Mass Transfer Calculations

In ammonia-water absorption, the vapor contains both refrigerant (ammonia) and absorbent (water). In addition, both the refrigerant and the absorbent are absorbed by the solution flowing over the tubes. This absorption process results in a different concentration of the mass absorbed at the vapor-liquid interface than of the bulk vapor, with no direct way to measure this concentration. In this section, the details of the calculations to estimate the overall mass transfer coefficient for the absorber are presented.

4.4.1 Absorber Inlet Vapor Condition Change

Refrigerant vapor is produced in the evaporator and flows through the pre-cooler before it enters the absorber. Upon entry into the absorber shell, it is assumed that due to the large chamber volume, the vapor occupies the chamber and forms a quiescent vapor medium in this chamber. The solution pool at the bottom of the absorber also presents a large surface area to the vapor. Although the inlet vapor conditions can be obtained from the measured temperature and pressure and the refrigerant concentration, it is assumed that vapor inventory in the chamber obtains different conditions before absorption into the falling film through interaction with the solution pools in the chamber. The

temperature of the inlet vapor is usually lower than that of the solution in the absorber, thus the large surface area of the solution film and solution pool can affect the vapor condition presented to the film falling over the tube bank. In this study, the bulk vapor is assumed to achieve saturation corresponding to the minimum temperature of the solution film in the absorber. In the following section, the method of obtaining the minimum temperature of the solution in the absorber is described.

4.4.2 Solution Temperature Profile

During the experiments, solution temperatures at each tube row and the corresponding coolant temperatures in the coolant headers were recorded. The dilute solution entering the absorber is collected in the drip tray and distributed over the tube

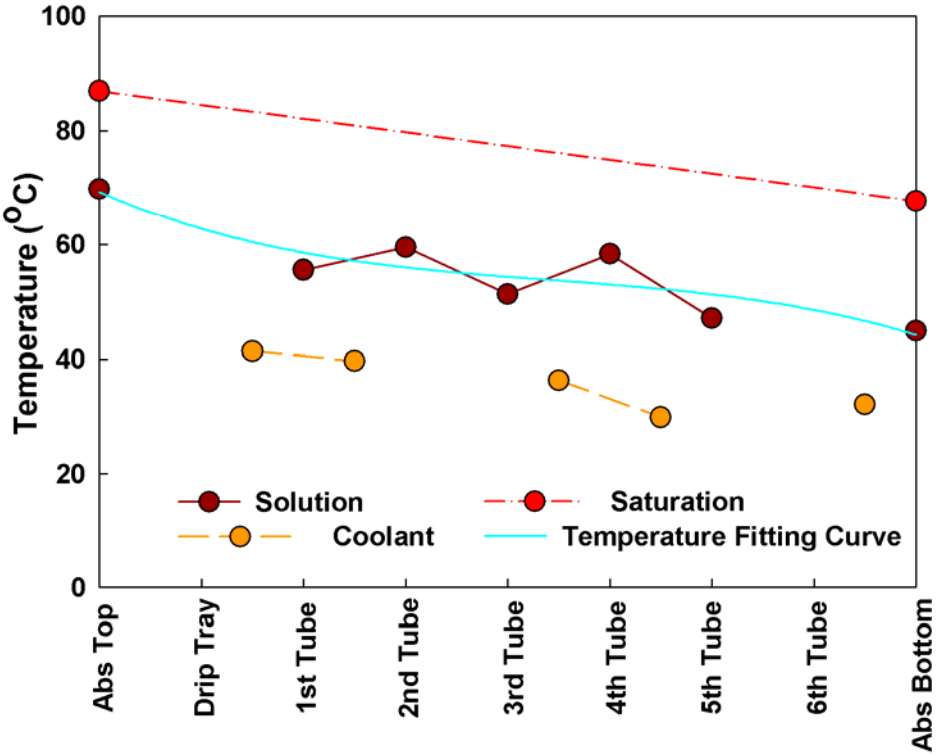

Figure 4.11 Representative temperature profiles in the absorber for a case of 350 kPa, 15%, and 0.02646 kg/s

array through very small diameter capillary tubes. The dilute solution then flows downward under the influence of gravity from one tube to the next tube below it. To measure the solution temperature at each of the tube rows, thermocouples were attached on one tube of each row. However, the local temperatures measured on the ammonia-water side depend upon whether they are in contact with the liquid phase or the vapor phase during measurement. Further, solution flow patterns are easily influenced by various factors such as gravity, flow rate, and solution property changes. Therefore, due to the dynamic behavior of the solution film, these thermocouples could record a liquid-film temperature or a vapor temperature, or a combination. The measured temperatures were therefore used to develop a smoothed temperature profile along the absorber rows using a 3rd degree polynomial. Figure 4.11 shows a representative temperature profile for the case with a pressure of 345 kPa, a nominal solution inlet concentration of 15%, and a flow rate of 0.02646 kg/s. The measured solution and coolant temperatures, the solution saturation temperatures at the absorber inlet and outlet, and the solution temperature profile used for data analysis are shown in this figure. The minimum temperature in the absorber is obtained using the solution temperature profile from a 3rd order polynomial curve-fit. The vapor equilibrium temperature is the lowest of the absorber outlet, the measured solution pool temperature, and the minimum solution temperature based on the curve fit of the solution-side thermocouple measurements. In a most of the test cases, the temperature of the solution pool or at the exit of the tube array is the minimum.

$$T_{\min} = f\left(T_{\text{Abs,out}}, T_{sol,pool}, T_{\min,profile}\right) \tag{4.98}$$

$$T_{\min} = f\left(31°C, 29.8°C, 31.8°C\right) = 29.8°C \tag{4.99}$$

The bulk vapor concentration for absorption is obtained from the vapor saturation state corresponding to the minimum solution temperature and the average absorber pressure.

$$P_{\text{Abs,ave}} = \frac{P_{Abs,in} + P_{Abs,out}}{2} \tag{4.100}$$

$$P_{\text{Abs,ave}} = \frac{351.8 + 350.6}{2} = 351.2\,\text{kPa} \tag{4.101}$$

$$x_{\text{V,bulk}} = f\left(T_{\min}, P_{Abs,ave}, q = 1\right) \tag{4.102}$$

$$x_{\text{V,bulk}} = f\left(29.8°C, 351.2\text{kPa}, \text{q} = 1\right) = 0.9965 \tag{4.103}$$

Therefore, the bulk vapor state is fully defined.

4.4.3 Calculation of Overall Mass Transfer Coefficient in Vapor-Phase

In the experiments, the refrigerant mass flow rate is known from measurements. With the bulk solution and the vapor conditions known, it is possible to calculate an overall mass transfer coefficient in the absorber. The absorption process can be understood as the progression of the vapor from the bulk to the interface, and finally into the bulk solution. The steps in this progression, represented as heat regions, are discussed here.

4.4.3.1 Mass Transfer with Binary Mixtures in Vapor Phase

Water and ammonia are both condensable gases. Therefore, the Colburn and Drew method (1937) may be used to model the ammonia/water absorption mass transfer as a binary fluid mixture condensation process. The mass transport equations in this section are derived from the general form of mass transfer equations for a binary mixture.

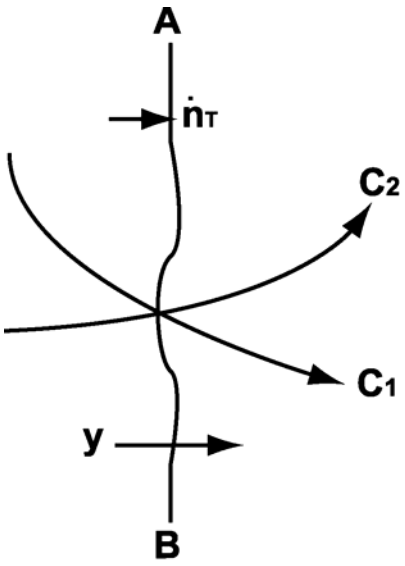

Figure 4.12 Binary Mixtures Diffusion

In the following discussion, 1 and 2 represent the components of a mixture, and $\tilde{y}$ represents the molar concentration of the vapor-phase, while $\tilde{x}$ represents the molar concentration of the liquid-phase. The total molar concentration of an ideal gas at pressure P (Pascal) and absolute temperature T (Kelvin) is given by the ideal gas law, where R is the gas constant.

$$C_T = \frac{P}{R \cdot T} \tag{4.104}$$

Consider the situation illustrated in Figure 4.12, where $\dot{n}_1$ (concentration C_1) and $\dot{n}_2$ (concentration C_2) are the molar fluxes through the plane AB of the respective components. For mass flux normal to the interface, mass flux away from the interface is conventionally defined as positive and towards the interface defined as negative. Therefore, $\dot{n}_1$ is defined as positive away from the interface. The sum of the each component becomes the total molar concentration.

$$C_T = C_1 + C_2 \tag{4.105}$$

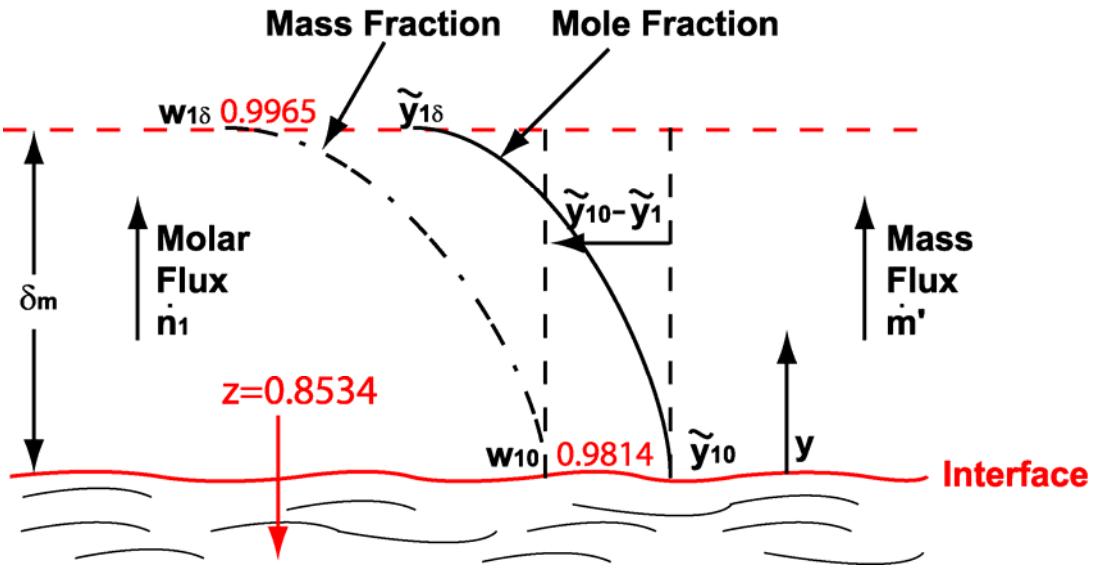

Figure 4.13 Parameters for Equivalent Laminar Layer Treatment of Mass Transfer

Fick's law of molar fluxes for binary mixtures is as follows:

$$\dot{n}_1 = -D_{12}\frac{dC_1}{dy} + \dot{n}_T\frac{C_1}{C_T} \tag{4.106}$$

$$\dot{n}_2 = -D_{12}\frac{dC_2}{dy} + \dot{n}_T\frac{C_2}{C_T} \tag{4.107}$$

where, D_{12} is the diffusion coefficient. In the above equation, diffusion is only considered in the y direction. The first term of the above equations represents the molar flux resulting from the concentration gradient. The second term represents the molar flux resulting from one component being carried in the bulk flow of the fluid, which is referred to as the bulk motion contribution. Before discussing the Colburn and Drew method further, an equivalent laminar film concept (Lewis and Whitman, 1924) is explained to evaluate the mass transfer process in condensation. The equivalent laminar film concept is based on the assumption of a fictitious laminar film layer for mass transfer. This assumption implies that all mass transfer resistances in the vapor-phase are

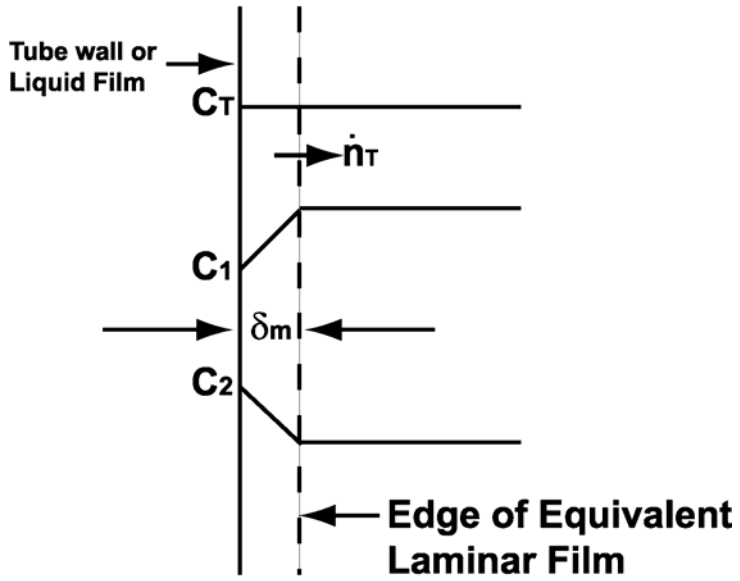

Figure 4.14 Equivalent Laminar Film Concept for Mass Transfer

present only in this layer. The equivalent laminar film concept assumes that a laminar boundary layer is immediately adjacent to the wall or liquid-phase (Hewitt *et al.*, 1994). This equivalent laminar film exhibits a concentration profile, while the region outside the equivalent laminar layer is considered to have a constant concentration. The thickness of the equivalent laminar layer is defined as δ_m. Figure 4.13 shows the parameters for the equivalent laminar layer for single-component condensation. Here, $\tilde{y}_{10}$ is the molar concentration at the interface and $\tilde{y}_{1\delta}$ is the molar concentration at the edge of the equivalent laminar layer. The varying mass fraction (w) is also shown in the figure. The concept of the equivalent laminar layer for a binary mixture is illustrated in Figure 4.14. Individual concentrations C_1 and C_2 may vary in opposite directions in the equivalent laminar film, however, C_T remains constant. Although this concept is typically applied to multi-component condensation, it can also be applied to absorption. For single component condensation, or binary mixture condensation with a non-condensable gas, the concentration of the condensate is 1. However, the concentration of condensate for

binary mixtures containing both condensable gases is not 1, since the condensate would be a mixture of two components. Therefore, for binary mixtures, it is required to define a concentration of the condensate that accounts for both condensable components. $\tilde{z}$ is defined as the mole fraction of component 1 in the *condensing flux* $\tilde{z} = \frac{\dot{n}_1}{\dot{n}_T} = \frac{\dot{n}_1}{\dot{n}_1 + \dot{n}_2}$. For convenience, the mole fraction of species i is also defined as $\tilde{y} = \frac{C_i}{C_T}$. The equation for the molar fluxes of the binary mixture can be written as follows:

$$\dot{n}_1 = \dot{n}_T \tilde{z} = -C_T \cdot D_{12} \frac{d\tilde{y}_1}{dy} + \dot{n}_T \tilde{y}_1 \tag{4.108}$$

The equation is then rearranged as follows:

$$\dot{n}_T \left(\tilde{z} - \tilde{y}_1 \right) = -C_T \cdot D_{12} \frac{d\tilde{y}_1}{dy} \tag{4.109}$$

$$\dot{n}_T dy = -\frac{C_T \cdot D_{12}}{\left(\tilde{z} - \tilde{y}_1 \right)} d\tilde{y}_1 \tag{4.110}$$

The above equation is integrated over the equivalent laminar film as follows:

$$\dot{n}_T \int_0^{\delta_m} dy = -C_T \cdot D_{12} \int_{y_{10}}^{y_{1\delta}} \frac{d\tilde{y}_1}{\left(\tilde{z} - \tilde{y}_1 \right)} \tag{4.111}$$

The above equation yields:

$$\dot{n}_T = -\frac{C_T \cdot D_{12}}{\delta_m} \ln \left[\frac{\tilde{z} - \tilde{y}_{10}}{\tilde{z} - \tilde{y}_{1\delta}} \right] \tag{4.112}$$

The mass transfer coefficient is defined as $\beta = D_{12} / \delta_m$. After substitution, the above equation is expressed as:

$$\dot{n}_T = -\beta \cdot C_T \ln\left[\frac{\tilde{z} - \tilde{y}_{10}}{\tilde{z} - \tilde{y}_{1\delta}}\right] \tag{4.113}$$

The above equation shows the total molar flux for the condensation of the binary mixture in terms of the mass transfer coefficient, total molar concentration and the logarithmic ratio of the concentration difference between the condensate and interface, and the condensate and the bulk-vapor. To obtain the interfacial concentration of $\tilde{y}_{10}$ in the vapor-phase for component 1, the value of $\tilde{x}_{10}$ in the liquid-phase for component 1 is obtained from the equilibrium saturated-liquid conditions at the measured pressure and temperature. The interfacial concentration $\tilde{y}_{10}$ is then calculated from the $\tilde{x}_{10}$ obtained in this manner. However, to calculate the mass transfer coefficient β, it is necessary to obtain the total molar flux and the concentration of the condensing flux $\tilde{z}$. The following sections will discuss these procedures.

4.4.3.2 Colburn-Drew Method for Binary Mixtures in Vapor Phase

The vapor-side mass transfer coefficient is obtained by using the Colburn and Drew (1937) method for a binary mixture. This method uses an energy balance equation iteratively between the solution-side and the coolant-side to obtain the concentration of the condensing flux $\tilde{z}$ and the total molar flux for condensation. The total molar concentration is calculated with the measured pressure and temperature, and the total molar flux $\dot{n}_T$ is obtained from the measured vapor mass flow rate from the following expression:

$$\dot{n}_T = \frac{-\dot{m}_{vap}}{Abs_{area} \cdot \left(\tilde{z} \cdot M_{NH_3} + \left(1 - \tilde{z}\right) M_{H_2O}\right)} \tag{4.114}$$

where $\dot{m}_{vap}$ is the measured vapor mass flow rate. The negative sign represents vapor being absorbed into the falling film, and Abs_{area} represents the mass transfer area. This mass transfer area is different from the heat transfer area used to calculate the heat transfer coefficient in the absorber, since heat transfer can occur only at the tube array where the solution contacts the absorber coolant, while mass transfer can occur not only at the tube arrays but also at the drip tray and solution pool where the solution can contact the vapor. Once the total molar flux is obtained, the Colburn-Drew method is applied with an assumed $\tilde{z}$ value, which is the mole fraction of component 1 in the condensing flux.

$$\dot{n}_T = \beta \cdot C_T \ln\left[\frac{\tilde{z} - \tilde{y}_{10}}{\tilde{z} - \tilde{y}_{1b}}\right] \tag{4.115}$$

where, $\tilde{y}_{1b}$ is the bulk concentration of component 1 in the vapor-phase. The negative sign is removed in the above equation because the absorption process is considered as a condensation process and the direction of condensation was considered in the calculation of the total molar flux from the measured vapor mass flow rate. The above equation is solved iteratively with the measured vapor flow rate to obtain a mass transfer coefficient. The following sections describe the heat regions in the absorption process and a method to obtain the $\tilde{z}$ value.

4.4.3.3 Interface Conditions and Heat Regions

Figure 4.15 shows the various heat regions in the process of absorption. In this figure, the bulk solution and the bulk vapor conditions are specified from the preceding analysis. However, it is necessary to specify the vapor-liquid interface conditions. The interface

during absorption is at different conditions than the bulk solution and vapor. However, the interface conditions cannot be measured directly, and have to be inferred from the measurements and appropriate assumptions. Here, it is assumed that the interface temperature is the same as the solution bulk temperature. In much of the literature, the

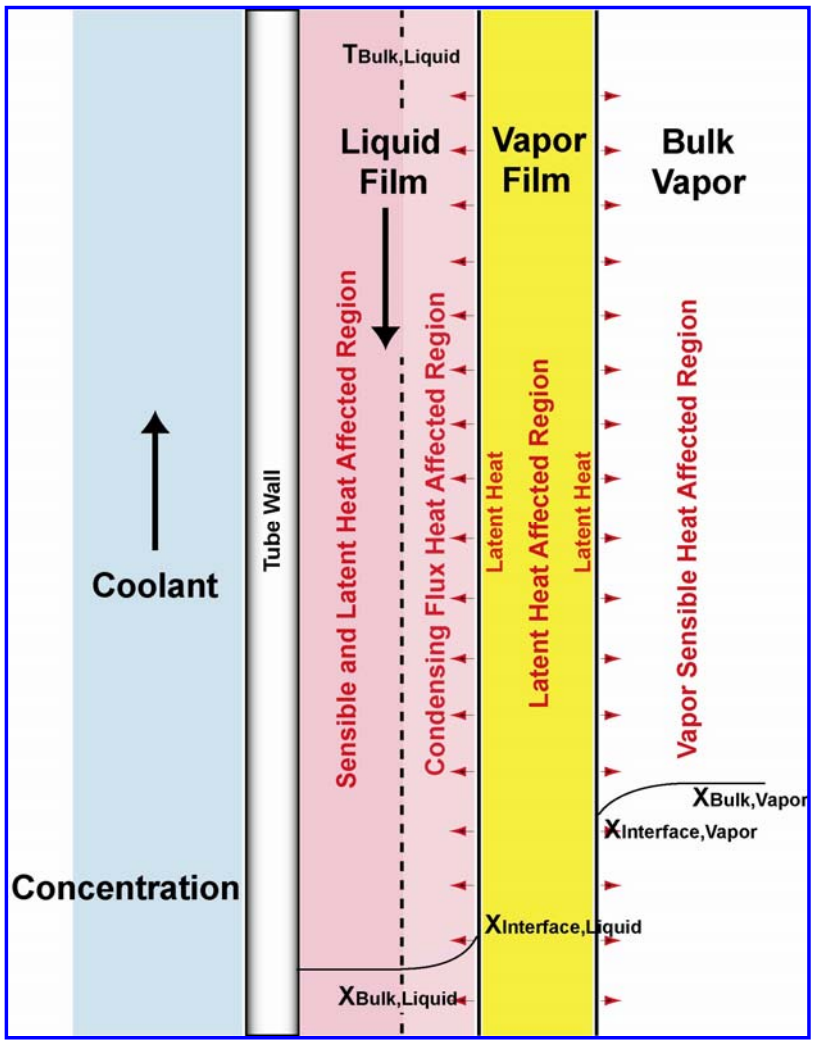

Figure 4.15 Absorption Regions

interface conditions are assumed to be those corresponding to saturated liquid at the solution bulk concentration. However, most of these studies involve saturated solution, therefore the interface temperature (estimated using the bulk concentration) does not differ significantly from the solution bulk temperature. But in the current experiments

with solution temperature imposed by system-level operation, the solution is typically considerably sub-cooled. In this study, the degree of sub-cooling varies between -0.36 and 17.16°C at the inlet and between 15.1 and 33.0°C at the outlet of the absorber. It is therefore more reasonable to assume the interface temperature to be equal to the solution bulk temperature (An assumption of interface saturation at the measured pressure and concentration does not correspond to the actual test conditions, and would result in unrealistically high interface temperatures.). The average solution temperature is computed as the average of the solution temperature at the absorber inlet and outlet. .

$$T_{\text{int}} = T_{\text{sol,ave}} = \frac{T_{Abs,in} + T_{Abs,out}}{2} \tag{4.116}$$

Using the average solution temperature and absorber pressure, the vapor and liquid concentrations at the interface can be estimated.

$$x_{\text{sol,int}} = f\left(T_{\text{int}}, P_{\text{int}}, q = 0\right) \tag{4.117}$$

$$x_{\text{V,int}} = f\left(T_{\text{int}}, P_{\text{int}}, q = 1\right) \tag{4.118}$$

All the bulk and interface conditions for Figure 4.15 are now specified. Four distinct regions can be identified here. The region between the vapor bulk and the interface is the vapor sensible cooling or heating region (depending on the interface temperature). In addition, there is a latent heat region at the interface, a region from the interface to the solution bulk representing the condensed vapor sub-cooling region, and finally, the solution sub-cooling region. The heat duties for these various heat regions can be estimated once the various temperatures and concentrations are known. The heat duty for the vapor sensible cooling or heating is calculated as follows. The heat duty is defined as positive when heat is transferred from the bulk vapor to the bulk solution.

$$Q_{\mathrm{V,sensible}} = \dot{m}_{V,in} \cdot \left(h_{\mathrm{V,bulk}}(T_{V,bulk}, P_{Abs,ave}, q=1) - h_{V,\mathrm{int}}(T_{\mathrm{int}}, P_{\mathrm{int}}, q=1) \right) \quad (4.119)$$

$$-0.185\,\mathrm{kW} = 0.002826\ \mathrm{kg/s} \times \left(1351\,\mathrm{kJ/kg} - 1416\,\mathrm{kJ/kg} \right) \quad (4.120)$$

The latent heat duty is calculated as follows:

$$Q_{\mathrm{V,latent}} = \dot{m}_{V,in} \cdot \left(h_{\mathrm{V,int}}(T_{\mathrm{int}}, P_{\mathrm{int}}, q=1) - h_{sol,\mathrm{int}}(T_{\mathrm{int}}, P_{\mathrm{int}}, q=0) \right) \quad (4.121)$$

$$3.992\,\mathrm{kW} = 0.002826\ \mathrm{kg/s} \times \left(1416\,\mathrm{kJ/kg} - 3.489\,\mathrm{kJ/kg} \right) \quad (4.122)$$

For the condensed vapor sub-cooling region, the heat duty is,

$$Q_{\mathrm{V,sensible,cond}} = \dot{m}_{V,in} \cdot \left(h_{sol,\mathrm{int}}(T_{\mathrm{int}}, P_{\mathrm{int}}, q=0) - h_{sol,bulk}(T_{sol,bulk}, P_{\mathrm{int}}, x = x_{Abs,ave}) \right) \quad (4.123)$$

$$-0.071\,\mathrm{kW} = 0.002826\ \mathrm{kg/s} \times \left(3.489\,\mathrm{kJ/kg} - 28.73\,\mathrm{kJ/kg} \right) \quad (4.124)$$

Finally, for the solution sub-cooling region, the sub-cooling duty is:

$$Q_{\mathrm{sol,sensible}} = Q_{\mathrm{Abs,C}} - (Q_{\mathrm{V,sensible}} + Q_{\mathrm{V,latent}} + Q_{\mathrm{V,sensible,cond}}) \quad (4.125)$$

$$4.218\,\mathrm{kW} = 7.954\,\mathrm{kW} - \left((-0.185\,\mathrm{kW}) + (3.992\,\mathrm{kW}) + (-0.071\,\mathrm{kW}) \right) \quad (4.126)$$

Here, $Q_{Abs,C}$ is calculated using the flow rate, and the inlet and outlet temperatures of the coolant in the absorber that are known from measurements. By computing the heat duties in the various heat regions, the relative contributions of the different processes to absorption can be estimated. It is found that the heat duties of the phase-change (absorption) at the interface and of the subsequent sub-cooling of the solution are the largest contributors to the overall absorption heat duty (that will be removed by the coolant in the absorber). In addition, the latent heat duty is used for determining the condensing flux concentration as discussed in the next section.

4.4.3.4 Calculation of Condensing Flux Concentration

It was mentioned above that the concentration of the condensing mass flux is different from the vapor bulk concentration. This concentration is referred to as the concentration of the condensing flux. To calculate this concentration, an energy balance is performed at the interface. It is assumed that the latent heat generated at the interface is due to the phase change of the ammonia and water from the vapor to the liquid phase at the absorber pressure.

$$h_{\mathrm{fg,NH_3}} = h_{NH_3}\left(P_{\mathrm{int}}, q=1\right) - h_{NH_3}\left(P_{\mathrm{int}}, q=0\right) \tag{4.127}$$

$$h_{\mathrm{fg,H_2O}} = h_{H_2O}\left(P_{\mathrm{int}}, q=1\right) - h_{H_2O}\left(P_{\mathrm{int}}, q=0\right) \tag{4.128}$$

The latent heat of absorption is calculated as follows:

$$h_{V,latent} = \left(h_{\mathrm{V,int}}(T_{\mathrm{int}}, P_{\mathrm{int}}, q=1) - h_{sol,\mathrm{int}}(T_{\mathrm{int}}, P_{\mathrm{int}}, q=0)\right) \tag{4.129}$$

$$h_{V,latent} = \left(1416\,\mathrm{kJ/kg} - 3.489\,\mathrm{kJ/kg}\right) = 1412.5\,\mathrm{kJ/kg} \tag{4.130}$$

Using an energy balance at the interface,

$$h_{V,latent} = z \cdot h_{fg,NH_3} + (1-z) \cdot h_{fg,H_2O} \tag{4.131}$$

It can be seen from the above calculations that the concentration of the vapor mass absorbed at the interface is different from both the bulk vapor ($x_{\mathrm{V,bulk}} = 0.9965$) and the vapor concentration at the liquid-vapor interface ($x_{\mathrm{V,int}} = 0.9814$). This is typical of binary vapors where both the components have the potential to condense (or to be absorbed). Note that water has a higher boiling point than that of ammonia, so as absorption occurs, water will first condense out of the vapor preferentially to ammonia. This is why z (e.g. 0.8534 for the representative case) is generally lower than $x_{v,bulk}$ (e.g. 0.9965 for the representative case), because the condensing flux is removing water from

Table 4.1 Condensing Flux, Vapor Interface, and Bulk Vapor Concentrations

Mass Concentration	Molar Concentration
$z = 0.8534$	$\tilde{z} = 0.8603$
$x_{V,int} = 0.9814$	$\tilde{x}_{V,int} = 0.9824$
$x_{V,bulk} = 0.9965$	$\tilde{x}_{V,bulk} = 0.9967$

the vapor phase; hence it contains more water and therefore a lower ammonia concentration. The smaller value of z compared to the interface vapor concentration may also mean that there is accumulation of the vapor at the interface that provides resistance to absorption. This concentration of the condensing flux will be used to calculate the mass transfer coefficient.

4.4.3.5 Calculation of Vapor Mass Transfer Coefficient

All the information required to compute the mass transfer coefficient is now known. The Colburn-Drew (1937) method is used to calculate the mass transfer coefficient in the absorber where both the components are absorbed or condensed. To implement this method, all mass concentrations are converted to molar concentrations using following equation.

$$\tilde{x} = \frac{x/M_{NH_3}}{x/M_{NH_3} + (1-x)/M_{H_2O}} \tag{4.132}$$

In this equation, x is a generic concentration. The substitution of bulk or interface concentration will yield the corresponding molar concentration (sample values are shown in Table 4.1). The molar flux is calculated next using the amount of vapor absorbed. (Here, a negative sign denotes absorption).

$$\dot{n}_t = \frac{-\dot{m}_V}{Abs_{area,M} \cdot (\tilde{z} \cdot M_{NH_3} + (1-\tilde{z}) \cdot M_{H_2O})} \tag{4.133}$$

$$= \frac{0.0004721\,\text{kmol/s-m}^2}{\text{-}0.002826\,\text{kg/s}} \tag{4.134}$$
$$0.3487\,\text{m}^2 \times (0.8603 \times 17.03\,\text{kg/kmol} + (1-0.8603) \times 18.02\,\text{kg/kmol})$$

It is also necessary to know the total molar concentration in the absorber. This is obtained using the ideal gas law for ammonia vapor at the average absorber pressure and temperature.

$$C_T = \frac{P_{Abs,ave}}{R \cdot (T_{\min} + 273.15K)} \tag{4.135}$$

$$C_T = \frac{351.2 \times 10^3\ \text{Pa}}{8314\,\text{J/kmol-K} \times (29.84°C + 273.15\text{K})} \tag{4.136}$$

Finally, the mass transfer coefficient is calculated as follows:

$$\beta_V = \frac{\dot{n}_t}{C_T \cdot \ln\left[\frac{\tilde{z} - \tilde{x}_{V,\text{int}}}{\tilde{z} - \tilde{x}_{V,bulk}}\right]} \tag{4.137}$$

$$0.0304\,\text{m/s} = \frac{0.0004721\,\text{kmol/s-m}^2}{0.1394\,\text{kmol/m}^3 \times \ln\left[\frac{0.8603 - 0.9824}{0.8603 - 0.9967}\right]} \tag{4.138}$$

4.4.4 Calculation of Overall Mass Transfer Coefficient in Liquid Phase

Since the refrigerant mass flow rate is known from the measurements of the bulk solution with the known condensing flux concentration, it is possible to calculate an overall mass transfer coefficient in the liquid-phase. In this section, the absorption

process from the liquid-vapor interface to the bulk solution is presented. The steps in this mass transfer process, represented as convective mass transfer, are discussed here.

4.4.4.1 Mass Transfer with Binary Mixtures in Liquid Phase

Mass transfer in the liquid-phase is treated primarily as convective mass transfer rather than as diffusive mass transfer as was the case for the vapor-phase, since fluid motion in the liquid-phase has a more important role. The convective mass transfer in the liquid phase occurs between the bulk liquid solution and the condensing flux which is condensed at the liquid-vapor interface. This convective mass transfer depends on the transport properties and dynamic characteristics of the flowing fluid. The convective mass transfer coefficient can be determined as follows:

$$\dot{n}_A = \beta_L \cdot \Delta C_A \tag{4.139}$$

where, $\dot{n}_A$ is the measured molar mass of species A that is the absorbed into the falling-film, ΔC_A is the difference between the molar concentration at the boundary and the average molar concentration of the bulk fluid stream, and β_L is the convective mass transfer coefficient in the liquid-phase. The relationship between the molar and mass based equation is as follows:

$$\rho_A = c_A M_A \tag{4.140}$$

where, ρ_A is the mass density of species, and M_A is the molar mass.

The molar based convective mass transfer equation can be written on a mass basis equation as follows:

$$\dot{m}_A = \beta_L \cdot Abs_{area,M} \cdot \Delta\rho_A \tag{4.141}$$

The mass concentration is defined as follows:

$$x_A = \rho_A \Big/ \rho \tag{4.142}$$

Where, ρ is the total mass density of the mixture.

Therefore, the convective mass transfer equation in the liquid-phase, based on mass, is given as follows:

$$\dot{m}_A = \dot{m}_T \cdot x_{vap,in} = \beta_L \cdot Abs_{area,M} \cdot \left(z_{A,sol,\text{int}} \cdot \rho_{sol,\text{int}} - x_{A,sol,bulk} \cdot \rho_{sol,bulk} \right) \tag{4.143}$$

$$\begin{aligned} 0.002764\,\text{kg/s} &= 0.002826\,\text{kg/s} \times 0.9781 \\ &= 2.313\times10^{-5}\,\text{m/s} \times 0.3487\,\text{m}^2 \left(0.8534 \times 706.2\ \text{kg/m}^3 - 0.3 \times 865.8\ \text{kg/m}^3 \right) \end{aligned} \tag{4.144}$$

From the above equation, a convective mass transfer coefficient in liquid-phase can be obtained.

4.5 Energy Balances and Uncertainties for the Current Experiments

4.5.1 Component Energy Balances

Table 4.2 shows the number of data within bands of energy balances for the absorber, condenser and evaporator. For each of these components, energy balances were calculated between the two sides of the exchangers. The criterion for acceptability was to ensure that the calculated energy balances are within 15% for all three

Table 4.2 Energy Balances for Absorber, Condenser and Evaporator

Component	Number of Data within				Average Absolute Difference
	±(0 – 5) %	±(5 – 10) %	±(10 – 15) %	±(15 – 18) %	
Absorber	20	14	2		4.8%
Condenser	12	17	5	2	7.1%
Evaporator	12	17	4	3	7.3%

components. As Table 4.2 shows, a significant number of the data points have energy balances within 5% or 10%, with all the data having absorber energy balances within 15%. The average difference between the heat duties on the two sides of the absorber for the whole text matrix is 4.8%. (For 3 data points in the matrix, the condenser and/or evaporator balances are outside this limit.)

4.5.2 Uncertainty Calculations

A rigorous uncertainty propagation analysis was also conducted on the data obtained in this study. The main parameters of interest are the various solution stream concentrations, the absorber heat duties, and the coolant, the overall and the film heat transfer coefficients, the mass transfer coefficient in the absorber, and the reflux flow rate. The calculation of heat duties, heat and mass transfer coefficients and reflux flow rate will be affected both directly by errors in the measurements of temperature, pressure and flow rate, and indirectly due to errors in the estimation of various concentrations based on the measured temperatures and pressures at various state points in the system. The effects of the following measurement uncertainties are accounted for in the uncertainty calculations for the parameters of interest:

- *Pressures and Temperatures at*: Desorber outlet, rectifier inlet and outlet, reflux outlet, separator liquid outlet, absorber solution inlet and outlet, and absorber vapor inlet
- *Flow rate of*: Dilute, concentrated, and refrigerant flow rates
- *Coolant Side*: Inlet and outlet temperatures, and coolant flow rate
- *Geometry*: Tube ID, OD, and length

Table 4.3 Uncertainties of the Pressure Transducers

Location	Model	Calibrated Span (psi)	Accuracy (of Cal Span)	Total Uncertainty (psi)
$P_{Abs,in}$	2088	800	±0.25%	±2
$P_{Abs,out}$	3051 TA4	4000	±0.075%	±3
$P_{Abs,V,in}$	3051 TA5	10000	±0.075%	±7.5
$P_{Des,in}$	2088	800	±0.25%	±2
$P_{Des,out}$	2088	800	±0.25%	±2
$P_{Sep,out}$	2088	800	±0.25%	±2
$P_{Reflux,out}$	3051 TA5	10000	±0.075%	±7.5
$P_{Con,in}$	2088	800	±0.25%	±2
$P_{Con,out}$	3051 TA5	10000	±0.075%	±7.5
$P_{Evap,in}$	3051 TA5	10000	±0.075%	±7.5
$P_{Evap,out}$	3051 TA4	4000	±0.075%	±3
$DP_{Abs,C}$	3051 CD	2000	±0.075%	±1.5

As discussed in the previous chapter, the absolute pressures in the system were measured using pressure transducers manufactured by Rosemount, the temperatures were measured using T-type thermocouples and RTDs, the solution flow rates were measured using coriolis mass flow meters by Micromotion, and the coolant flow rates were measured using various magnetic, positive displacement and coriolis type flow meters. Instrument uncertainties for the pressure transducers and flow meters are shown in Tables 4.3 and 4.4, respectively. The absolute uncertainty in temperature measurement is taken as $\pm 0.5^{o}C$, while the uncertainty in geometrical parameters of the absorber tube array such as tube diameter and length is taken as ±0.0025 mm (±0.0000025 m). The results corresponding to the uncertainty analysis described in this section are reported in the following chapter.

Table 4.4 Uncertainties of the Solution and Coolant Flow Meters

Locations	Model	Calibrated Span	Accuracy	Total Uncertainty
Dilute Solution	CMF025 Elite (Micromotion)	0–80 lb_m/min 0–10 GPM	±0.1% (Flow) ±0.5kg/m^3 (Density)	Relative
Concentrated Solution	CMF025 Elite (Micromotion)	0–80 lb_m/min 0–10 GPM	±0.1% (Flow) ±0.5kg/m^3 (Density)	Relative
Refrigerant	C25 (Micromotion)	0–3 lb_m/min	±0.1%	Relative
Absorber Coolant	8711 (Rosemount)	0–20 GPM	±0.5%	Relative
Condenser Coolant	CMF100 Elite (Micromotion)	0–1000 lb_m/min	±0.1% (Flow) ±0.5kg/m^3 (Density)	Relative
Evaporator Coolant	JVM–60KL (AW Company)	2 – 20 GPM	±0.5% @ $\nu = 3 \times 10^{-5}$ m^2/s	Relative

CHAPTER 5. RESULTS

This chapter presents the results obtained using the analysis techniques described in the previous chapter. Absorber heat duty and heat and mass transfer results, including the effects of inlet solution concentration, flow rate, and pressure are discussed. The results are also compared with those from other studies in the literature.

5.1 Overall Heat Transfer Results

This section presents overall heat transfer results for the entire absorber. In the presentation of the results that follows, the concentrated solution flow rates are shown in terms of the linear mass flux based on the tube length. Thus, the concentrated solution flow rate is divided by the total length of the four tubes over which the solution flows, and further divided by a factor of two to account for the fact that the solution flows around two sides of a tube. This yields a concentrated solution mass flux $\Gamma = \dot{m} / \left(2 \times L_{tube} \times N_{tube} \right)$. Therefore, a nominal flow rate of 0.019 kg/s (2.5 lb_m/min) corresponds to 0.0081 kg/m-s, 0.026 kg/s (3.5 lb_m/min) corresponds to 0.0113 kg/m-s and 0.034 kg/s (4.5 lb_m/min) corresponds to 0.0146 kg/m-s. In the discussion of the trends, however, the flow rate in kg/s is used for ease of comprehension.

5.1.1 Absorber Heat Duty

Figure 5.1 shows the absorber heat duties measured in this study as a function of concentrated solution flow rate, which has a significant effect on the heat duty. At any pressure or solution concentration, as expected, the absorber heat duty increases with

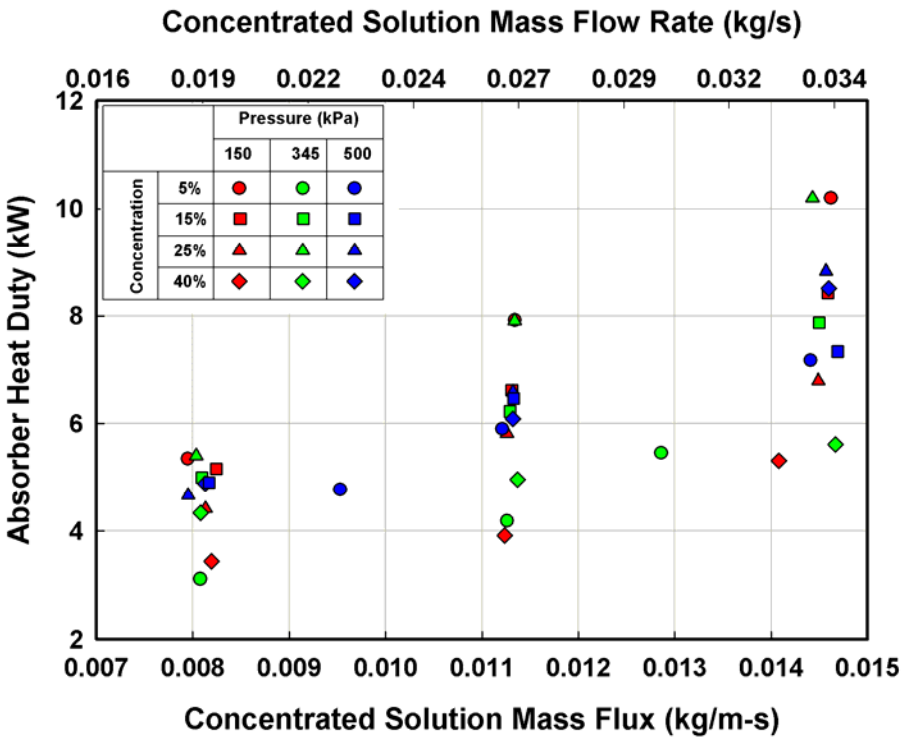

Figure 5.1 Variation of Absorber Heat Duty with Solution Flow Rate

increasing solution flow rate, ranging from 3.1 to 10.2 kW. No other significant conclusions should be drawn about absorption heat and mass transfer from these heat duty graphs, because the duty depends to a large extent on the coolant flow rates and the driving temperature difference provided.

5.1.2 Overall Heat Transfer Coefficient

Figure 5.2 shows the overall heat transfer coefficient U as a function of the concentrated solution flow rate. The U varies from 753 to 1853 W/m^2-K over the entire test matrix depending on the test conditions, in general increasing as the concentrated solution flow rate is increased. Once again, the overall U is a function of tube-side and

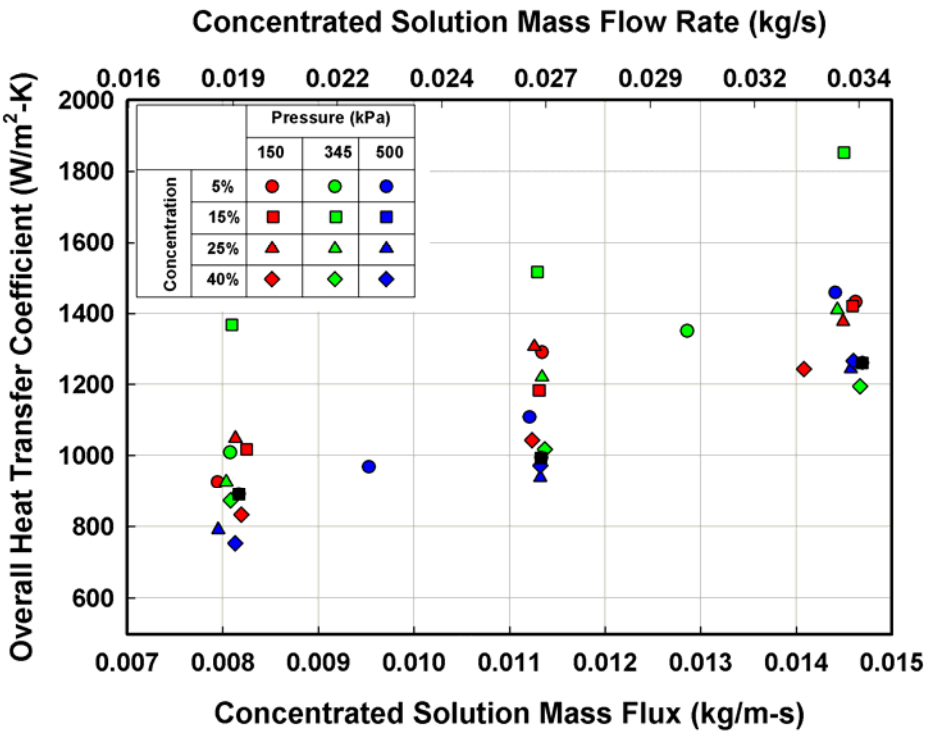

Figure 5.2 Variation of Overall Heat Transfer Coefficient with Solution Flow Rate

solution-side phenomena, and therefore, no significant conclusions should be drawn about absorption phenomena from these graphs.

5.1.3 Solution Heat Transfer Coefficient

Figure 5.3 shows the solution heat transfer coefficient for all the data points obtained in the current study. It should be noted that the solution heat transfer coefficients are based on the entire tube surface area (assuming complete wetting). The solution heat transfer coefficient ranges from 923 to 2857 W/m^2-K, depending on the test condition. An important aspect can be observed by comparing the graphs in Figure 5.2 and 5.3: The trend in the solution heat transfer coefficient is similar to the trend in the overall *U*. This is due to the large absorber coolant heat transfer coefficients for most of the test conditions. By keeping the coolant heat transfer coefficient high, the solution-side resistance becomes dominant and the effect of the coolant-side heat transfer

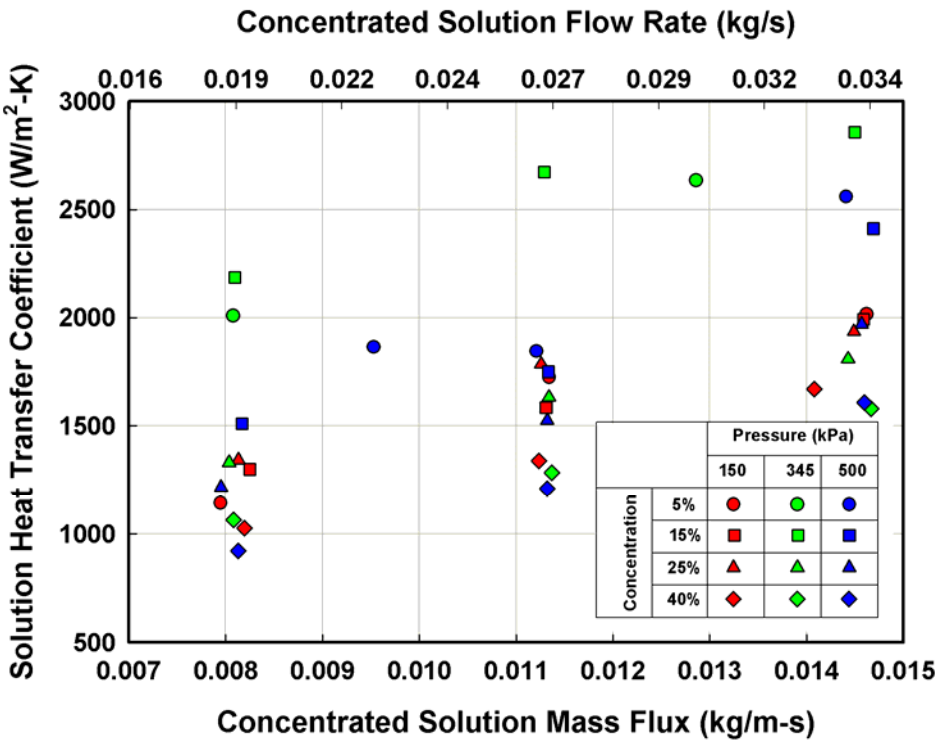

Figure 5.3 Variation of Solution Heat Transfer Coefficient with Solution Flow Rate

coefficient is minimized, which yields low uncertainties in the absorption heat transfer coefficients. This phenomenon is further illustrated in Appendix C, where the overall *U*, coolant *h*, and solution-side *h* for each test are plotted together. The graphs in this appendix clearly demonstrate that the test procedures successfully maintained the solution-side resistance as the dominant resistance for most of the data points over this wide range of solution flow rates, pressures and concentrations. As expected, Figure 5.3 shows that the solution heat transfer coefficient increases with the solution flow rate. The effects of the dilute solution concentration and absorber pressure on the solution heat transfer coefficient are discussed in detail in the following sections.

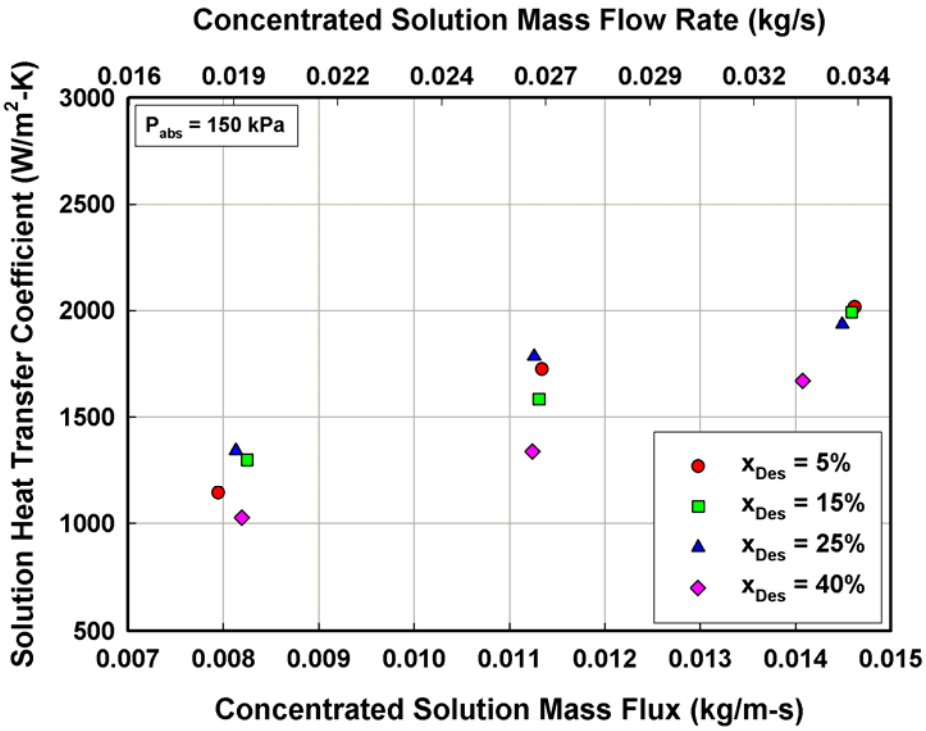

Figure 5.4 Effect of Dilute Solution Concentration on Solution α at P_{abs}=150 kPa (21.8 psi)

5.1.4 Effect of Dilute Solution Concentration

Figures 5.4 - 5.6 show the effect of dilute solution concentration on the solution heat transfer coefficient at nominal pressures of 150, 345, and 500 kPa (21.8, 50.0, and 72.5 psi), respectively. The solution heat transfer coefficient increases almost linearly with increasing concentrated solution flow rate regardless of the dilute solution concentration at all three pressures. However, there are no general trends that demonstrate a strong influence of dilute solution concentration at a given absorber pressure. At a nominal pressure of 150 kPa (21.8 psi) (Figure 5.4), at a given concentrated solution flow rate, the solution heat transfer coefficient decreases with increasing dilute solution concentration, although the effect is not very pronounced at a flow rate of 0.019 kg/s (2.5 lb_m/min). Solution heat transfer coefficients are the highest

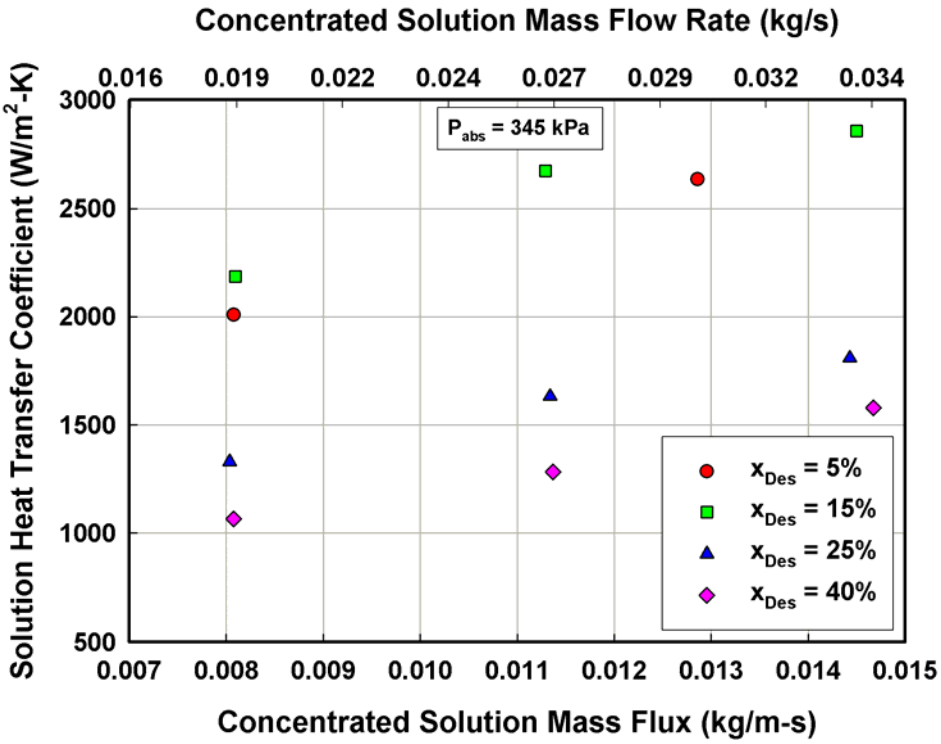

Figure 5.5 Effect of Dilute Solution Concentration on Solution α at P_{abs}=345 kPa (50 psi)

for the 5% nominal concentration case, and increase significantly when the flow rate is increased from 0.019 to 0.026 kg/s (2.5 to 3.5 lb_m/min). At a nominal concentration of 40%, the heat transfer coefficients are lower than those for 5% and 15% for all flow rates.

The low absorber pressures of 150 kPa (21.8 psi) necessitate the use of the subcooler described in Chapter 3 for solution concentrations of 15%, 25% and 40%. This results in some of the sensible heat being removed prior to the solution entering the absorber, which reduces absorber heat duties and could cause a decrease in the solution heat transfer coefficient. In other words, the sensible heat fraction in the 5% nominal solution concentration case is larger (because the subcooler is not used) compared to the data at the other concentrations, leading to larger absorber heat duties. It should also be noted that due to the challenges described in the previous chapter, the nominal

combination of low pressure (150 kPa or 21.8 psi) and high concentration (40%) was in reality tested at somewhat higher absorber inlet pressures (241 – 276 kPa or 35 – 40 psi, depending upon the flow rate). These different actual pressures for the same nominal pressure could also contribute to some of the differences in heat transfer coefficients, and therefore the trends seen in Figure 5.4 represent the combined influence of changes in concentration as well as operating pressure.

Figure 5.5 shows the solution heat transfer coefficient as a function of the concentrated solution flow rate with the dilute solution concentration as a parameter at a nominal pressure of 345 kPa (50.0 psi). The solution heat transfer coefficient increases as the concentrated solution flow rate increases for each concentration, although there is no monotonous, systematic effect of concentration. For example, the 5%, and 15% concentration cases show higher heat transfer coefficients than those for the 25%, and 40% nominal concentrations, mostly due to the larger concentration range at the absorber. The lowest solution heat transfer coefficients are observed for the 40% dilute solution concentration case. The data at the 15% nominal concentration show an increase in solution heat transfer coefficient between a solution flow rate of 0.019 kg/s (2.5 lb_m/min) and 0.026 kg/s (3.5 lb_m/min), and a less significant influence at the higher flow rates. This may be partly because the actual measured inlet concentrations at the 5% and 15% nominal concentrations are somewhat close to each other at the higher flow rates of 0.026 kg/s (3.5 lb_m/min) and 0.030 kg/s (4.0 lb_m/min). The use of the subcooler at 345 kPa (50.0 psi) and 40% may also have caused lower heat transfer coefficients.

Figure 5.6 shows the solution heat transfer coefficient as a function of the concentrated solution flow rate with the dilute solution concentration as a parameter at a

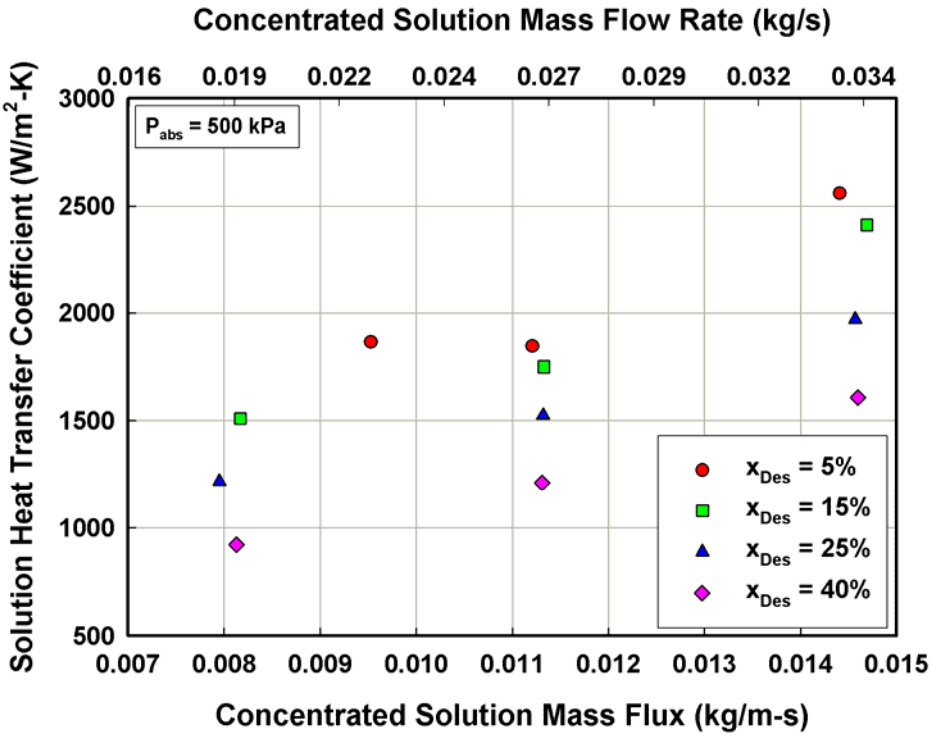

Figure 5.6 Effect of Dilute Solution Concentration on Solution α at P_{abs}=500 kPa (72.5 psi)

nominal absorber pressure of 500 kPa (72.5 psi). At low flow rates, the solution heat transfer coefficients for the 25% and 40% concentration are lower than those for the 5%, and 15% concentrations. The 5% and 15% nominal concentration cases required very low coolant flow rates to maintain the higher absorber pressures, which resulted in very large coolant ΔTs. To keep the coolant temperature difference within reasonable limits, the coolant inlet temperature is increased by using a cartridge heater in the absorber coolant loop, which resulted in different driving temperature difference profiles along the absorber. This may have affected the absorption rates and heat transfer coefficients. The heat transfer coefficients for 40% concentration are in general lower than those at 25% except at the highest flow rate, which may be because of the smaller driving concentration gradients available for absorption into the solution richer in ammonia.

5.1.5 *Effect of Absorber Pressure*

Figures 5.7 - 5.10 show the effect of absorber inlet pressure on the solution heat transfer coefficient for nominal dilute solution concentrations at the desorber outlet of 5%, 15%, 25%, and 40%, respectively. As discussed in the previous section on the effect of dilute solution concentration, the solution heat transfer coefficient increases almost linearly as the flow rate increases for any given concentration.

Figure 5.7 shows the effect of the absorber inlet pressure on the solution heat transfer coefficient for the nominal 5% concentration cases. The heat transfer coefficient increases continuously as the flow rate is increased from 0.019 to 0.034 kg/s (2.5 to 4.5 lb_m/min) for all pressures, except at the absorber pressure of 500 kPa (72.5 psi), where the heat transfer coefficient decreases slightly from 0.019 to 0.026 kg/s (2.5 to 3.5

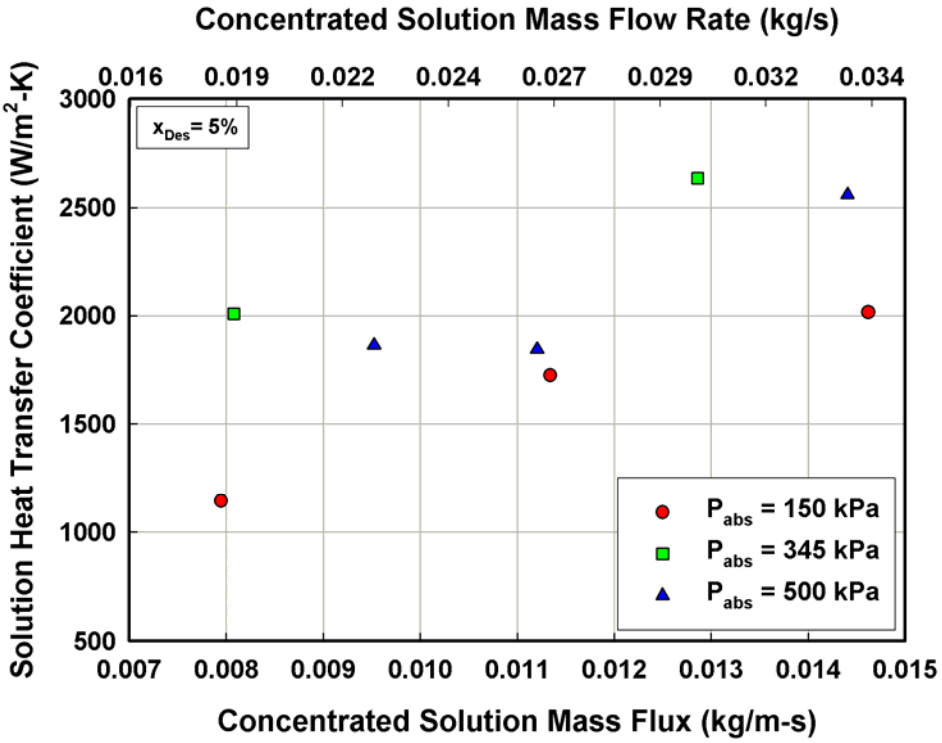

Figure 5.7 Effect of Absorber Pressure on Solution α at $x_{des,out}$ = 5%

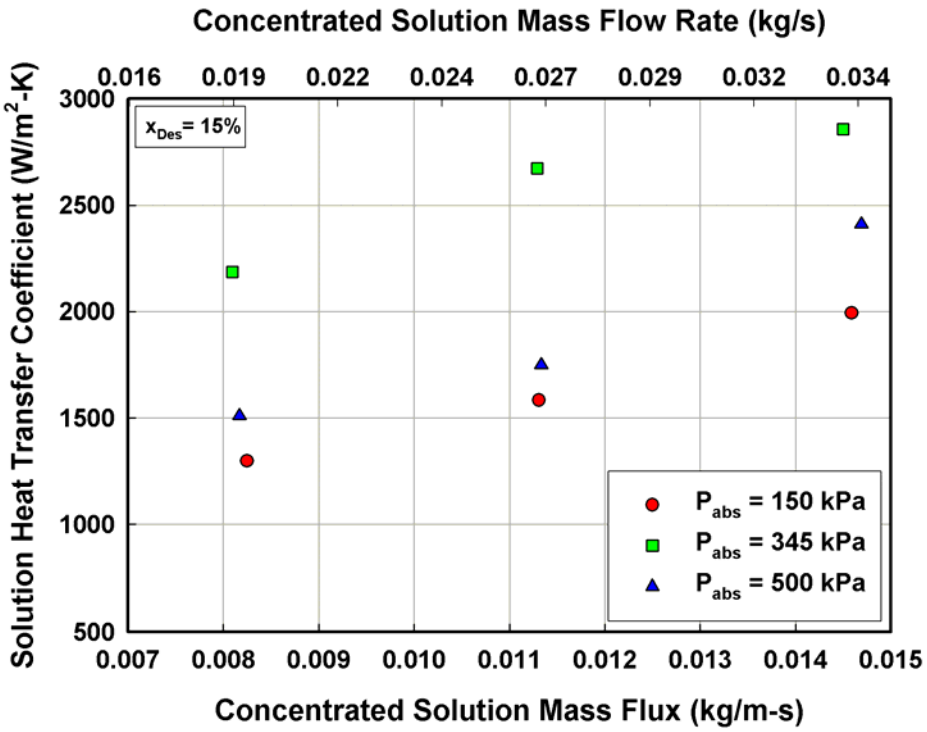

Figure 5.8 Effect of Absorber Pressure on Solution α at $x_{des,out}$ = 15%

lb_m/min). The heat transfer coefficients at 345 kPa (50 psi) are larger than those at other pressures.

Figure 5.8 shows the effect of the absorber inlet pressure on the solution heat transfer coefficient at a nominal concentration of 15%. The solution heat transfer coefficient increases almost linearly with increasing solution flow rate. The heat transfer coefficients at 345 kPa (50 psi) are the highest, followed by the heat transfer coefficients at 500 (72.5 psi) and 150 kPa (21.8 psi). (The lower solution heat transfer coefficient at 150 kPa (21.8 psi) may again be due to the use of the subcooler to obtain these data).

Figure 5.9 shows the effect of the absorber inlet pressure on the solution heat transfer coefficient at a nominal concentration of 25%. The heat transfer coefficients at all pressures are relatively close to each other. Except at the concentrated solution flow

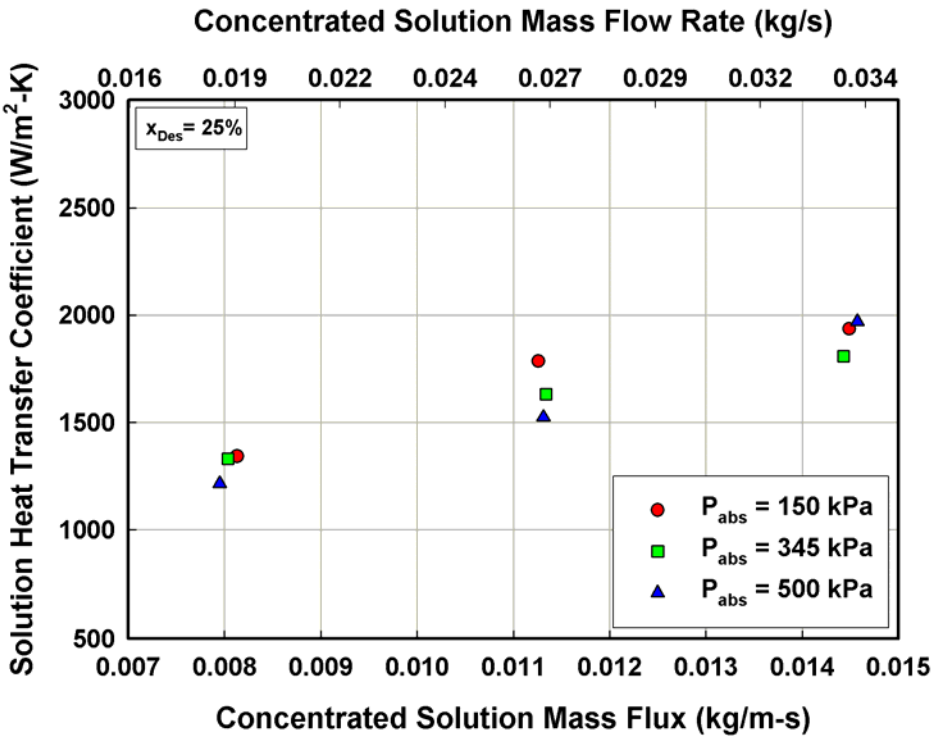

Figure 5.9 Effect of Absorber Pressure on Solution α at $x_{des,out}$ = 25%

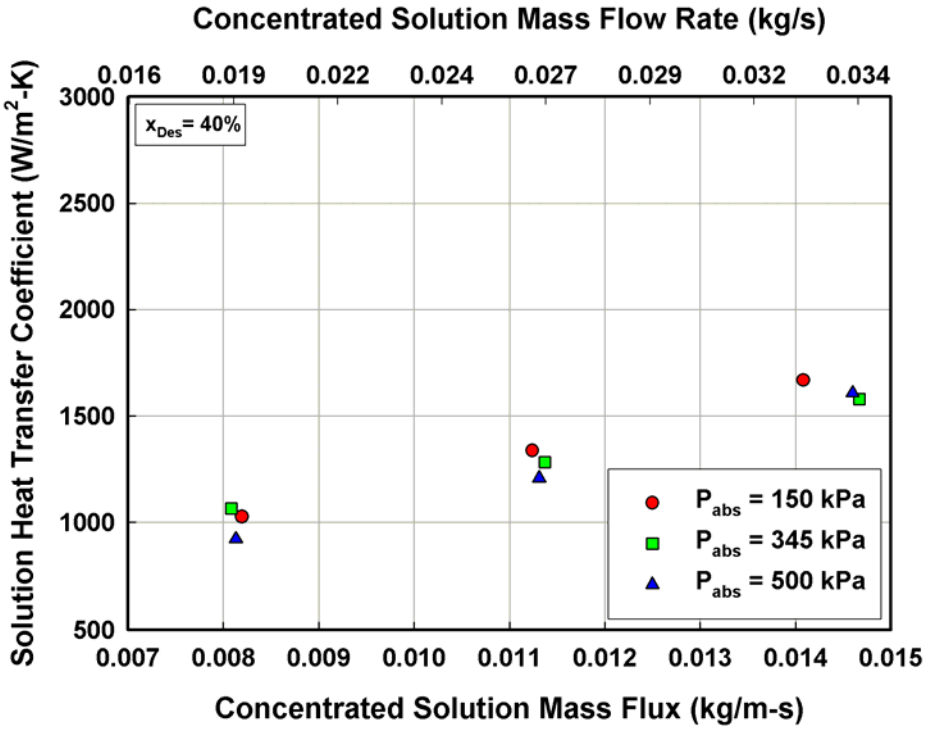

Figure 5.10 Effect of Absorber Pressure on Solution α at $x_{des,out}$ = 40%

rate of 0.034 kg/s (4.5 lb_m/min), the heat transfer coefficient decreases as the absorber pressure increases. At 0.034 kg/s (4.5 lb_m/min), the heat transfer coefficient is the highest for the absorber pressure of 500 kPa.

Figure 5.10 shows the effect of absorber inlet pressure on the solution heat transfer coefficient for a nominal dilute solution concentration of 40%. The heat transfer coefficients at all pressures are close to each other for a given concentrated solution flow rate. The heat transfer coefficients for 40% are smaller than those for 5%, 15%, and 25% concentration at all the absorber pressures.

5.1.6 Relevant Non-Dimensional Parameters

In this section, several non-dimensional parameters are discussed to assist in the interpretation of the heat transfer results and to compare the present results with the literature. These parameters are also used for the development of a heat transfer correlation. In the previous section, film heat transfer coefficients were presented as a function of the normalized concentrated solution flow rate. The effects of dilute solution concentration and absorber pressure on the heat transfer coefficients were discussed. Both the normalized concentrated solution flow rate and the heat transfer coefficient are non-dimensionalized here to obtain the Reynolds and Nusselt numbers of the solution, respectively.

A solution Reynolds number (Re_l) is defined using the normalized concentrated solution flow rate Γ_l and the dynamic viscosity of the solution as follows:

$$\mathrm{Re}_l = \frac{4 \times \Gamma_l}{\mu_l} \tag{5.1}$$

where $\Gamma_l = \dfrac{\dot{m}_l}{N_{t,pr} \cdot L_t \cdot 2}$, and $\dot{m}_l$ is the average (of the inlet and outlet) solution mass flow rate, $N_{t,pr}$ is the number of tubes in each row of the tube array, and L_t is the length of the tubes. The solution flow rate is divided by 2 because the solution flows on two sides of the tubes. The solution Prandtl number (Pr_l) is defined as follows:

$$\mathrm{Pr}_l = \frac{\mu_l \cdot C_{p,l}}{k_l} \tag{5.2}$$

Here, $C_{p,l}$ is the specific heat capacity, and k_l is the thermal conductivity of the solution. The solution heat transfer coefficient is non-dimensionalized to obtain the solution Nusselt number as follows:

$$Nu_l = \frac{\alpha_l \cdot \delta_l}{k_l} \tag{5.3}$$

Here, to define a solution Nusselt number (Nu_l), the solution film thickness is used as the characteristic dimension. The solution film thickness is the preferred characteristic

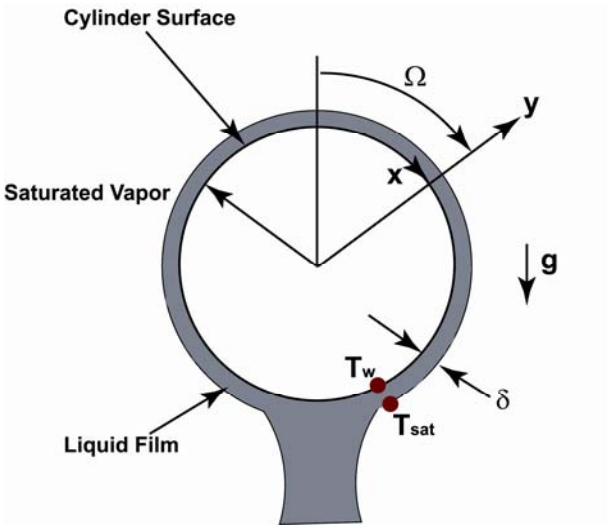

Figure 5.11 Solution Film Thickness on a Horizontal Cylindrical Tube

dimension in falling-film flow. The Nusselt condensation film thickness definition (Bird *et al.*, 2002) is used in this study for the solution film thickness. Figure 5.11 shows a schematic of the falling-film on a horizontal tube. As can be seen in this figure, the component of gravitational body force acting tangential to the surface is expressed as $g \sin\Omega$, since the tube has a cylindrical geometry. Using a no slip condition at the wall, the velocity profile can be obtained as follows:

$$u = \frac{(\rho_l - \rho_v) \cdot g \cdot \sin\Omega}{\mu_l} \left(y \cdot \delta_l - \frac{y^2}{2} \right) \tag{5.4}$$

Here, ρ_l and ρ_v are the densities of the solution and vapor, respectively, y is the distance along the transverse coordinate, and δ_l is the solution film thickness. The mass flow rate per unit width of the surface can be obtained by integrating the above velocity profile across the film.

$$\dot{m}_l = \rho_l \cdot \int_0^{\delta_l} u \, dy = \frac{\rho_l (\rho_l - \rho_v) \cdot \delta_l^3 \cdot g \cdot \sin\Omega}{3 \cdot \mu_l} \tag{5.5}$$

The average Nusselt condensation film thickness over the horizontal cylinder is then obtained using a mass balance across the film. Since the solution flows on the two sides of the cylinder, to obtain the average film thickness, the above equation is integrated from 0 to $\pi/2$.

$$\delta_l = \left[\frac{3 \cdot \mu_l \cdot \Gamma_l}{g \cdot \rho_l^2} \right]^{1/3} \cdot \frac{2}{\pi} \cdot \int_0^{\pi/2} \sin^{-1/3}\Omega \cdot d\Omega \tag{5.6}$$

$$\delta_l = \left[\frac{3 \cdot \mu_l^2 \cdot \mathrm{Re}_l}{4 \cdot g \cdot \rho_l^2} \right]^{1/3} \cdot \frac{2}{\pi} \cdot (2.10327) \tag{5.7}$$

Once the film thickness is obtained, the solution Nu_l can be obtained using the solution heat transfer coefficient, the solution thermal conductivity, and the film thickness.

5.1.7 Comparison with Literature

There are very few studies in the literature that provide correlations for Nu_l in the horizontal tube falling-film configuration for ammonia-water absorption. The available correlations with any relevance to the present study are used here for comparison

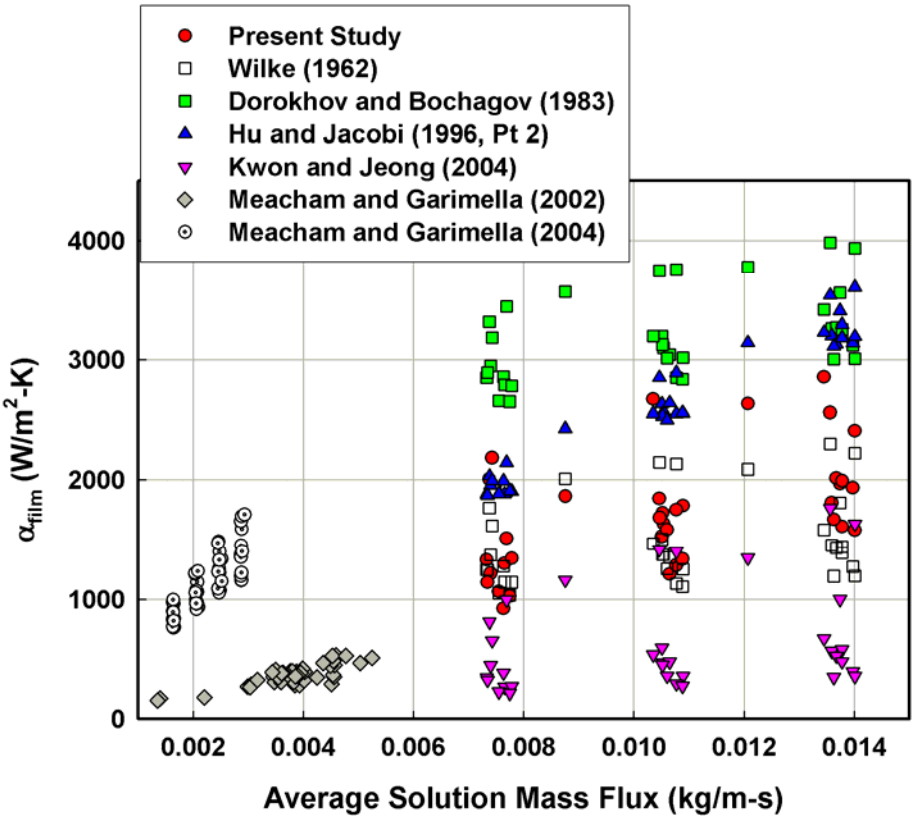

Figure 5.12 Comparison of Overall Solution Film Heat Transfer Coefficients with the Literature

with the present data. It should be noted that these studies use different definitions for some of the parameters such as the solution *Re*, mass flux and the film thickness. The differences in these definitions were appropriately accounted for while using these correlations to predict the present data. To avoid confusion due to the different

definitions, the falling-film heat transfer coefficients from this study, rather than the Nusselt numbers, are compared with the predictions from the literature.

Figure 5.12 shows a comparison of the heat transfer coefficients obtained in the present study with the predictions from Wilke (1962), Dorokhov and Bochagov (1983), Hu and Jacobi (1996b), Kwon and Jeong (2004), and the data of Meacham and Garimella (2002a; 2004). A summary of the correlations is provided in Table 5.1. It should be noted that none of these correlations was developed for a falling-film tube absorber in an ammonia-water system (except for the data of Meacham and Garimella, which were on horizontal tube banks with tubes of 1.575 mm O.D.). Wilke (1962) developed Nusselt number correlations for the flow of a water-glycol mixture over a vertical tube (42 mm O.D. and 2.4 m long) for different ranges of the solution Reynolds number ($Re_l < 400$; $400 < Re_l < 800$; $Re_l > 800$). It can be seen that this correlation shows reasonable agreement with the present data. The disagreement between his predictions and the present data may be due to the differences in geometry and the range of Reynolds numbers. For most of the data from the present study, the solution *Re* is less than 100. Also, his study did not involve any gas absorption and was simply a study of single-phase heat transfer in a falling film. Dorokhov and Bochagov (1983) developed a *Nu* correlation as a function of the solution Peclet number ($Pe_l = \mathrm{Re}_l \cdot \mathrm{Pr}_l$), film thickness and a characteristic length (half of the tube periphery in the case of a cylindrical tube) for the flow of water/LiBr (57% LiBr by weight) over a column of six horizontal tubes, where the heat duties were measured only for the last two tubes.

Table 5.1 Summary of Relevant Heat Transfer Studies

	Type and Fluid	Mass Transfer /Phase Change	Geometry	Test Conditions	Γ_l (kg/m–s)	Film Thickness δ (m)	Re_l	Nu_l	Applicability
Wilke (1962)	Vertical Tube (H_2O/ Glycol mixture)	No	Tube Length: 2.5 m Tube OD: 42	Water /Glycol 0, 16%, 55.5%, 77.1%, 95% (%Glycol)	$\frac{\dot{m}}{N_{tube} \cdot L_{tube} \cdot 2}$	$\left[\frac{3 \cdot \mu_l \cdot \Gamma_l}{g \cdot \rho_l^2}\right]^{1/3} \cdot \frac{2}{\pi} \int_0^{\pi/2} \sin^{-1/3}\Omega \cdot d\Omega$	$\frac{\Gamma}{\mu}$	$0.0614 \cdot Re^{8/15} Pr^{0.344}$ $0.00112 \cdot Re^{6/5} Pr^{0.344}$ $0.0066 \cdot Re^{14/15} Pr^{0.344}$	Re < 400 400 < Re < 800 Re > 800
Dorokhov and Bochagov (1983)	Horizontal Tube (H_2O/ LiBr)	Yes	Tube OD:19 Tube Length: 240 Tube Spacing: 28.12	57% LiBr Pressure: –10 kPa Flow Rate: 0.05 – 0.25 kg/m–s	$\frac{\dot{m}}{N_{tube} \cdot L_{tube} \cdot 2}$	$\left[\frac{3 \cdot \mu_l \cdot \Gamma_l}{g \cdot \rho_l^2}\right]^{1/3} \cdot \frac{2}{\pi} \int_0^{\pi/2} \sin^{-1/3}\Omega \cdot d\Omega$	$\frac{\Gamma}{\mu}$	$1.03 \cdot \left(2 \cdot Pe \cdot \delta / \pi \cdot d_{o,t}\right)^{0.44}$	$1 < 2 \cdot Pe \cdot \delta / \pi \cdot d_{o,t} < 20$
Hu and Jacobi (1996b)	Horizontal Tube (H_2O and Glycol and mixtures)	No	Tube OD:15.88, 19.05, 22.22 Tube Spacing: 5–50 Groove Depth : 0.51, 0.76 Groove Width : 2.54, 0.81	Flow Rate: – 0.72 kg/m–s T_{in}: 20–40°C Heat Flux: -1.15×10^5 W/m^2	$\frac{\dot{m}}{N_{tube} \cdot L_{tube}}$	$\delta = \left(\frac{\nu^2}{g}\right)^{1/3}$, $Ar = \frac{d_{o,t}^3 \cdot g}{\nu^2}$	$\frac{2\Gamma}{\mu}$	$2.194 \cdot Re^{0.28} Pr^{0.14} Ar^{-0.20} (s/d_{o,t})^{0.07}$	Sheet Mode
								$1.387 \cdot Re^{0.42} Pr^{0.26} Ar^{-0.23} (s/d_{o,t})^{0.08}$	Jet Mode
								$0.113 \cdot Re^{0.85} Pr^{0.85} Ar^{-0.27} (s/d_{o,t})^{0.04}$	Droplet mode
Meacham and Garimella (2002a)	Horizontal Tube Micro–channel (NH_3 /H_2O)	Yes	Tube OD:1.575 Tube Length: 0.14 m Tube Pitch : 4.76 Tube Row Vertical Pitch: 4.76 Tubes per Row: 27 Rows per Pass: 16 Number of Passes: 5 Height: 0.508 m Absorber Area: 1.50 m^2	Solution FR: 0.010 – 0.040 kg/s Vapor Generation Fraction: 10 – 50% x_{vapor}= 0.8697 $x_{concentraed}$ = 0.3807 x_{dilute} = 0.2289	$\frac{\dot{m}}{N_{tube} \cdot L_{tube}}$	$\left[\frac{3 \cdot \mu_l \cdot \Gamma_l}{g \cdot \rho_l^2}\right]^{1/3} \cdot \frac{2}{\pi} \int_0^{\pi/2} \sin^{-1/3}\Omega \cdot d\Omega$	$\frac{4\Gamma}{\mu}$		
Meacham and Garimella (2004)	Horizontal Tube Micro–channel (NH_3 /H_2O)	Yes	Tube OD:1.575 Tube Length: 0.137 m Tube Pitch: 7.94 Tube Row Vertical Pitch: 7.94 Tubes per Row: 33 Rows per pass: 2 Number of Passes: 10 Height: 0.15 m	Solution FR: 1.51×10^{-2}– 2.66×10^{-2} kg/s Vapor Fraction: 15%, 20%, 25%, 30% x_{vapor}= 0.93–0.98 T_{in} and (Pressure) 52°C (355 kPa) 81°C (680 kPa)	$\frac{\dot{m}}{N_{tube} \cdot L_{tube}}$	$\left[\frac{3 \cdot \mu_l \cdot \Gamma_l}{g \cdot \rho_l^2}\right]^{1/3} \cdot \frac{2}{\pi} \int_0^{\pi/2} \sin^{-1/3}\Omega \cdot d\Omega$	$\frac{4\Gamma}{\mu}$		

Table 5.1 Summary of Relevant Heat Transfer Studies (Continued)

	Type and Fluid	Mass Transfer /Phase Change	Geometry	Test Conditions	Γ_l (kg/m–s)	Film Thickness δ (m)	Re_l	Nu_l	Applicability
			Absorber Area: $0.45m^2$						
Kwon and Jeong (2004)	Helical Coil (NH_3/ H_2O)	Yes	OD: 12.7 L_{abs}: 600 Coil OD: 82.7 Coil Windings: 30	Solution Flow Rate 4.43–90.0 g/s–m x_{dilute} = 3.13%, 14%, 30% T_{in} = 45 °C, 55 °C, 60 °C $T_{Coolant}$ = 30°C P = 0.17–1.93 bar	$\frac{\dot{m}}{N_{tube} \cdot L_{tube}}$	$\delta = \left(\frac{\nu^2}{g}\right)^{1/3}$	$\frac{2\Gamma}{\mu}$	$1.975 \times 10^{-3} \cdot Re^{0.6895}\ \tau^{-0.0249}$	Parallel Flow 10 < Re < 250
								$1.683 \times 10^{-4} \cdot Re^{0.8672}\ \tau^{-0.3018}$	Counter Flow 10 < Re < 250

Their correlation predicts much higher values of heat transfer coefficients compared to the data from the present study. The disagreement between their predictions and the present data may be due to the very small absorber pressures (~10 kPa) characteristic of LiBr-H_2O systems and the higher solution mass flux in their study. It should be also noted that LiBr-H_2O is a fluid pair with a non-volatile absorbent whereas NH_3-H_2O has a volatile absorbent. Their solution mass flux varies between 0.05 and 0.25 kg/m-s, which is significantly higher than the highest mass flux (0.015 kg/m-s) in the present study. In addition, their correlation is valid for $1 < 2 \cdot Pe_l \cdot \delta_l / (\pi \cdot d) < 20$; and the data from the present study are towards the lower limit ($2 \cdot Pe_l \cdot \delta_l / (\pi \cdot d) \sim 1$) of the validity of their correlation. Hu and Jacobi (1996b) developed Nu correlations using Re_l, Pr_l, Archimedes number ($Ar_l = \left(\sigma_l^3 \middle/ \left(\nu^4 \cdot \rho^2 \cdot g \cdot (\rho_l - \rho_v) \right) \right)^{1/2}$), tube spacing, and the tube diameter as the parameters for the flow of a Water/Glycol mixture and several other fluids on a horizontal tube. Different flow regimes were defined based on the modified Galileo number ($Ga_l = \left(\rho_l \cdot \sigma_l^3 \right) \middle/ \left(\mu_l^4 \cdot g \right)$). All the data from the present study fall under the droplet flow regime according to their flow regime map. Therefore, the correlation developed for the droplet mode is used here to predict the film heat transfer coefficient from the present study. Their correlation also predicts higher heat transfer coefficients for the range of conditions tested in the present study. The higher predictions of the heat transfer coefficient may be due to the different film thickness definition used by them. This definition, $\delta = \left(\frac{\nu^2}{g} \right)^{1/3}$, makes the film thickness independent of the solution flow rate. In addition, their correlation does not account for gas absorption and is only for single-phase heat transfer in films falling around horizontal tubes. Kwon and Jeong (2004)

developed Nu_l correlations for a helical coil absorber used in ammonia/water absorption for both counter-current and parallel flow arrangements using the solution Re and liquid-vapor interfacial shear stress ratio. They used a 12.7 mm diameter tube coiled over an 82.7 mm diameter for this study. The absorber was 600 mm long with a shell diameter of 114 mm. The solution mass flux varied from 4.43×10^{-3} kg/m-s to 90.9×10^{-3} kg/m-s at dilute solution concentrations of 3.13%, 14% and 30.0%. They noted that Nu_l is primarily affected by the solution *Re* and the effect of liquid-vapor interfacial shear stress can be neglected in the parallel flow arrangement. As can be seen in Figure 5.12, their correlation predicts much smaller solution heat transfer coefficients than the present values. This may be due to the different driving temperature differences used in the two studies. Their solution temperatures are close to saturation temperatures corresponding to the absorber pressure and solution concentrations in their study, while the solution is considerably sub-cooled in the present study. The disagreement is more pronounced for the extreme concentration conditions (5% and 40%). This is probably due to the higher uncertainty of their correlation at lower concentrations (as they reported higher uncertainties for the 3% solution concentration cases), and the limited applicability at dilute solution concentrations higher than 30% (as the highest dilute solution concentration is 30% in their study). In addition, the absorber pressures are also low (17 - 193 kPa) in their study compared to the range 170 – 520 kPa in the present study. Meacham and Garimella (2002a) conducted absorption experiments on a micro-channel falling-film absorber. The absorber geometry consists of short lengths (14 mm) of microchannel tubes (1.575 mm O.D.) arranged in a square array. These tubes were arranged in 5 passes, where each pass consists of 16 tube rows. Each of the tube rows

had 27 tubes in it. The total surface area of the absorber was 1.5 m^2. Their solution mass flux varied in the range 0.0014 – 0.0053 kg/m-s and the vapor concentration varied in the range 5 – 50%. The average absorber heat duties transferred were 4.86 - 16.23 kW with solution heat transfer coefficients of 155 - 530 W/m^2-K (corrected here for the difference in the LMTD definitions used in the two studies). The data of Meacham and Garimella (2002a) show much smaller experimental heat transfer coefficients; however, it should be kept in mind that the mass fluxes in their study are much smaller than those in the present study. This is because, although the mass flow rates used by them were similar (0.010 to 0.040 kg/s) to those in the present study (0.019-0.034 kg/s), the solution was distributed over 27 tubes, 0.140 m long for a total length of 3.78 m, whereas in the present study the total tube length per row was 1.17 m. The data of Meacham and Garimella (2004) show much higher film heat transfer coefficients compared to the results from their previous study (Meacham and Garimella, 2002a). The increase was attributed to significant improvement in the solution distribution over the tube array. It can also be seen that their newer data have heat transfer coefficients comparable to those from the present study even at much smaller solution mass fluxes. The differences between their experimental values and the present data may be due to the microchannel geometry used by them.

5.2 Overall Mass Transfer Results in Vapor-Phase

This section discusses the results for the overall mass transfer coefficient in the vapor phase. The calculation methodology was described in the previous chapter. For the presentation of the results, the concentrated solution flow rates are shown in terms of the linear mass flux based on the tube length. In the discussion of the trends, however,

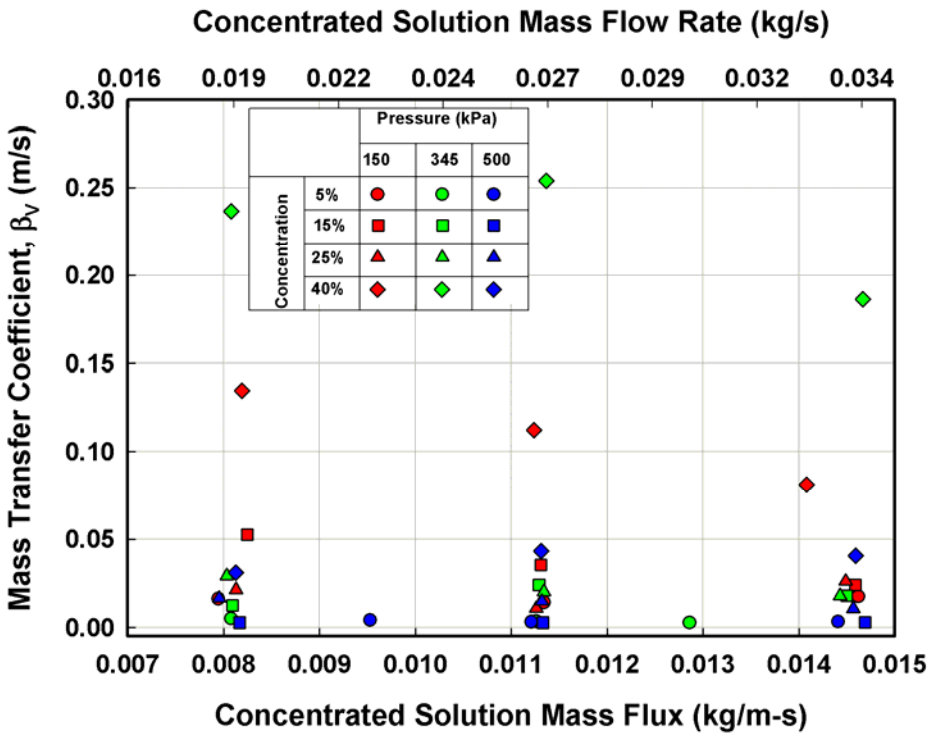

Figure 5.13 Variation of Overall Vapor Mass Transfer Coefficient with Solution Flow Rate

the flow rate in lb_m/min or kg/s is used for ease of comprehension.

5.2.1 Mass Transfer Coefficient

Figure 5.13 shows the variation of the overall mass transfer coefficient in the absorber. For the range of experiments conducted, the mass transfer coefficient varies between 0.0025 m/s and 0.26 m/s. The highest mass transfer coefficient is observed for 40% at 345 kPa (50 psi), while the smallest value is observed for 15% at 500 kPa. It is found that higher mass transfer coefficients at any pressure are obtained as the dilute solution concentration increases. It is also found that the mass transfer coefficient is not very sensitive to the concentrated solution flow rate.

5.2.2 *Effect of Dilute Solution Concentration*

Figures 5.14 - 5.16 show the variation in the mass transfer coefficient with the concentrated solution flow rate for a given absorber pressure. In general, the mass transfer coefficient does not change appreciably as the concentrated solution flow rate increases. This trend is different from that for the heat transfer coefficient, where the heat transfer coefficient increases monotonously with an increase in concentrated solution flow rate. At 150 and 345 kPa, as seen in Figures 5.14 and 5.15 respectively, the 40% concentration cases have significantly higher mass transfer coefficients than those for the other concentrations. However, the effect of concentration at 500 kPa (Figures 5.16) is less pronounced than those at other pressures. These different trends in mass transfer coefficient can be attributed in part to the use of different inlet conditions and driving

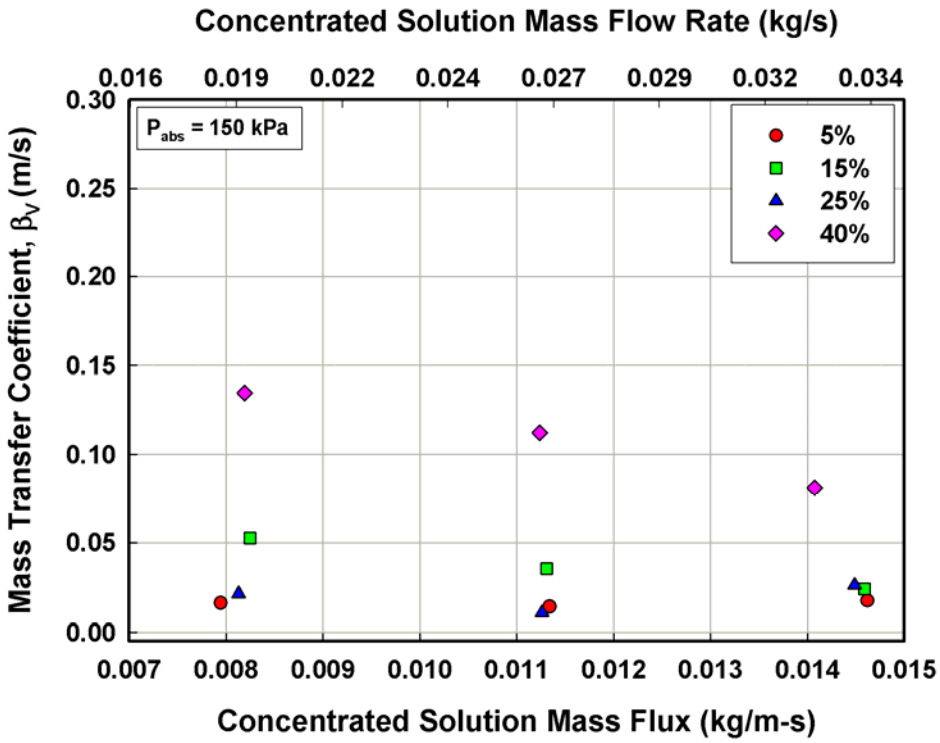

Figure 5.14 Effect of Dilute Solution Concentration on β_V at P_{abs}=150 kPa (21.8 psi)

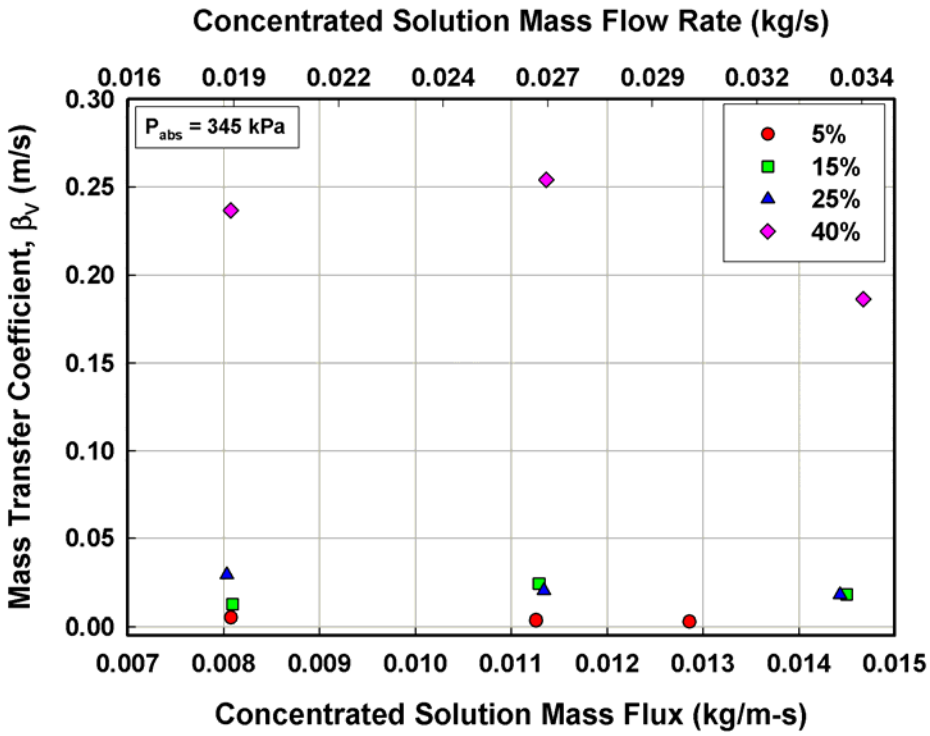

Figure 5.15 Effect of Dilute Solution Concentration on β_V at P_{abs}=345 kPa (50 psi)

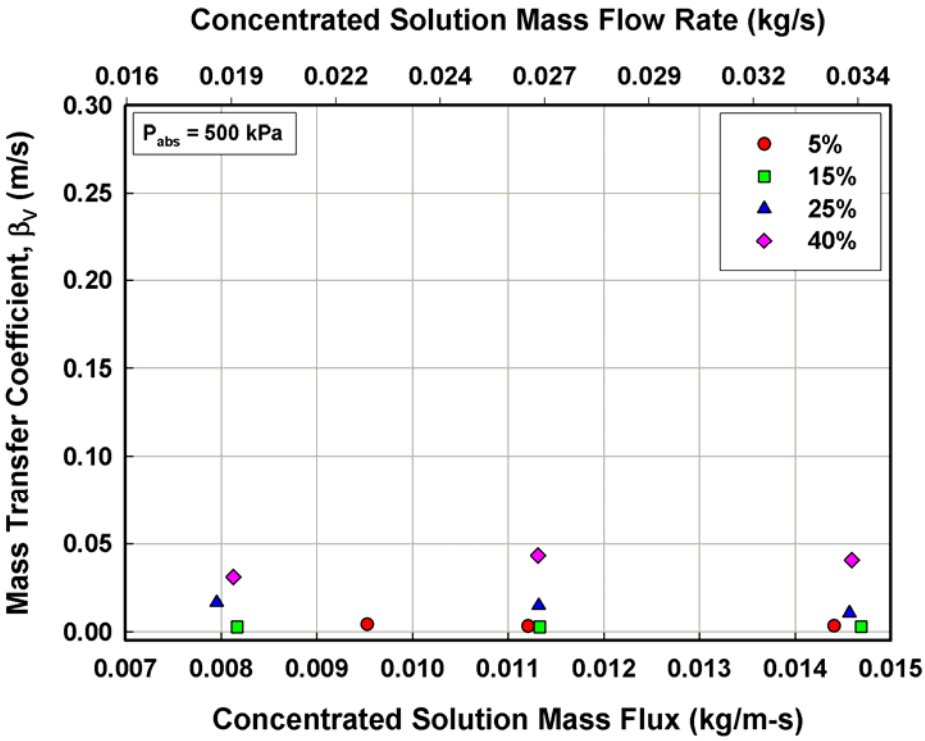

Figure 5.16 Effect of Dilute Solution Concentration on β_V at P_{abs}=500 kPa (72.5 psi)

potential differences that had to be maintained to achieve these vastly different state points. Differences in coolant flow rates, coolant temperatures, degree of sub-cooling, and refrigerant mass flow rates all contribute simultaneously to these changes in mass transfer coefficient. Figure 5.14 shows the mass transfer coefficient at an absorber pressure of 150 kPa (21.8 psi). The mass transfer coefficient decreases for the 15% and 40% cases as the concentrated solution flow rate increases. For the 5% and 25% cases, however, the 0.026 kg/s (3.5 lb_m/min) flow rate shows relatively smaller mass transfer coefficients. At any given flow rate, except for the 25% cases, the mass transfer coefficient increases as the dilute solution concentration increases. This is attributed to the fact that the vapor concentration increases as the dilute solution concentration increases. It should, however, be kept in mind that the 40% cases were actually tested at relatively higher absorber pressures of about 240 kPa (35 psi) than the nominal pressure and involved a significant amount of sub-cooling to enable the lower absorber pressure.

Figure 5.15 shows the mass transfer coefficients at an absorber pressure of 345 kPa (50 psi). Again, the mass transfer coefficients for the 40% dilute solution concentration are higher than those at other pressures. For the other concentrations, the much lower mass transfer coefficients also do not show an appreciable dependence on the solution flow rate.

Figure 5.16 shows mass transfer coefficients at an absorber pressure of 500 kPa (72.5 psi). As opposed to the trends observed at the 150 and 345 kPa absorber pressure cases, the dependence on solution concentration appears to be relatively small. Also, the mass transfer coefficients are relatively insensitive to the concentrated solution flow rate.

5.2.3 Effect of Absorber Pressure

Figures 5.17 - 5.20 show the variation in the mass transfer coefficients with the concentrated solution flow rate for a given dilute solution concentration. As seen in the previous graphs, the concentrated solution flow rate does not seem to affect the mass transfer coefficient to any appreciable degree. As can be seen in Figures 5.17 and 5.18, for the 5% and 15% cases respectively, the mass transfer coefficient decreases as the absorber pressure increases. In Figures 5.19 and 5.20, for 25% and 40% cases, respectively, the mass transfer coefficient for any given flow rate is the highest at an absorber pressure of 345 kPa. By comparing Figure 5.17 and 5.20, it can also be seen that the mass transfer coefficients for the 5% dilute solution concentration cases at a given pressure are significantly smaller than those for the 40% dilute solution concentration. The mass transfer coefficients for the 5% and 25% cases do not show a significant dependence on the absorber pressure; however, the mass transfer coefficients for 15%, and especially the 40% cases show a significant dependence on the absorber pressure variation.

Some overall conclusions can be drawn from these graphs of the mass transfer coefficient variations. The relative insensitivity of the mass transfer coefficient to the solution flow rate implies that the mass transfer process is governed by the vapor-phase mass transfer resistance. Since in the present study, the vapor phase is essentially a quiescent medium in the absorption chamber, this trend is as expected. The relatively large vapor-phase mass transfer resistance should not be influenced by the liquid-phase solution flow rate. The effect of pressure and concentration can be understood in terms of the respective phase properties and driving potentials.

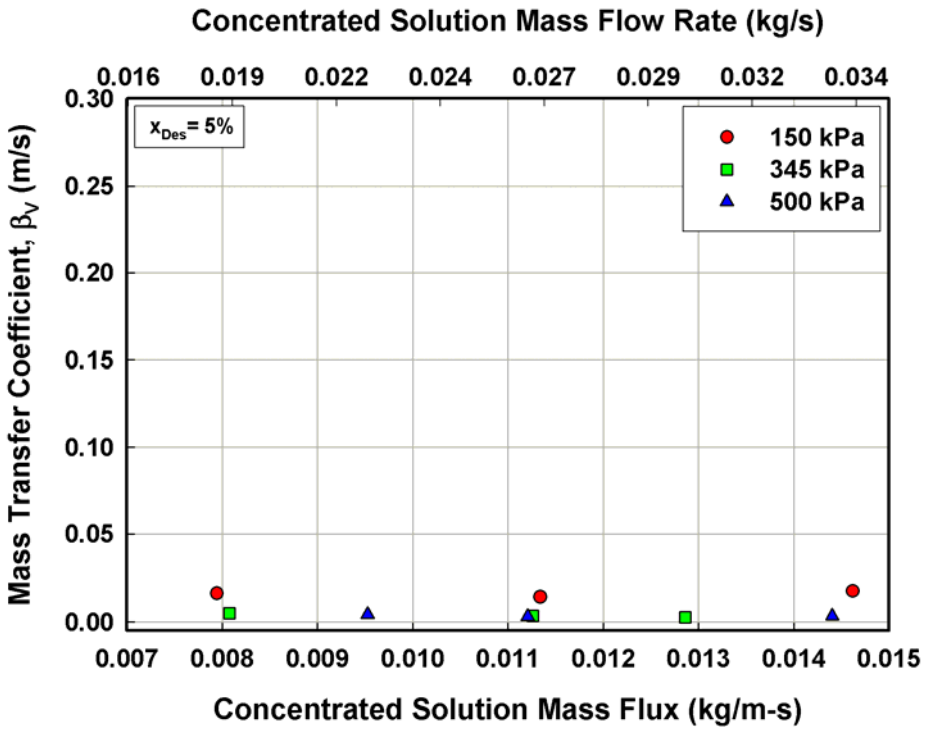

Figure 5.17 Effect of Absorber Pressure on β_V at $x_{des,out}$ = 5%

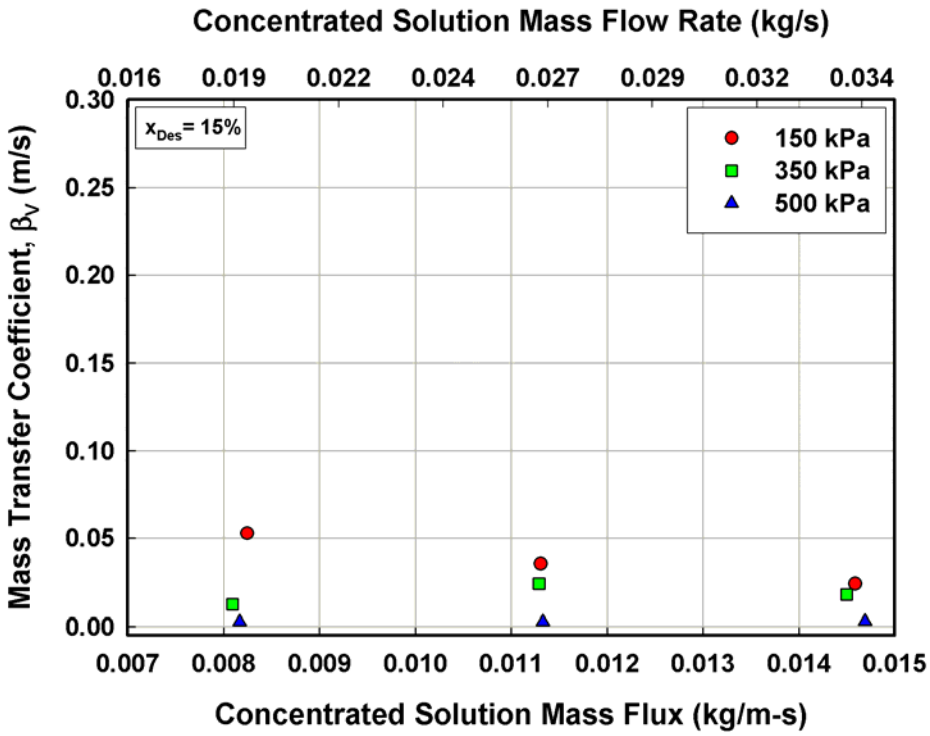

Figure 5.18 Effect of Absorber Pressure on β_V at $x_{des,out}$ = 15%

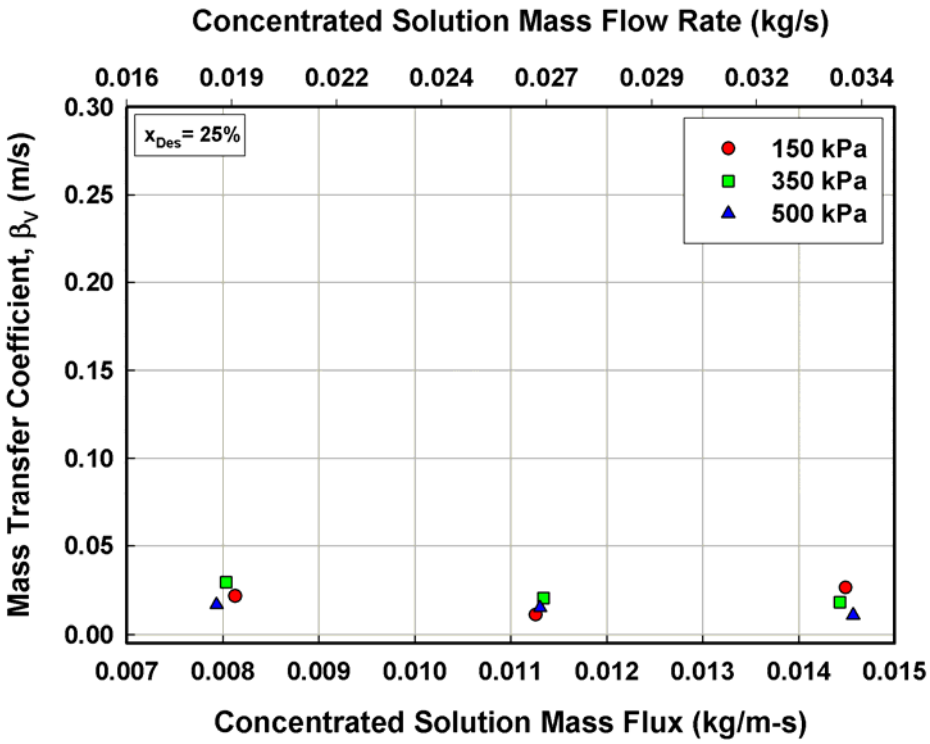

Figure 5.19 Effect of Absorber Pressure on β_V at $x_{des,out}$ = 25%

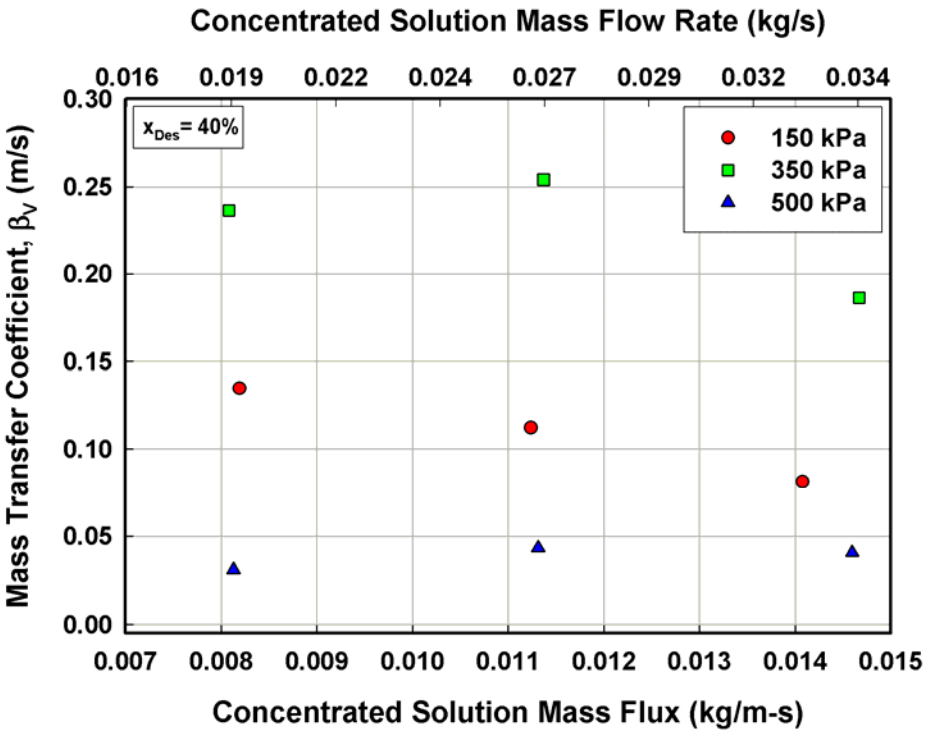

Figure 5.20 Effect of Absorber Pressure on β_V at $x_{des,out}$ = 40%

Table 5.2 shows the effect of variations of the absorber pressure, the dilute solution concentration and the concentrated solution flow rate on the mass transfer coefficient parametrically through the corresponding changes in vapor-phase properties. The table is divided into three distinct blocks according to the parameter being varied while keeping the other two constant. In each of the blocks, two extreme test conditions are shown with representative values of the various parameters. From a review of these blocks, it can be seen that the main parameters influencing the mass transfer coefficients are the bulk solution temperature, the bulk vapor temperature, the bulk vapor concentration, and the difference between the bulk vapor and the bulk solution concentration. For a constant absorber pressure (e.g. 345 kPa) and concentrated solution flow rate (e.g. 0.026 kg/s), the bulk solution temperature decreases from 78^{o}C to 27^{o}C, and the bulk vapor temperatures decreases from 65^{o}C to 18^{o}C, while the bulk vapor concentration increases from 95.6% to 99.9% as the dilute solution concentration increases from 17 to 41%. The lower bulk solution temperature results in higher liquid side Pr number (2.08 to 6.6 as the temperature decreases from 78^{o}C and 27^{o}C) and higher liquid side Sc number thereby facilitating the removal of the heat of absorption and transport of the mass absorbed. The higher bulk vapor concentration results in smaller vapor enthalpy (1477 kJ/kg-K to 1320 kJ/kg-K), again, presenting favorable conditions for the mass transfer; therefore the mass transfer coefficient increases from 0.003 m/s to 0.167 m/s with an increase in the dilute solution concentration (from 17% to 41%). As the absorber pressure increases from 150 to 500 kPa, the bulk solution temperature increases from 43^{o}C to 84^{o}C, and the bulk vapor temperature increases from 27^{o}C to 66^{o}C, while the bulk vapor concentration decreases from 99.1% to 96.9% at a given

dilute solution concentration (15% nominal) for a given concentrated solution flow rate (0.034 kg/s). The higher bulk solution temperature and lower bulk vapor concentration is an adverse condition for mass transfer; therefore, the mass transfer coefficient decreases from 0.017 m/s to 0.002 m/s as the absorber pressure increases (from 150 to 500 kPa). The change in the viscosity and the specific heat of the vapor are counter-acted by the change in the conductivity of the vapor (a constant Prandtl number), so these properties may not have a significant effect on the mass transfer coefficient as the absorber pressure varies. Finally, for a constant absorber pressure (e.g. 500 kPa) and a constant dilute solution concentration (e.g. nominal 15%), it is seen that all the properties remain constant. Therefore, no significant effect of the concentrated solution flow rate on mass transfer is observed.

Table 5.2 Parametric Effect of Test Conditions on the Mass Transfer Coefficient in the Vapor–Phase

	Controlled Parameters			Affected Parameters									Dependent Parameter
Effect of	P_{abs} (kPa)	x_{dil} (%)	Flow Rate (kg/s)	$T_{l,bulk}$ (^{o}C)	$T_{v,bulk}$ (^{o}C)	$x_{v,bulk}$ (%)	$(x_{v,bulk}-x_{l,bulk})$ (%)	ρ_v (kg/m^3)	$C_{P,v}$ (kJ/kg–K)	k_v (W/m–K)	μ_v (kg/m–s)	$D_{aw,v}$ (m^2/s)	β_V (m/s)
Effect of Dilute Solution Concentration @ nominal Absorber Pressure = 350 kPa, Concentrated Solution Flowrate = 0.026 kg/s													
Concentration	↔	↑	↔	↓	↓	↑	↓	↑	↓	↓	↓	↓	↑
5%	365	17	0.026	78	65	95.6	75	2.28	2.37	0.033	1.19×10^{-05}	9.77×10^{-06}	0.003
40%	352	41	0.026	27	18	99.9	57	2.59	1.53	0.028	1.03×10^{-05}	7.691×10^{-06}	0.167
Effect of Absorber Pressure @ nominal Dilute Solution Concentration = 15%, Concentrated Solution Flowrate = 0.034 kg/s													
Pressure	↑	↔	↔	↑	↑	↓	↔	↑	↑	↑	↑	↓	↓
150 kPa	177	20	0.034	43	27	99.1	76	1.24	2. 20	0.029	1.06×10^{-05}	1.62×10^{-05}	0.017
500 kPa	486	17	0.034	84	66	96.9	78	3.05	2.35	0.033	1.2×10^{-05}	7.37×10^{-06}	0.002
Effect of Concentrated Solution Flowrate @ nominal Absorber Pressure = 500 kPa, Dilute Solution Concentration = 15%													
Flow Rate	↔	↔	↑	↔	↔	↔	↔	↔	↔	↔	↔	↔	↔
0.019 kg/s	481	16	0.019	81	62	97.4	78	3.05	2.45	0.033	1.18×10^{-05}	7.32×10^{-06}	0.002
0.034 kg/s	486	17	0.034	84	66	96.9	78	3.05	2.35	0.033	1.2×10^{-05}	7.37×10^{-06}	0.002

5.2.4 Relevant Non-Dimensional Parameters

Vapor-phase mass transport can be affected by several properties such as the viscosity, density, specific heat, and binary diffusion coefficient. To study the combined influence of these properties, they are arranged in the non-dimensional groups Prandtl number (Pr_v) and Schmidt number (Sc_v). These are defined as:

$$\mathrm{Pr}_v = \frac{\mu_v \cdot C_{p,v}}{k_v} \tag{5.8}$$

$$Sc_v = \frac{\mu_v}{\rho_v \cdot D_{aw}} \tag{5.9}$$

The vapor phase mass transfer coefficient is non-dimensionalized to obtain Sherwood number (Sh_v) as follows:

$$Sh_v = \frac{\beta_v \cdot d_{o,t}}{D_{aw,v}} \tag{5.10}$$

5.2.5 Comparison with Literature

There are again few studies in the literature that provide correlations for mass transfer in ammonia-water absorption. The mass transfer coefficients from this study are therefore compared with those obtained using a heat and mass transfer analogy and those reported by Onda *et al.* (1968). In general, the heat and mass transfer analogy is used to address the coupled heat and mass transfer process in analytical studies. However, the use of the heat and mass transfer analogy and correlations from the literature require the vapor-phase heat transfer coefficient, which in turn requires a vapor-phase Reynolds number (Re_v). Although due to the large absorption chamber occupied by the vapor in this study, no obvious definition of vapor-phase *Re* emerges, for the purpose of

comparison, $Re_{v,max}$ for the present study is defined based on the minimum flow area in the tube array along the solution flow path. The vapor velocity is calculated first as follows:

$$V_{v,frontal} = \frac{\dot{m}_{v,in}}{\rho_v \cdot A_{frontal}} \tag{5.11}$$

$$V_{v,effective} = \frac{A_{frontal}}{A_{free}} \cdot V_{v,frontal} \tag{5.12}$$

where $A_{frontal}$ is taken as the bottom area of the tube array and A_{free} is the area excluding the projected tube area of tubes $d_{o,t} \times L_t \times N_{t,pr}$. Also, $\dot{m}_{v,in}$ is the mass flow rate of the vapor-phase entering the absorber. Once the effective vapor velocity is obtained, the vapor-phase Re is calculated as follows:

$$\mathrm{Re}_{v,\max} = \frac{\rho_v \times V_{v,effective} \times d_{o,t}}{\mu_v} \tag{5.13}$$

The vapor-phase Sh_v is calculated from the heat and mass transfer analogy, where the heat transfer coefficient is estimated using the correlation of Churchill and Bernstein (1977) for cross flow over cylinders.

$$Sh_v = \frac{\beta_v \cdot d_{o,t}}{D_{aw,v}} = Nu_v \cdot \left(\frac{Sc_v}{\mathrm{Pr}_v} \right)^{1/3} \tag{5.14}$$

$$Nu_v = 0.3 + \frac{0.62 \cdot \mathrm{Re}_{effective,v}^{1/2} \cdot \mathrm{Pr}_v^{1/3}}{\left[1 + \left(0.4/\mathrm{Pr}_v \right)^{2/3} \right]^{1/4}}; \qquad \mathrm{Re}_{effective,v} < 10^4 \tag{5.15}$$

Onda et al. (1968) developed a correlation for mass transfer coefficient between gas and liquid phases in packed columns during gas absorption and desorption. The packed column used various random packings, such as Raschig rings and Berl Saddels,

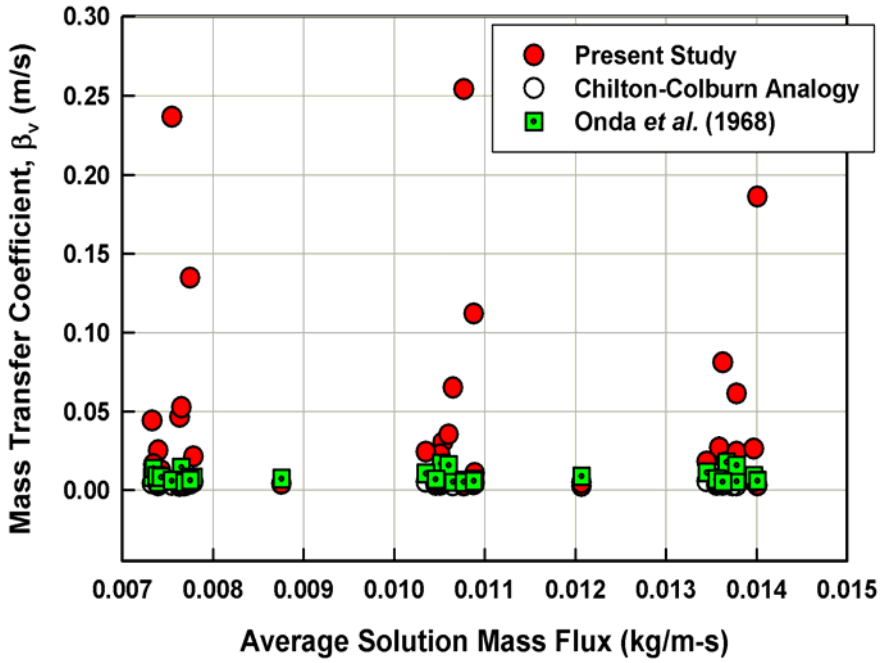

Figure 5.21 Comparison of Overall Vapor Mass Transfer Coefficients with the Literature

with a nominal size of 6 – 50 mm. The liquid-side mass transfer correlation was developed for gas absorption and desorption with water and organic solvents such as methanol and carbon tetrachloride, while the gas-side mass transfer correlation was developed for gas absorption and vaporization with an air-water system. Again, solely for the purpose of comparison, the tube array under consideration is approximated to be analogous to the metal Raschig rings investigated by Onda *et al* (1968).

$$Sh_v = \frac{\beta_v}{D_{aw,v} \cdot a} = 2.0 \cdot \left(a \cdot d_{o,t}\right)^{-2.0} \cdot \mathrm{Re}_{effective,v}{}^{0.7} \cdot \mathrm{Pr}_v^{1/3} \tag{5.16}$$

where a (m^2/m^3) is the inverse of the characteristic length of the packing. The characteristic lengths for various commercial packings are tabulated in Mills (1995) for different sizes. From these values, the characteristic length was approximated using a curve-fit for the tube size of the present study.

Figure 5.21 shows a comparison of β_v obtained from the data, the heat and mass transfer analogy, and from the correlation of Onda *et al.* (1968). As seen in Figure 5.21, the mass transfer coefficients from the heat and mass transfer analogy and Onda *et al.* (1968) are significantly lower compared with the data from present study. The discrepancies may be due to an inadequate definition of vapor *Re* for the sake of comparison, because the vapor is essentially deemed to be quiescent in the present study. The predictions of Onda *et al.* (1968) can also differ from the data from the present study due to differences in geometry and the fluids investigated in their study. It is also seen that the predicted mass transfer coefficients are relatively similar for all the data and do not show appreciable effects of absorber pressure or dilute solution concentration. Therefore, it may be necessary to study the influence of vapor and liquid-phase properties and develop correlations in terms of property changes.

5.3 Overall Mass Transfer Results in Liquid-phase

This section discusses the mass transfer coefficients in the liquid-phase obtained from the current study.

5.3.1 Mass Transfer Coefficient

Figure 5.22 shows the variation of the overall mass transfer coefficient in the liquid-phase. Effects of pressure and concentration can be seen in this figure; however, the concentrated solution flow rate does not appreciably affect the mass transfer coefficients in the liquid-phase except for the cases with a pressure of 500 kPa and a concentration of 40%. For the conditions investigated, the mass transfer coefficient varies between 5.51×10^{-6} m/s and 3.31×10^{-5} m/s. The highest mass transfer coefficient is

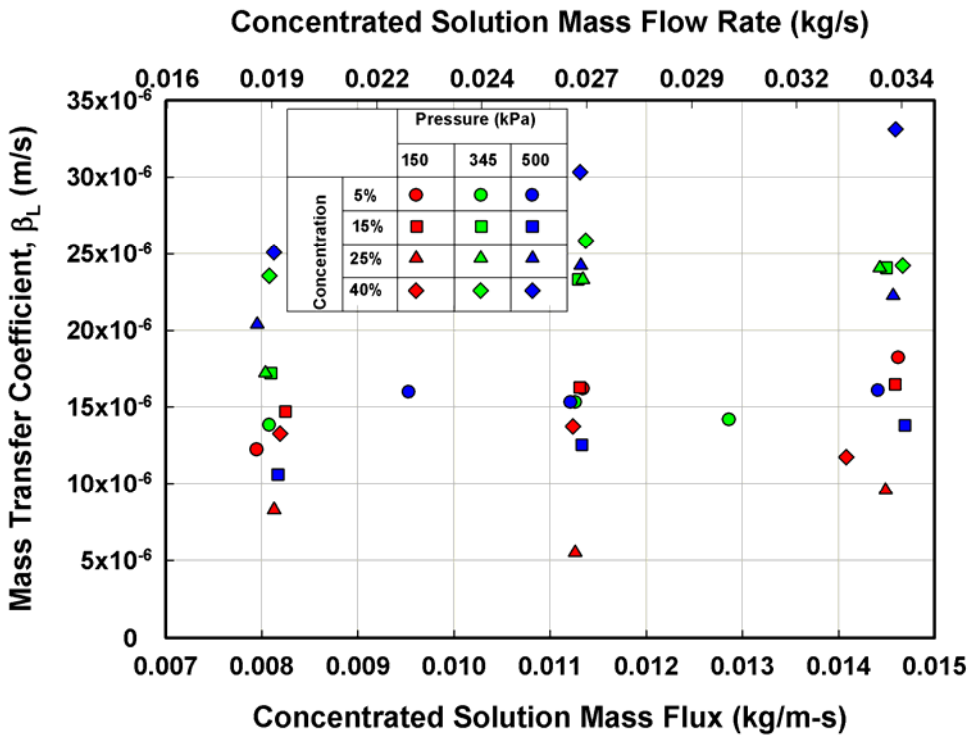

Figure 5.22 Variation of Overall Liquid Mass Transfer Coefficient with Solution Flow Rate

observed for 40% at 500 kPa (72 psi), while the smallest value is observed for 25% at 150 kPa.

5.3.2 Effect of Dilute Solution Concentration

Figures 5.23 - 5.25 show the effect of solution concentration on mass transfer coefficients in the liquid-phase at different absorber pressures. Higher mass transfer coefficients are obtained as the dilute solution concentration increases at a pressure of 500 kPa. Mass transfer coefficients increase with an increase in concentration at high pressures. However, mass transfer coefficients in the liquid phase are not sensitive to the concentrated solution flow rate.

As seen in Figure 5.23 at 150 kPa, the 25% concentration cases have significantly lower mass transfer coefficients than those at other concentrations. It should be kept in

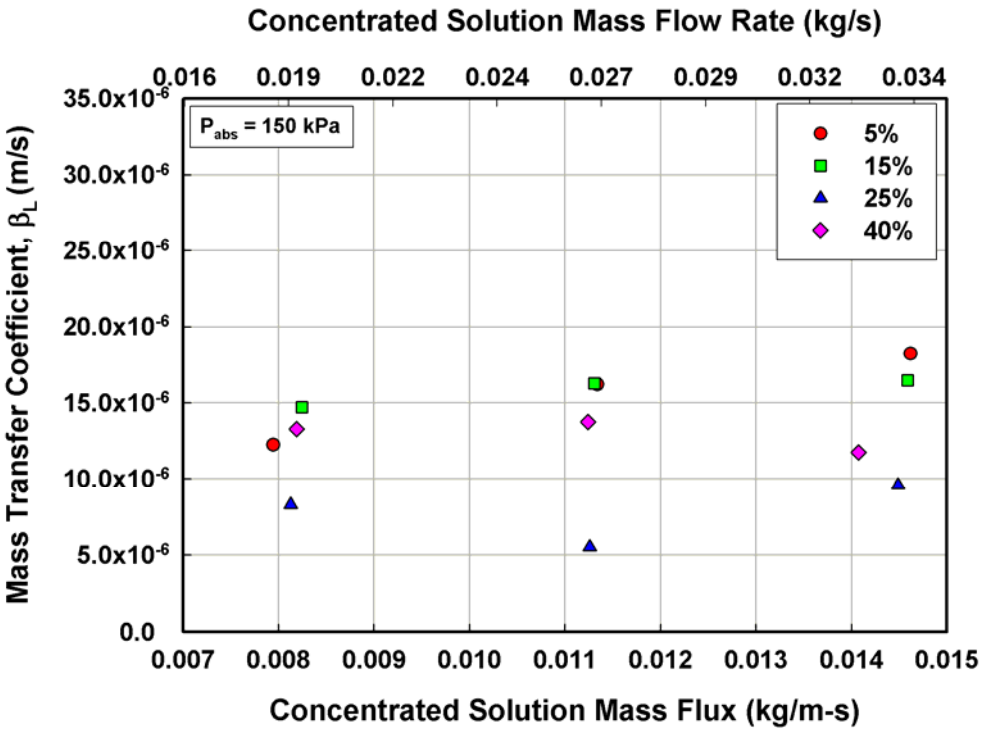

Figure 5.23 Effect of Dilute Solution Concentration on β_L at P_{abs}=150 kPa (21.8 psi)

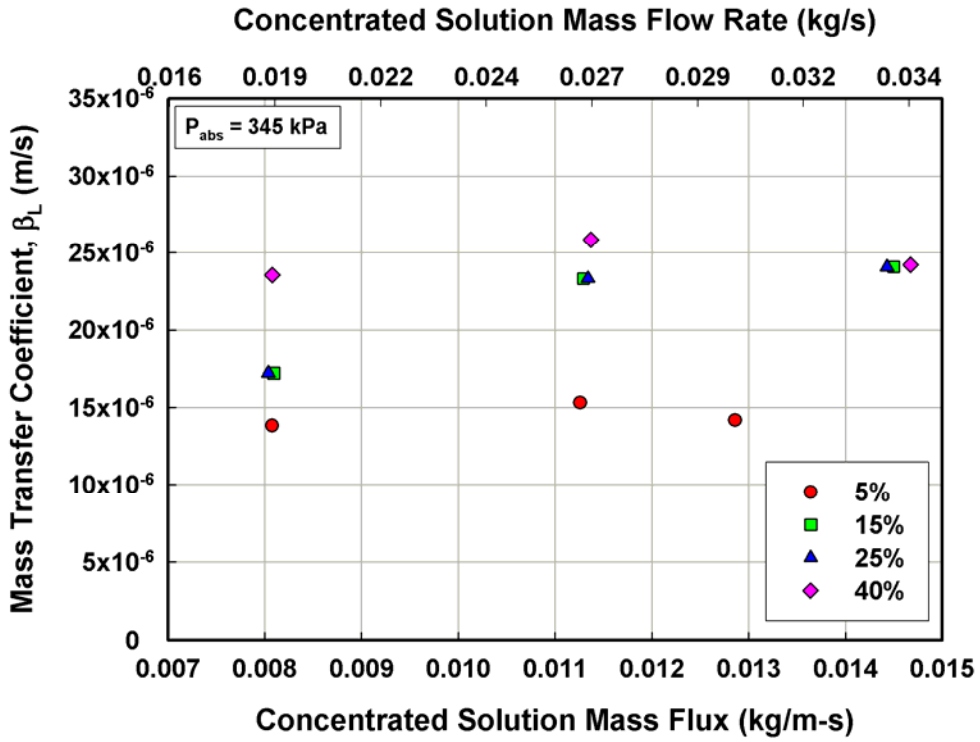

Figure 5.24 Effect of Dilute Solution Concentration on β_L at P_{abs}=345 kPa (50 psi)

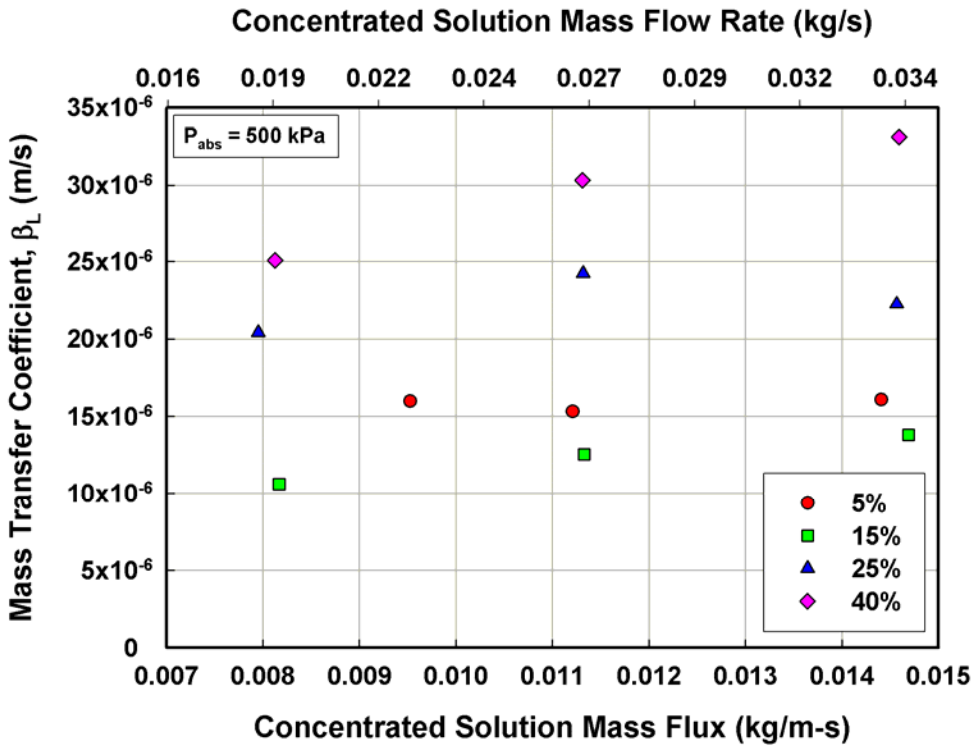

Figure 5.25 Effect of Dilute Solution Concentration on β_L at P_{abs}=500 kPa (72.5 psi)

mind that the tests 150 kPa and concentrations of 25% and 40% were conducted using a subcooler to obtain the lower pressure conditions. Also, the 40% cases could only be tested at a pressure of 240 kPa (35 psi), which is higher than the nominal pressure of 150 kPa.

As seen in Figure 5.24 at 345 kPa, cases with 40% concentration have higher mass transfer coefficients than those with other concentrations, while cases with 5% concentration have significantly lower mass transfer coefficients. The mass transfer coefficients at concentrations of 15 % and 25% show similar values.

Figure 5.25 shows that at 500 kPa, the effect of concentration is more pronounced than that at other pressures. At a 40% concentration, the mass transfer coefficients increase as the concentrated solution flow rate increases. The mass transfer coefficients

at other concentrations tend to increase and then decrease as the concentrated solution flow rate increases.

5.3.3 *Effect of Absorber Pressure*

Figures 5.26 - 5.29 show the effect of absorber pressure on mass transfer coefficient in the liquid-phase at different dilute solution concentrations. The concentrated solution flow rate does not affect the mass transfer coefficient in the liquid-phase to any appreciable degree. Absorber pressure appears to be an important parameter in determining liquid-phase mass transfer coefficient at all concentration except 5%. For the 15% cases shown in Figure 5.27, higher mass transfer coefficients are obtained at a pressure of 345 kPa, while for the 25% cases shown in Figure 5.28 and for the 40% cases shown in Figure 5.29, higher mass transfer coefficients are obtained at 500 kPa.

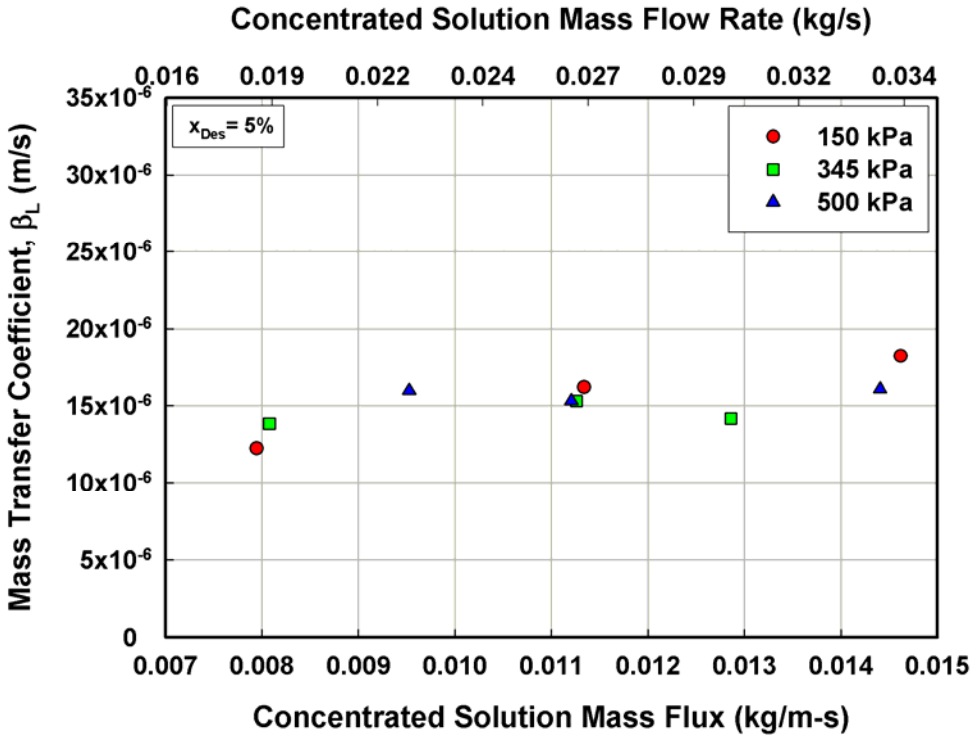

Figure 5.26 Effect of Absorber Pressure on β_L at $x_{des,out}$ = 5%

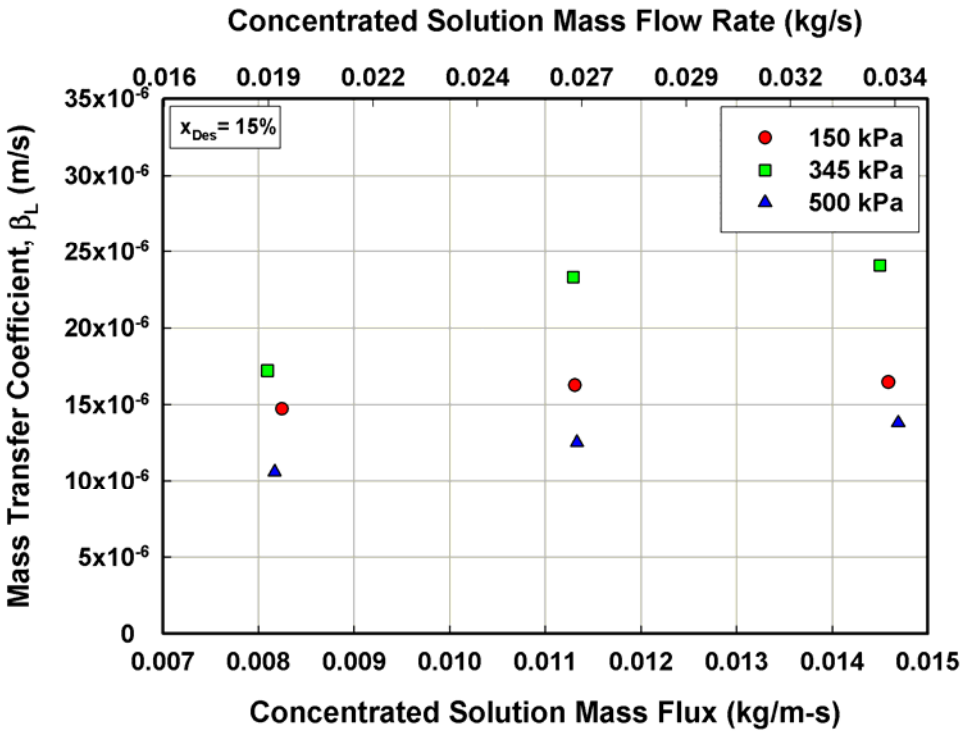

Figure 5.27 Effect of Absorber Pressure on β_L at $x_{des,out}$ = 15%

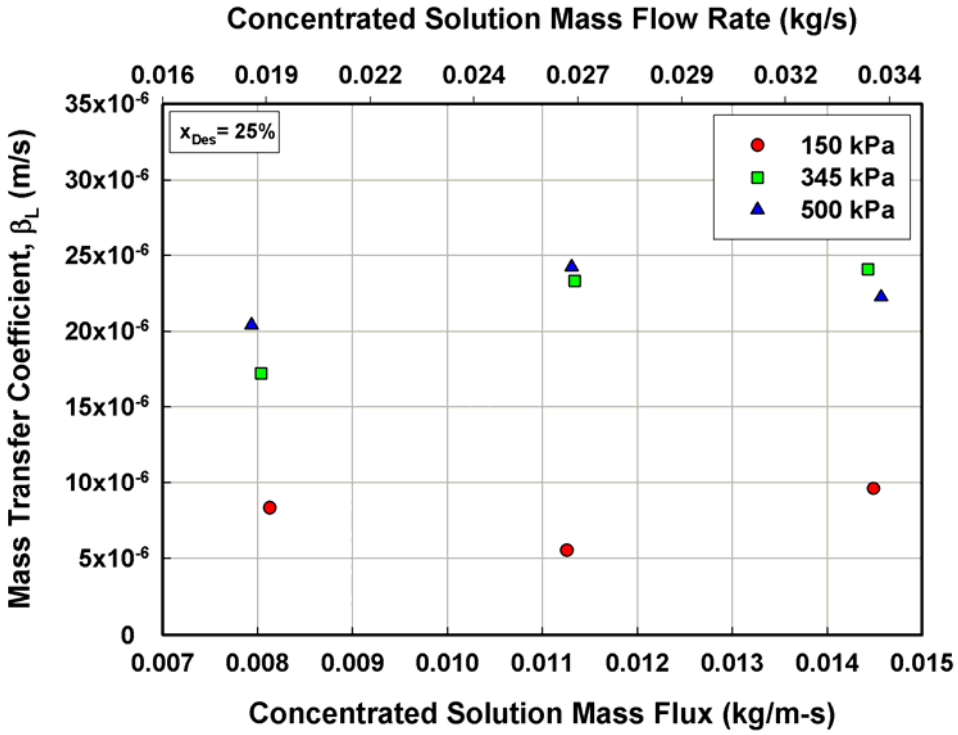

Figure 5.28 Effect of Absorber Pressure on β_L at $x_{des,out}$ = 25%

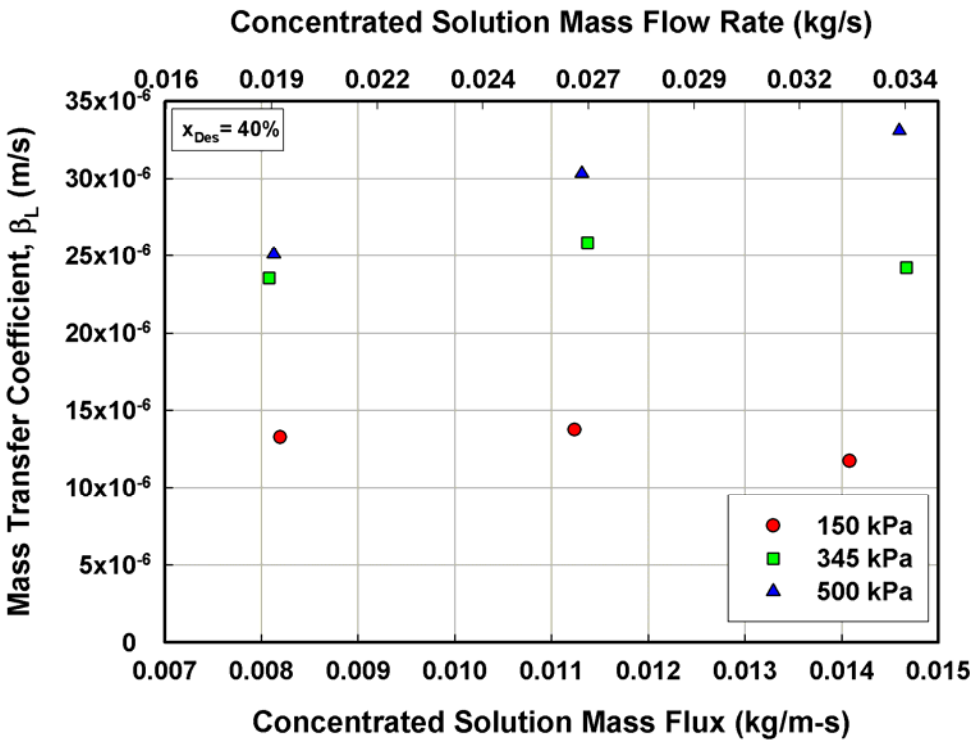

Figure 5.29 Effect of Absorber Pressure on β_L at $x_{des,out}$ = 40%

From these graphs, it appears that the mass transfer process is governed by the transport properties in the liquid-phase, since concentration and pressure affect the mass transfer coefficient in the liquid-phase more than the solution flow rate does. Table 5.3 shows the effects of variations in the absorber pressure, dilute solution concentration and concentrated solution flow rate on the mass transfer coefficient in the liquid-phase parametrically through the corresponding changes in the liquid-phase properties. Changes in viscosity and binary diffusion coefficient are more prominent than those in the other properties with the variation of concentration and absorber pressure.

At an absorber pressure of 345 kPa and a concentrated solution flow rate of 0.026 kg/s, with an increase in concentration from 5% to 40%, the viscosity decreases from 3.8×10^{-3} kg/m-s to 0.965×10^{-3} kg/m-s, and the binary diffusion coefficient decreases from 8.32×10^{-9} m^2/s to 3.58×10^{-9} m^2/s, while the mass transfer coefficient in the liquid-phase

increases from 1.53×10^{-5} m/s to 2.58×10^{-5} m/s. At a constant dilute solution concentration of 15% and concentrated solution flow rate of 0.034 kg/s, with an increase in absorber pressure from 150 kPa to 500kPa, the viscosity decreases from 0.826×10^{-3} kg/m-s to 0.344×10^{-3} kg/m-s, while binary diffusion coefficient increases from 4.03×10^{-9} m^2/s to 7.94×10^{-9} m^2/s and the mass transfer coefficient in the liquid-phase decreases from 1.65×10^{-5} m/s to 1.38×10^{-5} m/s.

At a constant absorber pressure of 500 kPa and a dilute solution concentration of 15%, with an increase in concentrated solution flow rate from 0.019 kg/s to 0.034 kg/s, changes in viscosity and binary diffusion coefficient are almost negligible, while the mass transfer coefficient in the liquid-phase increases from 1.06×10^{-5} m/s to 1.38×10^{-5} m/s.

Table 5.3 Parametric Effect of Test Conditions on the Mass Transfer Coefficient in the Liquid–Phase

	Controlled Parameters			Affected Parameters									Dependent Parameter
Effect of	P_{abs} (kPa)	x_{dil} (%)	Flow Rate (kg/s)	$T_{l,bulk}$ (^{o}C)	$T_{v,bulk}$ (^{o}C)	$x_{v,bulk}$ (%)	$(x_{v,bulk}-x_{l,bulk})$ (%)	ρ_l (kg/m^3)	$C_{P,l}$ (kJ/kg–K)	k_l (W/m–K)	μ_l (kg/m–s)	$D_{aw,l}$ (m^2/s)	β_L (m/s)
Effect of Dilute Solution Concentration @ nominal Absorber Pressure = 345 kPa, Concentrated Solution Flowrate = 0.026 kg/s													
Concentration	↔	↑	↔	↓	↓	↑	↓	↔	↑	↓	↓	↓	↑
5%	365	17	0.026	78	65	95.6	75	887	4.316	0.605	3.8×10^{-03}	8.32×10^{-09}	1.53×10^{-05}
40%	352	41	0.026	27	18	99.9	57	851	4.419	0.553	0.965×10^{-03}	3.58×10^{-09}	2.58×10^{-05}
Effect of Absorber Pressure @ nominal Dilute Solution Concentration = 15%, Concentrated Solution Flowrate = 0.034 kg/s													
Pressure	↑	↔	↔	↑	↑	↓	↔	↔	↔	↔	↓	↑	↓
150 kPa	177	20	0.034	43	27	99.1	76	907	4.287	0.59	0.826×10^{-03}	4.03×10^{-09}	1.65×10^{-05}
500 kPa	486	17	0.034	84	66	96.9	78	888	4.272	0.611	0.344×10^{-03}	7.94×10^{-09}	1.38×10^{-05}
Effect of Concentrated Solution Flowrate @ nominal Absorber Pressure = 500 kPa, Dilute Solution Concentration = 15%													
Flow Rate	↔	↔	↑	↔	↔	↔	↔	↔	↔	↔	↔	↔	↑
0.019 kg/s	481	16	0.019	81	62	97.4	78	890	4.264	0.611	0.365×10^{-03}	7.58×10^{-09}	1.06×10^{-05}
0.034 kg/s	486	17	0.034	84	66	96.9	78	888	4.272	0.611	0.344×10^{-03}	7.94×10^{-09}	1.38×10^{-05}

In summary, mass transfer coefficients in the liquid-phase are not influenced appreciably by an increase in the concentrated solution flow rate except at a pressure of 500 kPa and a concentration of 40%, although the mass transfer coefficient in the liquid-phase could be influenced by flow patterns that depend on the solution flow rate. In this study, however, all the data exhibited droplet mode flow. Concentration and pressure changes show stronger effects on the mass transfer coefficient in the liquid phase through changes in solution properties such as a binary diffusion coefficient and viscosity. Therefore, the mass transfer coefficients in liquid phase appear to be more dependent on changes in solution properties due to variations in concentration and pressure rather than solution flow rate.

5.3.4 Relevant Non-Dimensional Parameters

The primary non-dimensional groups for the liquid-phase transport properties are the Reynolds number (Re_l) and the Schmidt number (Sc_l). The Schmidt number in the liquid phase is defined as follows:

$$Sc_l = \frac{\mu_l}{\rho_l \cdot D_{aw,l}} \tag{5.17}$$

The liquid-phase mass transfer coefficient is non-dimensionalized to obtain the Sherwood number (Sh_l) as follows:

$$Sh_l = \frac{\beta_L \cdot \delta_l}{D_{aw,l}} \tag{5.18}$$

5.3.5 Comparison with Literature

Since there are few studies in the literature that provide correlations for convective mass transfer coefficient in the liquid-phase, the mass transfer coefficients

from this study are compared with those obtained using a heat and mass transfer analogy, and with a correlation developed by Inoue *et al.* (2004).

The heat and mass transfer analogy in the liquid-phase can be written as follows:

$$Sh_l = \frac{\beta_L \cdot \delta_{film}}{D_{aw,l}} = Nu_l \cdot \left(\frac{Sc_l}{\mathrm{Pr}_l} \right)^{1/3} \tag{5.19}$$

where β_L is the mass transfer coefficient in the liquid-phase, and δ_{film} is the film-thickness used in the Nusselt number Nu_l described previously.

Inoue *et al.* (2004) developed heat and mass transfer correlations for falling liquid films formed by distilled water on a horizontal tube during ammonia absorption. The absorber consisted of a steel shell with an inner diameter of 200 mm and length of 600 mm and the test tubes had an outer diameter of 17.3 mm and length of 600 mm. The absorber coolant flow rate was 1.0×10^{-4} m^3/s with an inlet temperature of 288 K. The flow rate of distilled water (absorbent) ranged from 1.64×10^{-3} kg/s to 4.17×10^{-3} kg/s at temperatures between 288 K and 303 K. Tests were conducted at pressures between 11.2 kPa and 14.7 kPa with an ammonia vapor concentration of 100%. Heat transfer coefficients were correlated with the liquid Reynolds number and a temperature ratio (the ratio of temperature differences between the solution inlet and the tube wall, and between the vapor temperature and the tube wall temperature). Mass transfer coefficients in the vapor-phase were correlated with the Schmidt number and Reynolds number of the vapor phase and the ratio between density of the vapor at the interface and the bulk vapor. Although they developed a heat transfer correlation for the liquid phase and a mass transfer correlation for the vapor phase, these correlations were not compared in earlier sections with the corresponding results from the present study, because these correlations

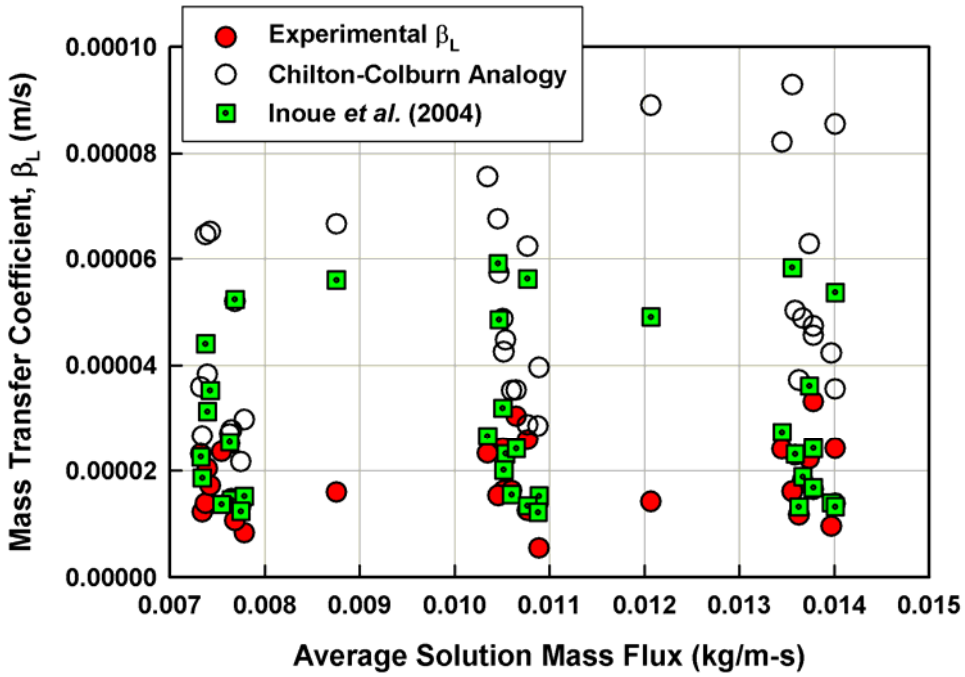

Figure 5.30 Comparison of Liquid Mass Transfer Coefficient with the Literature

of Inoue *et al.* (2004) were expressed in terms of the wall temperature and the vapor-phase Reynolds number, which would be inapplicable for the present study as discussed in the previous sections.

Inoue *et al.* (2004) did report a correlation for the mass transfer coefficient in the liquid phase in terms of the Reynolds and the Schmidt number of the liquid phase as follows:

$$Sh_l = \frac{\beta_L \cdot \delta_l}{D_{aw,l}} = 0.26 \cdot \mathrm{Re}_l^{-0.09}\, Sc_l^{0.005} \tag{5.20}$$

where δ_l is $\delta_l = \left(\nu_l^2 / g \right)^{1/3}$ in the above equation.

Figure 5.30 shows a comparison of β_L obtained in the present study, the heat and mass transfer analogy, and from the correlation of Inoue *et al* (2004). As seen in Figure 5.30, the mass transfer coefficients from the heat and mass transfer analogy are higher

than the data from the present study. The deviations in the mass transfer coefficient predicted by the analogy and the data from the present study increases as the flow rate increases. This is because the mass transfer coefficients from the present study did not increase proportionately with an increase in Nusselt number, while the mass transfer coefficient predicted by the analogy does so. This implies that mass transfer coefficients were not affected significantly by an increase in the solution flow rate, although the Nusselt numbers are affected by the solution mass flow rate. Values predicted by the correlation of Inoue *et al* (2004) show somewhat better agreement with the results from the present study, and in general, overpredict the current data to some extent. Also, the predictions of Inoue *et al* (2004) show a greater scatter at a given flow rate than the data from the present study. This scatter may be attributed to differences in the test conditions used by Inoue *et al* (2004) and the present study. Tests by Inoue *et al* (2004) were conducted at a single pressure without a change in solution concentration; however, tests for the present study were conducted at three different pressures and four different dilute solution concentrations.

5.4 Range of Uncertainties for the Current Experiments

Using the uncertainty values for the various measurements that were described in the previous chapters, the overall uncertainties in the various solution stream concentrations, absorber heat duties, and the coolant, overall and film heat transfer coefficients, the overall mass transfer coefficient, and the reflux flow rate were computed using an error propagation method (Taylor and Kuyatt, 1993). The results are summarized in Table 5.4. The uncertainty in the film heat transfer coefficient ranged between 4.2% and 20% with an average uncertainty of 11%. The uncertainties in the

mass transfer coefficients in the vapor phase ranged between 4.6% and 14.2% with an average uncertainty of 8%. The uncertainties in the mass transfer coefficients in the liquid phase ranged between 0.5% and 2.9% with an average value of 1.1%. There are 5 data points with uncertainties > 25% for the reflux flow rate; this is to be expected because of the relatively low flow rates of the reflux, and also the high sensitivity of the vapor phase properties to the vapor concentration in the vicinity of the rectifier. Among all variables, the absorber vapor inlet pressure contributes the greatest to the total uncertainty in the film heat transfer coefficient. The highest uncertainties in the reflux calculation are for data at 345 kPa (50 psi) and 40% desorber outlet concentration – this is because at such high solution concentrations, the reflux flow rate is very small.

An uncertainty analysis of this representative data point is shown in Appendix D.

It should be noted that the non-dimensional parameters pertaining to the vapor phase that are used to obtain vapor mass transfer coefficients introduce additional uncertainties over and above those reported in the foregoing discussion. This is because vapor properties are obtained here using the kinetic theory. It is shown in Appendix D that the agreement between the predictions of the kinetic theory and the vapor-phase transport properties available in the literature is only in the 4 - 15% range, which will introduce these additional uncertainties. Further discussion is provided in Appendix D.

Table 5.4 Uncertainties in the Current Experimental Data

Parameter	Range	Uncertainty Range(Absolute)	Uncertainty Range (%)	Average Uncertainty (%)
$X_{des,out}$	0.091 – 0.408	0.0028 – 0.0046	0.85 – 3.48	1.86
$X_{abs,in}$	0.152 – 0.418	0.0025 – 0.0185	0.92 – 9.52	2.88
$X_{abs,out}$	0.207 – 0.442	0.0022 – 0.0159	0.76 – 6.13	1.97
X_V	0.807 – 0.999	0.0001 – 0.0047	0.01 – 0.57	0.20
Reflux (kg/s)	1.9×10^{-5} – 0.00811	1.8×10^{-6} – 0.0012	4.35 – 107.94	16.99
Q_{abs} (kW)	3.26 – 10.75	0.06 – 1.54	1.31 – 20.51	6.18
Q_{abs_C} (kW)	2.96 – 9.79	0.17 – 1.63	3.32 – 30.27	13.31
Q_{abs_avg} (kW)	3.11 – 10.20	0.10 – 0.99	1.84 – 15.89	7.84
α_C (W/m^2–K)	2634 – 11408	14.99 – 114.3	0.42 – 1.46	0.63
U (W/m^2–K)	753.2 – 1853	24.11 – 170.1	2.43 – 15.63	7.95
α_{Film} (W/m^2–K)	922.8 – 2857	67.86 – 430.50	4.171 – 20.04	11.21
β_V (m/s)	0.002588 – 0.2541	0.0001 – 0.0171	4.63 – 14.2	7.91
β_L (m/s)	5.51×10^{-6} – 3.31×10^{-5}	7.34×10^{-7} – 4.97×10^{-8}	0.468–2.92	1.06

CHAPTER 6. HEAT AND MASS TRANSFER MODEL DEVELOPMENT

This chapter discusses the development of heat and mass transfer correlations based on the data obtained in the present study. The chapter is divided in two main sections: heat transfer correlation development, and mass transfer correlation development. With the insights gained from the trends in the results from this study, heat and mass transfer correlations are developed for the range of conditions tested in the present study.

6.1 Heat Transfer Correlation Development

From the discussion in the previous chapter, it can be seen that the available correlations from literature do not predict the heat transfer coefficients obtained in this study adequately. This section discusses a development of a correlation for the heat transfer coefficients obtained in this study. To develop a heat transfer correlation, it is necessary to understand the influences of various parameters affecting heat transfer characteristics first. The heat transfer correlation is developed based on the observed trends using pertinent non-dimensional parameters introduced in the previous chapter.

Figure 6.1 shows the variation of the overall Nu_l with solution Re. The higher Re_l can be obtained either with a higher mass flux or with a lower viscosity. The Nu_l increases as the Re_l increases at a constant absorber pressure. It can also be seen that absorber pressure has a significant effect on the Nu_l. At a higher pressure, a similar Nu_l is

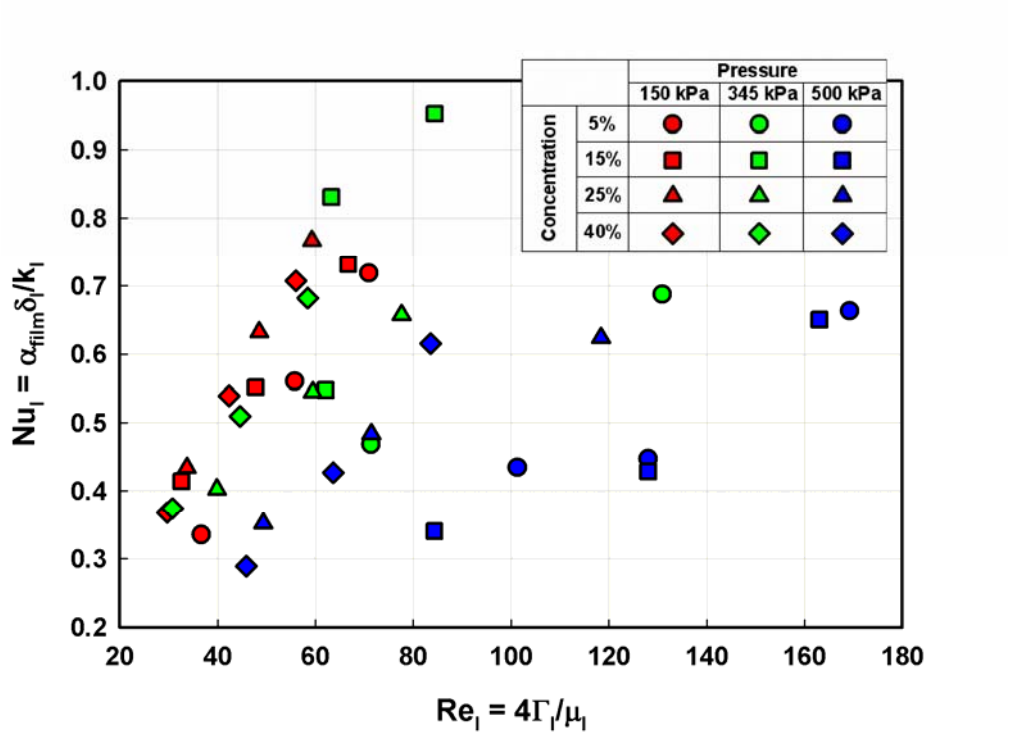

Figure 6.1 Variation of Nu_l with Re_l

obtained at a much higher Re_l (as can be seen with a rightward shift with an increase in the absorber pressure). In other words, as the absorber pressure increases, the Nusselt numbers for a given Re_l are smaller. Ammonia-water solution viscosity increases as solution concentration increases (4.14×10^{-4} kg/m-s at 20% to 9.74×10^{-4} kg/m-s at 40%); therefore, at a constant absorber pressure, for the same solution mass flux, the solution Re_l is smaller, which would yield a lower Nu_l. This means that a Re_l dependence could address the effect of the mass flow rate and the effect of the concentration change through the viscosity on Nu_l. However, the pressure effect cannot be accounted for by Re_l alone.

Figure 6.2 shows the variation of Nu_l with the solution Pr_l. Although the trends in Nu_l as Pr_l varies are not very clear, it can be seen that Nu_l decreases slightly at a constant absorber pressure and dilute solution concentration as the solution Pr_l increases. The

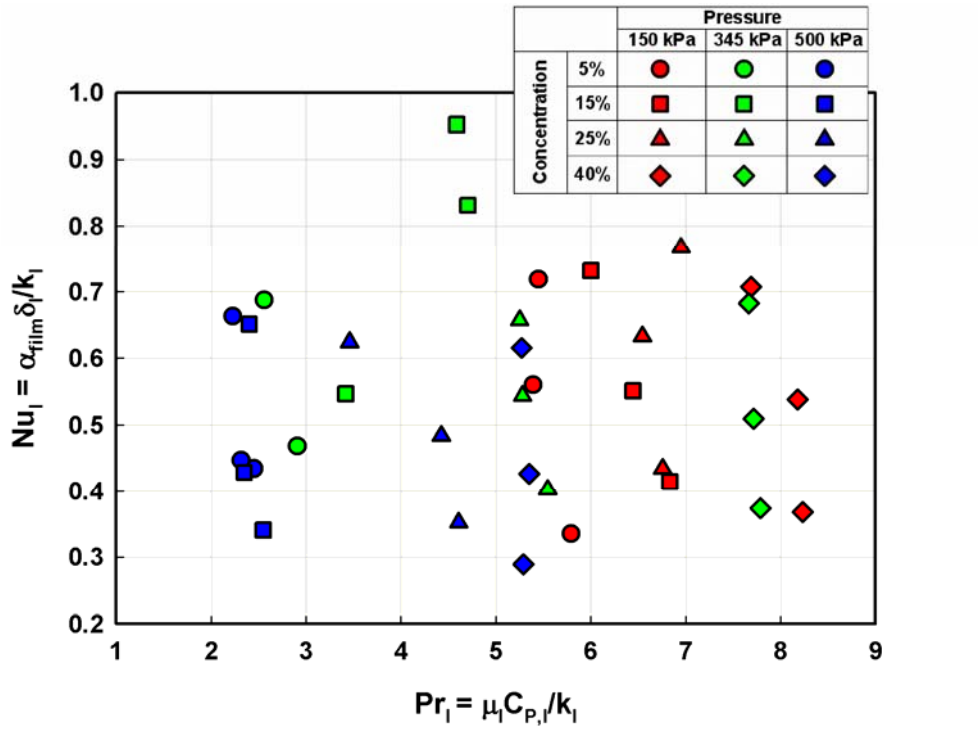

Figure 6.2 Variation of Nu_l with Pr_l

influence of the absorber pressure can be seen in this figure also, as the higher pressure cases are located towards the smaller Pr_l, while the lower pressure cases are located towards higher Pr_l. Based on these observations and because the absorber pressure is found to have a significant effect on Nu_l, the influences of Re_l, Pr_l and the absorber pressure are combined in the following form to develop a correlation for the present data. Similar forms have been used by other researchers (Wilke, 1962; Dorokhov and Bochagov, 1983; Hu and Jacobi, 1996b) in the past.

$$Nu_l = a \cdot \mathrm{Re}_l^{\,b}\, \mathrm{Pr}_l^{\,c} \left(\frac{P_{abs,ave}}{345\,kPa} \right)^d \tag{6.1}$$

Here, the constant a, and the exponents b, c, and d are determined using regression analysis. The last term accounts for the pressure dependence seen in the data. An absorber pressure of 345 kPa is chosen as the reference pressure because this is the

intermediate pressure tested in the present study and represents the normal ambient heat pump mode. The regression analysis yields the following Nusselt number correlation at the component level (for the entire absorber):

$$Nu_l = 3.22 \times 10^{-3} \cdot \mathrm{Re}_l^{0.945}\, \mathrm{Pr}_l^{0.743} \left(\frac{P_{abs,ave}}{345\,kPa} \right)^{-0.269} \tag{6.2}$$

Figure 6.3 shows a comparison between the experimentally obtained Nu_l in this study and the predictions of the above correlation. This correlation predicts 86% of the data from the present study within ±25%. The average absolute deviation is 10% for all the data. As can be seen from the exponent values, Nu_l is proportional to Re_l and Pr_l but is inversely proportional to the pressure ratio.

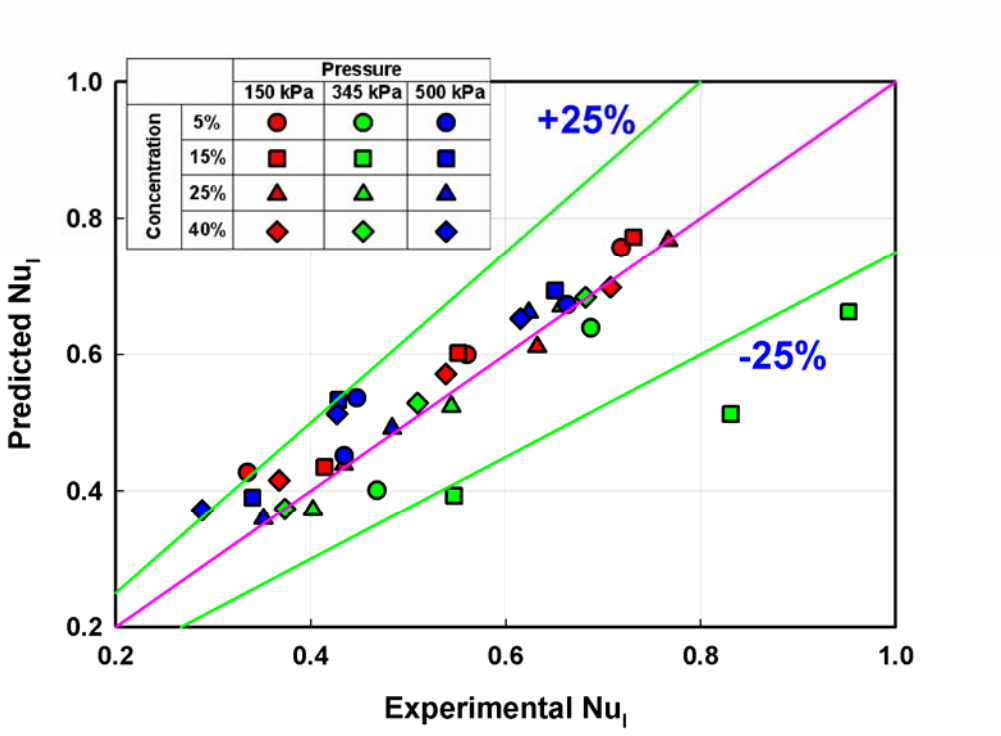

Figure 6.3 Experimental vs Predicted Nu_l

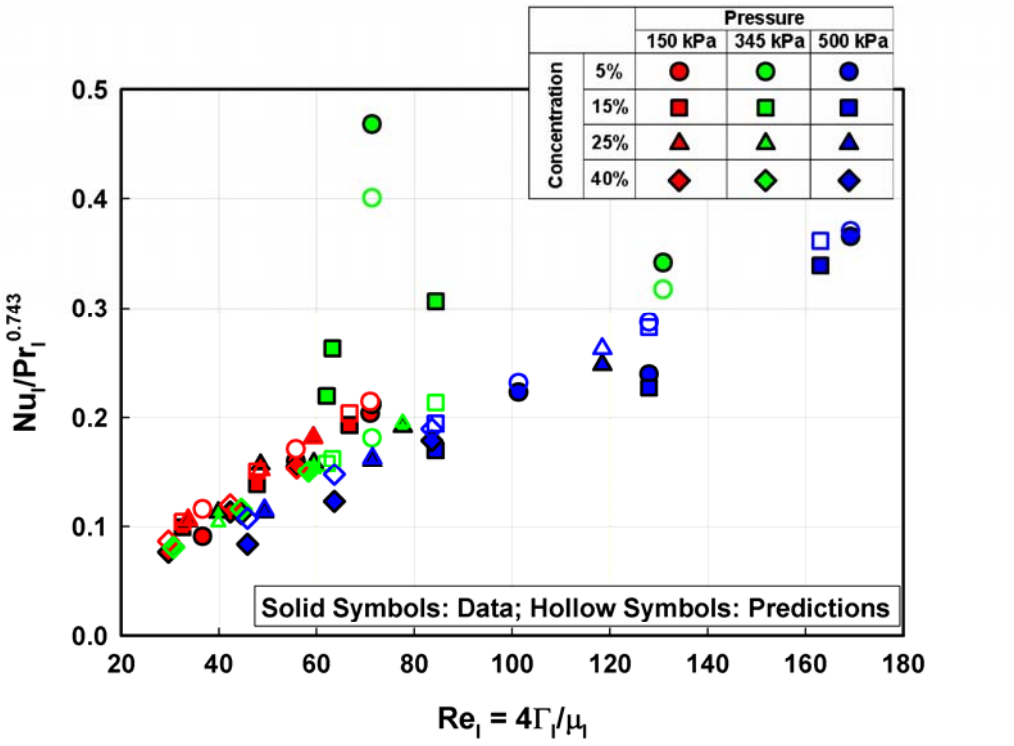

Figure 6.4 Comparison of Predicted and Experimental Nu_l

Figure 6.4 shows the experimental and predicted Nu_l as a function of Re_l. The experimental and predicted values are in good agreement over the entire range of conditions tested, and the developed correlation represents the trends in the data well. It can also be seen that inclusion of a pressure correction term improves the predictive capability of the correlation significantly. The larger discrepancies correspond to the 5 and 15% cases at higher pressures (especially 500 kPa). As mentioned before, establishing the operating conditions to obtain these data required circulating the coolant at substantially higher temperatures (-50^{o}C) and relatively smaller coolant flow rates. These conditions affect the heat transfer characteristics and the smaller coolant flow rates increase the coolant side thermal resistances, which introduce larger uncertainties in the solution heat transfer coefficients.

6.2 Mass Transfer Correlation Development

This section discusses the development of correlations for the mass transfer coefficients obtained in this study.

6.2.1 Mass Transfer Correlation in Vapor-Phase

The main parameters that influence the mass transfer coefficient are binary diffusion coefficient, viscosity, thermal conductivity, and density of the ammonia/water vapor mixture. The influence of these parameters is studied using several non-dimensional numbers. Since heat and mass transfer are coupled processes, the starting point for the correlation development is the use of the heat and mass transfer analogy. Therefore, a vapor-phase Sh_v can be obtained from the corresponding Nusselt number as follows:

$$Sh_v = Nu_v \times \left(\frac{Sc_v}{\mathrm{Pr}_v} \right)^{b1} \tag{6.3}$$

This equation requires an appropriate Nu_v to represent the heat transfer process during absorption in the present study. As mentioned in the previous chapters, the vapor inside the large absorber chamber is relatively quiescent; therefore, the heat transfer is considered to be taking place through natural convection because of the difference between liquid and vapor-phase temperatures, while the mass transfer occurs due to the corresponding concentration differences. The absorption process also involves phase change that needs to be accounted for. Therefore, the following form of Nu_v is considered:

$$Nu_v = a \times \left(\frac{Gr_v \times \mathrm{Pr}_v}{Ja_v} \right)^{b} \tag{6.4}$$

Here, the Grashof (Gr_v) and Prandtl (Pr_l) numbers account for the natural convection (and also include the relative importance of buoyancy and viscous forces in heat transfer within a quiescent medium), while the Jakob number (Ja_v) accounts for phase-change during absorption. A similar form is reported in Carey (1992) on page 369 for film condensation. Here, Gr_v is defined as follows:

$$Gr_v = \frac{g \times \left(T_{\text{int}} - T_{v,bulk}\right) \times d_{o,t}^3}{\left(T_{v,bulk} + 273.15\right) \times \nu_v^2} \tag{6.5}$$

The Jakob number (Ja_v), which accounts for the relative importance of sensible to latent heat during phase change is defined as,

$$Ja_v = \frac{C_{pv}(T_{\text{int}} - T_{v,bulk})}{h_{v,\text{int}} - h_{l,\text{int}}} \tag{6.6}$$

Thus, the vapor-phase Sh_v can be represented as follows:

$$Sh_v = a \times \left(\frac{Gr_v \times Sc_v}{Ja_v} \right)^b \tag{6.7}$$

The coefficient a, and the exponent b are to be found from regression of the data.

Figure 6.5 shows the dependence of Sh_v on $\frac{Gr_v \times Sc_v}{Ja_v}$. It can be seen from this figure that Sh_v increases as $\frac{Gr_v \times Sc_v}{Ja_v}$ increases. In addition to this dependence, effects of absorber pressure and dilute solution concentration can also be seen in this figure.

It was also found that liquid-side properties influence the vapor-side mass transfer coefficient. The effect of heat and mass transfer as the condensed vapor is transported through the solution film is accounted for using the Lewis number (*Le*), which relates thermal and mass diffusivities.

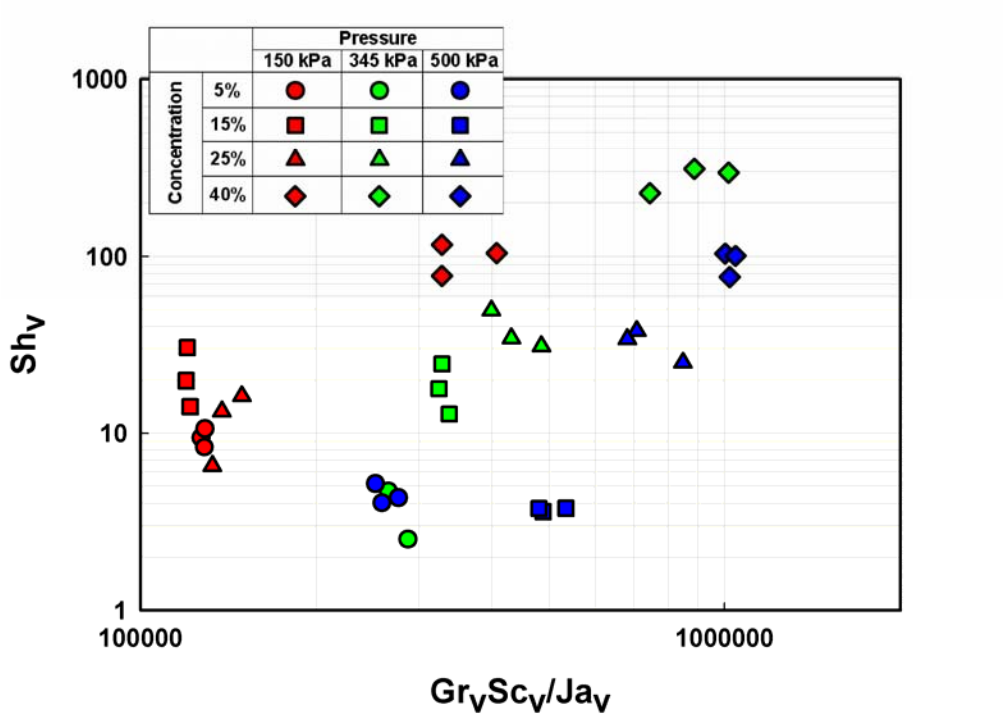

Figure 6.5 Variation of Sh_v with $\frac{Gr_v \times Sc_v}{Ja_v}$

$$Le_l = \frac{Sc_l}{\mathrm{Pr}_l} \tag{6.8}$$

Figure 6.6 shows the effect of liquid-side Le_l on Sh_v. This ratio is the ratio of the liquid-side thermal and mass diffusivities ($\frac{Sc_l}{\mathrm{Pr}_l} = \frac{\alpha_{th,l}(=k_l/\rho_l \cdot C_{p,l})}{D_{aw,l}}$). It can be seen from the figure that Sh_v increases as the Le_l increases. A larger Le_l implies a higher thermal diffusivity ($\alpha_{th,l}$) or a smaller mass diffusivity ($D_{aw,l}$). The Sh number is inversely proportional to the mass diffusivity; therefore a smaller $D_{aw,l}$ results in higher Sh_v. A larger thermal diffusivity facilitates removal of the heat of absorption, perhaps leading to an increase in the mass transfer coefficient. Since Sh_v is directly proportional to the mass transfer coefficient, a higher thermal diffusivity results in higher Sh_v.

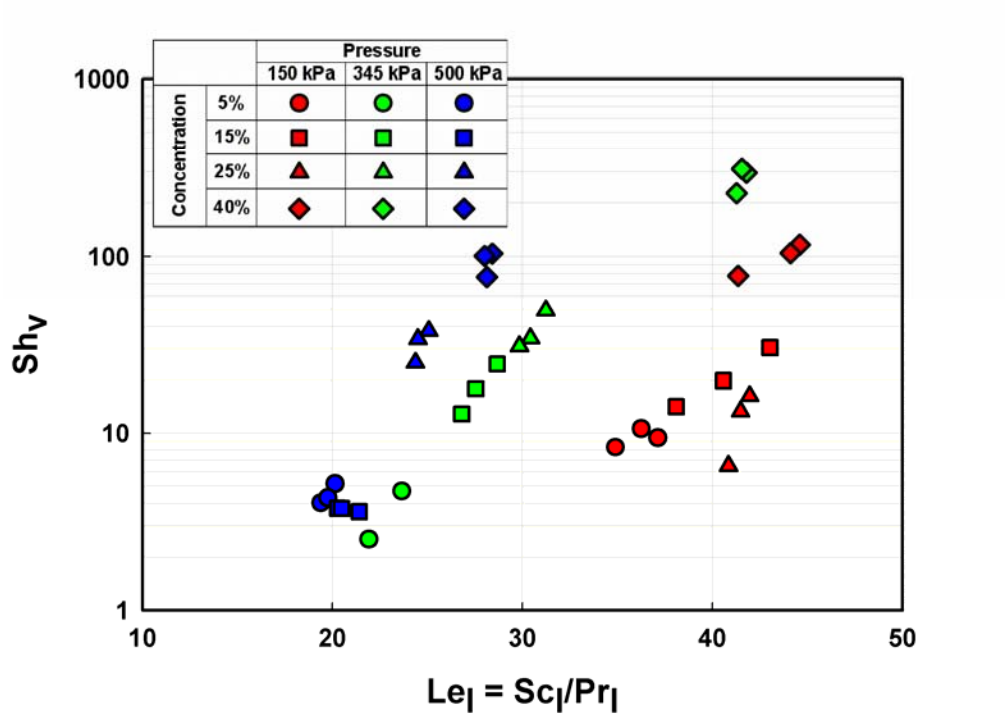

Figure 6.6 Variation of Sh_v with $Le_l = \frac{Sc_l}{\Pr_l}$

Although it appears that $(Gr_v \cdot Sc_v)/Ja_v$ and Le_l account for much of the variation in Sh_v, the data indicate that other liquid and vapor-phase properties could account for some of the residual scatter. It was found that the difference between liquid and vapor-side viscosities also influences Sh_v.

Figure 6.7 shows the effect of $\frac{\mu_l - \mu_v}{\mu_v}$ on the Sh_v. It can be seen that Sh_v increases as this ratio increases. The increase in this ratio is mostly due to an increase in liquid viscosity (For the range of conditions tested, the liquid-phase viscosity varies from 3.21×10^{-4} - 1.042×10^{-3} kg/m-s, while the vapor-phase viscosity varies from 1.006×10^{-5} - 1.204×10^{-5} kg/m-s). The liquid viscosity increases as the dilute solution becomes concentrated by absorbing ammonia vapor. The difference in viscosities affects the shear

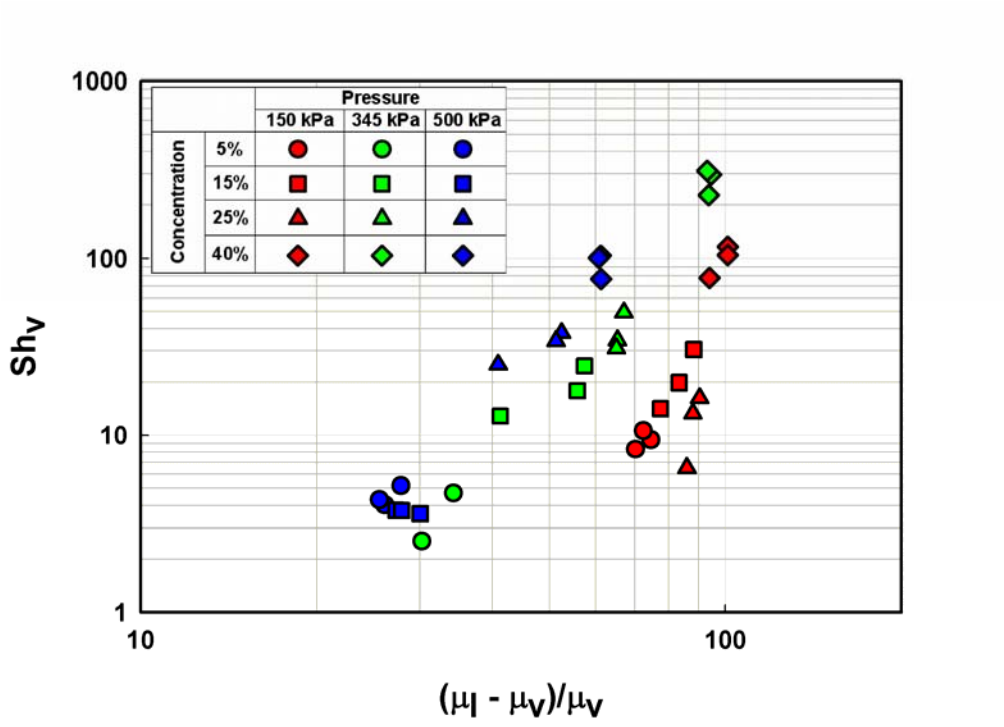

Figure 6.7 Variation of Sh_v with $\frac{\mu_l - \mu_v}{\mu_v}$

stresses at the interface as well within the solution film, which in turn affects the mass transfer coefficients. The shear stresses at the interface can influence the movement of the vapor towards the interface while the shear stress in the liquid can influence mixing within the liquid-phase, thereby affecting the mass transfer. The higher viscosities are observed for the higher dilute solution concentration cases. As the dilute solution concentration increases, the specific volume of the vapor in equilibrium with the solution decreases. The smaller specific volume implies smaller velocities and therefore smaller shear stresses. The smaller vapor shear can improve mass transfer in counter flow, because it does not result in a thickening of the liquid film, resulting in higher Sh_v. Kwon and Jeong (2004) also observed similar trends for solution-side Nusselt number in the counter-flow arrangement where Nu_l decreases as the vapor shear increases. Based on

these considerations, the following functional form of the mass transfer correlation was developed:

$$Sh_v = a \times \left(\frac{Gr_v \times Sc_v}{Ja_v} \right)^b \times \left(\frac{\mathrm{Pr}_l}{Sc_l} \right)^c \times \left(\frac{\mu_l - \mu_v}{\mu_v} \right)^d \tag{6.9}$$

Here, constant *a* and exponents *b, c* and *d* are obtained using regression analysis. The resulting correlation is,

$$Sh_v = 2.708 \times 10^{-11} \times \left(\frac{Gr_v \times Sc_v}{Ja_v} \right)^{1.256} \times \left(\frac{\mathrm{Pr}_l}{Sc_l} \right)^{-1.681} \times \left(\frac{\mu_l - \mu_v}{\mu_v} \right)^{1.426} \tag{6.10}$$

Figure 6.8 shows a comparison of the measured and predicted Sh_v. This correlation predicts 58% of the data within ±25%, with an average absolute deviation of 38% for all the data. It can be seen from the above expression that Sh_v increases with an

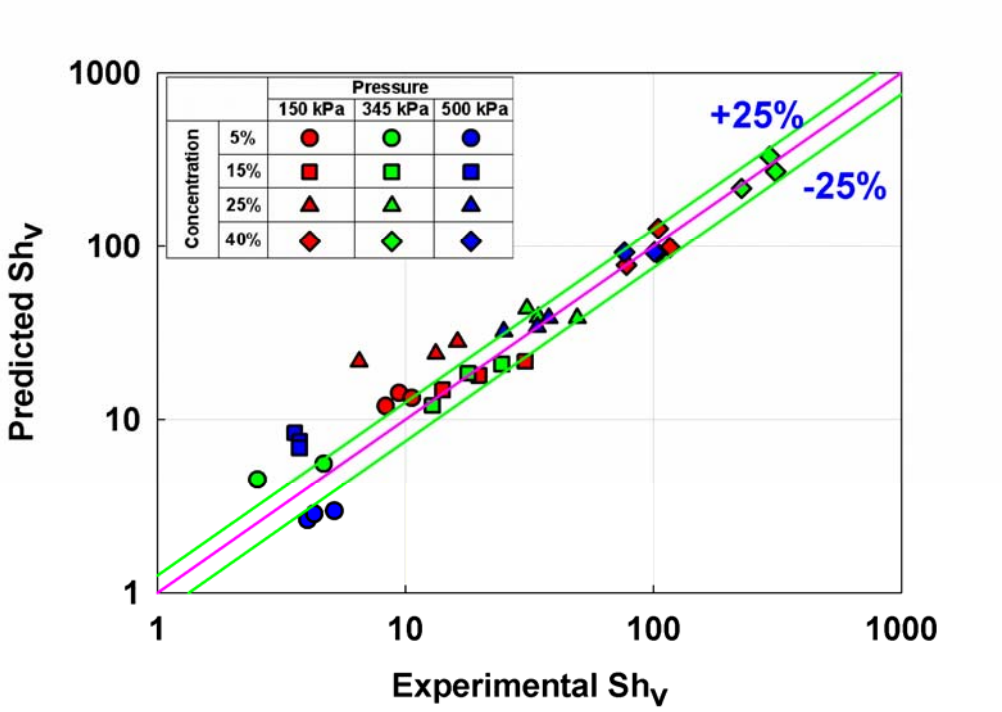

Figure 6.8 Experimental vs Predicted Sh_v

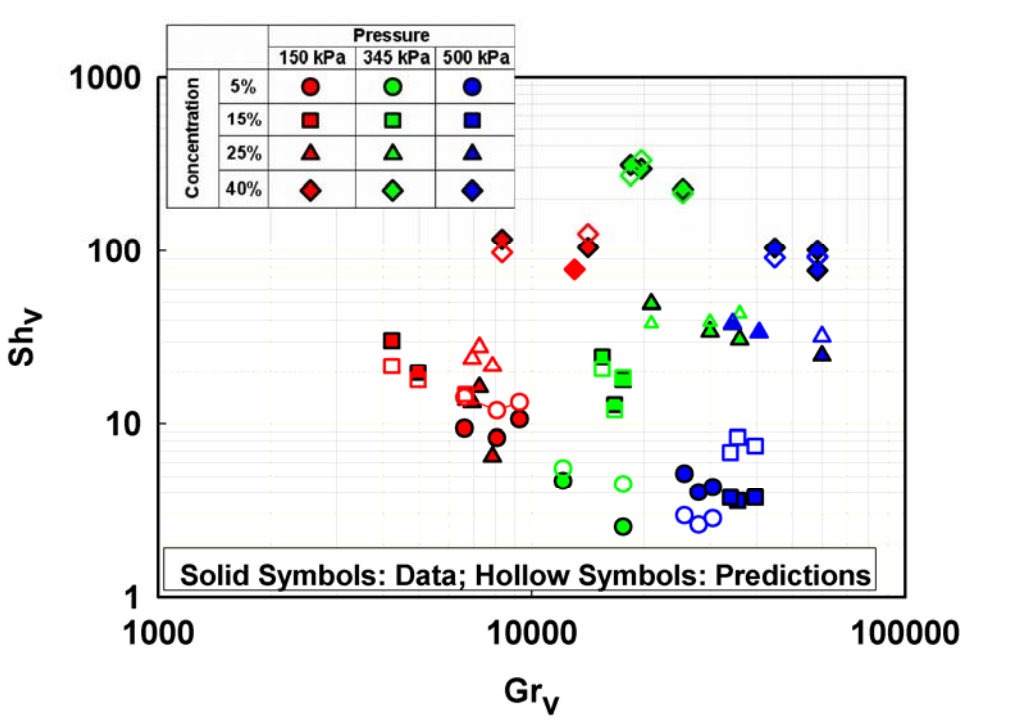

Figure 6.9 Comparison of Experimental and Predicted Sh_v

increase in Gr_v, Sc_v, Sc_l, and the difference between liquid and vapor viscosities, and decreases with an increase in Ja_v and Pr_l. Figure 6.9 shows the measured and predicted Sh_v for all the data from present study. It can be seen that this correlations predicts the trends reasonably well. The extreme conditions of 5% and 15% dilute solution concentration at 500 kPa show the largest discrepancies. This prediction is similar to the heat transfer correlation predictions, where these conditions showed the largest discrepancies. Larger discrepancies are also seen for the data at 25% dilute solution concentration and 150 kPa. This is another extreme of the test conditions where a large amount of sub-cooling was used to obtain the desired absorber pressure. The average uncertainties for these cases are more than ±10% whereas the average uncertainty in mass transfer coefficient for all the data is ±7.9%.

6.2.2 Mass Transfer Correlation in The liquid-phase

This section discusses the development of a correlation for mass transfer coefficients in the liquid phase. As discussed in the previous chapter, the main parameters that influence the mass transfer coefficient in the liquid-phase are binary diffusion coefficient, viscosity, thermal conductivity, and density of the ammonia/water mixture. For convective mass transfer, the solution Reynolds, Prandtl, and Schmidt numbers are considered for the development of the correlation.

Figure 6.10 shows the dependence of Sh_l on Re_l. It can be seen from this figure that concentration and pressure affect Sh_l through changes in solution viscosity with a relatively smaller influence of solution flow rate. Sh_l decreases as Re_l increases, with considerable scatter introduced due to changes in pressure and dilute solution concentration.

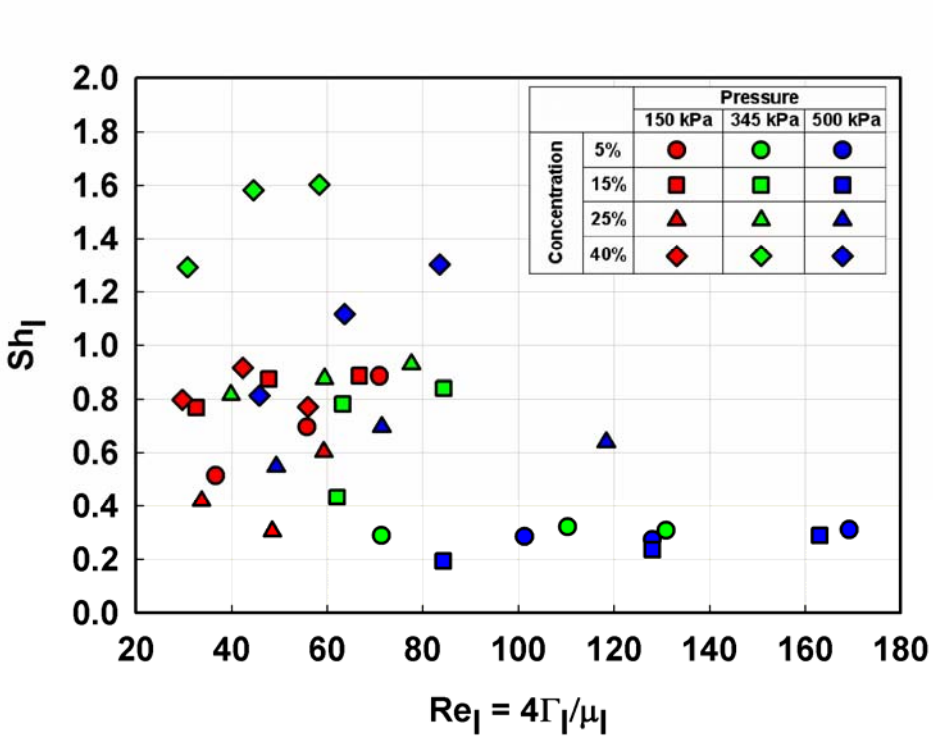

Figure 6.10 Variation of Sh_l with Re_l

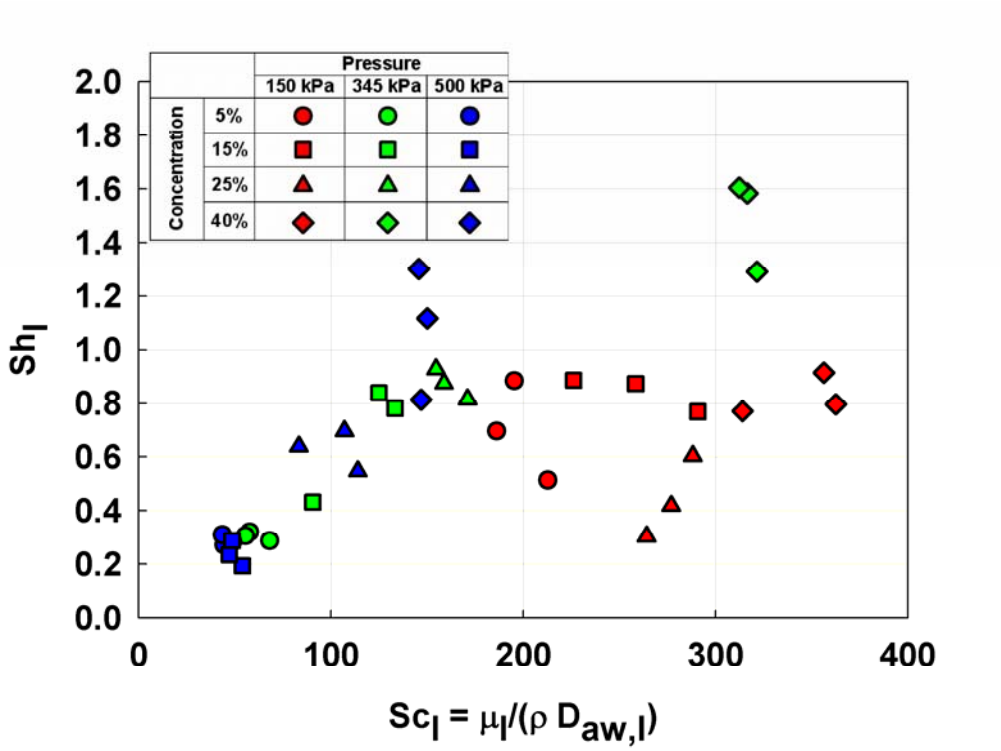

Figure 6.11 Variation of Sh_l with Sc_l

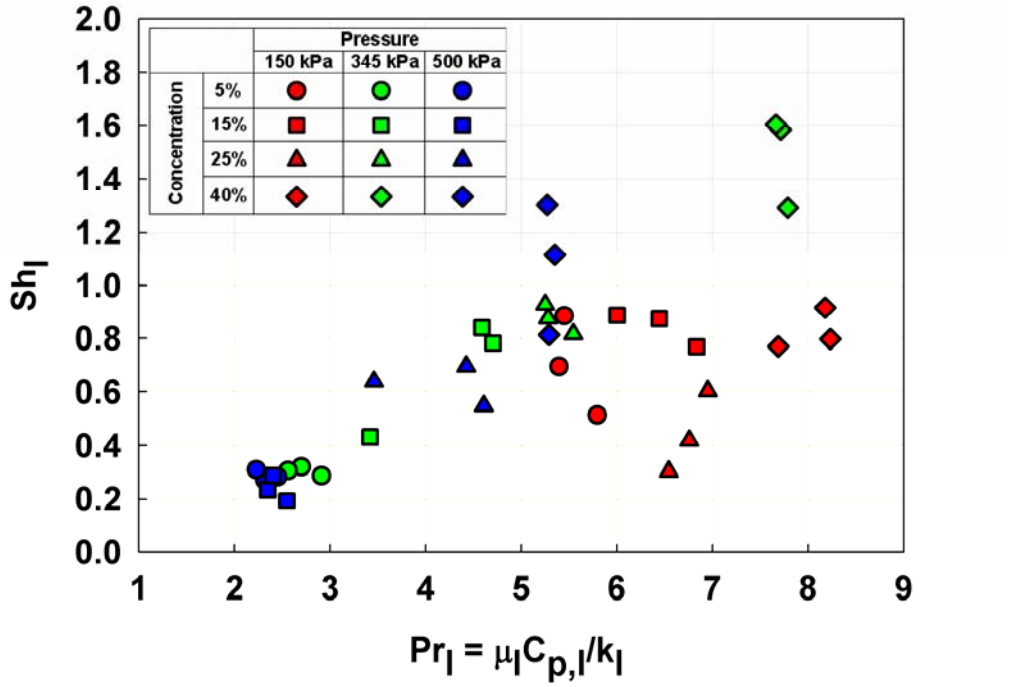

Figure 6.12 Variation of Sh_l with Pr_l

Figures 6.11 and 6.12 show the dependence of Sh_l on Sc_l and Pr_l respectively. It can be seen from these figures that the dependence of Sh_l on Sc_l and Pr_l is very similar, illustrating the coupled nature of liquid-phase heat and mass transfer. For the 345 kPa and 500 kPa cases, Sh_l increases as the dilute solution concentration increases, however, there is no clear effect of concentration on Sh_l for the 150 kPa cases.

Figure 6.13 shows the dependence of Sh_l on the pressure ratio for different dilute solution concentrations. At dilute solution concentrations of 5% and 15%, the Sh_l decreases as the pressure ratio increases. However, for the cases at dilute solution concentrations of 25% and 40%, the Sh_l increases as the pressure increases to 345 kPa and then decreases as the pressure increases. As mentioned in the previous chapter, the system shut-down pressure increases as the ammonia concentration charged in the system

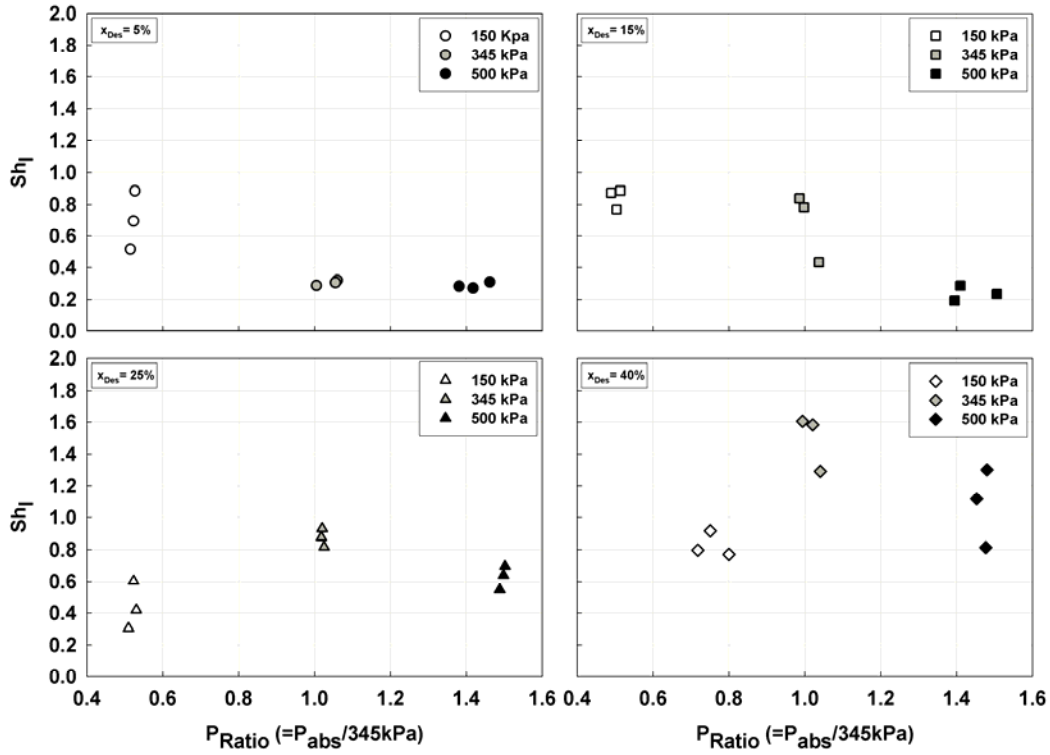

Figure 6.13 Variation of Sh_l with Pressure Ratio

increases, and the system could be operated without using the auxiliary heater in the absorber coolant loop and the subcooler at operating pressures close to the shut-down pressure. Thus, these Sh_l changes may be because an increase in the dilute concentration increases the equilibrium pressure corresponding to the dilute concentration. Therefore, the mass transfer in liquid phase is influenced by a combination of the dilute solution concentration and absorber pressure.

In Figure 6.13, for each concentration with a similar pressure ratio, symbols with the same shape and fill represent the combined effect of the concentrated solution flow rate and solution property changes due to pressure and temperature. For the cases with a concentration of 5% and a pressure of 150 kPa, concentrations of 15% and 40% and a pressure of 350 kPa, and a concentration of 40% and a pressure of 500 kPa, these symbols show some scatter. These scattered symbols imply that there are conditions when the concentrated solution flow rate can affect Sh_l appreciably, although Sh_l is not affected appreciably by the concentrated solution flow rate in the other cases. (For the case with a concentration of 5% and a pressure of 150 kPa, Sh_l increases from 0.51 to 0.88, i.e., by 72%, as the concentrated solution flow rate increases from 1.86×10^{-2} to 3.42×10^{-2} kg/s (by 84%). For the cases with concentrations of 15% and 40% and a pressure of 345 kPa, Sh_l increase from 0.43 to 0.78 (by 35%) and from 1.29 to 1.58 (by 37%), respectively, as the concentrated solution flow rates increase from 1.89×10^{-2} to 2.64×10^{-2} kg/s (by 40%), with other solution properties such as a liquid viscosity, density, and binary diffusion coefficient being within 10%. However, the Sh_l increases only slightly, from 0.78 to 0.84 (by 6.3%) and from 1.58 to 1.60 (by 1.3%), respectively, as concentrated solution flow rates increase from 2.6×10^{-2} to 3.4×10^{-2} kg/s (by 30%). For

the case with a concentration of 40% and a pressure of 500 kPa, Sh_l increases from 0.81 to 1.3 (by 60%) as the concentrated solution flow rate increases from 1.9×10^{-2} to 3.4×10^{-2} kg/s (by 80%) with other solution properties such as a liquid viscosity, density, and binary diffusion coefficient being within 10%).

Based on these observations, and because the absorber pressure is found to influence Sh_l, the influences of Re_l, Sc_l and the absorber pressure are combined in the following form to develop a correlation for the present data.

$$Sh_l = a\times\left(\mathrm{Re}_l\right)^b\times\left(Sc_l\right)^c\times\left(\frac{P_{abs}}{345\,kPa}\right)^d \tag{6.11}$$

Here, constant a and exponents b, c and d are obtained using regression analysis. The resulting correlation is,

$$Sh_l = 7.437\times10^{-4}\times\left(\mathrm{Re}_l\right)^{0.3971}\times\left(Sc_l\right)^{1.04}\times\left(\frac{P_{abs}}{345\,kPa}\right)^{0.8841} \tag{6.12}$$

Figure 6.14 shows a comparison of the measured and predicted Sh_l. This correlation predicts 70% of the data within ±25%, with an average absolute deviation of 27% for all the data. It can be seen from the above expression that Sh_l increases with an increase in Re_l, Sc_l, and absorber pressure ratio. Figure 6.15 shows the measured and predicted Sh_l for all the data from the present study. It can be seen that this correlation predicts the trends reasonably well. The extreme conditions of 5% and 15% dilute solution concentration at 500 kPa, and 25% and 40% dilute solution concentration at 150 kPa show the largest discrepancies. These predictions are similar to the predictions for the heat transfer results, where these conditions showed the largest discrepancies. Larger discrepancies are also seen for the data with 15% dilute solution concentration

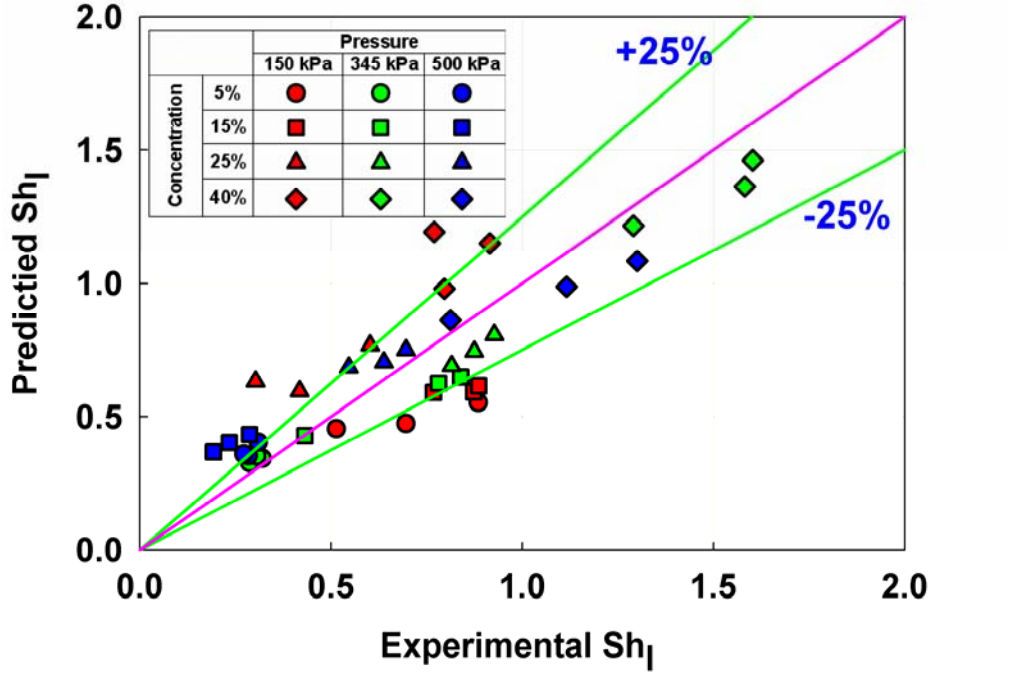

Figure 6.14 Experimental vs Predicted Sh_l

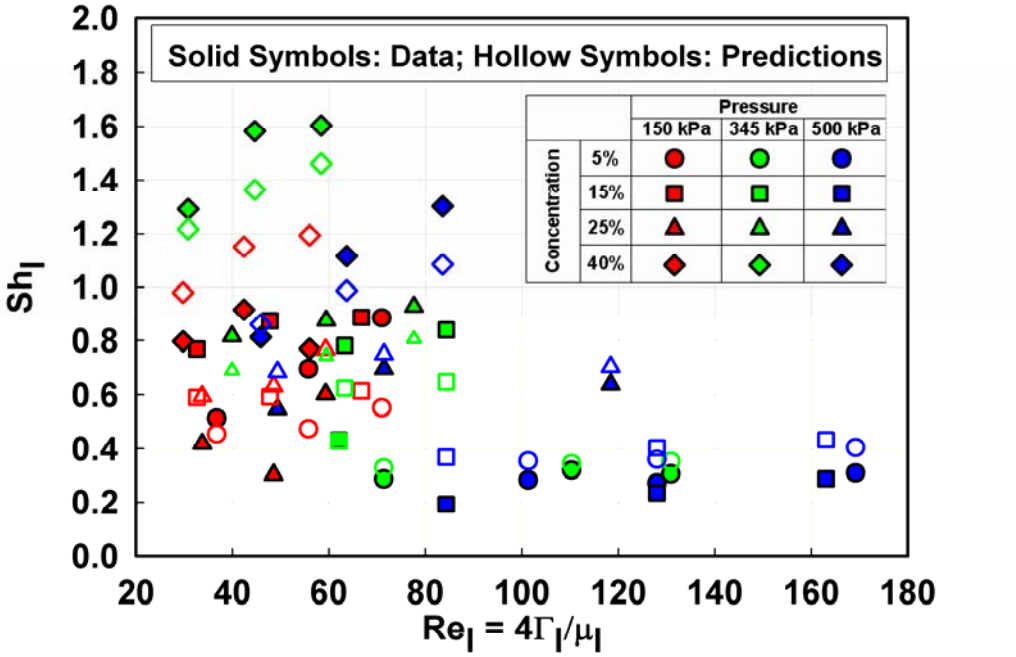

Figure 6.15 Comparison of Experimental and Predicted Sh_l

at 500 kPa. This test condition had a large amount of sub-cooling, which was necessary to obtain the desired absorber pressure.

Based on the test data from which the correlations in this study were developed, their applicability is limited to the ranges of parameters shown in Table 6.1. Use of these correlations beyond these ranges is likely to lead to less reliable predictions. It should be noted that the vapor-phase mass transfer correlation is also subject to additional uncertainty due to the approximate nature of the evaluation of vapor-phase transport properties, as discussed in section 5.4 and Appendix D.

Table 6.1 Range of Validity of Heat and Mass Transfer Correlations

Absorber Mass Flow Rate	
Concentrated Solution	1.86×10^{-2} – 3.43×10^{-2} kg/s
Inlet Vapor	7.86×10^{-4} – 3.77×10^{-3} kg/s
Absorber Temperature	
$T_{Abs,in}$	34.7 – 105.4 °C
$T_{Abs,out}$	14.8 – 68.6°C
$T_{Abs,V,in}$	-10.5 – 28.2°C
Absorber Concentration	
$x_{Abs,in}$	15.2 – 41.8%
$x_{Abs,out}$	20.7 – 44.2%
$x_{Abs,V,in}$	80.7 – 99.9%
Absorber Pressure	
$P_{Abs,ave}$	169 – 520 kPa
Non-Dimensional Parameters	
Re_l	29.7 – 169.2
Pr_l	2.2 – 8.2
Sc_l	43.6 – 362.7
Pr_v	0.5 – 0.93
Ra_v	14800 – 202534
Gr_v	4223 – 59893
Sc_v	0.5 – 0.53
Ja_v	9.8×10^{-3} – 3.87×10^{-2}

CHAPTER 7. CONCLUSIONS AND RECOMMENDATIONS

7.1 Conclusions

An experimental investigation of ammonia-water absorption in horizontal tube banks was conducted. A large test facility was designed and constructed with numerous design features and control and plumbing options to enable absorption experiments over a large range of flow rates (0.019 – 0.034 kg/s or 2.5 – 4.5 lb_m/min), concentrations (5 - 40%) and pressures (150 – 500 kPa or 21.8 – 72.5 psi). Care was taken to develop a facility that would allow measurements of fundamental phenomena such as heat and mass transfer coefficients in a specific component (the absorber) while a full scale absorption system was operating over a wide range of operating conditions. Numerous challenges presented by the requirements of tests over this wide range of conditions were addressed by developing supplemental heating and cooling loops, auxiliary heat sources and sinks, bypass lines and multiple expansion valves, redundant flow rate measurements, and multiple energy balances to validate the computation of each individual state point and process. These features were included in the test facility as needed, particularly when testing was conducted at the extreme conditions of the test matrix. Care was also taken throughout the study to not only establish the desired conditions, but also to maintain the solution-side thermal resistance so that absorption heat and mass transfer phenomena could be measured accurately. For some of the desired conditions, when the exact

nominal conditions could not be obtained, conditions as close to the nominal values as possible were established. Measured quantities such as temperatures, pressures and flow rates at numerous locations around the test loop were analyzed to obtain absorber heat duties, overall and solution heat transfer coefficients and mass transfer coefficients for the various test conditions.

For the range of experiments conducted, the absorber heat duty varied from 3.11 to 10.2 kW, the overall heat transfer coefficient varied from 753 to 1853 W/m^2-K, the solution heat transfer coefficient varied from 923 to 2857 W/m^2-K, the mass transfer coefficient in the vapor phase varied from 0.0026 to 0.25 m/s, and the mass transfer coefficient in the liquid phase varied from 5.51×10^{-6} to 3.31×10^{-5} m/s depending on the test condition. The absorber heat duty, the overall heat transfer coefficient, and the solution heat transfer coefficient were found to increase with increasing solution flow rate. In general, the solution heat transfer coefficient was found to decrease with increasing pressure and dilute solution concentration at a given solution flow rate. The mass transfer coefficient showed little effect of the solution flow rate; instead, it is found to be primarily determined by the operating conditions (that affect both the solution and vapor properties).

Few studies in the literature have addressed falling-film ammonia-water absorption in horizontal tube banks. The studies that addressed somewhat similar geometries or processes reported correlations that did not adequately represent the present data. Heat and mass transfer correlations were developed from the data obtained in this study in terms of the relevant dimensionless parameters. The correlation developed for the solution heat transfer coefficient predicts 86% of the data within ±25%

with an average absolute deviation of 10% for all the data. The correlation accounts for the solution flow rate and property variations through Re_l, and Pr_l. A pressure correction term improved the predictive capability of the correlation significantly.

$$Nu_l = 3.22 \times 10^{-3} \cdot \mathrm{Re}_l^{0.945}\, \mathrm{Pr}_l^{0.743} \left(\frac{P_{abs,ave}}{345\,kPa} \right)^{-0.269} \tag{7.1}$$

Due to the coupled nature of heat and mass transfer processes in ammonia-water absorption, the vapor-phase mass transfer correlation was developed on the basis of the heat and mass transfer analogy. The effect of liquid-side properties was also included in the mass transfer correlation to account for the transport of absorbed ammonia through the liquid phase. The resulting correlation is as follows:

$$Sh_v = 2.708 \times 10^{-11} \times \left(\frac{Gr_v \times Sc_v}{Ja_v} \right)^{1.256} \times \left(\frac{\mathrm{Pr}_l}{Sc_l} \right)^{-1.681} \times \left(\frac{\mu_l - \mu_v}{\mu_v} \right)^{1.426} \tag{7.2}$$

This correlation was developed using a vapor-phase Grashof number as the basis, because it was deemed that the vapor is relatively quiescent in the large absorption chamber with no obvious forced flow related parameters. Thus, the heat and mass transfer processes are idealized to be governed primarily by temperature and concentration differences, respectively, between the liquid and vapor phases.

A liquid-phase mass transfer correlation was also developed on the basis of the heat and mass transfer analogy. The effect of liquid-side flow rate and properties were included in the mass transfer correlation to account for the solution flow characteristics and transport properties. The resulting correlation is as follows:

$$Sh_l = 7.437 \times 10^{-4} \times \left(\mathrm{Re}_l\right)^{0.3971} \times \left(Sc_l\right)^{1.04} \times \left(\frac{P_{abs}}{345\,kPa}\right)^{0.8841} \tag{7.3}$$

These correlations can be used to design horizontal tube falling-film absorbers for use in ammonia-water absorption systems operating at conditions similar to those considered in the present study.

7.2 Recommendations

This section presents recommendations of further research based on the accomplishments of the present study. The recommendations are provided on several different aspects: analysis at local level for varying flow modes, investigation of absorber types with different geometries, test facility design and experimental procedures, and investigation of different working fluid pairs such as water/LiBr.

7.2.1 Flow Mode and Local-Level Analyses

At the fundamental level, the findings of the present study, and the underlying modeling of the flow phenomena, would be further aided by detailed investigations on a single tube to understand the evolution of the falling film, the formation of droplets, etc., and the resulting species concentration profiles in ammonia-water absorbers. These studies should be conducted using computational techniques as well as localized measurements of solution temperatures at different transverse and circumferential locations within the liquid film and along the tube length. Such studies, combined with the component and row-level measurements, would assist in strengthening the hydrodynamic bases used for the correlations developed in the present study.

7.2.2 Variations in Absorber Geometry

The present study was conducted only on tubes of a specific diameter (9.5 mm) with a specific transverse (30.6 mm) and longitudinal (20.1 mm) pitch. This study should be extended to tubes of different diameters and pitches to increase the range of applicability of the results. The absorber fabricated in this study consisted of a rectangular assembly of 24 tubes placed in a cylindrical shell with a variety of flanges and penetrations for inlets, outlets, instrumentation, illumination and visualization. Under the conditions investigated, this tube array-in-shell geometry resulted in a large vapor space, which was thought to yield a relatively quiescent vapor phase. This led to some challenges in defining vapor phase parameters, with the choice being ultimately made to model vapor-phase transport being analogous to natural convection due to the similarly quiescent medium in natural convection. While this approach resulted in a reasonable understanding of the respective phenomena, and the resulting correlations were able to represent the trends in the data well, this may not in fact be the most representative absorber geometry for ammonia-water absorbers in an actual implementation of an absorption heat pump. Because the vapor density of ammonia is much larger than that of water vapor in Water-Lithium Bromide systems, vapor-phase pressure drop is not a critical issue in determining saturation conditions in ammonia-water absorbers, and such large vapor spaces are not necessary in ammonia-water absorption systems. Similarly, the horizontal tube bank, falling-film geometry for the liquid solution phase is not essential, because pressure drop incurred in the liquid phase is not a critical penalty in ammonia-water systems, unlike H_2O-LiBr systems, which almost necessarily must have negligible pressure drops in the absorbers. Therefore, other

configurations with smaller vapor spaces and greater forced-convective transport in both phases should be studied in future investigations on ammonia-water absorption. Examples include plate heat exchangers, shell-and-tube heat exchangers, and innovative enhanced geometries for bubble-type absorbers that capitalize on the properties of the ammonia-water fluid pair. Along the lines of the above discussion, ammonia-water absorbers are amenable to miniaturization, which has been shown to yield significant reductions in component size by Meacham and Garimella (2002a; 2004). Thus, absorption in miniaturized geometries should be investigated in further detail, which will benefit small capacity and portable heat pump applications, and also small-scale absorption systems driven by solar energy and waste heat, issues that are gaining prominence in today's energy landscape.

Additionally, enhanced liquid mixing techniques to decrease mass transfer resistance in the liquid phase should be investigated to improve absorber performance. There are several techniques to increase absorber performance such as using grooved tubes to increase mixing and wetting of the liquid phase by changing solution flow characteristics, using additives to increase solution wetting and heat and mass transfer coefficients by changing solution properties, and using microchannel tubes to increase solution mixing due to increased droplet impingement sites on the tube as well as an increase in coolant-side heat transfer coefficients.

7.2.3 Test Facility Design and Experimental Procedures

Systematic experiments were conducted over a wide range of air-conditioning and heat pumping operating conditions in this study to understand heat and mass transfer in falling-film ammonia-water absorbers. Such a study that attempts to understand

component level heat and mass transfer in a full-fledged ammonia-water absorption heat pump facility over realistic operating conditions has not been conducted before.

The challenges stemming from this objective of testing over such a wide range of conditions during heat pump operation have been described in previous chapters of this dissertation. The complete absorption system used in this study also introduces additional uncertainties in establishing the dilute solution concentration and flow rate entering the absorber, and in the other important flow rates and concentrations, i.e., of the concentrated solution and the ammonia vapor. This is because mass, species and energy balances must be satisfied iteratively and simultaneously in all the major components (desorber, separator, rectifier, condenser, expansion device, refrigerant pre-cooler, evaporator, and absorber, and their respective coupling loops.) In particular, for example, the reflux liquid stream exiting the rectifier can alter the dilute solution conditions to varying degrees; but the typically very low flow rates of the reflux stream make it very difficult to measure accurately. Rectification and desorption are other coupled heat and mass transfer processes that must be understood for improved design of ammonia-water absorption systems. Thus, studies on the details of heat and mass transfer in rectifiers and desorbers should also be conducted.

7.2.4 Absorption System with Other Working Fluid Pair

The present study on absorption heat and mass transfer was conducted with an ammonia/water mixture. Since ammonia and water are both volatile components, the results are not directly applicable for the prediction of heat and mass transfer in other fluid pairs that have nonvolatile absorbents. Therefore, similar studies on other fluid pairs would assist in the understanding of coupled heat and mass transfer processes in

space-conditioning, chemical processing, waste heat recovery, and other diverse applications.

APPENDIX A: TEST CONDITIONS FOR THE REPRESENTATIVE DATA POINT

APPENDIX A. Representative Data Point

Measured Quantity	Value	Instrumentation
Absorber		
Absorber Solution Inlet Mass Flow Rate	$\dot{m}_{Dilute} = 0.02276$ kg/s	Coriolis Mass Flow Meter (CMF025)
Absorber Solution Inlet Temperature	$T_{Abs,in} = 70.4°C$	Thermocouple T-Type
Absorber Solution Inlet Pressure	$P_{Abs,in} = 351.8$ kPa	2088 Pressure Transducer
Absorber Solution Outlet Mass Flow Rate	$\dot{m}_{Concentrated} = 0.02651$ kg/s	Coriolis Mass Flow Meter (CMF025)
Absorber Solution Outlet Temperature	$T_{Abs,out} = 31°C$	Thermocouple T-Type
Absorber Solution Outlet Pressure	$P_{Abs,out} = 350.6$ kPa	3051 Pressure Transducer
Absorber Vapor Inlet Mass Flow Rate	$\dot{m}_{\mathrm{Ref},Measured} = 0.002826$ kg/s	Coriolis Mass Flow Meter (C25)
Absorber Vapor Inlet Temperature	$T_{Abs,V,in} = -0.3°C$	Thermocouple T-Type
Absorber Vapor Inlet Pressure	$P_{Abs,V,in} = 362.8$ kPa	3051 Pressure Transducer
Absorber Coolant Flow Rate	$\dot{V}_{Abs,c} = 3.04\times10^{-4}$ m^3/s	Magnetic Flow Meter (8711)
Absorber Coolant Inlet Temperature	$T_{Abs,C,in} = 12.5°C$	Thermocouple T-Type
Absorber Coolant Outlet Temperature	$T_{Abs,C,out} = 18.75°C$	Thermocouple T-Type
Desorber		
Desorber Inlet Temperature	$T_{\mathrm{Des,in}} = 87.4°C$	RTD
Desorber Inlet Pressure	$P_{\mathrm{Des,in}} = 1191$ kPa	2088 Pressure Transducer
Desorber Outlet Temperature	$T_{Des,out} = 122.4°C$	RTD
Desorber Outlet Pressure	$P_{Des,out} = 1110$ kPa	2088 Pressure Transducer
Separator		
Separator Outlet Temperature	$T_{Sep,out} = 119°C$	RTD

APPENDIX A. Continued

Measured Quantity	Value	Instrumentation
Separator Outlet Pressure	$P_{Sep,out} = 1115$ kPa	2088 Pressure Transducer
Rectifier		
Rectifier Inlet Temperature	$T_{\mathrm{Rec},in} = 119.6°C$	Thermocouple T-Type
Rectifier Vapor Outlet Temperature	$T_{\mathrm{Rec},V,out} = 81°C$	Thermocouple T-Type
Rectifier Reflux Outlet Temperature	$T_{\mathrm{Reflux}} = 51.4°C$	Thermocouple T-Type
Rectifier Reflux Outlet Pressure	$P_{\mathrm{Reflux}} = 1121$ kPa	3051 Pressure Transducer
Rectifier Coolant Flow Rate	$\dot{V}_{\mathrm{Rec},c} = 2.65\times10^{-5}$ m^3/s	Rotameter
Rectifier Coolant Inlet Temperature	$T_{\mathrm{Rec},C,in} = 9.57°C$	Thermocouple T-Type
Rectifier Coolant Outlet Temperature	$T_{\mathrm{Rec},C,out} = 41.78°C$	Thermocouple T-Type
Condenser		
Condenser Inlet Temperature	$T_{Con,in} = 57.51°C$	RTD
Condenser Inlet Pressure	$P_{Con,in} = 1127$ kPa	2088 Pressure Transducer
Condenser Outlet Temperature	$T_{Con,out} = 20.93°C$	RTD
Condenser Outlet Pressure	$P_{Con,out} = 1133$ kPa	3051 Pressure Transducer
Condenser Coolant Flow Rate	$\dot{m}_{\mathrm{Con},C} = 0.3313$ kg/s	Coriolis Mass Flow Meter (CMF100)
Condenser Coolant Inlet Temperature	$T_{\mathrm{Con},C,in} = 16.79°C$	Thermocouple T-Type
Condenser Coolant Outlet Temperature	$T_{\mathrm{Con},C,out} = 20.38°C$	Thermocouple T-Type
Evaporator		
Evaporator Inlet Temperature	$T_{Eva,in} = -3.781°C$	RTD
Evaporator Inlet Pressure	$P_{Eva,in} = 378.9$ kPa	3051 Pressure Transducer

APPENDIX A. Continued

Measured Quantity	Value	Instrumentation
Evaporator Outlet Temperature	$T_{Eva,out} = -1.906°C$	Thermocouple T-Type
Evaporator Outlet Pressure	$P_{Eva,out} = 351$ kPa	3051 Pressure Transducer
Evaporator Heating Fluid Flow Rate	$\dot{m}_{Eva,C} = 0.2056$ kg/s	Gear Flow Meter (JVM-60KL)
Evaporator Heating Fluid Temperature	$T_{Eva,C,in} = 17.14°C$	Thermocouple T-Type
Evaporator Heating Fluid Temperature	$T_{Eva,C,out} = 13.01°C$	Thermocouple T-Type

APPENDIX B: REPRESENTATIVE CALCULATIONS FOR HEAT DUTY, HEAT AND MASS TRANSFER COEFFICIENTS

APPENDIX B. Representative Data Analysis

Inputs	Equations	Results
Concentration		
$T_{Des,out} = 122.4°C$ $P_{Des,out} = 1110$ kPa $T_{Rec,V,out} = 80.99°C$ $P_{Con,in} = 1127$ kPa $T_{Reflux} = 51.4°C$ $P_{Reflux} = 1121$ kPa	$x_{Dilute,Des} = f\left(T_{Des,out},\ P_{Des,out},\ q=0\right)$ $x_{V,Des} = f\left(T_{Des,out},\ P_{Des,out},\ q=1\right)$ $x_{V} = f\left(T_{Rec,V,out},\ P_{Con,in},\ q=1\right)$ $x_{Reflux} = f\left(T_{Reflux}, P_{Reflux}, q=0\right)$	$x_{Dilute,Des} = 0.2386$ $x_{V,Des} = 0.8427$ $x_{V} = 0.9781$ $x_{Reflux} = 0.6182$
$x_{V,Des} = 0.8427$ $\dot{m}_{Ref,Measured} = 0.002826$ kg/s $x_{Reflux} = 0.6182$ $x_{V} = 0.9781$	$x_{V,Des} = x_{Sep,V,out} = x_{Rec,in}$ $\dot{m}_{Reflux} = \dot{m}_{Rec,in} - \dot{m}_{Ref,Measured}$ $\dot{m}_{Rec,in} \cdot x_{V,Des} = \dot{m}_{Reflux} \cdot x_{Reflux} + \dot{m}_{Ref,measured} \cdot x_{V}$	$\dot{m}_{Rec,in} = 0.004532$ kg/s $\dot{m}_{Reflux} = 0.001706$ kg/s
$\dot{m}_{Dilute} = 0.02276$ kg/s $\dot{m}_{Reflux} = 0.001706$ kg/s $\dot{m}_{Ref,Measured} = 0.002826$ kg/s $\dot{m}_{Concentrated} = 0.02651$ kg/s $x_{V} = 0.9781$ $x_{Reflux} = 0.6182$	$\dot{m}_{Sep,out} = \dot{m}_{Dilute} - \dot{m}_{Reflux}$ $x_{Dilute} \cdot \dot{m}_{Dilute} = \dot{m}_{Reflux} \cdot x_{Reflux} + \dot{m}_{Sep,out} \cdot x_{Dilute,Des}$ $x_{Concentrated} \cdot \dot{m}_{Concentrated} = \dot{m}_{Ref,Measure} \cdot x_{V} + \dot{m}_{Dilute} \cdot x_{Dilute}$	$\dot{m}_{Sep,out} = 0.02105$ kg/s $x_{Dilute} = 0.2671$ $x_{Concentrated} = 0.3336$
Absorber Solution-Side		
$T_{Abs,in} = 70.4°C$ $P_{Abs,in} = 351.8$ kPa $x_{Dilute} = 0.2671$	$h_{Abs,in} = f\left(T_{Abs,in}, P_{Abs,in}, x_{Dilute}\right)$ $h_{Abs,out} = f\left(T_{Abs,out}, P_{Abs,out}, x_{Concentrated}\right)$	$h_{Abs,in} = 128.9$ kJ/kg $h_{Abs,out} = -69.93$ kJ/kg

APPENDIX B. Continued

Inputs	Equations	Results
$T_{Abs,out} = 31°C$ $P_{Abs,out} = 350.6$ kPa		
$x_{Concentrated} = 0.3336$ $T_{Abs,V,in} = -0.3°C$ $P_{Abs,V,in} = 362.8$ kPa $x_V = 0.9781$ $\dot{m}_{Dilute} = 0.02276$ kg/s $\dot{m}_{\mathrm{Ref},Measured} = 0.002826$ kg/s $\dot{m}_{Concentrated} = 0.02651$ kg/s	$h_{Abs,V,in} = f\left(T_{Abs,V,in}, P_{Abs,V,in}, x_V\right)$ $Q_{Abs} = \dot{m}_{Dilute} \cdot h_{Abs,in} + \dot{m}_{\mathrm{Ref},Measured} \cdot h_{Abs,V,in} - \dot{m}_{Concentrated} \cdot h_{Abs,out}$	$h_{Abs,V,in} = 1086$ kJ/kg $Q_{Abs} = 7.854$ kW
Absorber Coolant-Side		
$T_{Abs,c,in} = 12.47°C$ $T_{Abs,c,out} = 18.75°C$ $\dot{V}_{Abs,c} = 3.04\times10^{-4}$ m³/s $\rho_{Abs,C} = 997.1$ kg/m³ $Q_{Abs} = 7.854$ kW $Tube_{Cross,Area} = 5.156\times10^{-5}$ m² $N_{Column} = 4$ $Tube_{ID} = 8.103\times10^{-3}$ m $\mu_{Abs,C} = 8.9808\times10^{-4}$ kg/m·s $k_{Abs,C} = 0.595$ W/m-K	$T_{Abs,C,Ave} = \frac{T_{Abs,C,in} + T_{Abs,C,out}}{2}$ $Cp_{\mathrm{Abs,C}} = f\left(T_{Abs,C,Ave}\right)$ $\dot{m}_{Abs,c} = \dot{V} \cdot \rho_{Abs,C}$ $Q_{\mathrm{Abs,C}} = \dot{m}_{Abs,c} \cdot Cp_{Abs,C} \cdot (T_{Abs,C,out} - T_{Abs,C,in})$ $Error_{Abs} = \left\lvert \left(Q_{Abs} - Q_{\mathrm{Abs,C}}\right) / Q_{Abs} \right\rvert \times 100$ $V_{Abs,C} = \dot{V} / \left(Tube_{Cross,Area} \cdot N_{Column}\right)$ $\mathrm{Re}_{Abs,C} = \frac{\rho_{Abs,C} \cdot V_{Abs,C} \cdot Tube_{ID}}{\mu_{Abs,C}}$	$T_{Abs,C,Ave} = 15.61°C$ $Cp_{\mathrm{Abs,C}} = 4.183$ kJ/kg·°C $\dot{m}_{Abs,c} = 0.3028$ kg/s $Q_{Abs,c} = 7.954$ kW $Error_{Abs} = 1.27\%$ $V_{Abs,C} = 1.472$ m/s $\mathrm{Re}_{Abs,C} = 13353$

APPENDIX B. Continued

Inputs	Equations	Results
$Nu_{Abs,C} = 104.3$	$\alpha_{Abs,C} = \dfrac{k_{Abs,C} \cdot Nu_{Abs,C}}{Tube_{ID}}$	$\alpha_{Abs,C} = 7653 \ \mathrm{W/m^2\text{-}K}$
Desorber Solution-Side		
$T_{\mathrm{Des,in}} = 87.4°C$ $P_{\mathrm{Des,in}} = 1191 \ \mathrm{kPa}$ $x_{\mathrm{Concentrated}} = 0.3336$	$h_{\mathrm{Des,in}} = f\left(T_{\mathrm{Des,in}}, P_{\mathrm{Des,in}}, x_{\mathrm{Concentrated}}\right)$	$h_{\mathrm{Des,in}} = 177.9 \ \mathrm{kJ/kg}$
		$h_{\mathrm{Sep,out}} = 357.3 \ \mathrm{kJ/kg}$
$T_{Sep,out} = 119°C$ $P_{Sep,out} = 1115 \ \mathrm{kPa}$ $x_{\mathrm{Dilute,Des}} = 0.2386$	$h_{\mathrm{Sep,out}} = f\left(T_{\mathrm{Sep,out}}, P_{\mathrm{Sep,out}}, x_{\mathrm{Dilute,Des}}\right)$ $h_{Sep,in} = h_{Des,out}$	$h_{Sep,in} = 177.9 \ \mathrm{kJ/kg}$
		$h_{Des,out} = 575.6 \ \mathrm{kJ/kg}$
$T_{Sep,V,out} = 122.4°C$ $P_{Sep,V,out} = 1115 \ \mathrm{kPa}$ $x_{Des,V} = 0.8427$	$h_{Sep,V,out} = f\left(T_{Sep,V,out}, P_{Sep,V,out}, x_{Des,V}\right)$	$h_{Sep,V,out} = 1707 \ \mathrm{kJ/kg}$
	$h_{Des,out}\,\dot{m}_{Concentrated} = \left(\dot{m}_{\mathrm{Ref},Measured} + \dot{m}_{\mathrm{Reflux}}\right) \cdot h_{Sep,V,out} + \left(\dot{m}_{Dilute} - \dot{m}_{\mathrm{Reflux}}\right) \cdot h_{Sep,out}$	$h_{Des,out} = 575.6 \ \mathrm{kJ/kg}$
$\dot{m}_{Dilute} = 0.02276 \ \mathrm{kg/s}$ $\dot{m}_{\mathrm{Ref},Measured} = 0.002826 \ \mathrm{kg/s}$ $\dot{m}_{Concentrated} = 0.02651 \ \mathrm{kg/s}$ $\dot{m}_{\mathrm{Reflux}} = 0.001706 \ \mathrm{kg/s}$	$Q_{Des} = h_{Des,out}\,\dot{m}_{Concentrated} - \left(\begin{array}{c}\left(\dot{m}_{\mathrm{Ref},Measured} + \dot{m}_{\mathrm{Reflux}}\right) \cdot h_{Sep,V,out} \\ + \left(\dot{m}_{Dilute} - \dot{m}_{\mathrm{Reflux}}\right) \cdot h_{Sep,out}\end{array}\right)$	$Q_{Des} = 10.54 \ \mathrm{kW}$
Evaporator Refrigerant-Side		
$T_{Eva,in} = -3.781°C$ $P_{Eva,in} = 378.9 \ \mathrm{kPa}$	$h_{\mathrm{Eva,in}} = f\left(T_{Eva,in}, P_{Eva,in}, x\right)$	$h_{\mathrm{Eva,in}} = -33.28 \ \mathrm{kJ/kg}$

APPENDIX B. Continued

Inputs	Equations	Results
$x = 0.9781$ $T_{Eva,out} = \text{-}1.906°C$ $P_{Eva,out} = 351$ kPa $x = 0.9781$ $\dot{m}_{\text{Ref},Measured} = 0.002826$ kg/s	$h_{\text{Eva,out}} = f\left(T_{Eva,out}, P_{Eva,out}, x\right)$ $Q_{\text{Eva}} = \dot{m}_{\text{Ref},Measured} \cdot \left(h_{Eva,out} - h_{Eva,in}\right)$	$h_{\text{Eva,out}} = 1051$ kJ/kg $Q_{Eva} = 3.065$ kW
Evaporator Coolant-Side		
$T_{Eva,C,in} = 17.14°C$ $T_{Eva,C,out} = 13.01°C$ $\dot{m}_{Eva,C} = 0.2056$ kg/s $Q_{Eva} = 3.065$ kW	$T_{Eva,C,Ave} = \dfrac{T_{Eva,C,in} + T_{Eva,C,out}}{2}$ $Cp_{\text{Eva,C}} = f\left(T_{Eva,C,Ave}\right)$ $Q_{\text{Eva,C}} = \dot{m}_{Eva,C} \cdot Cp_{Eva,C} \cdot \left(T_{Eva,C,in} - T_{Eva,C,out}\right)$ $Error_{Eva} = \left\lvert \left(Q_{Eva} - Q_{\text{Eva,C}}\right) / Q_{Eva} \right\rvert \times 100$	$T_{Eva,C,Ave} = 15.07°C$ $Cp_{\text{Eva,C}} = 3.299$ kJ/kg·°C $Q_{Eva,c} = 2.801$ kW $Error_{Eva} = 8.61\%$
Condenser Refrigerant-Side		
$T_{\text{Con},in} = 57.51°C$ $P_{Con,in} = 1127$ kPa $x = 0.9781$ $T_{Con,out} = 20.93°C$ $P_{Con,out} = 1133$ kPa	$h_{\text{Con,in}} = f\left(T_{Con,in}, P_{Con,in}, x\right)$ $h_{\text{Con,out}} = f\left(T_{Con,out}, P_{Con,out}, x\right)$ $Q_{\text{Con}} = \dot{m}_{\text{Ref},Measured} \cdot \left(h_{Con,in} - h_{Con,out}\right)$	$h_{\text{Con,in}} = 1321$ kJ/kg $h_{\text{Con,out}} = 82.3$ kJ/kg $Q_{Con} = 3.501$ kW

APPENDIX B. Continued

Inputs	Equations	Results
$\dot{m}_{\text{Ref},Measured} = 0.002826 \text{ kg/s}$		
Condenser Coolant-Side		
$T_{\text{Con},C,in} = 16.79°C$ $T_{\text{Con},C,out} = 20.38°C$ $\dot{m}_{\text{Con},C} = 0.3313 \text{ kg/s}$ $Q_{Con} = 3.501 \text{ kW}$	$T_{Con,C,Ave} = \frac{T_{Con,C,in} + T_{Con,C,out}}{2}$ $Cp_{\text{Con,C}} = f\left(T_{Con,C,Ave}\right)$ $Q_{\text{Con,C}} = \dot{m}_{\text{Con},C} \cdot Cp_{\text{Con,C}} \cdot \left(T_{\text{Con},C,out} - T_{\text{Con},C,in}\right)$ $Error_{Con} = \left\lvert \left(Q_{Con} - Q_{\text{Con,C}}\right) / Q_{Con} \right\rvert \times 100$	$T_{Con,C,Ave} = 18.59°C$ $Cp_{\text{Con,C}} = 3.323 \text{ kJ/kg} \cdot °C$ $Q_{Con,c} = 3.952 \text{ kW}$ $Error_{Con} = 12.9\%$
Rectifier Refrigerant-Side		
$T_{\text{Rec},in} = 119.6°C$ $P_{\text{Rec},in} = 1115 \text{ kPa}$ $x_{\text{Rec},in} = 0.8427$ $T_{\text{Rec},V,out} = 81°C$ $P_{\text{Rec},V,out} = 1127 \text{ kPa}$ $x_{\text{Rec},V,out} = 0.9781$ $T_{\text{Reflux}} = 51.4°C$ $P_{\text{Reflux}} = 1121 \text{ kPa}$	$h_{\text{Rec,in}} = f\left(T_{\text{Rec},in}, P_{\text{Rec},in}, x_{\text{Rec},in}\right)$ $h_{\text{Rec},V,out} = f\left(T_{\text{Rec},V,out}, P_{\text{Rec},V,out}, x_{\text{Rec},V,out}\right)$ $h_{\text{Reflux}} = f\left(T_{\text{Reflux}}, P_{\text{Reflux}}, x_{\text{Reflux}}\right)$ $Q_{\text{Rec}} = \left(\dot{m}_{\text{Ref},Measured} + \dot{m}_{\text{Reflux}}\right) \cdot h_{\text{Rec},in}$ $- \left(\dot{m}_{\text{Reflux}} \cdot h_{\text{Reflux}} + \dot{m}_{\text{Ref},Measured} \cdot h_{\text{Rec},V,out}\right)$	$h_{\text{Rec,in}} = 1648 \text{ kJ/kg}$ $h_{\text{Rec},V,out} = 1458 \text{ kJ/kg}$ $h_{\text{Re flux}} = 12.13 \text{ kJ/kg}$ $Q_{\text{Rec}} = 3.326 \text{ kW}$

APPENDIX B. Continued

Inputs	Equations	Results
$x_{\text{Reflux}} = 0.6182$ $\dot{m}_{\text{Ref},Measured} = 0.002826\ \text{kg/s}$ $\dot{m}_{\text{Reflux}} = 0.001706\ \text{kg/s}$		
Rectifier Coolant-Side		
$T_{\text{Rec},C,in} = 9.57°C$ $T_{\text{Rec},C,out} = 41.78°C$ $\dot{m}_{\text{Rec,c}} = 0.0277\ \text{kg/s}$ $Q_{\text{Rec}} = 3.326\ \text{kW}$	$T_{\text{Rec},C,Ave} = \frac{T_{Con,C,in} + T_{Con,C,out}}{2}$ $Cp_{\text{Rec,C}} = f\left(T_{\text{Rec},C,Ave}\right)$ $Q_{\text{Rec,C}} = \dot{m}_{\text{Rec},C} \cdot Cp_{\text{Rec},C} \cdot \left(T_{\text{Rec},C,out} - T_{\text{Rec},C,in}\right)$ $Error_{\text{Rec}} = \left\lvert \left(Q_{\text{Rec}} - Q_{\text{Rec,C}}\right) / Q_{\text{Rec}} \right\rvert \times 100$	$T_{\text{Rec},C,Ave} = 25.67°C$ $Cp_{\text{Rec,C}} = 3.494\ \text{kJ/kg}\cdot°C$ $Q_{\text{Rec,C}} = 3.125\ \text{kW}$ $Error_{\text{Rec}} = 6\%$
Absorber Heat Transfer Coefficient		
$T_{Abs,in} = 70.4°C$ $T_{Abs,out} = 31°C$ $T_{Abs,c,in} = 12.47°C$ $T_{Abs,c,out} = 18.75°C$ $Q_{Abs} = 7.854\ \text{kW}$ $Q_{Abs,c} = 7.954\ \text{kW}$ $Abs_{Area} = 0.2098\ \text{m}^2$	$LMTD_{\text{Abs}} = \frac{\left(T_{Abs,in} - T_{Abs,C,out}\right) - \left(T_{Abs,out} - T_{Abs,C,in}\right)}{\ln\left(\frac{T_{Abs,in} - T_{Abs,C,out}}{T_{Abs,out} - T_{Abs,C,in}}\right)}$ $Heat\ Duty_{Abs,ave} = \left(Q_{Abs} + Q_{\text{Abs,C}}\right)/2$ $U_{\text{Abs}} = \frac{Heat\ Duty_{Abs,ave}}{Abs_{Area} \cdot LMTD_{Abs}}$	$LMTD_{\text{Abs}} = 30.87\ °C$ $Heat\ Duty_{\text{Abs,ave}} = 7.904\ \text{kW}$ $U_{\text{Abs}} = 1221\ \text{W/m}^2\cdot°C$ $R_W = 5.267\times10^{-5}\ \text{m}^2\text{-K/W}$

APPENDIX B. Continued

Inputs	Equations	Results
$Tube_{ID} = 8.103\times10^{-3}$ m $Tube_{OD} = 9.525\times10^{-3}$ m $k_W = 14.64$ W/m-K $\alpha_{Abs,C} = 7653$ W/m^2-K	$R_W = \frac{Tube_{OD}}{2\cdot k_W}\ln\left(\frac{Tube_{OD}}{Tube_{ID}}\right)$ $\frac{1}{\alpha_{Abs,Film}} = \frac{1}{U_{Abs}} - \left(R_W + \frac{Tube_{OD}}{\alpha_{Abs,C}\cdot Tube_{ID}}\right)$ $R_{Solution} = \frac{1}{\alpha_{Abs,Film}}$, $R_{coolant} = \frac{Tube_{OD}}{\alpha_{Abs,C}\cdot Tube_{ID}}$ $RESISTANCE_{Ratio} = R_{Solution}/R_{coolant}$	$\alpha_{Abs,Film} = 1632$ W/m^2-K $R_{Solution} = 6.13\times10^{-4}$ m^2-K/W $R_{Coolant} = 1.54\times10^{-4}$ m^2-K/W $RESISTANCE_{Ratio} = 3.98$
Liquid-side Nusselt Number Calculation		
$\dot{m}_{l,ave} = 0.02463$ kg/s $N_{t,pr} = 4$ $L_t = 0.2921$ m $v_l = 1.139\times10^{-3}$ m^3/kg $\mu_l = 7.092\times10^{-4}$ kg/m-s $\alpha_{Abs,Film} = 1632$ W/m^2-K $k_l = 0.5769$ W/m-K	$\Gamma_l = \frac{\dot{m}_{l,ave}}{N_{t,pr}\cdot L_t\cdot 2}$ $\delta_{f,l} = \left[\frac{3\cdot\mu_l\cdot v_l^2\cdot\Gamma_l}{g}\right]^{1/3}\cdot\frac{2}{\pi}\int_0^{\frac{\pi}{2}}\sin^{-1/3}\theta\cdot d\theta$ $\mathrm{Re}_l = \frac{4\cdot\Gamma_l}{\mu_l}$ $Nu_l = \frac{\alpha_{Abs,Film}\cdot\delta_{f,l}}{k_l}$	$\Gamma_l = 1.054\times10^{-3}$ kg/m-s $\delta_{f,l} = 1.924\times10^{-4}$ m $\mathrm{Re}_l = 59.45$ $Nu_l = 0.5443$
$\mu_l = 7.092\times10^{-4}$ kg/m-s $c_{p,l} = 4.296$ kJ/kg-K $k_l = 0.5769$ W/m-K	$\mathrm{Pr}_l = \frac{\mu_l\cdot c_{p,l}}{k_l}$	$\mathrm{Pr}_l = 5.281$

APPENDIX B. Continued

Inputs	Equations	Results
Interface Concentration		
	$T_{\min} = f\left(T_{\text{Abs,out}}, T_{sol,pool}, T_{\min,profile}\right)$	
$T_{Abs,out} = 30.99°C$ $T_{sol,pool} = 29.84°C$ $T_{\min,profile} = 31.76°C$		$T_{\min} = 29.84°C$
$P_{Abs,in} = 351.8$ kPa $P_{Abs,out} = 350.6$ kPa	$P_{\text{Abs,ave}} = \frac{P_{Abs,in} + P_{Abs,out}}{2}$ $x_{\text{V,bulk}} = f\left(T_{\min}, P_{Abs,ave}, q = 1\right)$ $\tilde{x}_{\text{V,bulk}} = \frac{x_{\text{V,bulk}} / M_{NH_3}}{x_{\text{V,bulk}} / M_{NH_3} + 1 - x_{\text{V,bulk}} / M_{H_2O}}$	$P_{\text{Abs,ave}} = 351.2$ kPa $x_{\text{V,bulk}} = 0.9965$ $\tilde{x}_{\text{V,bulk}} = 0.9967$
$T_{Abs,in} = 70.42°C$ $T_{Abs,out} = 30.99°C$	$T_{\text{int}} = T_{\text{sol,ave}} = \frac{T_{Abs,in} + T_{Abs,out}}{2}$ $P_{\text{int}} = P_{\text{Abs,ave}}$	$T_{\text{int}} = 50.71^{\text{o}}\text{C}$
$M_{H_2O} = 18.02$ kg/mol $M_{NH_3} = 17.03$ kg/mol	$x_{\text{sol,int}} = f\left(T_{\text{int}}, P_{\text{int}}, q = 0\right)$ $\tilde{x}_{\text{sol,int}} = \frac{x_{\text{sol,int}} / M_{NH_3}}{x_{\text{sol,int}} / M_{NH_3} + 1 - x_{\text{sol,int}} / M_{H_2O}}$ $x_{\text{V,int}} = f\left(T_{\text{int}}, P_{\text{int}}, q = 1\right)$	$x_{\text{sol,int}} = 0.3716$ $\tilde{x}_{\text{sol,int}} = 0.3849$ $x_{\text{V,int}} = 0.9814$ $\tilde{x}_{\text{V,int}} = 0.9824$

APPENDIX B. Continued

Inputs	Equations	Results
	$\tilde{x}_{\mathrm{V,int}} = \dfrac{x_{\mathrm{V,int}} / M_{NH_3}}{x_{\mathrm{V,int}} / M_{NH_3} + (1 - x_{\mathrm{V,int}}) / M_{H_2O}}$	
Condensing Flux Concentration		
$P_{\mathrm{H_2O},l} = 351.8$ kPa $P_{\mathrm{NH_3},l} = 351.8$ kPa $T_{\mathrm{int}} = 50.71°C$	$h_{\mathrm{H_2O},v} = f\left(P_{\mathrm{H_2O},l}, x_{\mathrm{H_2O},l} = 0,1\right)$ $h_{\mathrm{H_2O},l} = f\left(P_{\mathrm{H_2O},l}, x_{\mathrm{H_2O},l} = 0,0\right)$ $h_{\mathrm{fg,H_2O}} = h_{\mathrm{H_2O},v} - h_{\mathrm{H_2O},l}$ $h_{\mathrm{NH_3},v} = f\left(P_{\mathrm{NH_3},l}, x_{\mathrm{NH_3},l} = 1,1\right)$ $h_{\mathrm{NH_3},l} = f\left(P_{\mathrm{NH_3},l}, x_{\mathrm{NH_3},l} = 1,0\right)$ $h_{\mathrm{fg,NH_3}} = h_{\mathrm{NH_3},v} - h_{\mathrm{NH_3},l}$ $h_{\mathrm{sol,int}} = f\left(T_{\mathrm{int}}, P_{\mathrm{int}}, q = 0\right)$ $h_{\mathrm{V,int}} = f\left(T_{\mathrm{int}}, P_{\mathrm{int}}, q = 1\right)$ $h_{\mathrm{V,bulk}} = f\left(T_{\mathrm{min}}, P_{Abs,ave}, q = 1\right)$	$h_{\mathrm{H_2O},v} = 2732$ kJ/kg $h_{\mathrm{H_2O},l} = 585.3$ kJ/kg $h_{\mathrm{NH_3},v} = 1262$ kJ/kg $h_{\mathrm{NH_3},l} = -24.32$ kJ/kg $h_{\mathrm{fg,H_2O}} = 2146$ kJ/kg $h_{\mathrm{fg,NH_3}} = 1287$ kJ/kg $h_{\mathrm{sol,int}} = 3.489$ kJ/kg $h_{\mathrm{V,int}} = 1416$ kJ/kg $h_{\mathrm{V,bulk}} = 1351$ kJ/kg
$\dot{m}_{\mathrm{Ref},Measured} = 0.002826$ kg/s $h_{\mathrm{V,bulk}} = 1351$ kJ/kg $h_{\mathrm{V,int}} = 1416$ kJ/kg $h_{\mathrm{sol,int}} = 3.489$ kJ/kg $h_{sol,bulk} = 28.73$ kJ/kg $Q_{Abs,c} = 7.954$ kW	$\dot{m}_{\mathrm{Ref},Measured} = \dot{m}_{V,in}$ $Q_{\mathrm{V,sensible}} = \dot{m}_{V,in} \cdot \left(h_{\mathrm{V,bulk}}(T_{V,bulk}, P_{Abs,ave}, q = 1) - h_{V,\mathrm{int}}(T_{\mathrm{int}}, P_{\mathrm{int}}, q = 1)\right)$ $Q_{\mathrm{V,latent}} = \dot{m}_{V,in} \cdot \left(h_{\mathrm{V,int}}(T_{\mathrm{int}}, P_{\mathrm{int}}, q = 1) - h_{sol,\mathrm{int}}(T_{\mathrm{int}}, P_{\mathrm{int}}, q = 0)\right)$	$\dot{m}_{V,in} = 0.002826$ kg/s $Q_{\mathrm{V,sensible}} = -0.185$ kW $Q_{\mathrm{V,latent}} = 3.992$ kW $Q_{\mathrm{V,sensible,cond}} = -0.071$ kW $Q_{\mathrm{sol,sensible}} = 4.218$ kW

APPENDIX B. Continued

Inputs	Equations	Results
	$Q_{\text{V,sensible,cond}} = \dot{m}_{V,in} \cdot \left(h_{sol,\text{int}}(T_{\text{int}}, P_{\text{int}}, q=0) - h_{sol,bulk}(T_{sol,bulk}, P_{\text{int}}, x = x_{Abs,ave}) \right)$ $Q_{\text{sol,sensible}} = Q_{\text{Abs,C}} - (Q_{\text{V,sensible}} + Q_{\text{V,latent}} + Q_{\text{V,sensible,cond}})$	
$h_{\text{fg,H}_2\text{O}} = 2146 \text{ kJ/kg}$ $h_{\text{fg,NH}_3} = 1287 \text{ kJ/kg}$	$h_{\text{V,latent}} = h_{\text{V,int}}(T_{\text{int}}, P_{\text{int}}, q=1) - h_{sol,\text{int}}(T_{\text{int}}, P_{\text{int}}, q=0)$ $h_{\text{V,latent}} = z \times h_{\text{fg,NH}_3} + (1-z) \times h_{\text{fg,H}_2\text{O}}$ $\tilde{z} = \dfrac{z / M_{NH_3}}{z / M_{NH_3} + 1 - z / M_{H_2O}}$	$h_{\text{V,latent}} = 1413 \text{ kJ/kg}$ $z = 0.8534$ $\tilde{z} = 0.8603$
Mass Transfer Coefficient in Vapor-Phase		
$Abs_{in} : L = 0$ $Abs_{out} : L = 8$ $T_{\text{Abs,out}} = 31°C$ $T_{sol,pool} = 29.8°C$ $\tilde{z} = 0.8603$ $\dot{m}_{\text{Ref,Measured}} = 0.002826 \text{ kg/s}$ $Abs_{area,M} = 0.3487 \text{ m}^2$ $P_{Abs,ave} = 351.2 \times 10^3 \text{ Pa}$	$T = 65.81 - 10.24 \times L + 1.39 \times L^2 - 0.084 \times L^3$ $T_{\text{min}} = f\left(T_{\text{Abs,out}}, T_{sol,pool}, T_{\text{min},profile}\right)$ $\dot{m}_{\text{Ref,Measured}} = \dot{m}_{vap}$ $\dot{m}_{\text{Ref,Measured}} = \dot{m}_{vap}$ $\dot{n}_T = \dfrac{-\dot{m}_{vap}}{Abs_{area,M} \cdot \left(\tilde{z} \cdot M_{NH_3} + (1-\tilde{z}) M_{H_2O}\right)}$ $x_{\text{V,bulk}} = \tilde{y}_{1b}, \; x_{\text{V,int}} = \tilde{y}_{10}$	$T_{\text{min}} = 29.84°\text{C}$ $\dot{m}_{vap} = 0.002826 \text{ kg/s}$ $\dot{n}_T = 0.0004721 \text{ kmol/s-m}^2$ $\tilde{y}_{1b} = 0.9967$ $\tilde{y}_{10} = 0.9824$ $C_T = 0.1394 \text{ kmol/m}^3$

APPENDIX B. Continued

Inputs	Equations	Results
$R = 8314$ J/kmol - K $M_{H_2O} = 18.02$ kg/kmol $M_{NH_3} = 17.03$ kg/kmol $\tilde{x}_{V,bulk} = 0.9967$ $\tilde{x}_{V,int} = 0.9824$	$C_T = \frac{P_{Abs,ave}}{R \cdot (T_{min} + 273.15K)}$ $\dot{n}_T = \beta_v \cdot C_T \ln\left[\frac{\tilde{z} - \tilde{y}_{10}}{\tilde{z} - \tilde{y}_{1b}}\right]$	$\beta_v = 0.0304$ m/s
Vapor-side Sherwood Number		
$D_{aw,v} = 8.438 \times 10^{-6}\ m^2/s$ $d_{o,t} = 9.525 \times 10^{-3}$ m $\beta_v = 0.0304$	$Sh_v = \frac{\beta_v \cdot d_{o,t}}{D_{aw,v}}$	$Sh_v = 34.32$
Vapor-side Heat and Mass Transfer Coefficients by Heat and Mass Transfer Analogy		
$\dot{m}_{v,i} = 3.522 \times 10^{-3}$ kg/s $\dot{m}_{v,o} = 0$ kg/s $L_t = 0.2921$ m $d_{o,t} = 9.525 \times 10^{-3}$ m $N_{t,pr} = 4$ $N_{t,pp} = 6$ $\mu_v = 1.068 \times 10^{-5}$ kg/m - s $v_v = 4.056 \times 10^{-1}$ m^3/kg	$\dot{m}_v = (\dot{m}_{v,i} + \dot{m}_{v,o})/2$ $A_{frontal} = L_t^2$ $A_{free} = A_{frontal} - N_{t,pr} \cdot d_{ot} \cdot L_t$ $V_{frontal,v} = \frac{\dot{m}_v \cdot v_v}{A_{frontal}}$ $V_{max,v} = \frac{A_{free}}{A_{frontal}} V_{frontal,v}$ $Re_{max,v} = \frac{V_{max,v} \cdot d_{ot}}{v_v \cdot \mu_v}$ $Re_{max,v} < 10^4$:	$\dot{m}_v = 1.761 \times 10^{-3}$ kg/s $A_{frontal} = 3.502 \times 10^{-2}$ m^2 $A_{free} = 2.389 \times 10^{-2}$ m^2 $V_{frontal,v} = 3.273 \times 10^{-2}$ m/s $V_{max,v} = 4.798 \times 10^{-2}$ m/s $Re_{max,v} = 105.5$

APPENDIX B. Continued

Inputs	Equations	Results
	$Nu_v = 0.3 + \frac{0.62 \cdot \mathrm{Re}_{\max,v}^{1/2} \cdot \mathrm{Pr}_v^{1/3}}{\left[1+(0.4/Pr)^{2/3}\right]^{1/4}}$ $2\times10^4 < \mathrm{Re}_{\max,v} < 4\times10^5$: $Nu_v = 0.3 + \frac{0.62 \cdot \mathrm{Re}_{\max,v}^{1/2} \cdot \mathrm{Pr}_v^{1/3}}{\left[1+(0.4/Pr)^{2/3}\right]^{1/4}}\left[1+\left(\frac{\mathrm{Re}_{\max,v}}{282,000}\right)^{1/2}\right]$ $4\times10^5 < \mathrm{Re}_{\max,v} < 5\times10^6$:	
$\mathrm{Re}_{\max,v} = 105.5$ $\mathrm{Pr}_v = 0.8664$ $k_v = 2.987\times10^{-2}$ W/m-K $\mu_v = 1.068\times10^{-5}$ kg/m-s $v_v = 4.056\times10^{-1}$ m^3/kg $D_{aw,v} = 8.438\times10^{-6}$ m^2/s $d_{o,t} = 9.525\times10^{-3}$ m	$Nu_v = 0.3 + \frac{0.62 \cdot \mathrm{Re}_{\max,v}^{1/2} \cdot \mathrm{Pr}_v^{1/3}}{\left[1+(0.4/Pr)^{2/3}\right]^{1/4}}\left[1+\left(\frac{\mathrm{Re}_{\max,v}}{282,000}\right)^{5/8}\right]^{4/5}$ $\alpha_v = \frac{Nu_v \cdot k_v}{d_{o,t}}$, $Sc_{v,\text{analogy}} = \frac{\mu_v \cdot v_v}{D_{aw,v}}$, $Sh_{v,\text{analogy}} = Nu_v \cdot \left[\frac{Sc_v}{\mathrm{Pr}_v}\right]^{1/3}$ $\beta_{v,\text{analogy}} = \frac{Sh_{v,test} \cdot D_{aw,v}}{d_{o,t}}$	$Nu_v = 5.699$ $\alpha_v = 17.87$ W/m^2-K $Sc_v = 0.5136$ $Sh_{v,\text{analogy}} = 4.788$ $\beta_{v,\text{analogy}} = 4.241\times10^{-3}$ m/s
Mass Transfer Coefficient in Liquid-Phase		
$\dot{m}_{\text{Ref},Measured} = 0.002826$ kg/s $x_{vap,in} = 0.9781$ $Abs_{area,M} = 0.3487$ m^2	$\dot{m}_A = \dot{m}_{\text{Ref},Measured} \cdot x_{vap,in}$ $\dot{m}_A = \beta_l \cdot Abs_{area,M} \cdot \left(z_{A,sol} \cdot \rho_{sol,\text{int}} - x_{A,sol,bulk} \cdot \rho_{sol,bulk}\right)$	$\dot{m}_A = 0.002826$ kg/s $\beta_l = 2.313\times10^{-5}$ m/s
Liquid-side Sherwood Number		

APPENDIX B. Continued

Inputs	Equations	Results
$\mu_l = 7.092\times10^{-4}$ kg/m-s $v_l = 1.139\times10^{-3}$ m^3/kg $D_{aw,l} = 5.09\times10^{-9}$ m^2/s $\beta_l = 2.313\times10^{-5}$ m/s $\delta_{f,l} = 1.924\times10^{-4}$ m	$Sc_l = \frac{\mu_l \cdot v_l}{\mathrm{D_{aw,l}}}$ $Sh_l = \frac{\beta_L \cdot \delta_l}{D_{aw,l}}$	$Sc_l = 158.8$ $Sh_l = 0.8745$
Liquid-side Heat and Mass Transfer Coefficients by Heat and Mass Transfer Analogy		
$Nu_l = 0.5443$ $\mathrm{Pr}_l = 5.281$ $Sc_l = 158.8$	$Sh_{l,\mathrm{analogy}} = \frac{\beta_L \cdot \delta_l}{D_{aw,l}} = Nu_l \cdot \left(\frac{Sc_l}{\mathrm{Pr}_l}\right)^{1/3}$	$Sh_{l,\mathrm{analogy}} = 1.692$
Ammonia Properties		
$T_{v,bulk} = 303\mathrm{K}$ $\varepsilon_a / k = 558\mathrm{K}$ $\sigma_a = 2.90\,\mathrm{\AA}$ $M_a = 17.03$ kg/kmol	$\Omega_{a,\mu} = 0.7221 - 1.5748\times10^{-3}\cdot\frac{T_{v,bulk}}{\varepsilon_a/k} + \frac{5.5435\cdot0.1859}{0.1859+\frac{T_{v,bulk}}{\varepsilon_a/k}}$ $\mu_{a,v} = 2.67\times10^{-6}\cdot\frac{\sqrt{M_a\cdot T_{v,bulk}}}{\sigma_a^{\,2}\cdot\Omega_{a,\mu}}$	$\Omega_{a,\mu} = 2.135$ $\mu_{a,v} = 1.068\times10^{-5}$ kg/m-s

APPENDIX B. Continued

Inputs	Equations	Results
$\Omega_{a,\mu} = 2.135$ $T_{v,bulk} = 303\text{K}$ $\sigma_a = 2.90\ \text{Å}$ $M_a = 17.03\ \text{kg/kmol}$ $N_{r,a} = 3$ $R = 8314\ \text{J/kmol-K}$ $\mu_{a,v} = 1.068\times10^{-5}\ \text{kg/m-s}$	$\Omega_{a,k} = \Omega_{a,\mu}$ $k_{a,v,translational} = 8.32\times10^{-2}\cdot\frac{\sqrt{T_{v,bulk}/M_a}}{\sigma_a^{\,2}\cdot\Omega_{a,k}}$ $c_{p,a,v} = (5+N_{r,a})\cdot\left[\frac{1}{2}\cdot\frac{R}{M_a}\right]$ $k_{a,v} = k_{a,v,translational} + 1.32\left(c_{p,a,v} - \frac{5}{2}\cdot\frac{R}{M_a}\right)\cdot\mu_{a,v}$	$\Omega_{a,k} = 2.135$ $k_{a,v,translational}$ $= 1.954\times10^{-2}\ \text{W/m-K}$ $c_{p,a,v} = 1953\ \text{J/kg-K}$ $k_{a,v} = 2.987\times10^{-2}\ \text{W/m-K}$
Water Vapor Properties		
$T_{v,bulk} = 303\text{K}$ $(\varepsilon_a/k)_\mu = 809.1\text{K}$ $\sigma_{w,\mu} = 2.641\ \text{Å}$ $M_a = 18.02\ \text{kg/kmol}$	$\Omega_{w,\mu} = 0.7221 - 1.5748\times10^{-3}\cdot\frac{T_{v,bulk}}{(\varepsilon_w/k)_\mu} + \frac{5.5435\cdot0.1859}{0.1859+\frac{T_{v,bulk}}{(\varepsilon_a/k)_\mu}}$ $\mu_{w,v} = 2.67\times10^{-6}\cdot\frac{\sqrt{M_w\cdot T_{v,bulk}}}{\sigma_{w,\mu}^{\,2}\cdot\Omega_{w,\mu}}$	$\Omega_{w,\mu} = 2.561$ $\mu_{w,v} = 1.105\times10^{-5}\ \text{kg/m-s}$

APPENDIX B. Continued

Inputs	Equations	Results
$\Omega_{w,\mu} = 2.561$ $T_{v,bulk} = 303\text{K}$ $M_w = 18.02$ kg/kmol $\sigma_a = 2.641\ \text{Å}$ $N_{r,w} = 3$ $R = 8314$ J/mol-K $\mu_{w,v} = 1.105\times10^{-5}$ kg/m-s	$\Omega_{w,k} = \Omega_{w,\mu}$ $k_{w,v,translational} = 8.32\times10^{-2}\cdot\frac{\sqrt{T_{v,bulk}/M_w}}{\sigma_w^{\,2}\cdot\Omega_{w,k}}$ $c_{p,w,v} = (5+N_r)\cdot\left[\frac{1}{2}\cdot\frac{R}{M_w}\right]$ $k_{w,v} = k_{w,v,translational} + 1.32\left(c_{p,w,v} - \frac{5}{2}\cdot\frac{R}{M_w}\right)\cdot\mu_{w,v}$	$\Omega_{w,k} = 2.561$ $k_{w,v,translational}$ $= 1.911\times10^{-2}$ W/m-K $c_{p,w,v} = 1846$ J/kg-K $k_{w,v} = 2.92\times10^{-2}$ W/m-K
Ammonia and Water Vapor Properties		
$\mu_{a,v} = 1.068\times10^{-5}$ kg/m-s $\mu_{w,v} = 1.105\times10^{-5}$ kg/m-s $M_a = 17.03$ kg/kmol $M_w = 18.02$ kg/kmol	$\Phi_{aw} = \frac{\left[1+(\mu_{a,v}/\mu_{w,v})^{\frac{1}{2}}\cdot(M_w/M_a)^{\frac{1}{4}}\right]^2}{\sqrt{8}\cdot\left[1+(M_a/M_w)\right]^{\frac{1}{2}}}$ $\Phi_{wa} = \frac{\left[1+(\mu_{w,v}/\mu_{a,v})^{\frac{1}{2}}\cdot(M_a/M_w)^{\frac{1}{4}}\right]^2}{\sqrt{8}\cdot\left[1+(M_w/M_a)\right]^{\frac{1}{2}}}$	$\Phi_{aw} = 1.011$ $\Phi_{wa} = 0.9885$

APPENDIX B. Continued

Inputs	Equations	Results
Binary Vapor Mixture Properties		
$x_{v,bulk} = 0.9965$ $M_a = 17.03$ kg/kmol $M_w = 18.02$ kg/kmol $\mu_{a,v} = 1.068\times10^{-5}$ kg/m - s $\mu_{w,v} = 1.105\times10^{-5}$ kg/m - s $k_{a,v} = 2.987\times10^{-2}$ W/m - K $k_{w,v} = 2.92\times10^{-2}$ W/m - K $\Phi_{aw} = 1.011$ $\Phi_{wa} = 0.9885$	$\frac{1}{M_{mix}} = \frac{x_{v,bulk}}{M_a} + \frac{1-x_{vbulk}}{M_w}$ $\tilde{x}_{v,bulk} = x_{v,bulk}\frac{M_{mix}}{M_a}$ $\quad \tilde{x}_a = \tilde{x}_{v,bulk}$ $\quad \tilde{x}_w = 1-\tilde{x}_{v,bulk}$ $\mu_v = \sum_{i=1}^{n} \frac{\tilde{x}_i \cdot \mu_{i,v}}{\sum_{j=1}^{n} \tilde{x}_j \cdot \Phi_{ij}}$ $k_v = \sum_{i=1}^{n} \frac{\tilde{y}_i, v \cdot k_{i,v}}{\sum_{j=1}^{n} \tilde{y}_{j,v} \cdot \Phi_{ij,v}}$	$M_{mix} = 17.03$ kg/kmol $\tilde{x}_{v,bulk} = 0.9967$ $\tilde{x}_a = 0.9967$ $\tilde{x}_w = 0.003266$ $\mu_v = 1.068\times10^{-5}$ kg/m - s $k_v = 2.987\times10^{-2}$ W/m - K
$T_{v,bulk} = 303$K $p_{v,bulk} = 351.2$ kPa $x_{v,bulk} = 0.9965$	$v_v = f(T_{v,bulk} \cdot P_{v,bulk}, x_{v,bulk})$ $h_0 = f(T_{v,bulk} \cdot x_{v,bulk}, q = 1)$ $p_0 = f(T_{v,bulk} \cdot x_{v,bulk}, q = 1)$ $h_0 = f(T_{v,bulk} + 1 \cdot P_o, x_{v,bulk})$ $c_{p,v} = h_1 - h_0$	$v_v = 4.056\times10^{-1}$ m^3/kg $h_0 = 1351$ kJ/kg - K $h_1 = 1352$ kJ/kg - K $c_{p,v} = 1.953$ kJ/kg - K
$\mu_v = 1.068\times10^{-5}$ kg/m - s $k_v = 2.987\times10^{-2}$ W/m - K $c_{p,v} = 1.953$ kJ/kg - k	$\mathrm{Pr}_v = \frac{\mu_v \cdot c_{p,v}}{k_v}$	$\mathrm{Pr}_v = 0.8664$

APPENDIX B. Continued

Inputs	Equations	Results
$\varepsilon_a / k = 558\text{K}$ $(\varepsilon_w / k)_D = 32\text{K}$ $\sigma_a = 2.90\ \text{Å}$ $\sigma_{w,D} = 3.737\ \text{Å}$ $T_{v,bulk} = 303\text{K}$ $M_a = 17.03$ kg/kmol $M_w = 18.02$ kg/kmol	$(\varepsilon_{aw} / k)_D = \sqrt{\varepsilon_a / k \cdot (\varepsilon_w / k)_D}$ $\sigma_{aw,D} = \frac{1}{2}(\sigma_a + \sigma_{w,D})$ $\Omega_{a,w} = 0.6716 - 1.8682x10^{-3} \cdot \frac{T_{v,bulk}}{(\varepsilon_{aw} / k)_D} + \frac{6.4284 \cdot 0.1369}{0.1369 + \frac{T_{v,bulk}}{(\varepsilon_a / k)_D}}$	$(\varepsilon_{aw} / k)_D = 133.6\text{K}$ $\sigma_{aw,D} = 3.319\ \text{Å}$ $\Omega_{aw,D} = 1.033$
$T_{v,bulk} = 303\text{K}$ $P_{v,bulk} = 351.2$ kPa $\sigma_{aw,D} = 3.319\ \text{Å}$ $\Omega_{aw,D} = 1.033$ $M_a = 17.03$ kg/kmol $M_w = 18.02$ kg/kmol	$D_{aw,v} = 1.867x10^{-7} \cdot \frac{\sqrt{T^3_{v,bulk} \cdot \left[\frac{1}{M_a} + \frac{1}{M_w}\right]}}{\sigma^2_{aw,D} \cdot \Omega_{aw,D} \cdot P_{v,bulk}}$	$D_{aw,v} = 8.438\times10^{-6}\ \text{m}^2/\text{s}$
Binary Liquid Properties		
$T_{l,ave} = 50.71°C$ $P_{l,ave} = 351.2$ kPa $x_{l,ave} = 0.3003$ $x_{l,ave} = 0.3003$	$T_{l,ave,F} = (\frac{9}{5}) \cdot T_{l,ave} + 32$ $P_{l,ave} = P_{v,bulk}$	$T_{l,ave,F} = 123.3°F$ $\sigma_{l,dyne/cm} = 36.32$ dyne/cm $\sigma_l = 3.632\times10^{-2}\ \text{kg/s}^2$

APPENDIX B. Continued

Inputs	Equations	Results
	$\sigma_{l,dyne/cm} = 1.1211\times10^{-6}\cdot T^{3}_{l,ave,F} - 1.1955\times10^{-3}\cdot T^{2}_{l,ave,F}$ $+0.2970413\cdot T_{l,ave,F} - 0.6204\times10^{1}\cdot x^{3}_{l,ave,F}$ $+103.3571\cdot x^{2}_{l,ave,F} - 4.857\times10^{1}\cdot x_{l,ave,F}$ $+39.92207 + 1.9450\times10^{-4}\cdot x^{2}_{l,ave,F}\cdot T^{2}_{l,ave,F}$ $+0.1851776\cdot x^{2}_{l,ave,F}\cdot T_{l,ave,F}$ $+0.140568\times10^{-3}\cdot x_{l,ave,F}\cdot T^{2}_{l,ave,F} - 7.0072\times10^{-1}\cdot T^{3}_{l,ave,F}$ $\sigma_l = \sigma_{l,dyne/cm}\cdot 9.7254\times10^{-4}$	
$T_{l,ave,F} = 123.3°F$ $x_{l,ave} = 0.3003$	$T_{l,ave,F} < 145^{o}F$: $\mu_{l,cp} = 2.5210 + 1.0675\cdot x_{l,ave} + 2.2685\times10^{-3}\cdot T_{l,ave,F}$ $-1.0675\cdot(1-x_{l,ave})\cdot T_{l,ave} - 5.2229\cdot x^{2}_{l,ave}$ $+112.90\times10^{-6}(1-x_{l,ave})^{2}\cdot T^{2}_{l,ave}$ $-0.8639\cdot x^{3}_{l,ave} + 2.4387\cdot x^{4}_{l,ave}$ $145^{o}F < T_{l,ave,F} < 195^{o}F$: $\mu_{l,cp} = 1.0816 - 0.2202\cdot x_{l,ave} + 2.17323\times10^{-3}\cdot T_{l,ave,F}$ $-1.9322\times10^{-3}\cdot(1-x_{l,ave})\cdot T_{l,ave} - 0.3905\cdot x^{2}_{l,ave}$ $T_{l,ave,F} > 195^{o}F$: $\mu_{l,cp} = 0.5279 + 0.1654\cdot x_{l,ave} + 1.8905\times10^{-3}\cdot T_{l,ave,F}$ $+734.47\times10^{-6}\cdot(1-x_{l,ave})\cdot T_{l,ave,F}$ $\mu_l = \mu_{l,cp}\cdot 1\times10^{-3}$	$\mu_{l,cp} = 0.7092$ cp $\mu_l = 7.092\times10^{-4}$ kg/m - s

APPENDIX B. Continued

Inputs	Equations	Results
$T_{l,ave} = 50.71°C$ $x_{l,ave} = 0.3003$	$k_l = 0.5727 + 1.0702\times10^{-3}\cdot T_{l,ave} - 0.0541\cdot x_{l,ave}$ $-5.8359\times10^{-6}\cdot T^2_{l,ave} + 8.4900\cdot\times10^{-9} x^2_{l,ave}$ $-3.3410\times10^{-3}\cdot T^2_{l,ave}\cdot x_{l,ave}$	$k_l = 0.5769$ W/m - K
$T_{l,ave} = 50.71°C$ $P_{l,ave} = 351.2$ kPa $x_{l,ave} = 0.3003$	$v_l = f(T_{l,ave}\cdot P_{l,ave}, x_{l,ave})$ $h_0 = f(T_{l,ave}\cdot x_{l,ave}, q = 0)$ $P_o = f(T_{l,ave}\cdot x_{l,ave}, q = 0)$ $h_1 = f(T_{l,ave} + 1\cdot P_o, x_{l,ave})$ $c_{p,l} = h_1 - h_0$	$v_l = 1.139\times10^{-3}$ m^3/kg $h_0 = 24.31$ kJ/kg - K $h_1 = 28.61$ kJ/kg - K $c_{p,l} = 4.296$ kJ/kg - K
$M_a = 17.03$ kg/kmol $M_w = 18.02$ kg/kmol $x_{l,ave} = 0.3003$ $T_{l,ave} = 50.71°C$ $R = 8314$ J/kmol - K	$\frac{1}{M_{l,mix}} = \frac{x_{l,ave}}{M_a} + \frac{1-x_{l,ave}}{M_w}$ $\tilde{x}_{l,ave} = x_{l,ave}\frac{M_{l,mix}}{M_a}$ $D_{aw,l} = (1.65+2.47\times x_{l,ave})\times10^{-6}\times e^{(-16600/(R\times(T_{l,ave}+273.15)))}$	$\tilde{x}_{l,ave} = 0.3124$ $D_{aw,l} = 5.09\times10^{-9}$ m^2/s

APPENDIX C: OVERALL, COOLANT, AND SOLUTION HEAT TRANSFER COEFFICIENTS

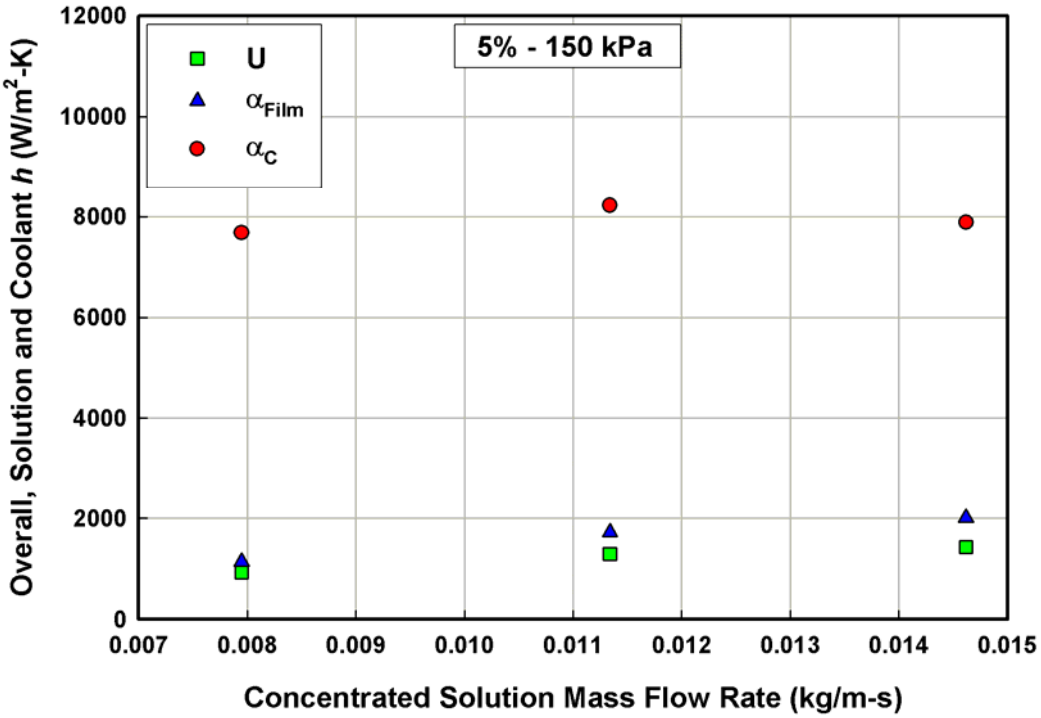

Figure C.1. Overall, Coolant, and Film Heat Transfer Coefficients at Nominal Conditions of 5%, 150 kPa (21.8 psi)

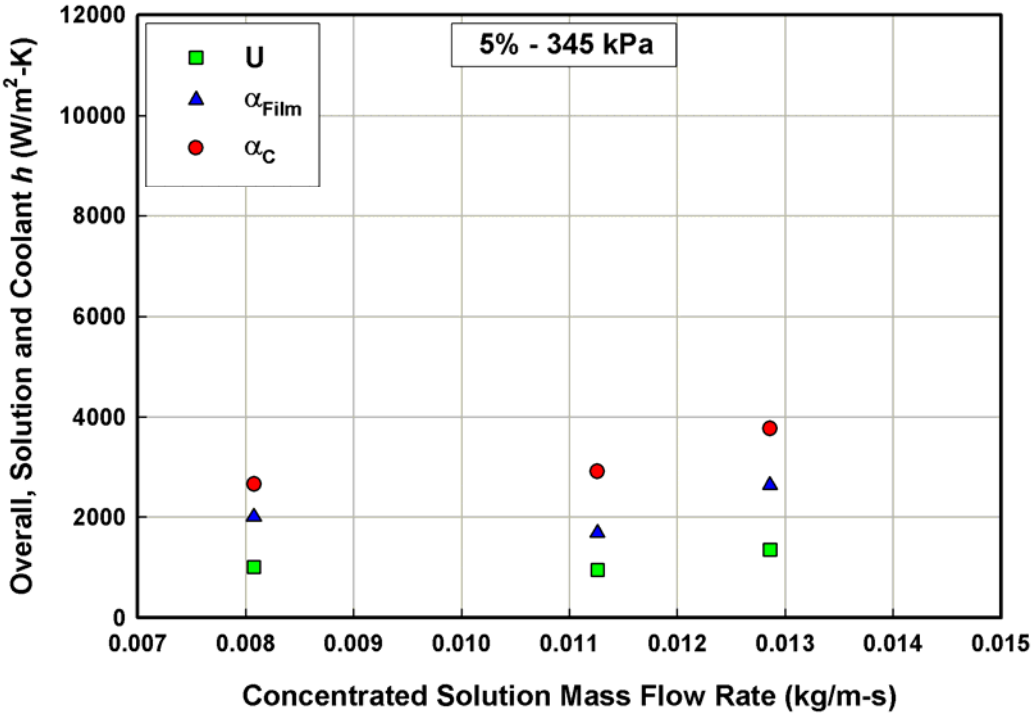

Figure C.2. Overall, Coolant, and Film Heat Transfer Coefficients at Nominal Conditions of 5%, 345 kPa (50.0 psi)

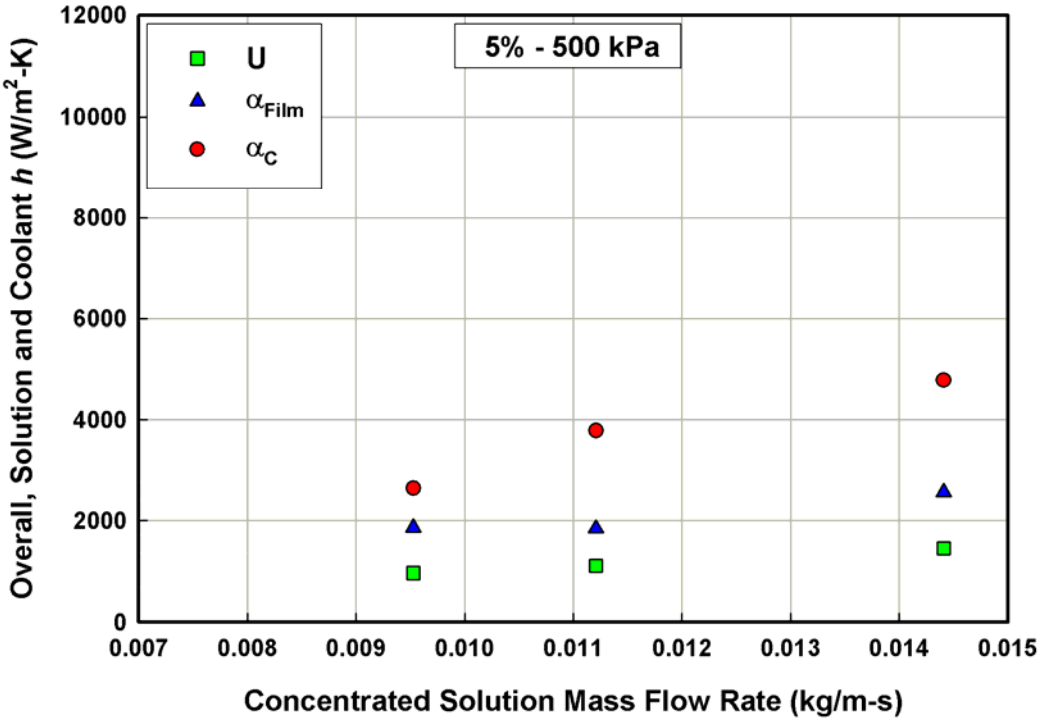

Figure C.3. Overall, Coolant, and Film Heat Transfer Coefficients at Nominal Conditions of 5%, 500 kPa (72.5 psi)

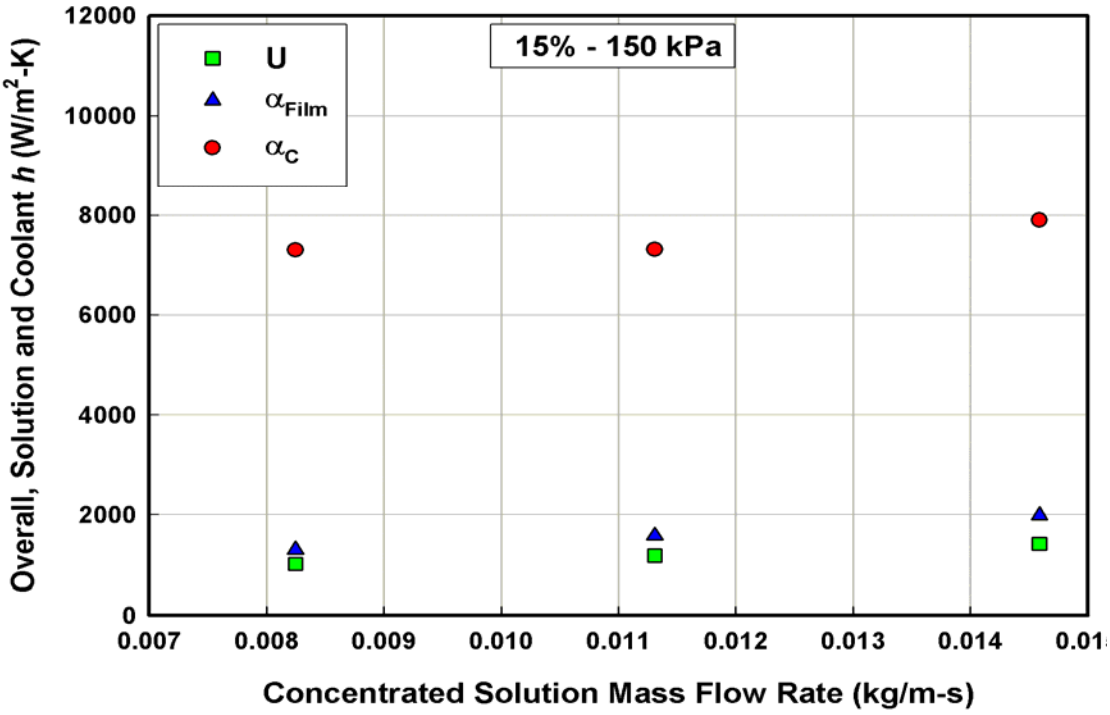

Figure C.4. Overall, Coolant, and Film Heat Transfer Coefficients at Nominal Conditions of 15%, 150 kPa (21.8 psi)

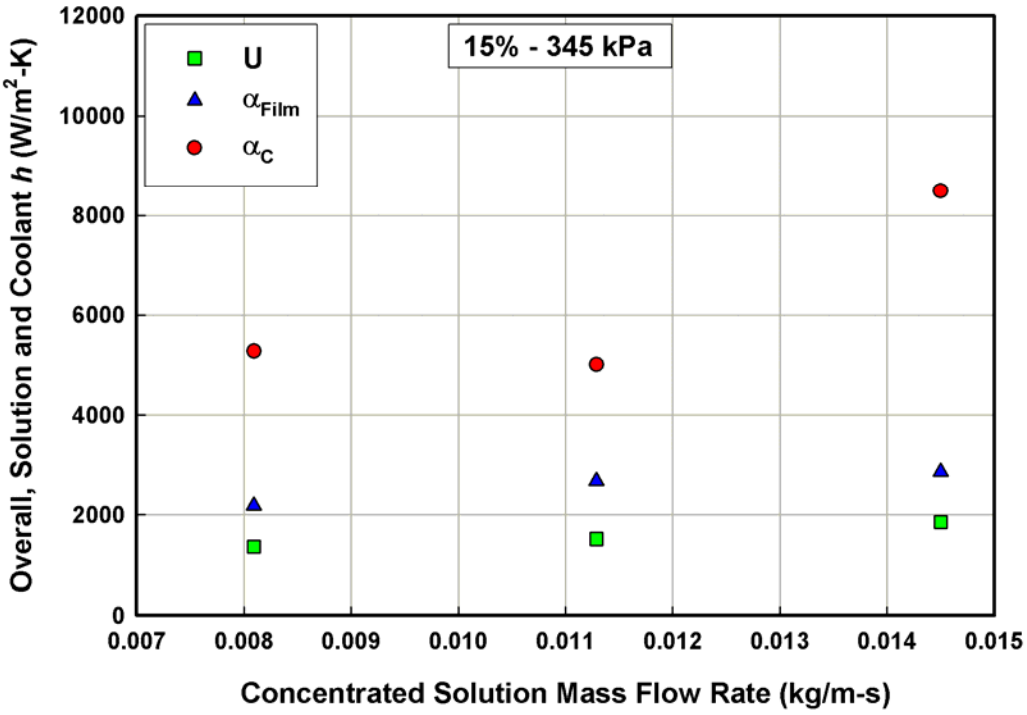

Figure C.5. Overall, Coolant, and Film Heat Transfer Coefficients at Nominal Conditions of 15%, 345 kPa (50.0 psi)

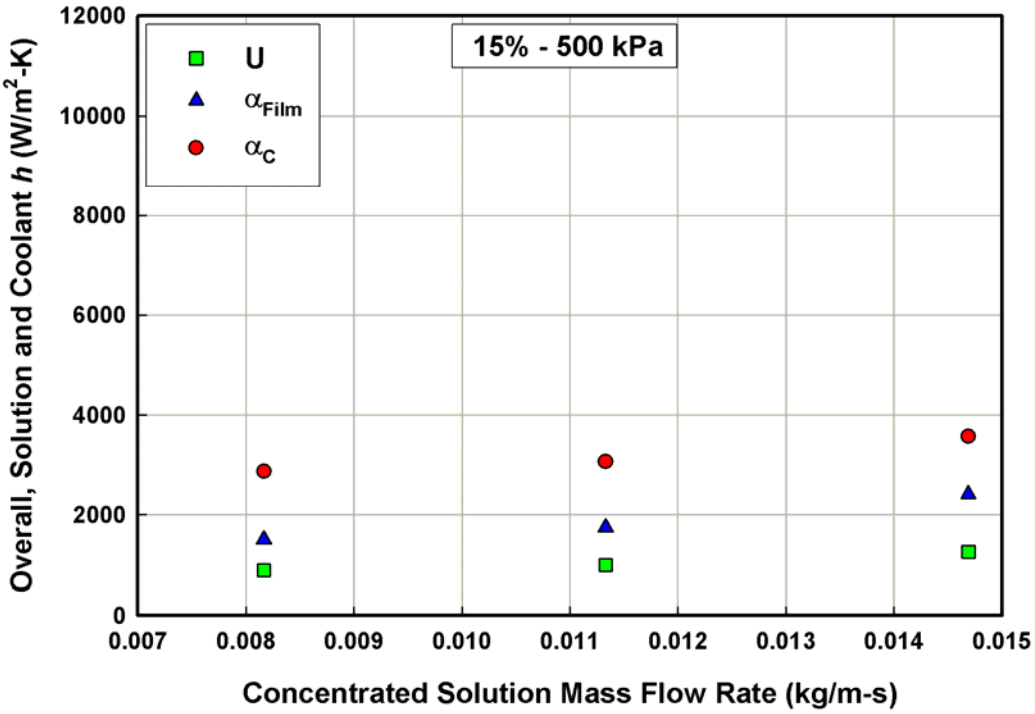

Figure C.6. Overall, Coolant, and Film Heat Transfer Coefficients at Nominal Conditions of 15%, 500 kPa (72.5 psi)

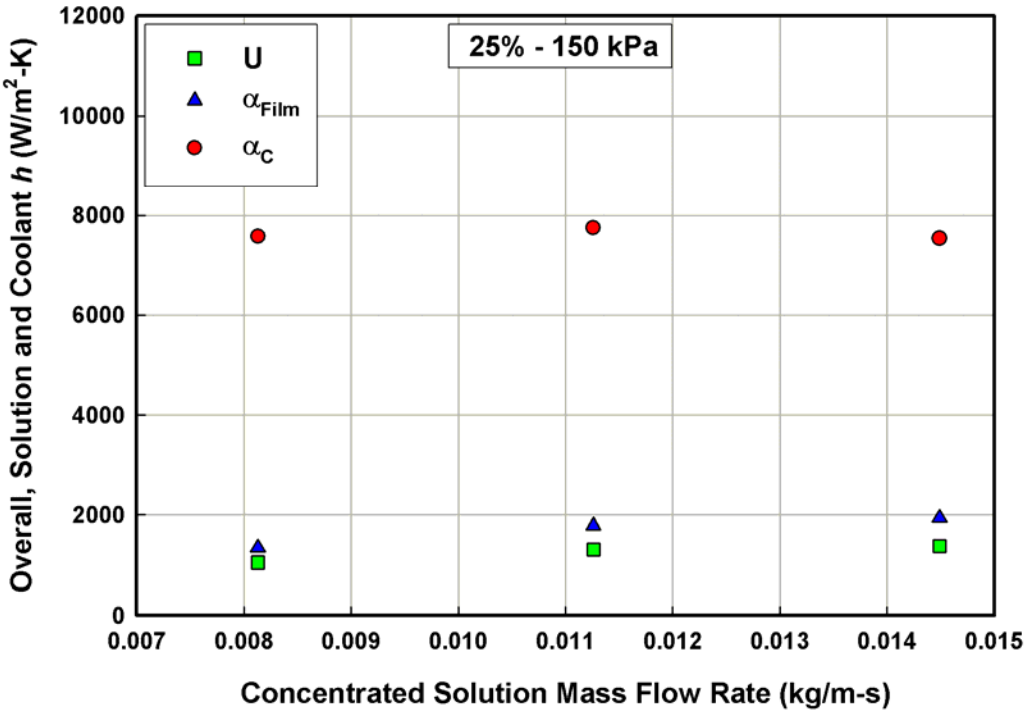

Figure C.7. Overall, Coolant, and Film Heat Transfer Coefficients at Nominal Conditions of 25%, 150 kPa (21.8 psi)

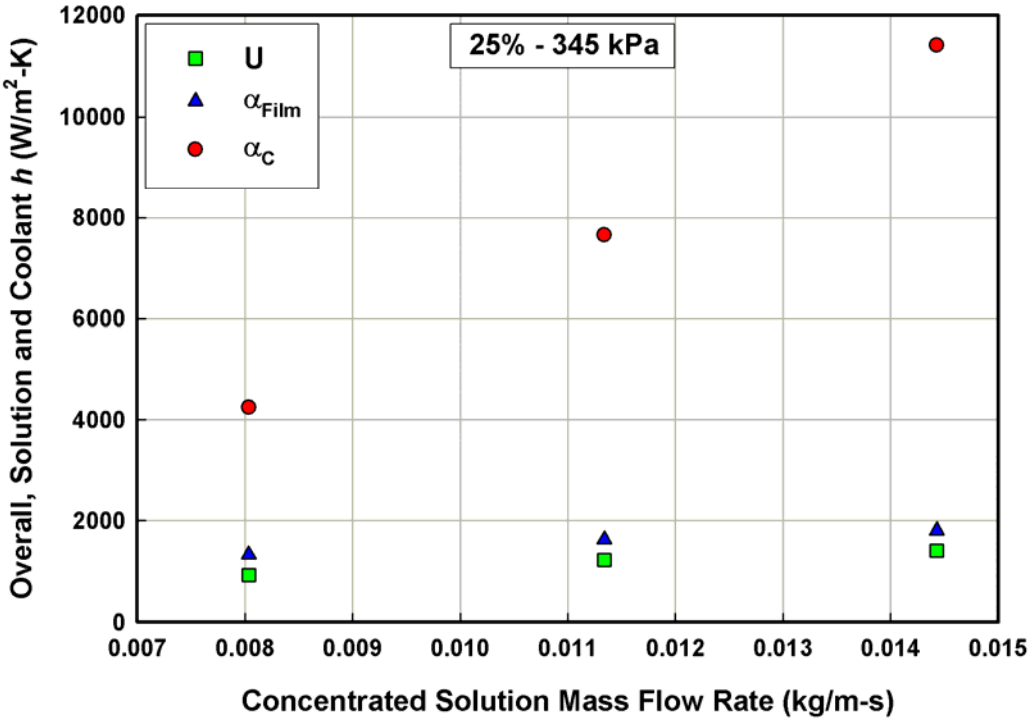

Figure C.8. Overall, Coolant, and Film Heat Transfer Coefficients at Nominal Conditions of 25%, 345 kPa (50.0 psi)

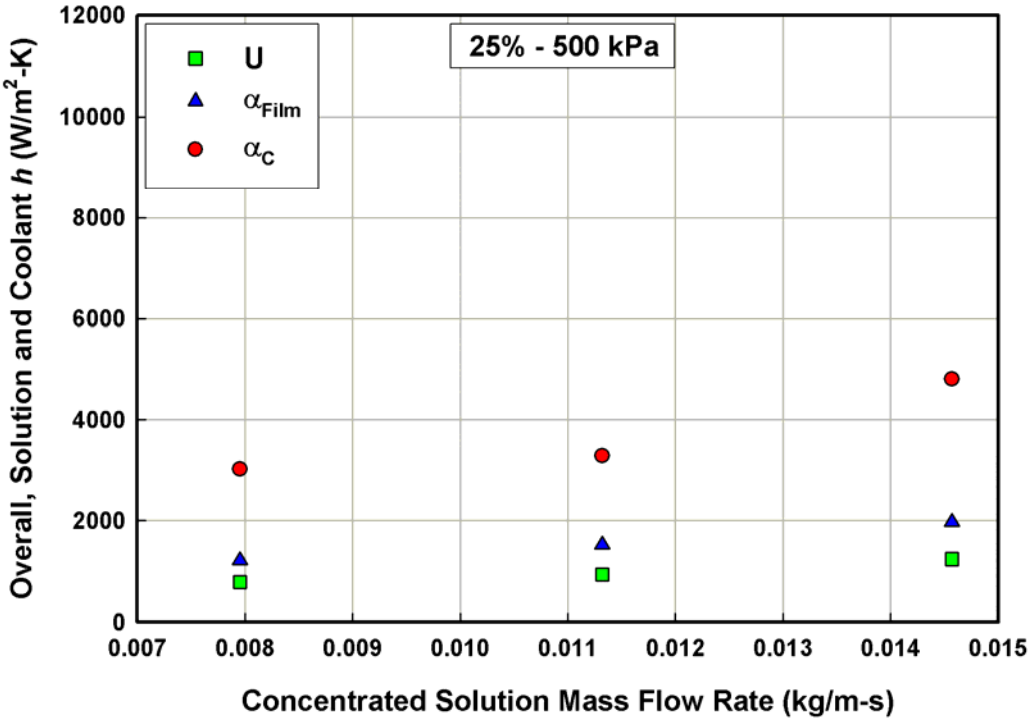

Figure C.9. Overall, Coolant, and Film Heat Transfer Coefficients at Nominal Conditions of 25%, 500 kPa (72.5 psi)

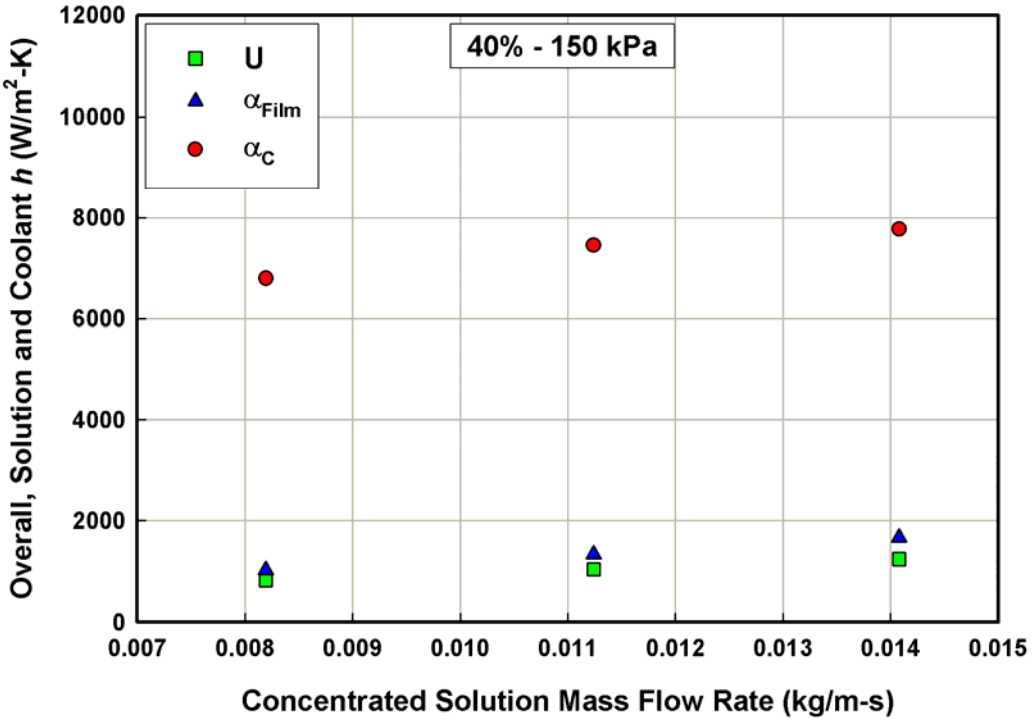

Figure C.10. Overall, Coolant, and Film Heat Transfer Coefficients at Nominal Conditions of 40%, 150 kPa (21.8 psi)

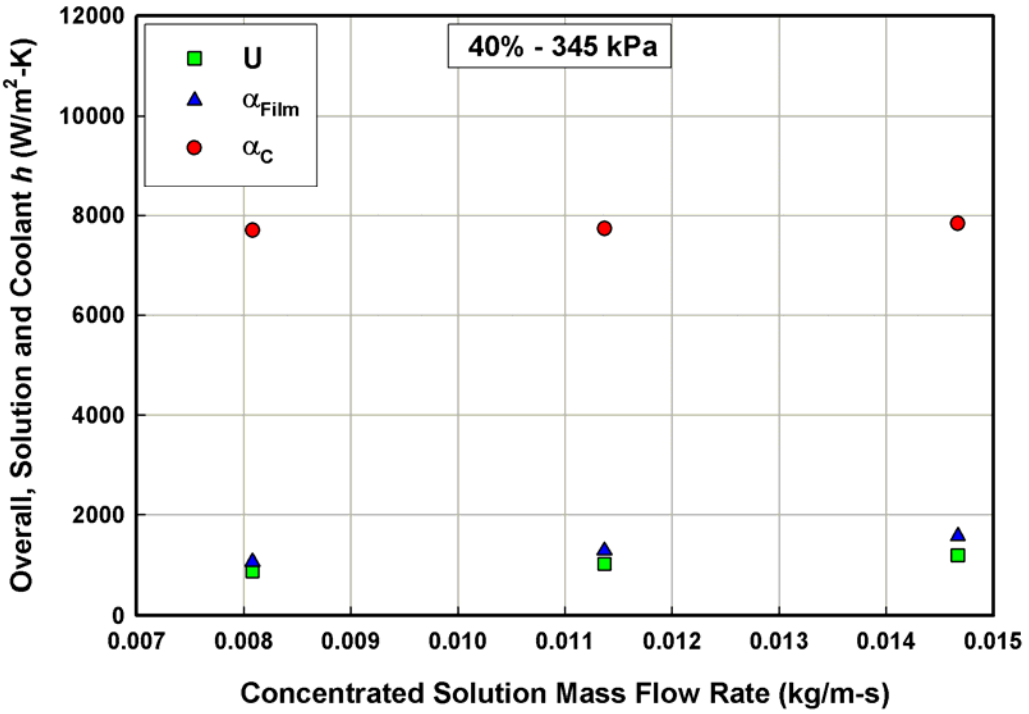

Figure C.11. Overall, Coolant, and Film Heat Transfer Coefficients at Nominal Conditions of 40%, 345 kPa (50.0 psi)

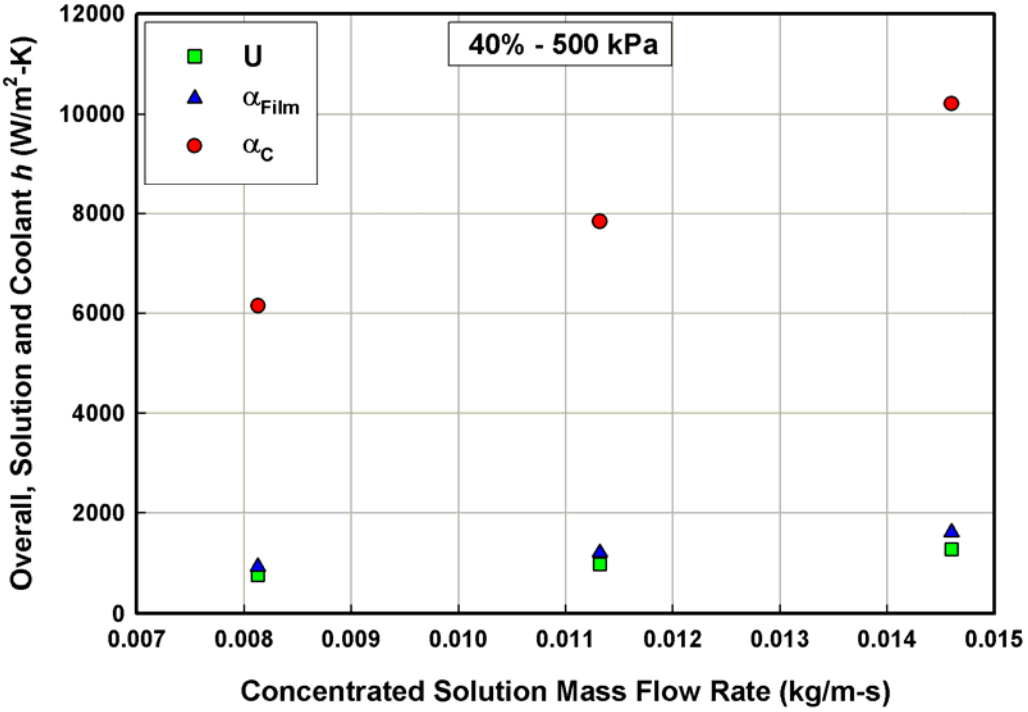

Figure C.12. Overall, Coolant, and Film Heat Transfer Coefficients at Nominal Conditions of 40%, 500 kPa (72.5 psi)

APPENDIX D: UNCERTAINTY CALCULATIONS

D.1 Sample Uncertainties

In the computation of the propagation of errors, the uncertainties in the dependent (or calculated parameters) are calculated as described below. Consider a calculated parameter, x, which is affected by uncertainties in measurements of several other parameters (*a*, *b*, *c*, *d*, *e*... *etc*).

$$x = f(a,b,c,d,e,....) \tag{D.1}$$

The total uncertainty in the calculation of x is given as:

$$U_x^2 = \left(\frac{\partial x}{\partial a}U_a\right)^2 + \left(\frac{\partial x}{\partial b}U_b\right)^2 + \left(\frac{\partial x}{\partial c}U_c\right)^2 + \left(\frac{\partial x}{\partial d}U_d\right)^2 + \left(\frac{\partial x}{\partial e}U_e\right)^2 + .. \tag{D.2}$$

where, U_a, U_b etc. are uncertainties in the measurements of *a*, *b*, and so on.

In determining uncertainties in the present study, the effects of 25 measured inputs were accounted for. Table D.1 lists these parameters with their nominal measured values and uncertainties in measurement for the representative data point at an absorber pressure of 345 kPa, dilute solution concentration of 25% and concentrated solution flow rate of 0.026 kg/s. Using the uncertainty values from Tables 4.3 and 4.4 for the various measurements, the overall uncertainties in the various solution stream concentrations, the absorber heat duties, and the coolant, overall and film heat transfer coefficients, the overall mass transfer coefficient, and the reflux flow rate are computed using an error propagation method (Taylor and Kuyatt, 1993) as implemented in *Engineering Equation Solver* (EES) V7.697-3D software (Klein, 2006). Table D.2 shows sample uncertainties for some of the parameters of interest at the absorber. In this table, partial derivatives and percent contributions to the total uncertainty for the respective calculated parameter as reported by EES are shown. Uncertainties in the coolant temperature measurement

(±0.5°C) are the largest contributor (~80%) followed by the vapor pressure measurement (~13%) to the overall uncertainty in the film heat transfer coefficient.

Table D.1 List of Parameters included in Uncertainty Analysis for Absorber (345 kPa, 25%, 0.026 kg/s)

Measured Parameter	Measured Value ± Uncertainty
Flow Rates	
$\dot{m}_{Abs,C}$ (gpm)	4.804 ± 0.02402
$\dot{m}_{Ref,Measured}$ (lb_m/min)	0.374 ± 0.0003738
$\dot{m}_{Dilute}$ (lb_m/min)	3.01 ± 0.00301
$\dot{m}_{Concentrated}$ (lb_m/min)	3.506 ± 0.00351
Absolute Pressures (Psi)	
$P_{Abs,in}$ (Absorber Inlet)	51.02 ± 2
$P_{Abs,out}$ (Absorber Outlet)	50.85 ± 3
$P_{Abs,V,in}$ (Absorber Vapor In)	52.62 ± 7.5
$P_{Con,in}$ (Condenser Inlet)	163.5 ± 2
$P_{Des,out}$ (Desorber Outlet)	161 ± 2
P_{Rec} (Rectifier)	162.6 ± 7.5
$P_{Sep,out}$ (Separator Outlet)	161.7 ± 2
Absorber Coolant Temperatures (°C)	
$T_{Abs,C,in}$ (Coolant In)	12.47 ± 0.5
$T_{Abs,C,out}$ (Coolant Outlet)	18.75 ± 0.5
Working Fluid Temperatures (°C)	
$T_{Abs,Dil,in}$ (Absorber Inlet)	70.42 ± 0.5
$T_{Abs,Conc,out}$ (Absorber Outlet)	30.99 ± 0.5
$T_{Abs,V,in}$ (Absorber Vapor In)	-0.25 ± 0.5
$T_{Des,out}$ (Desorber Outlet)	132.1 ± 0.5

Table D.1 Continued

Measured Parameter	Measured Value ± Uncertainty
$T_{Rec,in}$ (Rectifier Vapor In)	119..6 ± 0.5
$T_{Rec,out}$ (Rectifier Vapor Out)	80.99 ± 0.5
$T_{Reflux,out}$ (Reflux Outlet)	51.4 ± 0.5
$T_{Sep,out}$ (Separator Sol Out)	119 ± 0.5
$T_{Sep,V,out}$ (Separator Vapor Out)	122.4 ± 0.5
Geometrical Parameters (m)	
$Tube_{ID}$	0.008103 ± 0.0000025
$Tube_{Length}$	0.2921 ± 0.0000025
$Tube_{OD}$	0.009525 ± 0.0000025

Table D.2 Sample Uncertainties in Main Parameters of Interest

Partial Derivative	% Uncertainty (of Total)
$x_{des,out} = 0.2386 \pm 0.003083$ (±1.29%)	
$\partial x_{des,out} / \partial P_{Des,out} = 0.001144$	55.11%
$\partial x_{des,out} / \partial T_{Des,out} = -0.004132$	44.89%
$x_{abs,in} = 0.2671 \pm 0.003426$ (±1.28%)	
$\partial x_{abs,in} / \partial \dot{m}_{\text{Ref,measured}} = 0.07611$	0.01%
$\partial x_{abs,in} / \partial \dot{m}_{\text{Dilute}} = -0.009452$	0.01%
$\partial x_{abs,in} / \partial \dot{m}_{\text{Concentrated}} \sim 0$	0.00%
$\partial x_{abs,in} / \partial P_{Con,in} = 0.000043$	0.06%
$\partial x_{abs,in} / \partial P_{Des,out} = 0.000653$	14.53%
$\partial x_{abs,in} / \partial P_{\text{Rec}} = 0.000388$	72.25%
$\partial x_{abs,in} / \partial T_{\text{Rec},out} = -0.000271$	0.16%
$\partial x_{abs,in} / \partial T_{\text{Reflux}} = 0.001682$	6.02%
$\partial x_{abs,in} / \partial T_{\text{Sep,out}} = -1.138 \times 10^{-17}$	0.00%
$\partial x_{abs,in} / \partial T_{\text{Sep,V,out}} = -0.001808$	6.96%
$x_{abs,out} = 0.3336 \pm 0.002975$ (±0.9%)	
$\partial x_{abs,out} / \partial \dot{m}_{\text{Ref,measured}} = 0.3443$	0.19%
$\partial x_{abs,out} / \partial \dot{m}_{\text{Dilute}} = 0.06807$	0.47%
$\partial x_{abs,out} / \partial \dot{m}_{\text{Concentrated}} = -0.09515$	1.26%
$\partial x_{abs,out} / \partial P_{Con,in} = 0.000059$	0.16%
$\partial x_{abs,out} / \partial P_{Des,out} = 0.000561$	14.21%
$\partial x_{abs,out} / \partial P_{\text{Rec}} = 0.000333$	70.63%
$\partial x_{abs,out} / \partial T_{\text{Rec},out} = -0.000369$	0.39%
$\partial x_{abs,out} / \partial T_{\text{Reflux}} = 0.001444$	5.89%
$\partial x_{Dilute} / \partial T_{\text{Sep,out}} = -1.138 \times 10^{-17}$	0.00%
$\partial x_{abs,out} / \partial T_{\text{Sep,V,out}} = -0.001552$	6.81%

Table D.2 Continued

Partial Derivative	% Uncertainty (of Total)
$\partial x_{abs,out} / \partial P_{Des,out} = 0.000561$	14.21%
$\partial x_{abs,out} / \partial P_{Rec} = 0.000333$	70.63%
$\partial x_{abs,out} / \partial T_{Rec,out} = -0.000369$	0.39%
$\partial x_{abs,out} / \partial T_{Reflux} = 0.001444$	5.89%
$\partial x_{Dilute} / \partial T_{Sep,out} = -1.138 \times 10^{-17}$	0.00%
$\partial x_{abs,out} / \partial T_{Sep,V,out} = -0.001552$	6.81%
$x_V = 0.9781 \pm 0.000764$ (±0.08%)	
$\partial x_V / \partial P_{Con,in} = 0.000206$	28.99%
$\partial x_{Concentrated} / \partial T_{Rec,out} = -0.001288$	71.01%
$h_{abs,in} = 128.9 \pm 2.701$ kJ/kg (±2.09%)	
$\partial h_{abs,in} / \partial \dot{m}_{Ref,measured} = -35.9$	0.00%
$\partial h_{abs,in} / \partial \dot{m}_{Dilute} = 4.459$	0.00%
$\partial h_{abs,in} / \partial P_{abs,in} = 0.005016$	0.00%
$\partial h_{abs,in} / \partial P_{Con,in} = -0.02039$	0.02%
$\partial h_{abs,in} / \partial P_{Des,out} = -0.308$	5.20%
$\partial h_{abs,in} / \partial P_{Rec} = -0.1832$	25.86%
$\partial h_{abs,in} / \partial T_{Abs,in} = 4.329$	64.21%
$\partial h_{abs,in} / \partial T_{Rec,out} = 0.1276$	0.06%
$\partial h_{abs,in} / \partial T_{Reflux} = 0.7933$	2.16%
$\partial h_{abs,in} / \partial T_{Sep,V,out} = 0.8527$	2.49%
$h_{abs,out} = -68.93 \pm 2.444$ kJ/kg (±3.49%)	
$\partial h_{abs,out} / \partial \dot{m}_{Ref,measured} = -130.3$	0.04%
$\partial h_{abs,out} / \partial \dot{m}_{Dilute} = -25.76$	0.10%
$\partial h_{abs,out} / \partial \dot{m}_{Concentrated} = 36.01$	0.27%
$\partial h_{abs,out} / \partial P_{abs,out} = 0.006326$	0.01%
$\partial h_{abs,out} / \partial P_{Con,in} = -0.02235$	0.03%
$\partial h_{abs,out} / \partial P_{Des,out} = -0.2122$	3.02%

Table D.2 Continued

Partial Derivative	% Uncertainty (of Total)
$\partial h_{abs,out} / \partial P_{Rec} = -0.1262$	14.99%
$\partial h_{abs,out} / \partial T_{Abs,out} = 4.338$	78.77%
$\partial h_{abs,out} / \partial T_{Rec,out} = 0.1399$	0.08%
$\partial h_{abs,out} / \partial T_{Reflux} = 0.5465$	1.25%
$\partial h_{abs,out} / \partial T_{Sep,V,out} = 0.5874$	1.44%
h_V = 1086 ± 122.8 kJ/kg (±11.29%)	
$\partial h_V / \partial P_{Abs,V,in} = -16.19$	97.83%
$\partial h_V / \partial P_{Con,in} = 1.773$	0.08%
$\partial h_V / \partial T_{Abs,V,in} = 33.65$	1.88%
$\partial h_V / \partial T_{Rec,out} = -11.1$	0.20%
Q_{abs} = 7.854 ± 0.3552 kJ/kg (±4.5%)	
$\partial Q_{abs} / \partial \dot{m}_{Ref,measured} = 10.84$	0.01%
$\partial Q_{abs} / \partial \dot{m}_{Dilute} = 1.759$	0.02%
$\partial Q_{abs} / \partial \dot{m}_{Concentrated} = -0.4279$	0.00%
$\partial Q_{abs} / \partial P_{Abs,in} = 0.000114$	0.00%
$\partial Q_{abs} / \partial P_{Abs,out} = -0.000167$	0.00%
$\partial Q_{abs} / \partial P_{Abs,V,in} = -0.04575$	93.30%
$\partial Q_{abs} / \partial P_{Con,in} = 0.00514$	0.08%
$\partial Q_{abs} / \partial P_{Des,out} = -0.001385$	0.01%
$\partial Q_{abs} / \partial P_{Rec} = 0.0008236$	0.03%
$\partial Q_{abs} / \partial T_{Abs,in} = 0.09851$	1.92%
$\partial Q_{abs} / \partial T_{Abs,out} = -0.115$	2.62%
$\partial Q_{abs} / \partial T_{Abs,V,in} = 0.0951$	1.79%
$\partial Q_{abs} / \partial T_{Rec,out} = -0.03217$	0.21%
$\partial Q_{abs} / \partial T_{Reflux} = 0.003568$	0.00%
$\partial Q_{abs} / \partial T_{Sep,out} = 0.003835$	0.00%
$\alpha_{Film,abs}$ = 1632 ± 130.9 kJ/kg (±8.0%)	
$\partial \alpha_{Film,abs} / \partial \dot{m}_{Abs,C} = 159$	0.09%

Table D.2 Continued

Partial Derivative	% Uncertainty (of Total)
$\partial \alpha_{\text{Film,abs}} / \partial \dot{m}_{\text{Ref,measured}} = 1496$	0.00%
$\partial \alpha_{\text{Film,abs}} / \partial \dot{m}_{\text{Dilute}} = -58.74$	0.00%
$\partial \alpha_{\text{Film,abs}} / \partial \dot{m}_{\text{Concentrated}} = 242.6$	0.00%
$\partial \alpha_{\text{Film,abs}} / \partial P_{Abs,in} = 0.01574$	0.00%
$\partial \alpha_{\text{Film,abs}} / \partial P_{Abs,out} = -0.02312$	0.00%
$\partial \alpha_{\text{Film,abs}} / \partial P_{Abs,V,in} = -6.31$	13.06%
$\partial \alpha_{\text{Film,abs}} / \partial P_{Con,in} = 0.709$	0.01%
$\partial \alpha_{\text{Film,abs}} / \partial P_{Des,out} = -0.1911$	0.00%
$\partial \alpha_{\text{Film,abs}} / \partial P_{\text{Re}c} = -0.1136$	0.00%
$\partial \alpha_{\text{Film,abs}} / \partial T_{Abs,C,in} = -127.3$	23.62%
$\partial \alpha_{\text{Film,abs}} / \partial T_{Abs,C,out} = 196.7$	56.39%
$\partial \alpha_{\text{Film,abs}} / \partial T_{Abs,in} = 13.59$	0.27%
$\partial \alpha_{\text{Film,abs}} / \partial T_{Abs,out} = -65.57$	6.27%
$\partial \alpha_{\text{Film,abs}} / \partial T_{Abs,V,in} = 13.12$	0.25%
$\partial \alpha_{\text{Film,abs}} / \partial T_{\text{Re}c,out} = -4.438$	0.03%
$\partial \alpha_{\text{Film,abs}} / \partial T_{\text{Reflux}} = 0.4921$	0.00%
$\partial \alpha_{\text{Film,abs}} / \partial T_{\text{Sep,V,out}} = 0.5289$	0.00%
$\partial \alpha_{\text{Film,abs}} / \partial Tube_{\text{ID}} = -65719$	0.00%
$\partial \alpha_{\text{Film,abs}} / \partial Tube_{\text{OD}} = -80387$	0.00%
$\partial \alpha_{\text{Film,abs}} / \partial Tube_{\text{LengthID}} = -7465$	0.00%
$\beta_v = 0.0202 \pm 0.001233$ (±6%)	
$\partial \beta_V / \partial \dot{m}_{\text{Ref,measured}} = 0.05407$	0.03%
$\partial \beta_V / \partial P_{Abs,in} = 0.000258$	17.47%
$\partial \beta_V / \partial P_{Abs,out} = 0.000258$	39.32%
$\partial \beta_V / \partial T_{Abs,in} = -0.001096$	19.73%
$\partial \beta_V / \partial T_{Abs,out} = -0.001096$	19.73%
$\partial \beta_V / \partial T_{\text{min}} = -0.000476$	3.72%

D.2 Range of Uncertainties of Solution and Vapor Properties

In the present study, the solution and vapor properties were estimated using correlations from the literature that are functions of temperature, pressure and concentration. Therefore, uncertainties in these properties resulting from measurement errors in these parameters are also calculated. Table D.3 shows the range of uncertainties in solution and vapor properties as well as solution *Re* and *Pr* for the range of experiments conducted. These are the uncertainties estimated from an error propagation approach on the measurement uncertainties. In addition, for the vapor-phase transport properties, the deviations between the values estimated in this study and those reported in the literature for pure components were also calculated, and are reported below as additional vapor-phase uncertainties.

D.3 Validity of the Kinetic Theory for Vapor Property Evaluation

In the absence of any literature on ammonia-water vapor-phase mixture properties, transport properties of the ammonia-water vapor mixture were obtained using the Chapman-Enskog kinetic theory (Mills, 1995) for pure substances and mixture rules of Wilke (1950). It should be noted that ideal gas properties of pure ammonia and pure water vapor predicted using the kinetic theory were used instead of values available in the literature for the pure components to ensure consistency with the mixture rules. To estimate potential errors introduced by the use of this approach, in this section, the specific heat, thermal conductivity, and viscosity of ammonia obtained from the Lennard-Jones potential model are compared with real gas properties available in the internal library in EES (Klein, 2006), which uses correlations developed by Tillner-Roth et al.

(1993) for the ammonia vapor specific heat, Tufeu et al. (1984) for the ammonia vapor conductivity, and Fenghour et al. (1995) for the ammonia vapor viscosity.

Figures D.1 – D.3 show comparisons of the ammonia vapor properties of specific heat, thermal conductivity, and viscosity for temperatures between 10^{o}C and 90^{o}C and the three pressures of interest in this study, i.e., 150 kPa, 345 kPa and 500 kPa. The properties obtained from the kinetic theory are independent of pressure. This is because the kinetic theory is developed for an ideal gas; therefore, vapor properties are only dependent on temperature.

Figure D.1 shows a comparison of ammonia vapor specific heats obtained from the kinetic theory and those obtained from Tillner-Roth et al. (1993). The specific heat of ammonia obtained from the kinetic theory is lower than that obtained from Tillner-Roth et al. (1993). The specific heat decreases as pressure decreases, with a decreasing influence of pressure at the higher temperatures. The deviations ranged between 11.1% and 26.5% with an average deviation of 15.5%.

Figure D.2 shows a comparison of ammonia vapor thermal conductivities obtained from the kinetic theory and those obtained from Tufeu et al. (1984). The thermal conductivity of ammonia obtained from the kinetic theory is higher than that obtained from Tufeu et al. (1984). The conductivity increases as vapor temperature increases, while there is no significant effect of pressure. The deviations ranged between 10% and 17.7% with an average deviation of 14.6%.

Figure D.3 shows a comparison of ammonia vapor viscosities obtained from the kinetic theory and those from Fenghour et al. (1995). The viscosity of ammonia obtained from the kinetic theory is higher than that obtained from Fenghour et al. (1995). The

viscosity increases as the vapor temperature increases, while there is no significant effect of pressure. The deviations ranged between 2% and 6.2% with an average of 3.8%.

Table D.3 shows these deviations from the values in the literature as additional uncertainties in these vapor-phase properties, over and above those corresponding to measurement uncertainties.

Table D.4 shows the range of uncertainties in non-dimensional vapor parameters. Uncertainties in non-dimensional vapor-phase parameters such as Gr_v, Ra_v, Re_v, Pr_v, and Sc_v, are calculated based on the maximum property deviations between the literature and the kinetic theory. It should be noted that these additional uncertainties will also adversely affect the predictive capabilities of the vapor-phase mass transfer correlation developed in this study.

The uncertainties of Ra_v and Pr_v range from 16.1 to 19.9% with average uncertainties of 18.2% due to the component uncertainties in the thermal conductivity and specific heat. The uncertainties in Re_v and Sc_v range from 5.3 to 6.6% with average uncertainties of 6% due to the above mentioned deviations in the vapor viscosity. The uncertainties in Gr_v range from 10.6 to 13.4% with average uncertainties of 12.2% due to the deviations in the vapor viscosity.

Table D.3 Uncertainties in the Solution and Vapor Properties in the Present Study

Parameter		Range	Uncertainty Range(Absolute)	Uncertainty Range (%)	Average Uncertainty (%)
$C_{p,l}$ (kJ/kg-K)		4.22 – 4.42	8.69×10^{-5}– 0.08167	0.02 – 1.89	0.25
k_l (W/m-K)		0.55 – 0.62	5.0×10^{-4} – 3.78×10^{-3}	0.09 – 0.63	0.24
μ_l (kg/m-s)		3.21×10^{-4} – 1.04×10^{-3}	2.28×10^{-6} – 2.12×10^{-5}	0.35 – 2.15	0.81
ρ_l (kg/m^3)		841 – 908	0.94 – 5.69	0.11 – 0.65	0.25
$D_{aw,l}$ (m^2/s)		3.29×10^{-9} – 8.23×10^{-9}	2.83×10^{-11} – 9.05×10^{-11}	0.62 – 2.04	0.98
Re_l		29 – 170	0.21 – 1.27	0.36 – 2.20	0.81
Pr_l		2.23 – 8.23	0.016– 0.14	0.34– 1.8	0.86
$C_{p,v}$ (kJ/kg-K)	Measurement	2.06 – 2.39	0.001 – 1.15	0.06 – 54	7.8
	Deviation from Literature	2.20 – 2.66	0.244 – 0.703	11.1 – 26.5	15.5
k_v (W/m-K)	Measurement	0.026 – 0.029	4.87×10^{-5} – 4.9×10^{-5}	0.16 – 0.19	0.18
	Deviation from Literature	0.0237 – 0.0325	0.00324 – 0.00446	9.97 – 17.7	14.6
μ_v (kg/m-s)	Measurement	9.27×10^{-6} – 1.07×10^{-5}	1.75×10^{-8} – 1.79×10^{-8}	0.16 – 0.19	0.17
	Deviation from Literature	9.41×10^{-6} – 1.25×10^{-5}	2.5×10^{-7} – 5.79×10^{-7}	1.99 – 6.15	3.77
ρ_V (kg/m^3)		1.277 – 8.805	0.39 – 4.84	11.59 – 54.9	25.6
$D_{aw,v}$ (m^2/s)		4.9×10^{-6} – 1.53×10^{-5}	4.79×10^{-7} – 4.5×10^{-6}	9.78 – 29.85	16.95

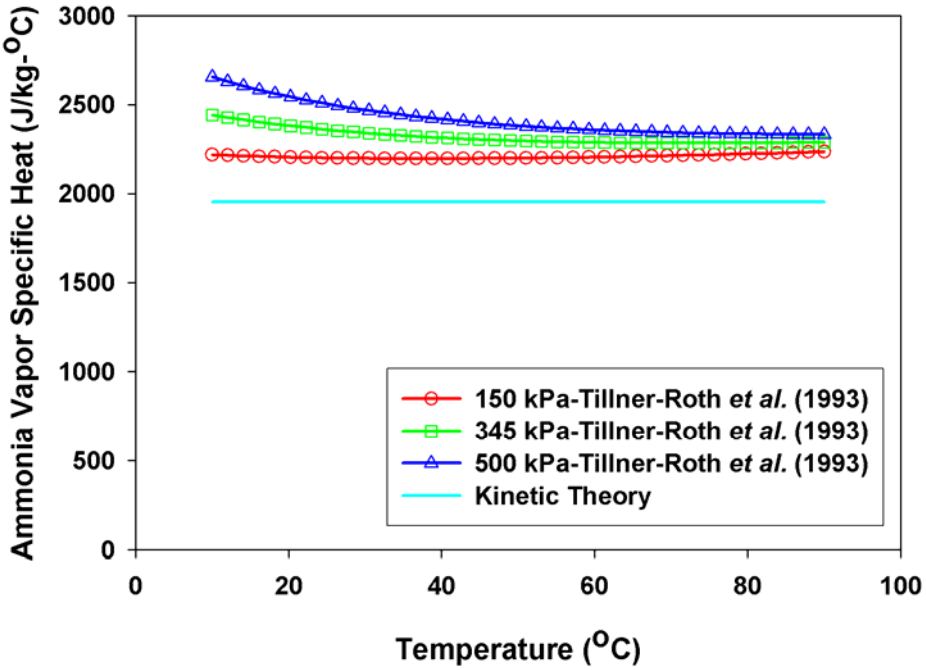

Figure D.1 Ammonia Vapor Specific Heat

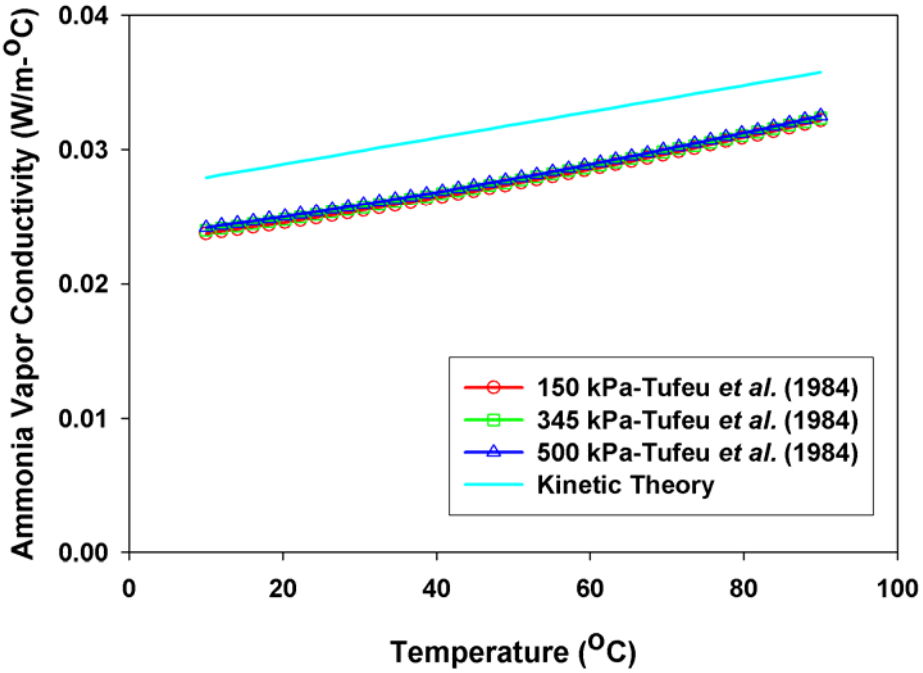

Figure D.2 Ammonia Vapor Conductivity

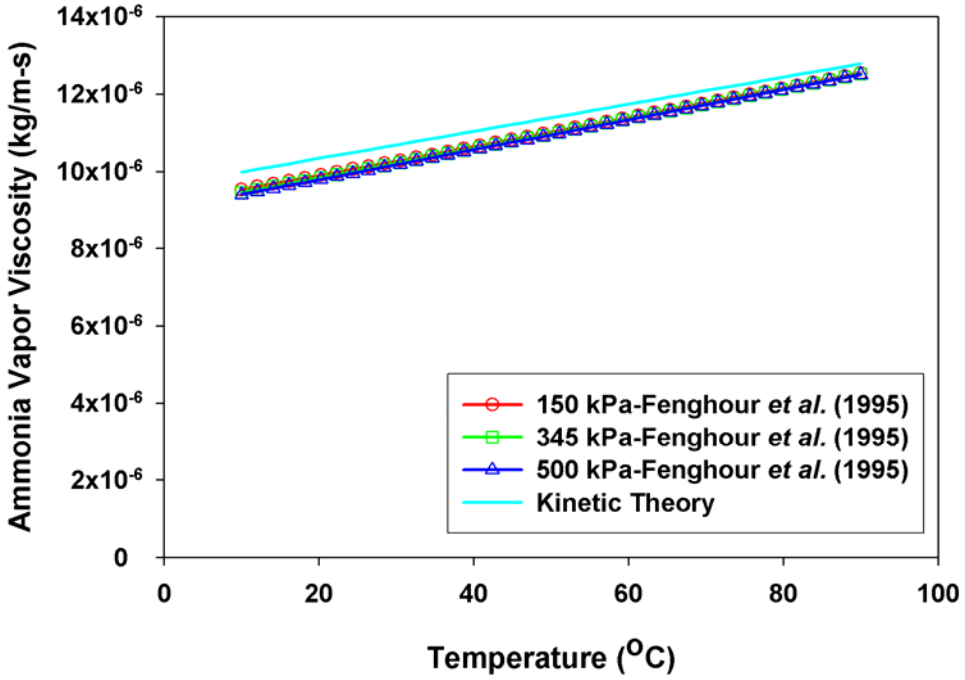

Figure D.3 Ammonia Vapor Viscosity

Table D.4 Uncertainties in Non-Dimensional Vapor Parameters

Parameter	Range	Uncertainty Range(Absolute)	Uncertainty Range (%)	Average Uncertainty (%)
Gr_v	4222 – 59879	52.87 – 722.6	10.6 – 13.4	12.2
Ra_v	3471 – 48824	657.4 - 9144	16.1 – 19.9	18.2
Re_v	30.37 – 134.1	1.94 – 7.819	5.3 – 6.6	6.0
Pr_v	0.671 – 0.898	0.1309 – 0.1687	16.1 – 19.9	18.2
Sc_v	0.504 – 0.527	0.02788 – 0.03356	5.3 – 6.6	6.0

REFERENCES

Andberg, J. W. and G. C. Vliet (1987), "Absorption of Vapors into Liquid Films Flowing over Cooled Horizontal Tubes," *Proceedings of the 1987 ASME-JSME Thermal Engineering Joint Conference.*, Honolulu, HI, USA, ASME, New York, NY, USA, pp. 533-541.

Bird, R. B., W. E. Stewart and E. N. Lightfoot (2002). *Transport Phenomena*. 2nd Ed. New York, J. Wiley.

Burgett, L. W., M. D. Byars and K. Schultz (1999), "Absorption Systems: The Furture, More Than a Niche?," *ISHPC 99 Proceedings of the International Sorption Heat Pump Conference*, Munich, Germany, pp. 13-24.

Carey, V. P. (1992). *Liquid-Vapor Phase-Change Phenomena: An Introduction to the Thermophysics of Vaporization and Condensation Processes in Heat Transfer Equipment*. Washington, D.C., Hemispehere Publishing Corporation.

Chen, W. and R. N. Christensen (2000), "Inlet Subcooling Effect on Heat and Mass Transfer Characteristics in a Laminar Film Flow," *International Journal of Heat and Mass Transfer* Vol. 43(2) pp. 167-177.

Churchill, S. W. (1977a), "Comprehensive Correlating Equations for Heat, Mass and Momentum Transfer in Fully Developed Flow in Smooth Tubes," *Industrial & Engineering Chemistry, Fundamentals* Vol. 16(1) pp. 109-116.

Churchill, S. W. (1977b), "Friction-Factor Equation Spans All Fluid-Flow Regimes," *Chemical Engineering* Vol. 84(24) pp. 91-92.

Churchill, S. W. and M. Bernstein (1977), "A Correlating Equation for Forced Convection from Gases and Liquids to a Circular Cylinder in Crossflow," *Transactions of the ASME. Series C, Journal of Heat Transfer* Vol. 99(2) pp. 300-306.

Colburn, A. P. and T. B. Drew (1937), "Condensation of Mixed Vapors," *American Institute of Chemical Engineers - Transactions* Vol. 33 pp. 197-212.

Dence, A. E., C. C. Nowak and H. Perez-Blanco (1996), "A Novel GAX Heat Exchanger for Cooling Applications," *International Ab-Sorption Heat Pump Conference*, Montreal, Canada, pp. 595-600.

DeVault, R. C. and J. Marsala (1990), "Ammonia-Water Triple-Effect Absorption Cycle," *ASHRAE Transactions* Vol. 96(1).

Dorokhov, A. R. and V. N. Bochagov (1983), "Heat Transfer to a Film Falling over Horizontal Cylinders," *Heat Transfer-Soviet Research* Vol. 15(2).

Engler, M., G. Grossman and H. M. Hellmann (1996), "Comparative Simulation and Investigation of Ammonia-Water Absorption Cycles for Heat Pump Applications," *International Ab-sorption Heat Pump Conference*, Montreal, Canada, pp. 209-219.

Erickson, D. C., A. Gomezplata and R. A. Papar (1998), "Use of the Colburn-Drew Equations to Model Mass Transfer," *International Communications in Heat and Mass Transfer* Vol. 25(1) pp. 93-98.

Fenghour, A., A. W. William, V. Vesovic, J. T. R. Watson, J. Millat and E. Vogel (1995), "The Viscosity of Ammonia," *Journal of Physical and Chemical Reference Data* Vol. 24(5) pp. 1649-1667.

Fernandez-Seara, J., J. Sieres, C. Rodriguez and M. Vazquez (2005), "Ammonia-Water Absorption in Vertical Tubular Absorbers," *International Journal of Thermal Sciences* Vol. 44(3) pp. 277-288.

Frank, M. J. W., J. A. M. Kuipers and W. P. M. van Swaaij (1996), "Diffusion Coefficients and Viscosities of CO2+H2O, CO2+CH3OH, NH3+H2O, and NH3+CH3OH Liquid Mixtures," *Journal of Chemical and Engineering Data* Vol. 41(2) pp. 297-302.

Garimella, S. (1999), "Miniaturized Heat and Mass Transfer Technology for Absorption Heat Pumps," *Proceedings of the International Sorption Heat Pump Conference*, Munich, Germany, pp. 661-670.

Garimella, S. (2000), "Microchannel Components for Absorption Space-Conditioning Systems," *2000 ASHRAE Winter Meeting, Feb 5-Feb 9 2000*, Dallas, TX, USA, Amer. Soc. Heating, Ref. Air-Conditoning Eng. Inc., Atlanta, GA, USA, pp. 453-462.

Garimella, S., R. N. Christensen and D. Lacy (1996), "Performance Evaluation of a Generator-Absorber Heat-Exchange Heat Pump," *Applied Thermal Engineering* Vol. 16(7) pp. 591-604.

Garimella, S., R. N. Christensen and S. E. Petty (1992), "Cycle Description and Performance Simulation of a Gas-Fired Hydronically Coupled Double-Effect Absorption Heat Pump System," *Winter Annual Meeting of the American Society of Mechanical Engineers, Nov 8-13 1992*, Anaheim, CA, USA, Publ by ASME, New York, NY, USA, pp. 7-14 BN - 10-7918-1113-7911.

Garimella, S., D. Lacy and R. E. Stout (1997), "Space-Conditioning Using Triple-Effect Absorption Heat Pumps," *Applied Thermal Engineering* Vol. 17(12) pp. 1183-1197.

Garrabrant, M. A. and R. N. Christensen (1997), "Modeling and Experimental Verification of a Perforated Plate-Fin Absorber for Aqua-Ammonia Absorption Systems," *Proceedings of the 1997 ASME International Mechanical Engineering Congress and Exposition, Nov 16-21 1997*, Dallas, TX, USA, ASME, Fairfield, NJ, USA, pp. 337-347.

Goel, N. and D. Y. Goswami (2005a), "Analysis of a Counter-Current Vapor Flow Absorber," *International Journal of Heat and Mass Transfer* Vol. 48(7) pp. 1283-1292.

Goel, N. and D. Y. Goswami (2005b), "A Compact Falling Film Absorber," *Journal of Heat Transfer* Vol. 127 pp. 957-965.

Gommed, K. and G. Grossman (1990), "Performance Analysis of Staged Absorption Heat Pumps Water-Lithium Bromide Systems," *ASHRAE Transactions* Vol. 96(1) pp. 1590 - 1598.

Gommed, K., G. Grossman and M. S. Koenig (2001), "Numerical Study of Absorption in a Laminar Falling Film of Ammonia-Water, Atalanta, GA, ASHRAE, pp. 453-462.

Grossman, G., M. Wilke and R. C. DeVault (1994), "Simulation and Performance Analysis of Triple-Effect Absorption Cycles," *Proceedings of the ASHRAE Winter Meeting*, New Orleans, LA, USA, ASHRAE, Atlanta, GA, USA, pp. 452-462.

Grossman, G., A. Zaltash and R. C. DeVault (1995), "Simulation and Performance Analysis of a Four-Effect Lithium Bromide-Water Absorption Chiller," *Proceedings of the 1995 ASHRAE Annual Meeting*, Chicago, IL, USA, ASHRAE, Atlanta, GA, USA, pp. 1302-1312.

Haselden, G. G. and S. A. Malaty (1959), "Heat and Mass Transfer Accompanying the Absorption of Ammonia in Water," *Institution of Chemical Engineers -- Transactions* Vol. 37(3) pp. 137-146.

Herbine, G. S. and H. Perez-Blanco (1995), "Model of an Ammonia-Water Bubble Absorber," *Proceedings of the 1995 ASHRAE Annual Meeting*, Chicago, IL, USA, ASHRAE, Atlanta, GA,USA, pp. 1324-1332.

Herold, K. E., R. Radermacher and S. A. Klein (1996). *Absorption Chillers and Heat Pumps*. Boca Raton, CRC Press LLC.

Hewitt, G. F., G. L. Shires and T. R. Bott (1994). *Process Heat Transfer*, Boca Raton : CRC Press : Begell House.

Higbie, R. (1935), "The Rate of Absorption of a Pure Gas into a Still Liquid During Short Periods of Exposure," *Transactions of the AICHE* Vol. 35 pp. 365 - 389.

Hu, X. and A. M. Jacobi (1996a), "The Intertube Falling Film: Part 1-Flow Characteristics, Mode Transition, and Hystersis," *Transactions of the ASME* Vol. 118 p. 616.

Hu, X. and A. M. Jacobi (1996b), "The Intertube Falling Film: Part 2-Mode Effects on Sensible Heat Transfer to a Falling Liquid Film," *Transactions of the ASME* Vol. 118 pp. 626-633.

Ibrahim, O. M. and S. A. Klein (1993), "Thermodynamic Properties of Ammonia-Water Mixtures, Chicago, IL, USA, Published by ASHRAE, Atlanta, GA, USA, pp. 1495-1502.

IIR (1994). *Thermodynamic and Physical Properties of NH3-H2O (Ammonia-Water)*. France, International Institute of Refrigeration.

Inoue, N., H. Yabuuchi, M. Goto and S. Koyama (2004), "Heat and Mass Transfer of Ammonia Gas Absorption into Falling Liquid Film on a Horizontal Tube," *Transactions of the Japan Society of Refrigerating and Air Conditioning Engineers* Vol. 21(4) pp. 299-308.

Ivester, D. N. and S. V. Shelton (1994), "Varying Heat Exchanger Parameters in the Triple-Effect Absorption Cycle," *International Absorption Heat Pump Conference*, New Orleans, LA, ASME AES, pp. 243-250.

Jeong, S. and S. Garimella (2002), "Falling-Film and Droplet Mode Heat and Mass Transfer in a Horizontal Tube," *International Journal of Heat and Mass Transfer* Vol. 45(7) pp. 1445-1458.

Jeong, S. and S. Garimella (2005), "Optimal Design of Compact Horizontal Tube LiBr/Water Absorbers," *HVAC and R Research* Vol. 11(1) pp. 27-44.

Jeong, S., K.-K. Koo and S. K. Lee (1998), "Heat Transfer Performance of a Coiled Tube Absorber with Working Fluid of Ammonia/Water," *Proceedings of the 1998*

ASHRAE Winter Meeting. Part 2 (of 2), Jan 18-21 1998, San Francisco, CA, USA, ASHRAE, Atlanta, GA, USA, pp. 1577-1583.

Kang, Y. T., A. Akisawa and T. Kashiwagi (1999), "Experimental Correlation of Combined Heat and Mass Transfer for NH_3/H_2O Falling Film Absorption," *International Journal of Refrigeration* Vol. 22(4) pp. 250-262.

Kang, Y. T., W. Chen and R. N. Christensen (1997), "Generalized Component Design Model by Combined Heat and Mass Transfer Analysis in NH_3/H_2O Absorption Heat Pump Systems," *Proceedings of the 1997 ASHRAE Winter Meeting, Jan 26-29 1997*, Philadelphia, PA, USA, ASHRAE, Atlanta, GA, USA, pp. 444-453.

Kang, Y. T. and R. N. Christensen (1994), "Development of a Counter-Current Model for a Vertical Fluted Tube GAX Absorber," *International Absorption Heat Pump Conference*, New Orleans, LA, ASME AES, pp. 7-16.

Kang, Y. T. and R. N. Christensen (1995), "Combined Heat and Mass Transfer Analysis for Absorption in a Fluted Tube with a Porous Medium in Confined Cross Flow," *Proceedings of the 1995 ASME/JSME Thermal Engineering Joint Conference. Part 1 (of 4), Mar 19-24 1995*, Maui, HI, USA, ASME, New York, NY, USA, pp. 251-260.

Kang, Y. T., R. N. Christensen and K. Vafai (1994), "Analysis of Absorption Process in a Smooth-Tube Heat Exchanger with a Porous Medium," *Heat Transfer Engineering* Vol. 15(4) pp. 42-55.

Kang, Y. T., T. Kashiwagi and R. N. Christensen (1998), "Ammonia-Water Bubble Absorber with a Plate Heat Exchanger," *Proceedings of the 1998 ASHRAE Winter Meeting. Part 2 (of 2)*, San Francisco, CA, USA, ASHRAE, Atlanta, GA, pp. 1565-1575.

Kang, Y. T., T. Nagano and T. Kashiwagi (2002), "Mass Transfer Correlation of NH_3/H_2O Bubble Absorption," *International Journal of Refrigeration* Vol. 25(7) pp. 878-886.

Killion, J. D. and S. Garimella (2001), "A Critical Review of Models of Coupled Heat and Mass Transfer in Falling-Film Absorption," *International Journal of Refrigeration* Vol. 24(8) pp. 755-797.

Killion, J. D. and S. Garimella (2003a), "Gravity-Driven Flow of Liquid Films and Droplets in Horizontal Tube Banks," *International Journal of Refrigeration* Vol. 26(5) pp. 516-526.

Killion, J. D. and S. Garimella (2003b), "A Review of Experimental Investigations of Absorption of Water Vapor in Liquid Films Falling over Horizontal Tubes," *HVAC and R Research* Vol. 9(2) pp. 111-136.

Killion, J. D. and S. Garimella (2004), "Simulation of Pendant Droplets and Falling Films in Horizontal Tube Absorbers," *Journal of Heat Transfer* Vol. 126(6) pp. 1003-1013.

Kirby, M. J. and H. Perez-Blanco (1994), "A Design Model for Horizontal Tube Water/Lithium Bromide Absorbers," *Heat Pump and Refrigeration Systems Design, Analysis and Applications* Vol. 32 pp. 1-10.

Klein, S. A. (2006). *Engineering Equation Solver*, Middleton, WI.

Kwon, K. and S. Jeong (2004), "Effect of Vapor Flow on the Falling-Film Heat and Mass Transfer of the Ammonia/Water Absorber," *International Journal of Refrigeration* Vol. 27(8) pp. 955-964.

Lee, C. H., Y. T. Kang, H. U. Kang and S. H. Kim (2005), "Numerical and Experimental Study of Falling Film in Ammonia Absorption Refrigeration Systems," *Journal of Chemical Engineering of Japan* Vol. 38(7) pp. 520-527.

Lee, K. B., B. H. Chun, J. C. Lee, J. C. Hyun and S. H. Kim (2002), "Comparison of Heat and Mass Transfer in Falling Film and Bubble Absorbers of Ammonia-Water," *Experimental Heat Transfer* Vol. 15(3) pp. 191-205.

Lewis, W. K. and W. G. Whitman (1924), "Principles of Gas Absorption," *Industrial and Engineering Chemistry* Vol. 16 pp. 1215-1220.

McGahey, K. R., S. Garimella, F. B. Cook and R. N. Christensen (1994), "Enhancement of the Ornl Absorption Model and Simulation of a Double-Effect Absorption Heat Pump," *Proceedings of the International Absorption Heat Pump Conference, Jan 19-21 1994*, New Orleans, LA, USA, Published by ASME, New York, NY, USA, pp. 141-148.

Meacham, J. M. (2002). *An Integrated Experimental and Analytical Study of Ammonia-Water Absorption in Microchannel Geometries*. Mechanical Engineering. Ames, Iowa State University p. 140.

Meacham, J. M. and S. Garimella (2002a), "Experimental Demonstration of a Prototype Microchannel Absorber for Space-Conditioning Systems," *Int. Sorption Heat Pump Conf.*, Shanghai, China, ISHPC'02

Meacham, J. M. and S. Garimella (2002b), "Miniaturized Shell-and-Tube Heat and Mass Exchangers for Absorption Heat Pumps," *12th International Heat Transfer Conference*, Grenoble, France

Meacham, J. M. and S. Garimella (2003), "Modeling of Local Measured Heat and Mass Transfer Variation in a Microchannel Ammonia-Water Absorber," *ASHRAE Transaction* Vol. 109(1) pp. 412-422.

Meacham, J. M. and S. Garimella (2004), "Ammonia-Water Absorption Heat and Mass Transfer in Microchannel Absorbers with Visual Confirmation," *2004 Winter Meeting - Technical and Symposium Papers, American Society of Heating, Refrigerating and Air-Conditioning Engineers, Jan 24-28 2004*, Anaheim, CA, United States, Amer. Soc. Heating, Ref. Air-Conditoning Eng. Inc., Atlanta, GA 30329, United States, pp. 513-520.

Merrill, T., T. Setoguchi and H. Perez-Blanco (1994), "Compact Bubble Absorber Design and Analysis," *Proceedings of the International Absorption Heat Pump Conference*, New Orleans, LA, USA, pp. 217-223.

Merrill, T. L., T. Setoguchi and H. Perez-Blanco (1995), "Passive Heat Transfer Enhancement Techniques Applied to Compact Bubble Absorber Design," *Journal of Enhanced Heat Transfer* Vol. V 2(n 3) pp. 199-208.

Mills, A. F. (1995). *Heat and Mass Transfer*, Concord, MA Richard D. Irwin, Inc.

Nomura, T., N. Nishimura, S. Wei, S. Yamaguchi and R. Kawakami (1994), "Heat and Mass Transfer Mechanism in the Absorber of Water/LiBr Convectional Absorption Refrigerator: Experimental Examination by Visualized Model," *Proceedings of the International Absorption Heat Pump Conference*, New Orleans, LA, USA, Published by ASME, New York, NY, USA, pp. 203-208.

Nosoko, T., A. Miyara and T. Nagata (2002), "Characteristics of Falling Film Flow on Completely Wetted Horizontal Tubes and the Associated Gas Absorption," *International Journal of Heat and Mass Transfer* Vol. 45(13) pp. 2729-2738.

Onda, K., H. Takeuchi and Y. Okumoto (1968), "Mass Transfer Coefficients between Gas and Liquid Phases in Packed Columns," *Journal of Chemical Engineering of Japan* Vol. 1(1) pp. 56-62.

Palmer, S. C. and R. N. Christensen (1996), "Experimental Investigation and Model Verification for a GAX Absorber," *International ab-sorption heat pump conference*, Montreal, pp. 367-374.

Panchal, C. B., W. C. Kuru, F. C. Chen and N. Domingo (1997), "Experimental and Analytical Study of Condensation of Ammonia-Water Mixtures," *AIChE Symposium Series*, p. 239.

Perez-Blanco, H. (1988), "A Model of an Ammonia-Water Falling Film Absorber," *ASHRAE Transactions,* Vol. 94 (1) pp. 467-483.

Potnis, S. V., A. Gomezplata, R. A. Papar, G. Anand and D. C. Erickson (1997), "GAX Component Simulation and Validation," *ASHRAE Transactions* Vol. 103(1) pp. 454-459.

Price, B. C. and K. J. Bell. (1973), "Design of Binary Vapor Condensers Using the Colburn-Drew Equations," *Alche Symposium*, pp. 163-171.

Ruhemann, M. (1947), "A Study of the Transfer of Heat and Matter in an Ammonia Absorber," *Transactions of the Institute of Chemical Engineering* pp. 158-162.

Takuma, M., A. Yamada and T. Matsuo (1993), "Condensation Heat Transfer Characteristics of Ammonia-Water Vapor Mixture on Tube Bundles," *Condensation and Condenser Design, ASME* pp. 207-217.

Taylor, B. N. and C. E. Kuyatt (1993). Guidelines for Evaluating and Expressing the Uncertainty of Nist Measurement Results. National Institute of Standards and Technology. Washington, DC, USA, NIST/TN 1297, 15 p.

Tillner-Roth, R., Harms-Watzenberg and B. F., H.D (1993), "Eine Neue Fundamentalgleichung Für Ammoniak," *DKV-Tagungsbericht* Vol. 20 pp. 167-181.

Tufeu, R., D. Y. Ivanov, Y. Garrabos and B. Le Neindre (1984), "Thermal Conductivity of Ammonia in a Large Temperature and Pressure Range Including the Critical Region," *Berichte der Bunsengesellschaft fuer Physikalische Chemie* Vol. 88(4) pp. 422-427.

Wilke, C. R. (1950), "A Viscosity Equation for Gas Mixtures," *Journal of Chemical Physics* Vol. 18 pp. 517-519.

Wilke, W. (1962), "Heat Transfer to Falling Liquid Films

Waermeuebergang an Rieselfilme," *VDI -- Forschungsheft*(490) p. 36.

Ziegler, F. and G. Alefeld (1994), "Comparison of Multi-Effect Absorption Cycles," *Proceedings of the International Absorption Heat Pump Conference, Jan 19-21 1994*, New Orleans, LA, USA, Published by ASME, New York, NY, USA, pp. 257-264.